In Situ and Operando X-ray Scattering Methods in Electrochemistry and Electrocatalysis

Olaf Magnussen, Jakub Drnec, Canrong Qiu, Isaac Martens, Jason Huang, Raphaël Chattot, Andrej Singer

In situ and operando X-ray scattering methods in electrochemistry and electrocatalysis

Olaf M. Magnussen,[*,†,†] Jakub Drnec,[*,¶] Canrong Qiu,[†,§] Isaac Martens,[¶] Jason J. Huang,[‖] Raphaël Chattot,[⊥] and Andrej Singer[‖]

†*Kiel University, Institute of Experimental and Applied Physics, 24098 Kiel, Germany*
‡*Ruprecht-Haensel Laboratory, Kiel University, 24118 Kiel, Germany*
¶*ESRF, Experiments Division, 38000 Grenoble, France*
§*New address: DESY, Notkestraße 85, 22607 Hamburg, Germany*
‖*Department of Materials Science and Engineering, Cornell University, Ithaca, NY 14853, USA*
⊥*ICGM, Univ. Montpellier, CNRS, ENSCM, 34095 Montpellier Cedex 5, France*

E-mail: magnussen@email.uni-kiel.de; drnec@esrf.fr

Abstract

Electrochemical and electrocatalytic processes are of key importance for the transition to a sustainable energy supply as well as for a wide variety of other technologically relevant fields. Further development of these processes requires in-depth understanding of the atomic, nano, and micro scale structure of the materials and interfaces in electrochemical devices under reaction conditions. We here provide a comprehensive review of *in situ* and *operando* studies by X-ray scattering methods, which are powerful and highly versatile tools for provide such understanding. We discuss the application of X-ray scattering to a wide range of electrochemical systems, ranging from metal and oxide single crystals to nanoparticles and even full devices, show how structural data on bulk phases, electrode-electrolyte interfaces, and nanoscale morphology can be obtained, and describes recent developments that provide highly local information and insight into the composition and electronic structure. These X-ray scattering studies provide structural insights in the double layer potential range as well as into the structural evolution during electrocatalytic processes and phase formation reactions, such as nucleation and growth during electrodeposition and dissolution, the formation of passive films, corrosion processes, and the electrochemical intercalation into battery materials.

Contents

1 Introduction

For the upcoming transition towards a sustainable society, economically viable technology is necessary that allows storing electric energy from renewable sources and converting it back for mobile and stationary applications. This need led to a renaissance of electrochemistry, which provides direct and efficient ways for electric energy conversion and storage. Extensive efforts are ongoing to further develop electrochemical devices, such as batteries, electrolysers, fuel cells, and processes for the electrochemical production of synthetic fuels and base chemicals. These require deeper knowledge of electrocatalytic reactions as well as electrochemical intercalation and phase formation processes. Intertwined with this are traditional fields of electrochemical science and engineering, such as electroplating, electrosynthesis, and corrosion. The latter are still important in their own right but also play new roles in the context of energy science, for example in the context of electrocatalyst preparation and stability. Progress in all these areas depends on understanding the involved electrochemical processes on the molecular scale, for which detailed knowledge on the structure of materials and their interfaces and structural changes under relevant conditions is a central prerequisite.

Most materials characterization is still done at ambient conditions. Typically, the structure of the as-prepared materials is compared with that after using the material in the studied electrochemical process. While this can still provide useful information, the problems of this approach are evident. First, the transfer of the sample out of the electrochemical environment can lead to structural changes that can be difficult to distinguish from changes caused by the electrochemical reaction itself. In particular, this transfer necessarily involves the loss of potential control. For the most important case – an electrode taken out of an (aqueous) electrolyte – this will result in a transient state, in which the electrode is covered by a thin, typically air-saturated film of electrolyte at open circuit potential. This situation is well-known in the context of atmospheric corrosion and often results in surface oxidation and material dissolution. Furthermore, transfer through the laboratory air may result in additional surface contamination. These problems are especially significant for studies aiming at understanding the surface structure and properties, e.g., of electrocatalysts. In contrast, studies of bulk materials are less affected. A second problem of this approach is that information on the structural evolution of the sample at different stages or times during the process can only be obtained by studying a large number of identical samples, exposed to different conditions. Such studies are tedious and ensuring comparability of the employed samples can be challenging.

The first approach to overcome these prob-

lems was developed in the 1980ies. It is based on the preparation of the electrode under ultra-high vacuum (UHV) combined with a careful transfer under inert gas into electrolyte solutions for electrochemical studies and back-transfer to UHV for analysis by surface science methods. In recent years, this *ex situ* approach has been rediscovered and is now often called somewhat euphemistically quasi *in situ*. Pioneering *ex situ* studies demonstrated that, dependent on the system, some but not necessarily all properties of the electrochemical environment can be maintained[1,2]. Often, the success of this approach depends on subtle details, such as the behavior of electrolyte species during emersion. In particular, *ex situ* studies are not possible in potential regimes where faradaic currents occur, because the open circuit conditions during transfer will necessarily result in a potential shift into the double layer range, with resulting changes in the geometric and electronic structure of the interface. This makes studies of the electrode structure under reaction conditions impossible.

True insights into the state of electrochemical material systems require *in situ* and *operando* methods, where structural data are obtained directly in electrochemical environment. These methods have to be capable of probing bulk materials and interfaces that are deeply buried in liquid or solid phases. Most typically used are techniques that are based exclusively on near-field effects, such as in scanning probe microscopy, or on the scattering or absorption of photons. The difference between *in situ* and *operando* measurements is often not clearly differentiated in electrochemical publications. We here follow the definition commonly employed in studies of thermal heterogeneous catalysis in the gas phase. According to this definition, *in situ* and *operando* studies both study materials or interfaces in their natural environment, i.e., in the case of electrochemical systems in the presence of the electrolyte and at controlled potential or current density. However, in contrast to *in situ* measurements, *operando* studies monitor structural or electronic properties of the material in parallel to properties that are linked with material function, e.g., the activity in the case of an electrocatalyst, and directly correlate both. In principle, *operando* studies are straightforward in electrochemistry, as the relevant functional property is often the electrochemical response, which is anyway recorded by the potentiostat. Typical examples are measurements where the structure is recorded during a cyclic voltammogram (CV) and features in the latter compared to parallel structural changes. However, in practice *operando* studies may not be that easy, because the experimental geometry may restrict mass transport and electric conductivity and thus the current density. This is, for example, the case in studies that employ a thin layer geometry, where *in situ* measurements in the electrolyte are still possible, but not *operando* studies at high current density or under gas evolution conditions.

This review focuses on *in situ* and *operando* studies by X-ray scattering and diffraction methods. X-ray diffraction (XRD) is a standard method in analytical chemistry to determine the atomic crystal structure of bulk materials and the basis of modern crystallography. It is typically performed using hard X-rays with photon energies in the range 5-25 keV. Since the atomic cross sections for the absorption and scattering of such photons are low, in particular for low-Z elements, X-rays can penetrate deep into the condensed matter and hence are well-suited for studies inside solid and liquid phases. Furthermore, the measurement is not impeding mass transport and electrochemical reactions, making *operando* much easier than most competing techniques. Whereas X-ray diffraction describes the scattering of X-rays by a crystal lattice, other X-ray scattering methods explore the atomic, nano, and micro scale structure of less ordered matter.

A wide range of structural features of material systems can be accessed, including the structure of nanoparticles, defects, surfaces and interfaces, and even the average structural arrangement within liquids and at liquid interfaces. Furthermore, modern approaches provide information on chemical composition and electronic structure as well as allow direct imaging of individual nanoobjects. In addition, X-ray scattering can deliver time-resolved data

over a wide temporal range, reaching from femtoseconds to days. This provides access to the kinetic behavior and nanoscale dynamics of the studied systems.

Many of the more advanced methods rely on the analysis of scattering signals that are several orders of magnitude lower than those originating from bulk crystals. Their development depends, therefore, on sufficiently intense sources of hard X-rays and thus has been strongly coupled to developments in synchrotron science. With the increasing performance and availability of synchrotron sources and the instrumentation provided there, also the capabilities and application ranges of X-ray scattering methods increase continuously. This opens up attractive opportunities for energy and electrochemical research.

In the following, we provide an introduction into *in situ* and *operando* structural studies of electrochemical systems by X-ray scattering and diffraction methods. The review's objectives are twofold: First, it aims at helping non-specialist readers to add these methods to their toolbox of advanced techniques for research in electrochemistry and energy science, by providing a basic understanding of these methods. This understanding will help in better assessing specialist papers employing modern X-ray scattering methods and to make first steps towards using these methods. Second, it gives a comprehensive overview over the results obtained in the area of electrochemistry by *in situ* and *operando* X-ray scattering since the beginning of this field in the 1990ies. The latter illustrates the capabilities of X-ray scattering methods as well as provides a resource for the corresponding community. We stress that we do not intend to provide an in-depth introduction to the theory of X-ray scattering and the technical aspects of the individual techniques, which are complex and require attention to many technical details that are too numerous to be treated within the scope of this review. A number of excellent books and reviews on these topics exists (see references in the individual sections), which discuss these techniques in much greater detail.

In chapter 2, we first discuss the origin of X-ray scattering and how it is influenced by the spatial distribution of matter on the atomic scale. This is required for a true understanding of X-ray scattering data that goes beyond a fingerprint type of interpretation of powder diffractograms or crystallographic data. Every scattering experiment effectively performs the equivalent of a Fourier transform of the sample structure and thus is best described in the Fourier space, commonly denoted as reciprocal space. This concept is not easily comprehensible but essential for the interpretation of scattering data. We try to convey this concept in a compact way and then show how this applies to various relevant ensembles of atoms, such as crystals, liquids, crystal surfaces, interfaces, and nanoparticles. Subsequently, we treat in chapter 3 various experimental aspects, such as X-ray instrumentation, electrochemical cells for *in situ* and *operando* measurements, as well as potential detrimental effects of the X-ray beam on the sample. Chapter 4 describes in detail X-ray scattering techniques for *in situ* and *operando* studies of electrochemical systems. These are sorted by the type of samples to which they are typically applied to and the information that can be obtained from them.

The rest of the review summarizes the results obtained from *in situ* and *operando* studies by X-ray scattering methods. Chapter 5 gives an overview on studies of the structure of electrochemical interfaces. It describes X-ray scattering results on the surface structure of metal and oxide electrodes in liquid electrolytes and on the arrangement of various adsorbates at these electrodes. Because many of these results were already topics of more specialized previous reviews, this section is kept concise. Also included here are studies of more unconventional interfaces, such as interfaces to ionic liquids and liquid-liquid interfaces. Whereas chapter 5 predominantly focuses on the electrode structure in the absence of continuous faradaic reactions, the latter are the center of interest of the subsequent chapters.

In chapter 6, studies in the field of electrocatalysis are described. Here, we discuss X-ray scattering results on the interface and bulk structure of electrocatalysts under dif-

ferent electrode reactions. The research in this area encompasses studies of single crystalline model catalysts and catalyst nanoparticles. Furthermore, it includes direct studies of materials in devices for energy conversion, such as fuel cells and electrolyzers. Chapter 7 presents *in situ* and *operando* results on electrochemical phase formation processes. These include studies of electrodeposition and electrochemical dissolution, passivation and corrosion, and processes employed in the synthesis of electrocatalysts. Finally, chapter 8 provides an overview on the application of X-ray scattering methods to intercalation batteries. As the phase changes caused by electrochemical intercalation have been studied for a long time by X-ray diffraction, we here rather focus on more modern approaches that are capable of providing local structural data on particles or interfaces in batteries.

2 X-ray scattering

2.1 X-ray interactions with matter

In this chapter, we will give a brief introduction to the theory of X-ray scattering to provide some insight into the various types of signals produced by liquids, two-dimensional (2D) and three-dimensional (3D) crystals, as well as crystal surfaces. The reader is warned: scattering theory is a complex topic, and the treatment here will merely impart some basic ideas that are essential for understanding scattering studies. More technical aspects of the analysis of X-ray scattering data can be found in the literature[3–6].

The following treatment is limited to scattering within the kinematic approximation. Within this approximation, it is assumed that (i) no multiple scattering occurs within the sample, (ii) refraction effects can be neglected, and (iii) the scattering is elastic, i.e., the energies (or wavelengths, respectively) of the incident and scattered wave are identical. To a large extent, these assumptions are justified for X-ray scattering by the (non-perfect) samples typically used in most studies, including those of electrochemical interfaces: the probability for multiple scattering is low due to the low scattering cross-section of X-rays, the inelastic scattering contribution is much weaker than the elastic scattering in the typically employed photon energy range, and the index of refraction is very close to one for all materials. Nevertheless, the latter has to be considered to rationalize some characteristic effects in surface scattering. We will therefore revisit the role of refraction effects when discussing the specific surface scattering methods in chapters 4.3 and 4.4.

2.2 Fundamentals of X-ray scattering

All scattering processes have in common a change in the momentum and energy of the scattered objects. Methods for structure determination are based on elastic X-ray scattering. Here, all possible scattering events of a sample with a given orientation can be described by the involved momentum transfer. We assume in the following that the reader is familiar with the properties and the mathematical description of electromagnetic radiation and recall that (apart from the factor $\hbar$) the momentum of a photon is given by the wave vector $\mathbf{k}$, which is oriented parallel to the propagation direction and of magnitude $k = 2\pi/\lambda$. For an incident and scattered wave with wave vectors $\mathbf{k_i}$ and $\mathbf{k_f}$, respectively (see Figure 1a), the scattering process is hence described by the wave vector transfer or scattering vector $\mathbf{q} = \mathbf{k_f} - \mathbf{k_i}$, which is the central variable in scattering theory. q is commonly measured in units of Å^{-1} and the 3D space defined by it is therefore termed reciprocal space. Its modulus is related to the scattering angle 2θ via $q \equiv |\mathbf{q}| = 2k \cdot \sin(2\theta/2) = \frac{4\pi}{\lambda} \cdot \sin(2\theta/2)$ For elastic scattering, where $k_f = k_i = k$, the q vectors corresponding to the $\mathbf{k_f}$ of all elastically scattered waves are located on the surface of a sphere, whose center is given by $-\mathbf{k_i}$. This sphere is called the Ewald sphere. It plays an important role in the interpretation of scattering data, as it defines the q vectors probed at a

defined incident wave vector $\mathbf{k_i}$, e.g., by recording the intensity with an area detector.

In the following, we will first discuss in a more general way how the variation of the scattered intensity I with $\mathbf{q}$ depends on the spatial arrangement of the scatterers before turning to the description of scattering by solids, liquids, and interfaces. In classical Thompson scattering, the X-rays interact with electrons, and their scattering can be described by the process illustrated in Figure 1b for a linearly polarized incident X-ray wave propagation along the direction described by wave vector $\mathbf{k_i}$. The oscillating electric field of this wave excites a forced vibration of the electron, resulting in the emission of electric dipole radiation, i.e., of a spherical wave of identical wavelength. As for every dipole radiation, the emission is isotropic within the plane normal to the incident wave field vector ϵ_i, whereas for directions under an angle 2θ out of this plane, the emitted intensity is reduced by the polarization factor $\cos^2(2\theta)$. For the atomic nuclei, this Thomson scattering process can be neglected since their excitation is weak due to the much higher mass.

To understand the scattering by an ensemble of several electrons, we first consider the simple case of two electrons, separated by a distance-vector $\mathbf{r}$ (Figure 1c). The incident plane wave will excite spherical waves originating from the positions of the two electrons, which will interfere with each other. In a scattering experiment, we measure the intensity scattered in direction $\mathbf{k_f}$ with a detector that is much further away from the sample than the distance between the scattering electrons. The spherical waves can therefore be approximated by plane waves with the wave vector $\mathbf{k_f}$. Because the wave scattered by electron 2 travels a longer distance than that scattered by electron 1, the two waves are phase shifted to each other by a distance of $\mathbf{r}\cdot\mathbf{k_i}/k - \mathbf{r}\cdot\mathbf{k_f}/k$, i.e., a phase shift $-\mathbf{r}\cdot\mathbf{q}$, illustrating clearly the central role of the scattering vector. Employing the complex representation of plane waves, the electric field vector amplitudes of the two scattered waves only differ by the phase factor $\exp(-i\,\mathbf{r}\cdot\mathbf{q})$ and the superposition is described by adding up both of these complex amplitudes. Depending on

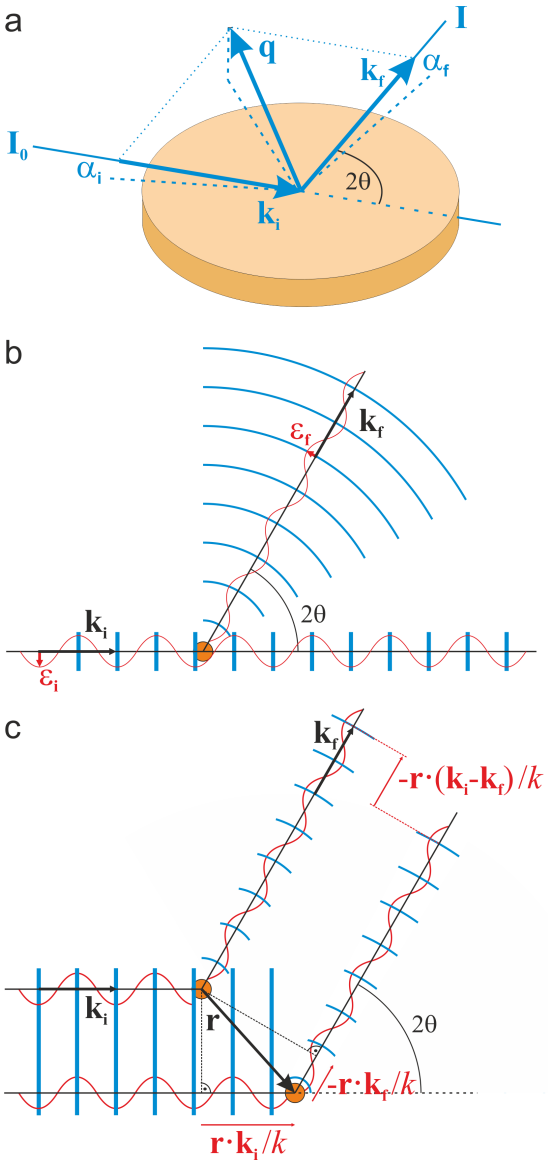

Figure 1: (a) Geometry of a scattering experiment. (b) Classical description of the scattering of electromagnetic waves by a charged particle. (c) Scattering by an ensemble of two scatterers, illustrating the resulting phase shift between the scattered waves.

the phase factor, i.e., on $\mathbf{r}$ and $\mathbf{q}$, the scattered waves will interfere constructively or destructively, resulting in enhancement or reduction of the scattered radiation.

This simple case illustrates a general, useful concept: The scattered intensity $I(\mathbf{q})$ probes spatial correlations of the electron density along the direction of scattering vector $\mathbf{q}$ on a length scale given by $2\pi/q$. However, as we will see below, these correlations are not necessarily directly identical to the distances between the atoms of the system. The key to understanding scattering experiments is to grow accustomed to the description of structure in the reciprocal space, defined by the scattering vector $\mathbf{q}$, rather than in real space.

The case of two scattering electrons can be easily generalized to an arbitrary spatial electron distribution, described by the electron density $\rho_e(\mathbf{r})$. The number of electrons in an infinitesimal volume element $d\mathbf{r}$ at position $\mathbf{r}$ is then $\rho_e(\mathbf{r})d\mathbf{r}$ and their contribution to the field vector of the scattered wave has to be multiplied by the corresponding phase factor for this position. By integrating over the entire sample (still assuming the sample size is much smaller than the sample-detector distance), we obtain the scattering amplitude:

$$S(\mathbf{q}) = \int \rho_e(\mathbf{r}) \cdot \exp(-i\mathbf{r}\cdot\mathbf{q}) d\mathbf{r} \qquad (1)$$

which is proportional to the field amplitude of the scattered wave. Therefore, $S(\mathbf{q})$ is the Fourier transform of the electron density and hence contains the full information about the structural arrangement. Yet a typical X-ray scattering experiment only measures the scattered intensity, which is (neglecting polarization, absorption, etc.) proportional to $|S(\mathbf{q})|^2 = S(\mathbf{q})S^*(\mathbf{q})$ (* denotes the complex conjugate) and does not contain the phase of the complex quantity $S(\mathbf{q})$:

$$\begin{aligned} |S(\mathbf{q})|^2 &= \iint \rho_e(\mathbf{r}) \cdot \exp(-i\mathbf{r}\cdot\mathbf{q}) \cdot \rho_e(\mathbf{r}') \\ &\quad \cdot \exp(i\mathbf{r}'\cdot\mathbf{q}) d\mathbf{r}' d\mathbf{r} \\ &= \iint \rho_e(\mathbf{r}) \cdot \rho_e(\mathbf{r}+\mathbf{R}) d\mathbf{r} \\ &\quad \cdot \exp(-i\mathbf{R}\cdot\mathbf{q}) d\mathbf{R} \end{aligned} \qquad (2)$$

Equation (2), where we have substituted the integration over $\mathbf{r}'$ by an integration over the difference vector $\mathbf{R} \equiv \mathbf{r} - \mathbf{r}'$, it becomes apparent that a scattering experiment measures spatial correlations within the sample. In the remainder of this chapter, we will use examples to develop a sense of how $I(\mathbf{q})$ depends on the structural arrangement within the sample.

2.3 Scattering by the atomic structure within condensed matter

2.3.1 Scattering by ensembles of atoms

Describing the sample as a continuous distribution of electrons, as we have done above, is convenient in some scattering experiments, especially for studies at small q, where the experiments only probe long-range correlations. However, in most cases, it is preferable to account for the atomic structure of condensed matter. The large majority of all electrons in a sample are located in the ion cores where their distribution $\rho_e^{\mathrm{atom}}(\mathbf{r})$ around the nucleus is given by the occupied atomic orbitals. The scattering amplitude Eq. (1) of a single atom (or ion) with Z electrons is called the atomic form factor:

$$f(\mathbf{q}) \equiv \int \rho_e^{\mathrm{atom}}(\mathbf{r}) \cdot \exp(-i\mathbf{r}\cdot\mathbf{q}) \mathrm{d}\mathbf{r} \qquad (3)$$

In practice, one usually ignores the small deviations of $\rho_e^{\mathrm{atom}}(\mathbf{r})$ from spherical symmetry and uses functions $f(q)$ that only take the dependence on the amplitude of the scattering vector into account. Atomic form factors smoothly decay with increasing q from (within the kinematic approximation) $f(0) = Z$ to 0. Parameterized functions, obtained by fits to the re-

sults of detailed quantum mechanical calculations, can be found for all atoms and many ions in the relevant literature (See, for example, International Tables for Crystallography (2006). Vol. C. Ch. 6.1, pp. 554-595).

A more precise quantum mechanical description shows that the scattering by an atom also depends on the binding strengths of the electrons to the nucleus, which for the core level electrons are determined by discrete energy levels. This correction gives rise to a change of the atomic form factor, which depends on the photon energy ε_{Ph} and, by convention, is denoted f'. Furthermore, the scattering may exhibit an additional phase-shift with respect to the field of the incident wave, especially if ε_{Ph} is in resonance with a core level energy, which can be described by an imaginary term if''. Both of these contributions are largely independent of $\mathbf{q}$. For a precise description of the scattering, $f'(\varepsilon_{Ph}) + if''(\varepsilon_{Ph})$ has to be added to the form factor $f(q)$ in Eq. 3. This is critical for resonant scattering (see section 2.5) and will otherwise be ignored in the following.

Next, we consider an ensemble of atoms, for example, a molecule or the atoms in the unit cell of a crystal, which have well-defined positions $\mathbf{r_j}$ with respect to a common origin. The electron density is then given by the sum over all atoms $\rho_e(\mathbf{r}) = \sum_j \rho_e^{\mathrm{atom},j}(\mathbf{r}-\mathbf{r_j})$ and the corresponding scattering amplitude conventionally termed structure factor $F(\mathbf{q})$. The latter can be calculated via Eq. 1 by replacing the integration over $\mathbf{r}$ in each summand by integration over the relative spatial coordinates $\mathbf{r}-\mathbf{r_j}$) and using Eq. 3, resulting in:

$$F(\mathbf{q}) = \sum_j f_j(q) \cdot \exp(-i\mathbf{r}_j \cdot \mathbf{q}). \qquad (4)$$

The effect of thermal vibrations of the atoms around the equilibrium positions $\mathbf{r}_j$ can be included in the atomic form factors by an additional Gaussian factor, i.e., by replacing $f_j(q)$ in Eq. (4) with:

$$f_j(q)\cdot\exp(-\frac{1}{2}q^2\cdot\langle\mathbf{u}^2_{j,\mathbf{q}}\rangle) \equiv f_j(q)\cdot\exp(-M_j) \quad (5)$$

Here $\langle\mathbf{u}^2_{j,\mathbf{q}}\rangle$ is the mean-square amplitude of vibration of atom j in direction $\mathbf{q}$ and M_j is called the Debye-Waller factor of the atom. Often, M_j is assumed to be isotropic in space (i.e., only dependent on q), but for species at interfaces, the difference between surface-normal and in-plane vibration amplitudes has to be considered explicitly.

We will use Eq. (4) in the following chapters to derive the scattering for the components in electrochemical systems. This includes bulk solids and liquids as well as (quasi-) 2D systems, such as crystal surfaces and adsorbate layers.

2.3.2 Scattering by three-dimensional and two-dimensional crystals

Scattering by periodic lattices results in discrete, well-defined intensity peaks at defined $S(\mathbf{q})$ values, an effect called diffraction. Although X-ray diffraction by bulk crystals is treated in every introduction to solid-state physics, we here briefly repeat the derivation of the basic equations, since those can be easily varied to describe the scattering by 2D lattices and crystal surfaces.

Let us consider a 3D crystal defined by the lattice vectors $\mathbf{a}_1, \mathbf{a}_2$, and $\mathbf{a}_3$. For simplicity, we assume that the crystal is a block consisting of N_1, N_2, and N_3 unit cells along the three lattice directions. The position of a unit cell is then given by the vector $\mathbf{R} = n_1\mathbf{a}_1 + n_2\mathbf{a}_2 + n_3\mathbf{a}_3$, and the scattering amplitude is:

$$S(\mathbf{q}) = F(\mathbf{q}) \sum_{n_1=0}^{N_1-1} \sum_{n_2=0}^{N_2-1} \sum_{n_3=0}^{N_3-1} \exp[-i(n_1\mathbf{a}_1 + n_2\mathbf{a}_2 + n_3\mathbf{a}_3)\cdot\mathbf{q}]$$
$$= F(\mathbf{q}) \sum_{n_1=0}^{N_1-1} \exp(-in_1\mathbf{a}_1\cdot\mathbf{q}) \sum_{n_2=0}^{N_2-1} \exp(-in_2\mathbf{a}_2\cdot\mathbf{q}) \sum_{n_3=0}^{N_3-1} \exp(-in_3\mathbf{a}_3\cdot\mathbf{q}) \quad (6)$$

Here, the possibility that the unit cell contains several atoms is accounted for by the structure factor $F(\mathbf{q})$, which can be calculated from Eq. (4) with the $\mathbf{r}_j$ given with respect to the origin of the unit cell. According to the second line of this equation, $S(\mathbf{q})$ is the product of the structure factor with three independent sums of the identical type that can be evaluated using the geometric series:

$$S_N(x) = \sum_{n=0}^{N-1} \exp(-inx) = \frac{1-\exp(-iNx)}{1-\exp(-ix)} \quad (7)$$

The scattered intensity is the square modulus of $S(\mathbf{q})$. It is identical to the "N-slit interference function" known from optics, which describes the intensity distribution of an ideal grating composed of N slits:

$$|S_N(x)|^2 = \frac{\sin^2(Nx/2)}{\sin^2(x/2)} \quad (8)$$

This function has pronounced primary maxima at $x = 2\pi n$ (with n being an integer), which have a height N^2, a full width at half maximum (FWHM) of approximately $2\pi/N$ (the FWHM is converging to $0.88\cdot 2\pi/N$ for large N), and $N-2$ subsidiary maxima, which are negligibly small for large N as in typical crystals (Figure 2).

The scattered intensity for the 3D crystal is therefore given by:

$$|S(\mathbf{q})|^2 = |F(\mathbf{q})|^2 \cdot |S_{N_1}(\mathbf{a}_1\cdot\mathbf{q})|^2 \cdot |S_{N_2}(\mathbf{a}_2\cdot\mathbf{q})|^2 \cdot |S_{N_3}(\mathbf{a}_3\cdot\mathbf{q})|^2 \quad (9)$$

and exhibits peaks if all three interference functions are at a maximum, i.e., if the following three equations, called the Laue conditions, are

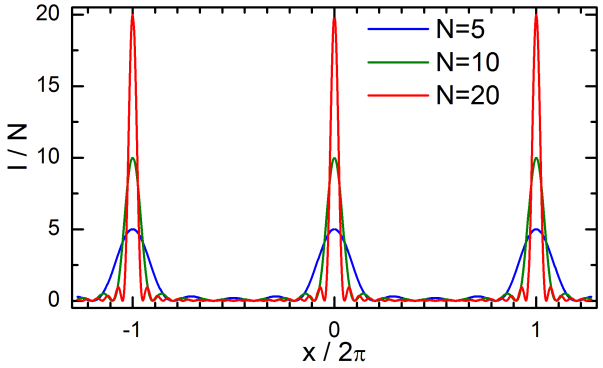

Figure 2: N-slit scattering function for a row of N equally spaced unit cells. Shown is the scattered intensity I normalized by N.

simultaneously fulfilled:

$$\mathbf{a}_1\mathbf{q} = 2\pi h; \quad \mathbf{a}_2\mathbf{q} = 2\pi k; \quad \mathbf{a}_3\mathbf{q} = 2\pi l \quad (10)$$

The integers h, k, and l are called Miller indices. Eq. (10) can be satisfied by $\mathbf{q}$ vectors of the type:

$$\mathbf{q} = h\cdot\mathbf{b}_1 + k\cdot\mathbf{b}_2 + l\cdot\mathbf{b}_3 \quad (11)$$

where $\mathbf{b}_1$, $\mathbf{b}_2$, and $\mathbf{b}_3$ are vectors in reciprocal space which obey the conditions (δ_{ij} is the Kroneker delta):

$$\mathbf{a}_j\cdot\mathbf{b}_k = \delta_{jk} \quad (12)$$

$\mathbf{b}_1$, $\mathbf{b}_2$, and $\mathbf{b}_3$ define a 3D lattice in reciprocal space and hence are called the reciprocal lattice vectors of the crystal. They can be calculated via:

$$\mathbf{b}_1 = \frac{2\pi}{V_c}\mathbf{a}_2\times\mathbf{a}_3; \quad \mathbf{b}_2 = \frac{2\pi}{V_c}\mathbf{a}_3\times\mathbf{a}_1; \quad \mathbf{b}_3 = \frac{2\pi}{V_c}\mathbf{a}_1\times\mathbf{a}_2 \quad (13)$$

where $V_c = \mathbf{a}_1\cdot(\mathbf{a}_2\times\mathbf{a}_3)$ is the volume of the crystal's unit cell. For crystals with cubic unit cells of length a, which covers a large fraction of the metals used commonly as electrode materials, the reciprocal lattice vectors $\mathbf{b}_j$ are parallel

to the corresponding lattice vectors $\mathbf{a}_j$ in real space and $|\mathbf{b}_j| = b = 2\pi/a$.

At the reciprocal space positions defined by Eq. (11), the scattered X-ray intensity exhibits peaks whose integrated intensity is proportional to:

$$|S(\mathbf{q})|^2 = |F(h \cdot \mathbf{b}_1 + k \cdot \mathbf{b}_2 + l \cdot \mathbf{b}_3)|^2 \cdot N_1 N_2 N_3 \tag{14}$$

i.e., scales with the structure factor measured at these $\mathbf{q}$ values and the total number of atoms in the sample. For large 3D crystals, the scattering between these peaks is negligible. This distribution $I(\mathbf{q})$ in reciprocal space is illustrated schematically in Figure 3a. The peaks are the Bragg reflections of the crystal, each defined by a triplet of Miller indices hkl. They originate from the constructive interference of atomic planes in the crystal lattice. For example, the 110 reflection of the cubic crystal in Figure 3a is observed at $q = \sqrt{2}b$, corresponding to the nearest neighbor spacing $2\pi/q = a\sqrt{2}$ between the diagonal planes of the atoms perpendicular to that direction. As discussed before, this inverse relationship between the peak positions in reciprocal space and the real space distances of the atoms in the sample is characteristic in scattering experiments.

A 2D lattice defined by vectors $\mathbf{a}_1$ and $\mathbf{a}_2$ can be treated analogously (Figure 3b). The scattering amplitude is now:

$$|S(\mathbf{q})|^2 = |F(\mathbf{q})|^2 \cdot |S_{N_1}(\mathbf{a}_1 \cdot \mathbf{q})|^2 \cdot |S_{N_2}(\mathbf{a}_2 \cdot \mathbf{q})|^2 \tag{15}$$

and consequently only two Laue conditions with the Miller indices h and k and corresponding reciprocal space vectors $\mathbf{b}_1$ and $\mathbf{b}_2$ exist. The component $q_\perp$ of $\mathbf{q}$ along the direction normal to this plane (i.e., parallel to $\mathbf{a}_1 \times \mathbf{a}_2$) only enters in the structure factor $F(\mathbf{q})$. If all atoms are located in the same plane as in a simple monolayer, $F(\mathbf{q})$ is independent of $q_\perp$, apart from the slow decay caused by the q-dependence of the atomic form factor. The distribution of the scattered intensity in reciprocal space then takes on the form of continuous rods that are oriented perpendicular to the crystal plane and arranged in a 2D lattice within this plane (Figure 3b). These diffraction rods are the hall-

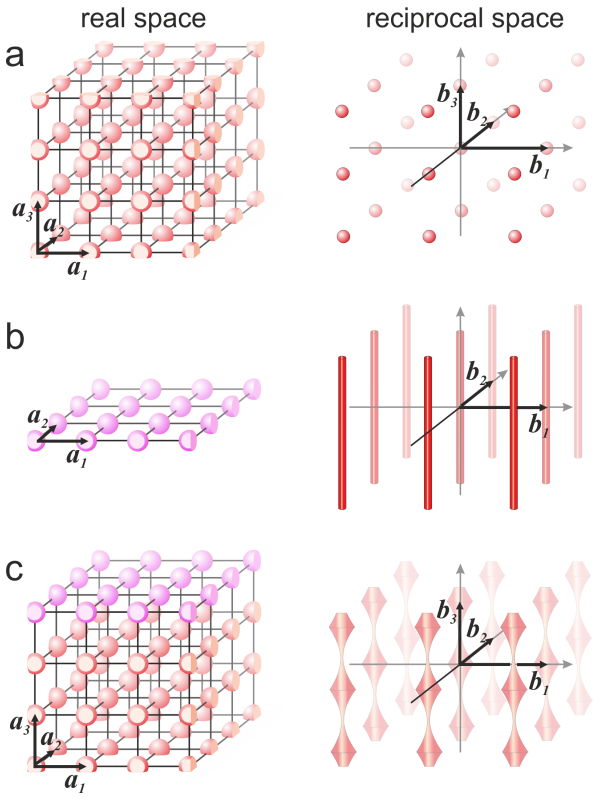

Figure 3: Real space structure (left) and distribution of scattered intensity in reciprocal space (right) for (a) a 3D crystal lattice, (b) a 2D lattice, and (c) the surface of a 3D crystal. The variation of the intensity along the diffraction rods shown in (b) and (c) is indicated by the rod diameter.

mark of any scattering by a (quasi-) 2D system and explain why the contribution of interfaces or adsorbed layers can easily be separated from that of the bulk, despite the much smaller number of contributing atoms: While the scattering from 3D bulk crystals is concentrated at discrete points in reciprocal space and hence only observed for certain well-defined orientations of sample and detector, the scattering by 2D lattices, although much weaker, is distributed over a wider region of reciprocal space. It, therefore, can be separated from the scattering by the 3D crystalline substrate by measuring at reciprocal space positions along the rods that are sufficiently far away from the Bragg peaks.

From the above derivation, it follows that the scattered intensity distribution not only contains information about the atomic distances but also about the shape of the scattering crystal. This shape determines the width of the main peak as well as the minor peaks in the N-slit scattering function (see Fig. 2). The intensity distribution for a simple 3D crystal with orthogonal edges is already given by Equation 9. The diffracted X-ray intensity from an arbitrarily shaped crystal can be calculated from the electron density via a Fourier transform by using the Ewald function $s(r)$, which is unity inside the crystal and zero outside[7,8]. For example, in a cubic perfectly crystalline particle, the diffraction intensity can be described as the product of three sinc functions, as described in section 2.3.2. In electrochemical systems, crystals are often distorted: the atomic positions deviate from the ideal lattice. If the crystalline planes are distorted, the positions of the unit cells $\mathbf{R} = \mathbf{R}_0 + \mathbf{u}(\mathbf{R})$, where $\mathbf{R}_0$ are the atomic coordinates of the undistorted lattice and $\mathbf{u}(\mathbf{R})$ is the displacement field. These distortions will result in a change of Laue fringes visible in Figure 2. It can be shown that the intensity in the vicinity of a Bragg peak hkl, can be well approximated with[8]

$$I(\mathbf{Q}) = |F_{hkl}|^2 \int s_{hkl}(\mathbf{r}) \exp\left(-i\mathbf{G}_{hkl} \cdot \mathbf{u}(\mathbf{r})\right) \mathrm{d}\mathbf{r} \tag{16}$$

, where F_{hkl} is the unit cell structure factor, $s_{hkl}(\mathbf{r})$ is the density of (hkl) Bragg planes multiplied by the Ewald function, and the momentum transfer, $\mathbf{Q} = \mathbf{q} - \mathbf{G}_{hkl}$, is the distance of the reciprocal space position from the reciprocal lattice point $\mathbf{G}_{hkl}$. Therefore, the intensity and shape of the interference fringes decorating the Bragg peak contain information on the crystal shape and the crystalline distortions within.

2.3.3 Scattering of surfaces and interfaces

We now analyze how the surface of a 3D crystal contributes to the scattering, following the literature on surface diffraction[4,5,9]. Specifically, we consider a semi-infinite crystal with lattice vector $\mathbf{a}_3$ along the surface normal and $\mathbf{a}_1$ and $\mathbf{a}_2$ are within the surface plane, see Figure 3c (this is always possible by choosing a suitable unit cell and conventionally used in surface diffraction studies). We further assume a scattering geometry as in Figure 1a where incident and scattered X-ray beam approach and leave through the free space on top of the crystal, respectively. Using Eq. (10) and taking into account that due to X-ray absorption each penetrated atomic layer of the crystal reduces the intensity by a factor $\exp(-\beta)$, we can rewrite Eq. (6) :

$$S(\mathbf{q}) = F(\mathbf{q}) \sum_{n_1=0}^{N_1} \exp(-2\pi i n_1 h) \sum_{n_2=0}^{N_2} \exp(-2\pi i n_1 k) \sum_{n_3=-\infty}^{0} \exp(-2\pi i n_3 l) \cdot \exp(-\beta n_3) \tag{17}$$

The first two sums are identical to those of a 2D crystal lattice with lattice vectors $\mathbf{a}_1$ and $\mathbf{a}_2$. Their contribution to the scattering is therefore given by Eq. (15) and, in the limit of an infinite extension of the crystal in the surface plane, will approach a set of delta functions located at reciprocal space positions defined by integers h and k. The last sum contains the specific influence of the termination of the crystal at

the surface. Evaluating it, we obtain

$$S_{CTR}(\mathbf{q}) = \sum_{n_3=-\infty}^{0} \exp[(-2\pi i l - \beta) \cdot n_3] = \frac{1}{1 - \exp(-2\pi i l - \beta)} \quad (18)$$

Typically, absorption only has a substantial influence near the Bragg peaks (i.e., if l is close to an integer value), where it results in a reduction of the peak intensity. Assuming $\beta \ll 1$, we obtain from Eq. (18):

$$S_{CTR}(\mathbf{q})^2 \approx \frac{1}{4\sin^2(\pi l)} \quad (19)$$

Hence, the intensity is a continuous function of l (defined through $\mathbf{a}_3\mathbf{q} = 2\pi l$) and again distributed in reciprocal space in the form of rods that are oriented along the surface normal (see Figure 3c) and pass through the Bragg peaks of the bulk crystal. Because these rods originate in the symmetry break at the surface of the semi-infinite lattice, they are called crystal truncation rods (CTRs). However, contrary to the rods for a single 2D layer, the intensity along the CTRs strongly varies with the surface normal component of the scattering vector $q_z = l\mathbf{b}_3$.

Specifically, the intensity rapidly decays to both sides of the Bragg peaks, reaching minima at half-integer l, the so-called anti-Bragg position, where it is of similar magnitude as the scattering by a single 2D layer. In other words, the presence of the surface induces streaks of scattering that extend out from the Bragg peaks. Summarizing these results, the scattered intensity from an ideal crystal surface is:

$$|S(\mathbf{q})|^2 = |F(\mathbf{q})|^2 \cdot |S_{N_1}(\mathbf{a}_1 \cdot \mathbf{q})|^2 \cdot |S_{N_2}(\mathbf{a}_2 \cdot \mathbf{q})|^2 \cdot |S_{CTR}(\mathbf{q})|^2 \quad (20)$$

At real surfaces and interfaces, the atomic spacings and the Debye-Waller factors M, which describe the thermal vibrations, usually deviate from those in the bulk lattice. Furthermore, the topmost layers may exhibit defects, such as adatom or vacancy islands, and hence be only occupied to a fraction $\theta_j \leq 1$. These effects can be addressed by a scattering amplitude that is the sum of a surface contribution, consisting of a finite number N_{surf} of atomic layers that are located at vertical positions z_j relative to the first bulk-like layer, and a bulk contribution given by the semi-infinite sum in Eq. (18). The corresponding intensities can be obtained numerically from this expression. In most cases, only a very small number of layers has to be considered explicitly. Nevertheless, even rather small deviations from the ideal lattice parameters can give rise to substantial changes in the CTRs, as will be discussed in more detail in chapter 4.4.2. Similarly, a finite number of surface layers in which the atoms occupy different in-plane positions than in bulk or consist of different chemical species can be included explicitly in Eq. 17 to describe surface reconstructions and adsorbates.

2.3.4 Scattering of liquids and amorphous materials

As the last case, we discuss the scattering by a liquid or amorphous material. These two cases are very similar; the main difference is that for the first the disorder is dynamic whereas for the second it is static. This difference is only relevant for more advanced cases, such as inelastic scattering, but can be ignored in the framework of the simple theory described here. Scattering by non-crystalline matter is a more advanced topic (see Ref.[10] for a more detailed description), which may be omitted upon first reading. Nevertheless, it is of significance for *in situ* studies of electrochemical systems, where it contributes significantly to the scattering originating from the electrolyte. Furthermore, electrode materials can be amorphous or highly disordered or become so under reaction conditions. For simplicity, we restrict ourselves to a simple single-component liquid of identical atoms or molecules, described by the form factor $f(q)$. We further assume that the liquid is homogeneous with a number density $\rho_n = N/V$ and is isotropic.

The spatial distribution of the atoms in the liquid at a given moment can be described by the particle density function, where the particle

positions are described by Dirac delta functions:

$$\bar{n}(\mathbf{r}) = \sum_j \delta(\mathbf{r} - \mathbf{r}_j) \tag{21}$$

Using this expression Eq. (4) can be written as:

$$S(\mathbf{q}) = f(q) \int \bar{n}(\mathbf{r}) \cdot \exp(-i\mathbf{r} \cdot \mathbf{q}) d\mathbf{r} \tag{22}$$

and the corresponding square modulus:

$$|S(\mathbf{q})|^2 = f(q)^2 \iint \bar{n}(\mathbf{r}) \cdot \bar{n}(\mathbf{r}') \cdot \exp[-i(\mathbf{r} - \mathbf{r}') \cdot \mathbf{q}] d\mathbf{r}' d\mathbf{r} \tag{23}$$

In a typical scattering experiment, we measure only the average over many configurations $\bar{n}(\mathbf{r})$, existing in the liquid. The relevant quantity to describe the scattered intensity is, therefore:[10]

$$\langle |S(\mathbf{q})|^2 \rangle = f(q)^2 \iint \langle \bar{n}(\mathbf{r}) \cdot \bar{n}(\mathbf{r}') \rangle \cdot \exp[-i(\mathbf{r} - \mathbf{r}') \cdot \mathbf{q}] d\mathbf{r}' d\mathbf{r} \tag{24}$$

where:

$$\langle \bar{n}(\mathbf{r}) \cdot \bar{n}(\mathbf{r}') \rangle = \left\langle \sum_{j,k} \delta(\mathbf{r} - \mathbf{r}_j) \cdot \delta(\mathbf{r}' - \mathbf{r}_k) \right\rangle \tag{25}$$

is the density-density correlation function. Since liquids per definition do not exhibit long-range order, the positions of the atoms become uncorrelated for large distance vectors $\mathbf{R} \equiv \mathbf{r} - \mathbf{r}'$. On the other hand, atoms cannot overlap physically and hence each atom can only be correlated with itself at small distances. Consequently, the density-density correlation function approaches the following limiting values, which only depend on the number density n of the atoms:

$$\langle \bar{n}(\mathbf{r}) \cdot \bar{n}(\mathbf{r}') \rangle = \begin{cases} \langle \bar{n}(\mathbf{r}) \rangle \cdot \langle \bar{n}(\mathbf{r}') \rangle = \rho_n^2 \\ \rho_n \cdot \delta(\mathbf{r} - \mathbf{r}') \end{cases} \quad \text{for} \quad \begin{cases} |\mathbf{r} - \mathbf{r}'| \to \infty \\ |\mathbf{r} - \mathbf{r}'| \to 0 \end{cases} \tag{26}$$

One of the most convenient functions to describe correlations in condensed matter is the pair distribution function $g(\mathbf{R})$, which is related to $\langle \bar{n}(\mathbf{r}) \cdot \bar{n}(\mathbf{r}') \rangle$ via:

$$\langle \bar{n}(\mathbf{r}) \cdot \bar{n}(\mathbf{r}') \rangle = \rho_n \cdot \delta(\mathbf{R}) + \rho_n^2 \cdot g(\mathbf{R}) \tag{27}$$

The pair distribution function can be interpreted in a simple, intuitive way. It provides the average probability to find in a small volume element at distance $\mathbf{R}$ from a reference atom (labeled as $j = 0$ with position $r_j = 0$) another atom of the liquid:

$$g(\mathbf{R}) = \rho_n^{-1} \langle \sum_{j \neq 0} \delta(\mathbf{R} - \mathbf{r}_j) \rangle \tag{28}$$

For a homogeneous (infinitive) liquid consisting of a single species, $g(\mathbf{R})$ is identical for each atom and thus independent of its position $\mathbf{r}$. Furthermore, because of the orientation isotropy of the liquid, $g(\mathbf{R})$ can be replaced by $g(R)$, which only depends on the absolute value R of the distance vector. The corresponding quantity $g(R)$ is known as radial distribution function, but is also often denoted as air distribution function in the literature (see Ref.[11] for a critical comparison of different correlations functions used in describing X-ray scattering). The probability to find another atom within a shell of radius R and thickness $\delta(R)$ around the reference atom is then given by $4\pi r^2 g(R)$ (Figure 4). Obviously, $g(R) \to 1$ for $R \to \infty$, where the atoms become uncorrelated. In most liquids, $g(R)$ is dominated by the repulsion of the ion cores and resulting packing constraints, which leads to a shell of direct neighbors at a spacing close to the minimum in the pairwise interaction energy (first maximum in $g(R)$) as well as several less-defined shells at larger R. The local correlations in water, which are of particular interest in electrochemical systems, are more complex due to the presence of local hydrogen bonds and are still strongly under debate. They manifest in an additional, temperature-dependent fine structure in the pair distribution function.

By inserting Eq. (27), we can write Eq. (24)

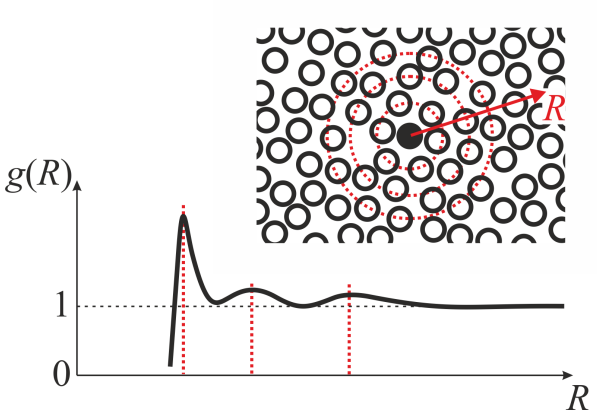

Figure 4: Typical configuration of atoms in a simple liquid, showing the characteristic short-range spatial correlations around a reference atom (black circle) and corresponding radial distribution function with maxima indicating first, second, and third shell of neighbor atoms (indicated in red).

as:

$$\begin{aligned}\langle|S(\mathbf{q})|^2\rangle &= f(q)^2 \iint \left[\rho_n \cdot \delta(\mathbf{R}) + \rho_n^2 \cdot g(\mathbf{R})\right] \\ &\quad \cdot \exp(-i\mathbf{R}\cdot\mathbf{q}) d\mathbf{R} d\mathbf{r} \\ &= f(q)^2 \cdot N \\ &\quad \cdot \left[1 + \rho_n \int g(\mathbf{R}) \cdot \exp(-i\mathbf{R}\cdot\mathbf{q}) d\mathbf{R}\right]\end{aligned} \tag{29}$$

In the calculation of the second expression, we have taken into account that the integration of the number density provides the number of atoms in the sample, i.e., $\int \rho_n d\mathbf{r} = N$. Eq. (29) shows that $g(R)$ can be directly obtained by Fourier transformation from the scattered intensity. In the literature on liquid scattering, the asymptotic value $g(R \to \infty) = 1$ is customarily subtracted from the pair distribution function within the integral. The Fourier transform of 1 is the δ-function, therefore:

$$\begin{aligned}\langle|S(\mathbf{q})|^2\rangle = f(q)^2 \cdot N \cdot \Big[1 + \rho_n \int (g(\mathbf{R}) - 1) \\ \cdot \exp(-i\mathbf{R}\cdot\mathbf{q}) d\mathbf{R} + (2\pi)^3 \cdot \delta(\mathbf{q})\Big]\end{aligned} \tag{30}$$

The last term in this expression only describes the (experimentally not measurable) forward scattering in the direction of the incident beam. The first two terms in the bracket are called the liquid structure factor $\mathcal{S}_L(\mathbf{q})$. Note that, in contrast to the normal structure factor $S(\mathbf{q})$, $\mathcal{S}_L(\mathbf{q})$ is proportional to the intensity rather than to the field. Performing the integration over the angular coordinates we obtain for an isotropic liquid:[3]

$$\mathcal{S}_L(q) = 1 + 4\pi\rho_n \int \frac{R}{q} \sin(qR)(g(R) - 1) dR \tag{31}$$

which – similar to $g(R)$ – also exhibits peaks, indicating the local correlations in the liquid that rapidly decay with increasing q (see also Figure 4). $g(R)$ can be extracted from $\mathcal{S}_L(\mathbf{q})$ by the pair distribution function method described in 4.2.4.

2.3.5 Scattering by liquid interface structure

The symmetry break near interfaces results in a distortion of the isotropic order in a liquid, which can be detected by scattering methods.[12] Often, this interface-induced ordering manifests in a molecular layering that decays into the bulk liquid. Such layering has been observed at the free surface of liquids as well as at liquid-solid and liquid-liquid interfaces. Typical examples where pronounced layering was observed are interfaces of liquid metals and ionic liquids (see section 5.5 and 5.2). The layering leads to oscillations of the electron density along the surface-normal direction, whereas the structure parallel to the interface remains liquid-like. Thus, the layering predominantly manifests along the specular axis, i.e., in the X-ray reflectivity (XRR).

The most common way to describe such surface layering is the distorted crystal model (DCM), which was originally derived by Magnussen et al. to describe the layering at the free surface of liquid Hg.[13] In this model, the scattering by the layered liquid is described by a semi-infinite series of atomic or molecular layers that are spaced at equal distances d. The layer directly at the interface has a finite Gaussian width σ_0 in surface normal direction z, corre-

sponding to a contribution to the Debye-Waller factor $M_z = q_z^2 \cdot \sigma_0^2/2$. The width of layer n is assumed to increase with increasing distance $z = n \cdot d > 0$ from the interface according to the following relationship:

$$\sigma_n^2 = \sigma_0^2 + n \cdot \bar{\sigma}^2 \tag{32}$$

This results in an oscillatory electron density profile that decays to the uniform average density within the bulk liquid (see Figure 27c for an example). The constant $\bar{\sigma}$ describes how fast the layering decays with z. The scattering from this series of broadening layers can be calculated in the same way as in Eq. 18. Now the Debye-Waller expression of eq. 5 has to be included within the sum used for calculating the structure factor:

$$S_{DCM}(q_z) = \sum_{n=0}^{\infty} \exp(-ind \cdot q_z) \cdot \exp(-\frac{1}{2}\sigma_n^2 \cdot q_z^2) \tag{33}$$

Assuming an increase in width as provided by eq. 33 an analytical expression for $S_{DCM}(q_z)$ can be obtained by using the geometric series:

$$S_{DCM}(q_z) = \frac{\exp(-\frac{1}{2}\sigma_0^2 \cdot q_z^2)}{1 - \exp(-id \cdot q_z) \cdot \exp(-\frac{1}{2}\bar{\sigma}^2 \cdot q_z^2)} \tag{34}$$

In the absence of any further structure, e.g., for the scattering of a free liquid surface that exhibits layering, Eq. 34 leads to a modulation of the Fresnel reflectivity of a perfect interface (see section 4.3.1) in form of a weak peak at $q_z \approx 2\pi/d$ (see e.g. Figure 27a,b). The width and height of this peak depend on the decay parameter $\bar{\sigma}$. In some cases, the layer(s) next to the interface can have a density, spacing, or width that differ from those assumed in the DCM. These effects can be implemented by adding one or more additional layers with deviating parameters to the sum in Eq. 33.

2.4 Scattering of nanoscale objects

The theory for scattering from nanoscale objects is based on the general scattering theory, as described in Section 2.2. The scattering amplitude $S(\mathbf{q})$ for a given electron density distribution $\rho_e(\mathbf{r})$ is given by Eq. 1, the corresponding scattered intensity $|S(\mathbf{q})|^2$ by Eq. 2. In the case of a single nanoscale object, the integration takes place throughout the volume of the whole object, and the electron density ρ_e is often substituted by the fluctuation of electron density $\Delta\rho_e$.

$$S(\mathbf{q}) = \int \Delta\rho_e(\mathbf{r}) \cdot \exp(-i\mathbf{r} \cdot \mathbf{q}) d\mathbf{r} \tag{35}$$

If the objects in the probed volume are randomly oriented, the intensity is proportional to their average

$$I(\mathbf{q}) \sim \langle |S(\mathbf{q})|^2 \rangle \tag{36}$$

$\langle |S(\mathbf{q})|^2 \rangle$ is often denoted as particle form factor $P(\mathbf{q})$ in the small-angle scattering literature and in section 4.5.1. Substituting from Eq. 2, this can be integrated to the form of the Debye scattering function for ensemble of particles[14]

$$I(q) \sim N\langle V^2 \Delta\rho^2 \rangle \int p(R) \frac{\sin qR}{qR} dR \tag{37}$$

$$p(R) = 4\pi R^2 \frac{\int \Delta\rho_e(r) \cdot \Delta\rho_e(r+R) dr}{\langle \Delta\rho_e^2 \rangle} \tag{38}$$

, where $p(r)$ is the normalized total pairwise distribution function. Eq. 37 shows that the scattered intensity is proportional to the number density of nano-objects in the scattering volume, N, as well as to the volume of the scattering elements, V. The integral term describes the interference effects associated with the distribution of electrons in an average object. This equation is the basis for an approximate description of the X-ray scattering by various nano-scale objects. In the case of spatial correlations between the objects, Eq. 37 is extended by a structure factor (see chapter 4.5.1). For perfectly spherical objects of radius R_p, the scattered intensity (form factor) can be expressed analytically as[15]

$$\langle |S(\mathbf{q})|^2 \rangle = \left[3 \frac{\sin qR_p - qR_p \cos qR_p}{(qR_p)^3} \right]^2 \tag{39}$$

.

2.5 Resonant X-ray scattering

The access to tunable photon energy at synchrotron X-ray sources also allows using the so-called resonant anomalous effects to obtain element-sensitive information from diffraction patterns. Such characterization is based on the dependence of the atomic form factors on the photon energy ε_{Ph} or X-ray wavelength λ, respectively, as already mentioned in chapter 2.3.1. To describe this effect, the atomic form factor has to be written as a complex number:

$$f(\mathbf{q}, \lambda) = f_0(q) + f'(\varepsilon_{Ph}) + if''(\varepsilon_{Ph}) \qquad (40)$$

Here $f_0(q)$ is the conventional form factor defined in Eq. 3. $f'(\varepsilon_{Ph})$ and $f'(\varepsilon_{Ph})$ are called dispersion coefficients and describe the correction to f_0 for photon energies close to the possible electron transitions of a particular element (Figure 5). These energies are often called absorption edges. This phenomenon is due to res-

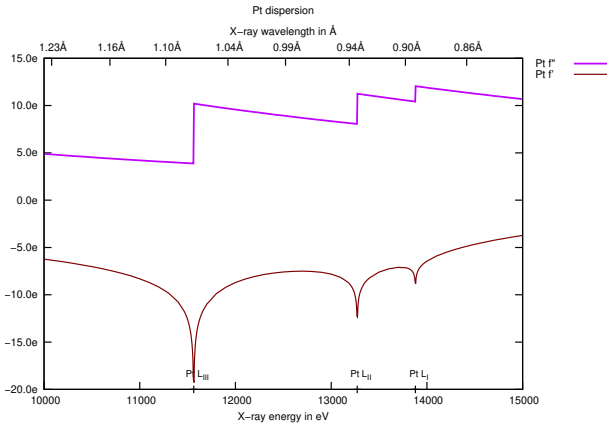

Figure 5: Anomalous energy dispersion of atomic scattering factor for Pt in the range of L absorption edges. Generated at http://skuld.bmsc.washington.edu/ scatter/ AS_form.html

onant effects near the adsorption edges, which lead to a direct alteration of the X-ray scattering length ($\Delta f'$) as well as to phase lags with respect to the driving field of the incoming wave that lead to dissipation ($i \cdot \Delta f''$).[3] The dependence of dispersion coefficients on $\mathbf{q}$ is very small and can be neglected. The resonant anomalous behavior of the form factors is typically used to solve the phase problem or highlight certain elements in the diffraction patterns in both small-angle X-ray[16] and wide-angle X-ray scattering[17,18] techniques (see section 4.7). It can also be used for effective background subtraction, where two diffraction patterns taken below the edge and at the edge are subtracted, leaving only the scattering from the element of interest[19–21].

3 Experimental aspects

This section aims to give an introduction to the technical aspects of *in situ* and *operando* experiments, as they often employ synchrotron sources and advanced instrumentation. Therefore basic understanding of the underlying principles of X-ray generation and X-ray scattering instrumentation are often needed to properly choose the appropriate X-ray source and/or synchrotron beamline. The design of *operando* electrochemical cell is equally important as well as understanding of how the X-ray beam influences the electrochemical environment. This knowledge forms a basis for successful experiment and data interpretation.

3.1 X-ray sources for in situ and operando studies

There is a wide variety of X-ray sources available for the *in situ* and *operando* X-ray scattering experiments. They are mainly characterized by the quality of emitted X-rays which defines their fundamental interactions with matter. The main parameters defining the optimal use in different experiments and measurements are photon energy, flux, and coherence. The energy of the X-ray photons determines its cross-section towards different modes of interaction with the atoms, of which the studied material consists. The X-ray energy parameter is therefore instrumental in the choice of a proper X-ray source for the particular experiment. In general (with the exception of anomalous scattering experiments), higher energies are better suited to diffraction experiments than lower energies. This is because at lower energies the photo absorption process dominates the interactions with the sample or the electrochemical

cell, and this causes undesired effects. First, the electrons emitted in the photo-absorption process interact with the sample and electrolyte, producing radicals that then affect the integrity of the sample or alter the electrochemical environment. Second, a higher fraction of the incident photons is absorbed in the parts of the electrochemical cell which are in the path of the X-ray beam, i.e., the photoabsorption cross-section, and thus the X-ray attenuation coefficient μ is higher. Following the Beer-Lambert law ($I(t) = I_0 e^{-\mu(E)*t}$, t is the thickness of the material), this increase in μ results in much lower transmission (penetration power), which significantly limits the design of suitable electrochemical cells and limits their performance.

The choice of the X-ray energy also defines the volume of reciprocal space which is accessible in a scattering experiment. In particular, it defines the reciprocal region that can be acquired in a single acquisition with a large 2D detector. High photon energies provide access to large reciprocal space volumes. This can significantly improve data acquisition time as the detector does not have to be moved during acquisition, allowing faster time-resolved experiments as well as a more accurate analysis of the obtained diffraction patterns. This is particularly important for experiments where fine Rietveld refinement or pair distribution function (PDF) analysis is needed. In surface-sensitive diffraction, the large reciprocal space volume acquired at high energies speeds up the measurements by an order of magnitude and also enables more reliable and detailed surface structure determination.

It should be noted, however, that for some *in-situ* and *operando* experiments use of lower energy X-rays is inevitable. This typically applies to resonant X-ray scattering measurements where energy around probed X-ray edge must be used. Another examples are experiments using coherent beams, which are normally available only at lower energies due to the physical constraints of synchrotron undulators. Experiments demanding high reciprocal space resolution are also often performed at low X-ray energies to increase the angular resolution of the setup.

Many topics of interest in *in situ* and *operando* studies, such as interfaces or poorly ordered materials, rely on the analysis of scattered intensities that are much weaker than that of bulk crystals. For such studies, high photon flux is required, especially for time-resolved studies. In addition, for some techniques, for example grazing incidence diffraction and nanodiffraction, the size of the incident X-ray beam at the sample position has to be in the (sub)micrometer range in one or two directions. This requires X-ray beams of high brilliance that can be well-focused. Furthermore, a sizable coherent fraction of the X-ray beam is necessary for some advanced methods (see 4.6.2).

3.1.1 Lab sources

Laboratory X-ray sources play an important part in the characterization workflows of many scientific fields. A common laboratory would be equipped with a standard rotating anode X-ray source with simple optics and a goniometer. Such instruments are ideal for *ex situ* characterization of materials, but the low flux and X-ray energy do not typically allow for *operando* experiments. However, recent advances in both X-ray source design and detector technology allow using high X-ray energies to penetrate *operando* cells and reasonably fast data acquisition by large area detectors, enabling studies with satisfactory time resolution.

Nowadays all major manufacturers provide advanced X-ray source and detection systems, suitable for both small-angle and wide-angle scattering experiments. The liquid metal jet X-ray source technology can be used for *operando* science as it provides relatively high flux even at high X-ray energies[22]. However, the brilliance of such systems is still orders of magnitude lower than that of 3 $^{\text{rd}}$ and 4 $^{\text{th}}$ generation synchrotron sources[23]. Given the fast progress of X-ray generation technologies, we expect that this inequality will change and more and more laboratory systems will be used for routine *operando* experiments.

3.1.2 Synchrotron sources

Synchrotron radiation is produced by charged particles with velocities close to the speed of light moving on a curved path due to an applied magnetic field. Its physical origin is the (centripetal) acceleration of the electric charge, resulting – similar to a radio antenna – in the emission of electromagnetic radiation. However, the angular distribution of this emission is not identical to that of a conventional (non-relativistic) oscillating electric dipole but strongly distorted in the forward direction due to relativistic effects. As a result an intense, collimated beam fans out from the curved path of the moving charge. Synchrotron radiation has a continuous spectrum and is almost perfectly polarized parallel to the plane of movement of the generating charge. Together with the orders of magnitude higher intensity and much lower angular divergence of the X-ray beam, these properties make synchrotron radiation by far superior to that produced by conventional X-rays tubes in laboratory instruments. Basics about synchrotron radiation are in the following paragraphs, but for more details we refer reader to specialized textbooks and reviews[24,25]

Synchrotron sources are storage rings where electrons or positrons are kept circulating under UHV conditions at a constant kinetic energy (typically $\sim$ GeV). The radiation is generated in the magnets that bend the beam to obtain a closed orbit or by optimized magnetic devices, called wigglers and undulators, that are inserted in the straight sections between the bending magnets. Arranged around the storage ring are synchrotron beamlines where the X-ray beams are further focused, collimated, monochromatized, and finally passed into experimental hutches, which contain one or several instruments for the actual experiments. This experimental layout is schematically depicted in Figure 6.

Before further discussing the different X-ray sources and the beamline instrumentation in a synchrotron we consider the actual experimental requirements for elastic scattering studies. First, such experiments employ highly monochromatic radiation, i.e., utilize only a small wavelength interval $\Delta\lambda$ of the beam. Second, well-defined angles between the beam and atomic planes in the sample are essential for all X-ray diffraction studies, which is only possible if the angular divergence of the beam is low. Third, focusing the beam to a small size is necessary. In particular surface studies often require the beam to impinge on the sample under a small gracing incidence angle α_i. The projection of the X-ray beam onto the surface is, therefore, a factor $1/\sin(\alpha_i)$ larger than the vertical beam size. To optimally utilize the incident intensity, the beam thus has to be focused to a small size (10 to 100 µm for a sample of several mm in width) and also should have a low divergence on the sample. These requirements can only be fulfilled if the radiation is emitted out of a small source area with low source divergence. For comparing different X-ray sources one needs a physical quantity that takes all this into account and provides a measure for the photon flux under these constraints. This quantity is the brilliance of the X-ray beam, which is customarily defined in synchrotron science as the number of photons per second, emitted by a 1 mm^2 large source into a solid angle of 1 mrad^2 and a 0.1% wide relative energy interval around a given photon energy. For the Cu K_α line of a typical laboratory X-ray tube, the brilliance is 10^8 photons/s/mm^2/mrad^2/0.1% bandwidth. Even bending magnet stations surpass this value by more than 6 orders of magnitude, enabling fundamentally different exper-

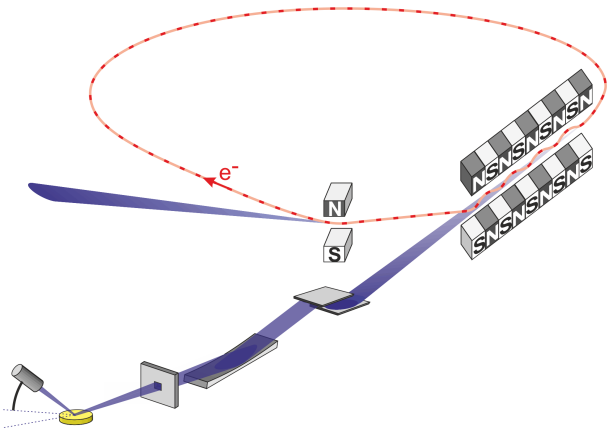

Figure 6: Schematic layout of a synchrotron source, showing bending magnets, insertion devices, and a typical beamline.

iments and explaining the rapid rise of X-ray science after the emergence of the first dedicated synchrotron facilities in the 1980s.

The central facilities of modern third-generation synchrotron sources, however, are insertion devices (or so-called undulators), which can provide a much higher brilliance, up to 10^{20} photons/s/mm^2/mrad^2/0.1% bandwidth. Both wigglers and undulators employ an array of magnets with alternating fields to force the charged particles in the storage ring onto an oscillatory path. The synchrotron radiation emitted at each bend in this path is superimposed, resulting in a more intense beam. In a wiggler, the emissions produced in each curve are independent and uncorrelated. The intensity is consequently directly proportional to the number of magnet pairs in the array and the energy spectrum corresponds to that of a bending magnet, i.e., is a broad, continuous distribution. In contrast, undulators are constructed in such a way that the electromagnetic waves emitted by the charged particle at each bend in its path can be in phase with each other. In this case, the field amplitudes are superimposed and the resulting intensity scales with the square of the number of magnet pairs, providing much higher amplification factors. Obviously, the condition for coherent superposition can only be met at one particular wavelength and its higher harmonics, making the emitted radiation quasi-monochromatic. By changing the gap between the upper and lower array of magnets and by this the magnetic field strength the energy of these emission maxima can be tuned continuously. Furthermore, since the deflection angles in undulators are small as compared to wigglers or bending magnets, their radiation cones are compressed. All this makes undulators the most brilliant sources employed in current synchrotrons.

Most diffraction beamlines have a setup as shown schematically in Figure 6. After the X-ray beam is generated, a single wavelength is selected by Bragg reflection at a crystal lattice. A common design is a double crystal monochromator, where the beam is reflected twice by two parallel-oriented, opposing silicon crystals, using Bragg reflection from the lattice planes parallel to the crystals' surfaces. This ensures that the beam maintains its direction and is only slightly vertically shifted. Silicon is the material of choice, since single crystals of extremely high perfection are easily available. Such crystals reflect the X-ray beam to almost 100% within a small (for Si(111) ≈0.1 mrad wide) angular range – the "Darwin widths" of the crystal – which is well adapted to the natural divergence of the synchrotron beam. The resulting monochromatized beams have relative spectral widths $\Delta\lambda/\lambda$ typically below $\approx 10^{-4}$, which is an important prerequisite for spectroscopic or high-resolution scattering studies. Modern high energy beamlines (E >50 keV) use monochromators in transmission mode (Laue monochromators), where the beam is passing through two 1 mm thick Si single crystals and photons are reflected from lattice planes that are nearly normal to the crystal surface. This geometry allows tuning the spectral width by bending the crystals with the trade-off in intensity, which is particularly advantageous for experiments where high intensity is necessary, such as total scattering measurements from amorphous materials or surface-sensitive studies.

Various other X-ray optical elements are employed for further configuring or characterizing the incident beam. Many beamlines employ curved X-ray mirrors, which allow additional focusing of the beam and define the beam at the sample position. Other focusing devices, such as arrays of refractive lenses or Fresnel zone plates, are also often used. If focusing is not used, the beam size at the sample position is controlled by horizontal and vertical slits. Because the number of electrons in the synchrotron ring gradually decays due to collisions with residual gas molecules, the incident X-ray intensity I_0 slowly decreases and has to be continuously monitored, which is usually done by measuring the ionization of a gas by the traversing beam or by inserting a photodiode in the beam path. Furthermore, many beamlines include an attenuator in front of the sample, consisting of several metal foils of different thicknesses. This allows measurements over many orders of magnitude in intensity, as required in surface studies, without damaging

the X-ray detectors.

The energy of the electrons in the storage ring, the used source magnets, and the optics layout define the properties of the X-ray beam at the end stations. Therefore each experiment requires consideration about what storage ring and instrument would fit best the needs. For *in situ* and *operando* experiments, energies $>$ 20 keV are advantageous due to the high penetration power of the X-rays. High photon energy allows using robust electrochemical cells and devices without making compromises in electrochemical performance due to constraints such as measurement geometry, cell wall size, electrolyte thickness in the beam path, and materials used for the cell manufacturing (see chapter 3.3). Another consideration is the needed reciprocal space resolution, which is a convolution of the spectral width, divergence of the beam, sample size, detector pixel size, and position of the detector. In this respect, low energy instruments (E = 5-10 keV) can have a superior resolution, particularly if analyzer crystals are used, but for the majority of *in situ* and *operando* experiments, the typical resolution of mid and high energy beamlines using 2D detectors is sufficient. Possibilities of focusing the X-ray beam to sub-micron sizes can be an advantage in experiments where high spatial resolution is demanded. Modern diffraction beamlines can achieve this focus range by using refraction optics or Fresnel plates, which are relatively easy to set up. Small focused beams are typically used for scanning experiments of heterogeneous materials and interfaces, an important part of studies of electrochemical devices.

Given the high brilliance of synchrotron sources, the amount of data generated during one experiment can easily surpass several terabytes. Therefore data handling, processing, and analysis is an essential aspect of the experiment. Each instrument will provide raw data sets which need to be further processed. Different instruments have different pipelines for data processing and the resulting diffraction patterns can be output in different formats, often only a raw form. Therefore postprocessing of the data by individual research groups is typically needed. The most efficient way is to use common scripting languages, such as Python or MATLAB, for data postprocessing and specialized software for further crystallographic analysis.

3.1.3 X-ray Free Electron Lasers

With the upcoming X-ray free electron lasers (XFELs), an even more powerful tool for X-ray science has emerged in recent years. XFELs are essentially linear accelerators equipped with very long undulators. Due to the interaction of the generated synchrotron radiation with the charged particles, the latter spontaneously organize into bunches that emit coherently. Hence, contrary to normal undulators, where the emissions of each particle at the subsequent bends are in phase, but the emissions by different particles are uncorrelated, the field amplitudes of all emitted radiation are superimposed constructively. The result is a fully coherent beam as in a laser, composed of femtosecond pulses with a ten orders of magnitude higher brilliance than current undulators at storage ring sources. XFELs offer exciting opportunities for radically new experiments that exploit these properties, such as time-resolved structural studies, but also pose substantial challenges in developing suitable beamline optics and experimental techniques. Currently, these instrumental questions are the focus of intense research efforts, whereas the application of these sources to more routine studies of surfaces and interfaces seems still a few years away.

3.2 X-ray diffractometers

The most common configurations found in commercial diffractometers in laboratories worldwide are the Bragg-Brentano (reflection mode) and Debye-Scherrer (transmission mode) geometries (Figure 7.a and 7.b, respectively). These setups consist of an X-ray source, a sample holder, and a detector, whose positions are precisely controlled by motorized stages. The adjustable X-ray source emits a beam of X-rays that is directed at the sample holder (goniometer), which precisely controls the position of the sample with respect to the incoming beam and

the detector. The detector is positioned to receive the scattered X-rays, which are diffracted at various angles due to the crystal structure of the sample. Commercial instruments differ in the choices of optics, detector physics and geometries, and beam characteristics, which can be tuned for specific experimental purposes. Older instruments are equipped with a one-dimensional (1D) point detector which can be scanned in a circle around the sample. Modern instruments use 2D detectors which can image larger volumes of reciprocal space, therefore speeding up the measurement.

Synchrotron instruments can have various geometries, depending on the main purpose of the beamlines. For all synchrotron instruments, the beam source is fixed in space, and only the sample and detector can change position with respect to the incident beam. The standard is a four-circle diffractometer, where the sample is mounted on an Eulerian cradle consisting of three circles (rotation axes), and the 2θ angle between the incident beam and detector is determined by the fourth circle (Figure 7c)[27]. This minimal arrangement allows to measure within a large volume of reciprocal space, and it is typically used for single-crystal diffraction experiments. However, powder diffraction experiments or measurements on thin films can also be performed on this diffractometer. For surface scattering experiments, diffractometers with a six-circle geometry are employed (Figure 7d)[28]. These allow setting with high precision any desired orientation of the sample with respect to the incident beam as well as choosing independently the angular position of the detector within and perpendicular to the surface plane. Specifically, this also allows fixing the incident angle α_i and exit angle α_k of the surface relative to the impinging and scattered beam, respectively (see Figure 1a). Six-circle diffractometers are over-determined with respect to their motional degrees of freedom and hence can be operated in different modes that are preferable for surface diffraction studies (e.g., measurements at constant α_i or at $\alpha_i = \alpha_k$). A specific type of surface diffractometer allows additional tilting of the incident beam, enabling studies of samples that cannot be tilted, for example, liquid interfaces.[29] Other diffractometer geometries, such as (2+3) type diffractometers[30], are also used, and all the described geometries can be utilized in laboratory settings.

Recently detector development underwent rapid evolution, and photon-counting large detectors are becoming a norm. This detector technology defines the optimal energy range for the experiment as well as the quality of the final data. For experiments up to 30 keV silicon-based photon counting detectors are suitable; for higher energies, CdTe or GaAs detectors need to be used as they provide enough absorption for high-energy photons. It is also common to use detectors based on scintillator material (typically CsI) in front of the standard complementary metal-oxide semiconductor (CMOS) detector. Such detectors have more counting noise, and therefore they are used for less demanding measurements. However, they still provide an acceptable alternative.

Large stationary 2D detectors are becoming heavily used at synchrotron beamlines as it is possible to obtain a large section of reciprocal space, e.g., full diffraction rings, in one acquisition without moving the detector. This allows very fast measurements but also requires different approaches in the analysis. To obtain standard 1D powder diffraction patterns, the raw images need to be radially integrated with specialized software[31]. Furthermore, for single crystal studies rotating the sample without moving the detector allows scanning of a large reciprocal space volume which significantly speeds up the measurement and allows more advanced analysis. This can also be achieved at lower energy beamlines by moving the 2D detector with the diffractometer arm, albeit at a slower pace. In these cases, the reflections are often binned and analyzed in 3D reciprocal space,[32] which for some techniques, such as Bragg coherent diffractive imaging (BCDI) or high energy surface X-ray diffraction (HESXRD), is a standard approach[33–35]. Binned data, or data reduced by other means, are then further processed by specialized software in order to get physical quantities of interest. Examples of established software are GSAS-II[36], TOPAS[37] and FullProf[38] for Rietveld analy-

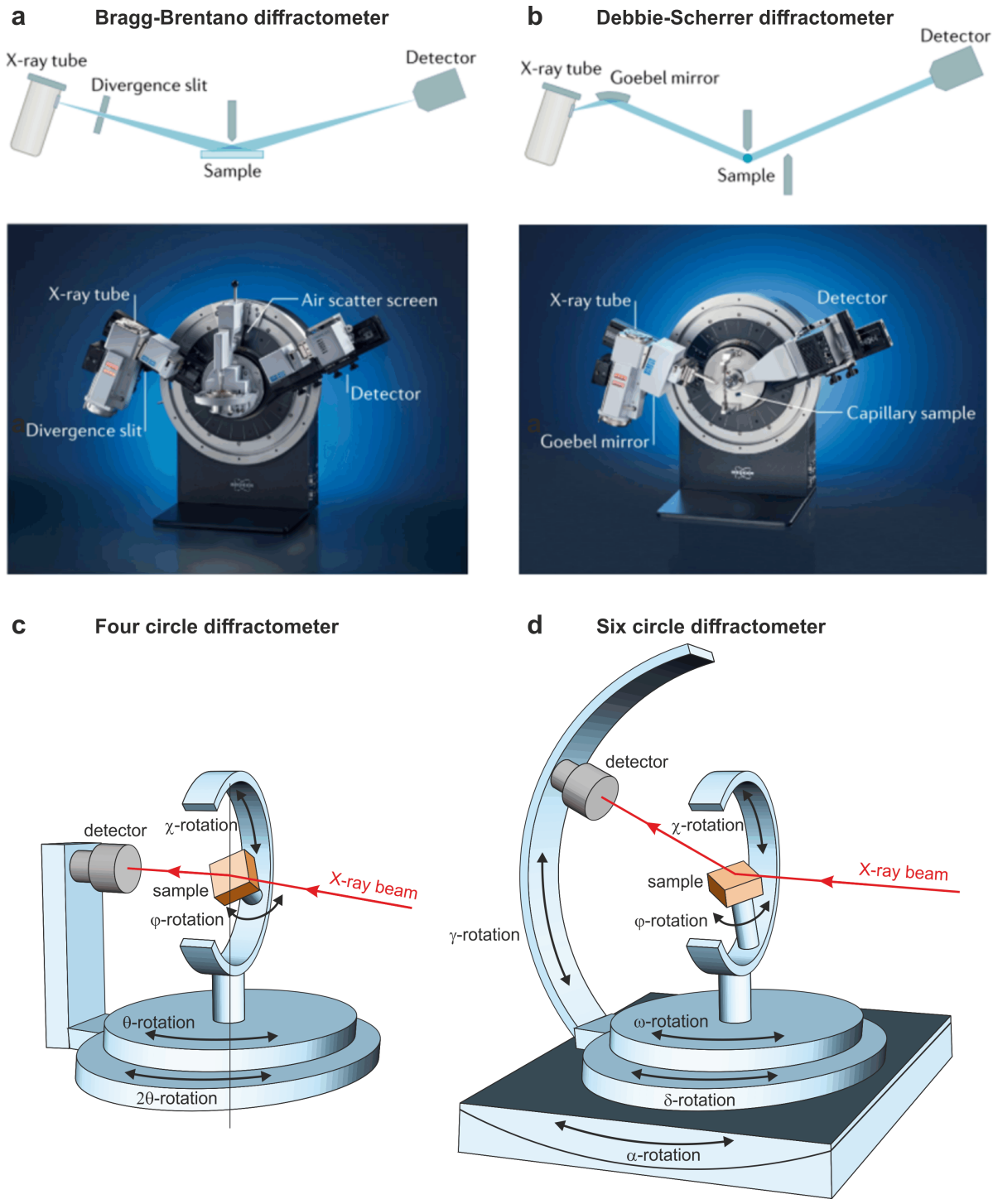

Figure 7: Schematic diffractometers geometries and exemplary pictures for (a) Bragg-Brentano, (b) Debye-Scherrer (Adapted from Ref.[26]. Copyright 2021 Springer Nature), (c) four-circle, and (d) six-circle instruments.

sis of powder XRD data, PDFGUI[39] and DISCUS[40] for pair distribution function analysis of X-ray total scattering, SASView for small-angle scatting[41], BornAgain for grazing incidence small angle X-ray scattering[42], GenX for X-ray reflectivity[43], ANA-ROD[44] and BINoculars[45] for surface X-ray diffraction data, and PyNX for Bragg coherent diffractive imaging[46]. A full list of software can be found on the IUCr website[47].

The use of 2D detectors also comes with set of challenges for *in situ* and *operando* measurements. The beam has to pass through various environments (cell walls and electrolyte), before hitting the sample and this inevitably causes unwanted diffraction signal in form of background or extra diffraction peaks. The standard background suppression strategies for point and 1D detectors are double slits and parallel Soller collimators[48,49]. In both cases only the beam scattered in the line-of-sight of the double slit or collimator is detected. As the slits are mounted on the diffractometer arm, they change the angle with the detector for angularly resolved data collection. For 2D detectors this strategy does not work due to the large angular space detection in one acquisition, and therefore different collimator geometries have to be used. The most promising strategy is to use a converging 2D Soller slits with the plates or foils of the slits pointing to the scattering centre. For full collimation, where the diffracted beam comes only from the small volume around the sample, a rectangular or honeycomb grid must be used[49]. In this case, radial foils or 3D printed slits can be manufactured, which is nowadays possible even from heavily absorbing materials such as tungsten[50,51]. 3D printed Soller slits allow complete suppression of the unwanted signals coming from the cell walls and significantly improve the quality and resolution of the acquired data[49]. This is one of the few strategies that permits X-ray diffraction experiments in large commercial cells without the need for laborious background subtraction routines.

3.3 Electrochemical cells for *in situ* and *operando* studies

For *in situ* studies of electrochemical interfaces, the X-ray beam has to pass through the electrolyte or, more rarely, the electrode. With increasing thickness d of the transmitted material, the beam is attenuated by absorption and scattering. This leads to a relative loss in intensity of $I/I_0 = \exp(-\mu d)$, which is determined by the (wavelength-dependent) linear attenuation coefficient μ. The thickness d should be minimized in *in situ* X-ray scattering and spectroscopy studies, making conventional electrochemical cells unsuitable for these experiments. To illustrate this, we consider X-rays with photon energies between 6 and 25 keV (corresponding to wavelengths λ of approximately 2 to 0.5 Å, respectively), which is the most commonly used range in X-ray diffraction. Over this energy range, the X-ray attenuation length μ^{-1} in water increases from 0.4 to 23 mm. Ideally, electrochemical cells for X-ray scattering should minimize the absorption and scattering contribution of the bulk phases for the employed wavelength, while simultaneously providing good electrochemical performance.

Initial *in situ* studies were performed at bending magnet sources optimized for photon energies of ≈10 keV and hence had to employ cells with a thin layer geometry, as that shown in Figure 8a. Here a thin window of an X-ray-stable polymer (e.g., prolene, polypropylene) is used to constrict the electrolyte during the X-ray studies to a several μm thick film on top of the sample, minimizing the beam path through the electrolyte. Nevertheless, since the incident angle α_i typically is small in surface-sensitive studies, the beam still has to travel through ≈ 1 mm of electrolyte, resulting in noticeable attenuation. For example, the intensity of a 10 keV beam will be reduced to 60% of its original value after traversing a 10 μm thick water layer at $\alpha_i = \alpha_k = 1°$. Due to the restricted mass transport and the high cell resistance in the thin electrolyte layer, electrochemical reactions are strongly kinetically hindered. Experiments are, therefore, typically performed by inflating the window between the actual measurements

via the introduction of additional liquid into the cell. After inflation, the electrolyte layer on the surface is several mm thick, which provides high conductivity and enables substantial mass transport of species from the electrolyte to the electrode. In these cells, true *in situ* investigations of electrochemical interfaces during processes such as electrodeposition, dissolution, or gas (e.g., H_2) evolution are obviously not possible and experiments have been restricted almost exclusively to potentials in the double layer regime. As a further disadvantage, not only the studied surface but also the sides of the sample are exposed to the electrolyte and hence contribute to the electrochemical current.

Insertion device beamlines at modern, hard X-ray, third-generation synchrotron sources can provide high brilliance beams in the photon energy range $\geq$ 20 keV. This allows the usage of electrochemical cells, where the beam passes through several millimeters or even centimeters of an extended electrolyte volume and/or cell casing. An example is provided by the cell depicted in Figure 8b, in which an electrolyte-filled glass tube establishes contact with the electrode surface via a free-standing meniscus within a compartment filled with an inert gas atmosphere. This arrangement resembles the "hanging meniscus" geometry commonly used in single crystal electrochemistry, resulting in a comparable electrochemical behavior, i.e., low cell constants and facile transport. The X-ray beam passes through the meniscus and is only scattered by the sample and the electrolyte solution. Due to this wall-free geometry, the scattered background intensity – although higher than in thin layer geometry – is given solely by the slowly changing scattering of the electrolyte solution (see chapter 2.3.4) and therefore varies much less with the scattering angle than in thin-layer cells, where a strong, non-uniform contribution from the powder scattering by the polymer X-ray window exists. Furthermore, problems caused by beam damage of the window material are avoided. Because the meniscus is stabilized by surface tension, the cell can be positioned on the X-ray diffractometer in arbitrary orientations as required by diffraction experiments. To avoid collapse of the meniscus during the measurements, the cell has to be perfectly tight and evaporation of the electrolyte has to be negligible over hours. As this is often difficult to achieve, such cells are often connected with precision pumps for adjusting the electrolyte remote-controlled, which also allows establishing electrolyte flow or exchange.

Under conditions of strong gas evolution at the electrode, a freestanding meniscus is not stable. Here, cells resembling conventional electrochemical cells have been employed (Figure 8c). The sample is embedded at the bottom of a narrow conical vessel, which is partly filled with the electrolyte. Near the sample, the cell walls are kept thin, and their distance is minimized to reduce X-ray absorption. A typical material for such cells is polyether ether ketone (PEEK), which has good stability in the X-ray beam. The background scattering of such cells is typically higher than in the "hanging meniscus" variant. Still, they offer almost unlimited possibilities for *operando* studies under reaction conditions up to very high current densities.

Various variations of thin layer and transmission cells have been developed, including cells that provide temperature control, allow direct transfer of the sample from a UHV system, or permit the exchange of the electrolyte during the X-ray studies by a remote-controlled pump system. The precise design often depends on the requirements of the specific experiment, both with respect to the electrochemical conditions as well as the geometric demands of the X-ray studies. While thin layer cells as in Figure 8a provide full access of the hemispherical angular space above the sample surface, other cell designs may restrict this geometrically to some extent (although this can often be compensated for by employing higher photon energies). For X-ray scattering methods that do not require a wide field of view, e.g., X-ray reflectivity, powder diffraction, or small-angle scattering, even more simple cell geometries are possible.

Investigations conducted on thin-film catalyst electrodes, have used different cell designs (featuring two or three electrodes) that enable diffraction measurements of the catalysts in liquid or solid electrolytes (Figure 8d-f). For thin films featuring high metal loading, transmission

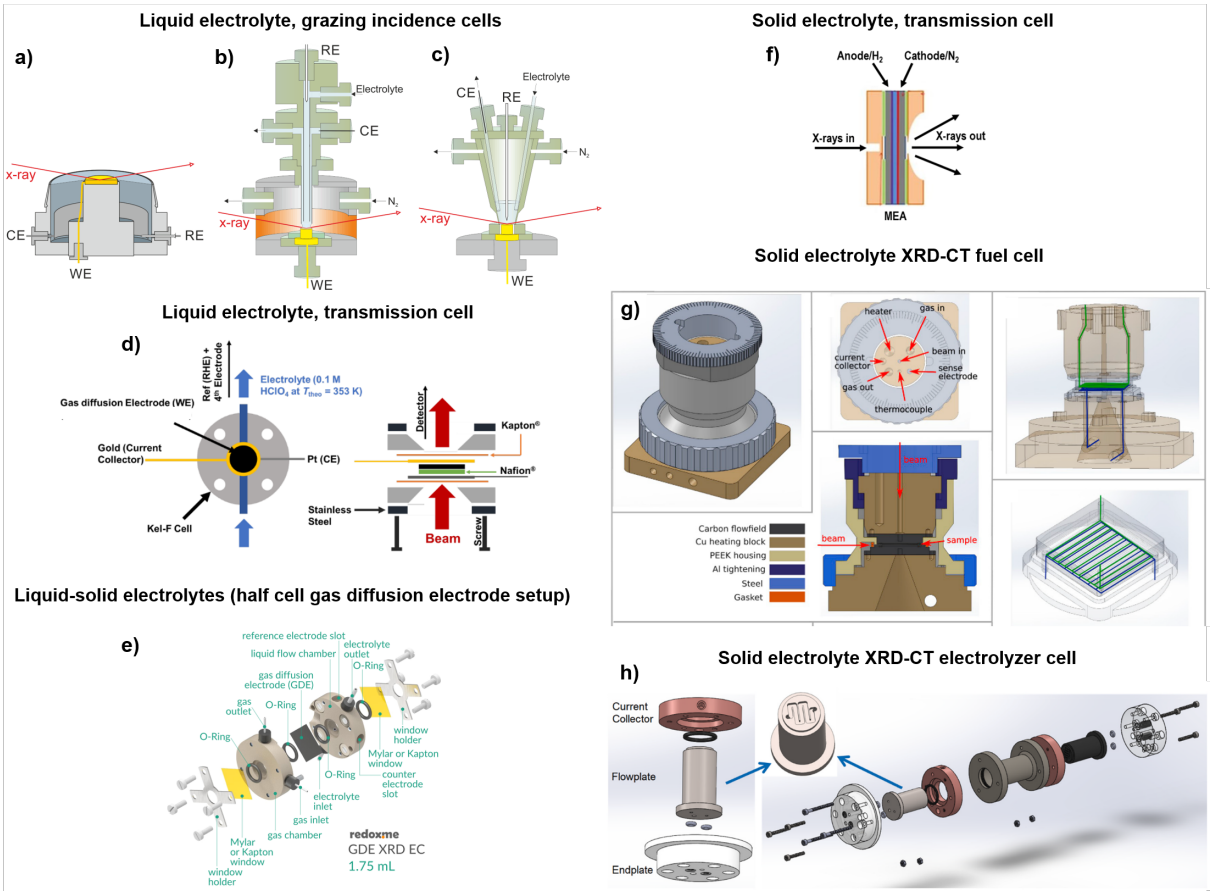

Figure 8: Schematic illustration of various electrochemical cells for X-ray diffraction studies. (a) Thin layer cell, (b) hanging meniscus cell (Adapted from Ref.[52]. Copyright 2023 Elsevier. , (c) transmission cell (Adapted from Ref.[53]. Copyright 2019 American Chemical Society), (d) liquid half-cell (Adapted with permission from Ref[54]. Copyright 2019 American Chemical Society), (e) commercial gas diffusion electrode cell (Courtesy from redoxme AB[55]), (f) modified standard single fuel cell (Adapted from Ref.[56]. Copyright 2018 Elsevier), (g) XRD-CT fuel cell (Adapted from Ref.[57]. Copyright 2019 Elsevier), and (h) XRD-CT electrolyzer cell (Adapted from Ref.[58]. Copyright 2023 Elsevier).

measurements through the film plane are possible as long as the counter-electrode is kept away from the beam path or has negligible metal loading compared to the working electrode. For example, Asset et al. used this transmission configuration on a 250 μg_{Pt} cm^{-2} film in liquid electrolyte with a Pt ring counter studied electrode (see Figure 8d).[54] Petkov and coworkers modified a standard single proton exchange membrane fuel cell for laboratory studies (Figure 8f) to allow transmission measurements of the catalyst in contact with the solid polymer electrolyte[56]. Here, the beam is probing both the anode and cathode, but the low Pt loadings of the anode as compared to the cathode allowed attributing the scattered signal mostly to the cathode. Another possible electrochemical cell is the gas diffusion electrode half-cell. In this configuration, the working gas diffusion electrode is fed with a gaseous reactant while the counter electrode is kept in a liquid electrolyte. Such a cell adapted for transmission X-ray diffraction measurements is commercially available from redoxme AG, Sweden (Figure 8e).[55]

For thin films featuring low metal loading, grazing incidence (or in-plane) measurement is by far the most efficient approach for collecting scattered signals with sufficiently high intensities. Despite requiring a more careful alignment with the X-ray beam as compared to the transmission configuration, this approach has been extensively employed and can be adapted to various electrolyte types (liquid, polymeric, solid oxides, etc.).[57–59] For example, Chattot et al. used this configuration to investigate the electrochemical strain dynamics on 20 μg_{Pt} cm^{-2} thin films in liquid electrolyte[60]. Finally, the careful design of electrochemical cells with rotation symmetry and 360 degrees free path for the beam in grazing incidence configuration allows measuring X-ray diffraction computed tomography (XRD-CT). Figure 8.g and h show examples of recently designed X-ray transparent fuel cells and electrolyzer cells for *operando* XRD-CT studies.[57,58]

In battery research, the same general principles for the cell design, as described above, hold. Conventional battery coin, prismatic and cylindrical cells, tubular ("Swagelok") cells, pouch cells, and capillary cells can be used (see chapter 8 Figure 41). Other cell geometries are also feasible in cells without liquid electrolytes, e.g., polymer electrolytes. In some cases, X-ray scattering techniques were also used to probe materials inside electrochemical devices, such as fuel cells. Particularly suited for this are XRD methods at very high photon energies of 70 keV or higher, where several cm of low-Z materials can be easily penetrated.

3.4 X-ray beam effects

For every *operando* method, it is crucial to always assess the effects of the used probe on the studied system. In comparison to electron probes, X-rays interact with electrons in materials only weakly, allowing them to penetrate the studied materials, as well as electrochemical cells, with relatively manageable beam effects (sometimes referred to as beam modulation or beam damage). However, the beam modulation is always present and needs to be assessed for each studied electrochemical system separately to avoid beam damage and misinterpretation of the data. Pioneering work by R. Henderson on a beam influence in biological systems forms a basis for a discussion in this section[61]. A comprehensive review of the possible X-ray beam effects is further provided in Ref.[62].

The fundamental process causing the beam modulation in matter is the photoelectric effect. In this process, the incoming photon is fully adsorbed by an electron bound in the atom, and this electron is ejected from the atom with the kinetic energy $\varepsilon_{el} = \varepsilon_{Ph} - \varepsilon_0$, where ε_{Ph} is the energy of the photon and ε_0 is the energy required to remove the electron from the surface of the material or from the atom/molecule. This typically results in the formation of holes and excited states in the case of metallic electrodes, the generation of radical molecules in the case of electrolytes and soft matter, as well as in heating. Furthermore, high-energy free electrons can propagate through the environment and further interact with the atoms and molecules of the studied system. This, in turn, causes an avalanche effect, where one en-

ergetic electron generates several radicals and secondary free electrons along the propagation pathway. The radicals then further interact with the environment inducing an interaction cascade and possibly generating new species. The mean free path between each collision is typically less than 50 nm, but for electrons excited by high energy X-rays (> 30 keV), the total traveled path is on the order of tens of microns. Therefore, the interaction cascade can extend far from the X-ray interaction volume, and the effects of the beam often reach outside of the beam path.

Thermal effects are the most obvious beam modulation. These are most pronounced at low temperatures, where the temperature of the material can increase even by tens of degrees upon beam exposure. However, this greatly depends on the energy of used probe, total photons absorbed, irradiated volume, as well as on the material density and heat capacity. For typical experiments at ambient temperatures, the in-beam sample temperature is unlikely to increase by more then several degrees, and this only for insulating samples. If precise temperature control is needed, the temperature of the sample should be taken as close to the beam as possible to account for beam heating effects[62].

The most severe beam modulation in electrochemical systems results typically from the radiolysis of liquid electrolytes (e.g. water, battery electrolytes). The photoelectrons causing the interaction cascade are often generated in the solid electrode itself and propagate far in the electrolyte. In the case of high Z elements, those photoelectrons are the main fraction, not the photoelectrons generated in the electrolyte itself. Therefore the highest concentration of electrolysis products are often produced at the electrode surface, which can be highly detrimental for *operando* experiments in electrocatalysis. The interactions between energetic electrons and the electrolyte molecules, the products in form of radicals, and the interaction cascade has been described by various authors from diverse backgrounds[63–70]. For the hydrolysis of water, the main radicals are hydrated electrons (e_{aq}^-), hydrogen and hydroxyl radicals ($H\cdot$, $OH\cdot$), which are further converted into the hydrolysis products OH^-, H^+, H_2, H_2O_2, and HO_2 in the time frame of 1×10^{-6} s (Figure 9a)[63]. These products can interfere with the surface chemistry or change substantially the pH in the vicinity of the X-ray beam, leading to undesired effects and wrong conclusions. These effects are often overseen, but there are several reports in the literature where beam modulation during in situ/*operando* experiments was explicitly discussed. Examples include the beam-induced Fe redox chemistry under the ESRF-EBS beam[71], the rate enhancement in metal electrodeposition and NP formation[62], and the oxidative etching of gold NPs[72]. It should be noted here, that the beam modulation is not only present in liquid or polymer electrolytes during electrochemical *in situ*/*operando* experiments, even though the effects here are most pronounced. Altering of the solid state structure of the materials in the form of permanent atomic displacement in crystalline materials (defect formation), induced phase transitions, formation of electron-hole pairs in semiconductors, and changes in the chemical state of the atoms is not unusual.[62]

Two main factors affect the beam modulation: the employed energy of the X-rays and the total dose in the probed volume of the sample. These two parameters can be controlled and careful beam modulation assessment and possible mitigation measures should take place ahead of each *in situ*/*operando* measurements. The evolution of cross sections for various X-ray/matter interactions with energy shows that higher X-ray energy is advantageous for diffraction experiments in terms of beam modulation, because of the favorable ratio of elastic versus photoelectric cross sections at higher energies (Figure 9b)[61]. However, this is a generalization that should be taken with a grain of salt, as more energetic electrons can induce higher concentrations of hydrolysis products, while also penetrating much larger distances in the electrolyte. The ideal energy for an experiment will depend on the electrode/electrolyte composition and the morphology of the materials. To proper assess all these effects, careful simulation should be performed, but to the best

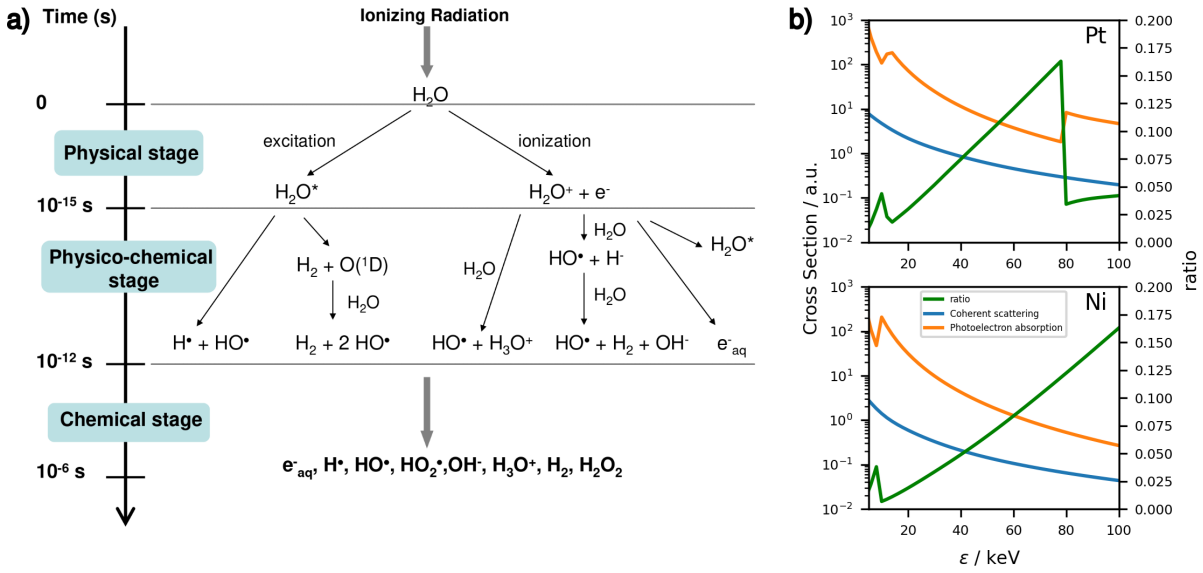

Figure 9: (a) Main reactions occurring during the three stages of water radiolysis (Adapted from [63]). (b) Cross sections of coherent scattering (blue) and photoelectron absorption (orange). Their ratio (green) is related to amount of useful scattering signal in comparison to the beam damage. Higher ratio means less photoelectrons per scattering event and possibly less beam modulation.

of our knowledge, the foundation has not been yet developed for electrochemical systems. In the case of protein diffraction, the ideal energy has been determined to be around 24-41 keV depending on crystal size[73].

In current *in situ* and *operando* studies, the maximum total dose at which significant beam modulation can be avoided is assessed and controlled experimentally. The easiest method to check whether severe beam modulation occurs is to expose the studied system to the X-ray beam and observe whether the scattered intensity changes with time under electrochemical conditions, where the sample should be stable. If no changes are detected, the measurement can proceed. If changes are detected, the dose needs to be decreased. In addition, the presence of radiolysis species may also manifest in the electrochemical data (e.g., CVs), which provides another check. Decreasing the dose can be achieved by several means, e.g., by lowering the incident flux of the beam, by defocusing the beam and spreading it over a larger sample volume, and by moving the beam across the sample. It is also good practice to measure at multiple spots on the sample: one spot at high temporal resolution and one (or multiple) spot(s) with a much lower dose as a control measurement. The golden rule is to keep the dose at a minimum while still getting data of reasonably high quality. Note that dose is defined as the total energy deposited by X-rays per unit mass (units Gray). This quantity is directly proportional to the incident X-ray flux and photoelectric cross sections of the composed matter. In the literature, the dose is often loosely defined as just proportional to the incident flux.

While it seems that the beam modulation problem is insurmountable, it is actually a solvable issue and it should not stop the experimentalist from doing the measurement. However proper design of the measurement protocol is often needed, together with extra time to understand the radiation damage of the electrochemical system in hand. Then appropriate precautions can be taken and high-quality data can be obtained.

4 In situ and operando methods

4.1 Overview

A large number of X-ray techniques exist, of which most are suitable for studies. Depending on the precise technique, different types of samples can be studied and these studies provide different types of structural information. A basic distinction is made between wide-angle X-ray scattering and small-angle X-ray scattering techniques. The former investigate the sample structure on the atomic scale, as described in Section 2.3.2-2.3.5; the latter analyze the scattering at much smaller **q** vectors (see Section 2.4) and thus provide structural data on length scales between several nanometers up to micrometers. In addition, X-ray scattering methods differ with respect to the central properties of the employed X-ray beam, such as photon energy, the degree of coherence, and the size of the beam at the sample position.

Available X-ray scattering techniques for *in situ* and *operando* studies are summarized (in alphabetic order) in Table 1. In the following sections, we provide short introductions to these techniques, sorted by the type of samples they can be applied to. We mostly focus on basic principles and aspects necessary to understand the information on electrochemical systems that can be gained by them. For an in-depth description of individual techniques, we refer to the reviews given in Table 1 and the subsequent sections.

4.2 Methods for studies of particle ensembles

4.2.1 Conventional powder X-ray diffraction

In contrast to scattering techniques for single-crystal materials, powder diffraction is dedicated to the study of crystallite ensembles, *i.e.*, to fine dispersions of single- or poly-crystals. Because it applies to most of the solid matter, powder diffraction receives considerable interest in applied materials science, with no exception for electrochemistry and electrocatalysis. Powder X-ray diffraction (PXRD) is a widely used non-destructive method that provides information on the molecular structure, lattice parameters, and crystallinity of a sample. One of the key advantages of PXRD is its ability to analyze complex mixtures of crystalline and amorphous materials. This makes PXRD a powerful tool for analyzing geological samples, pharmaceuticals, and catalysts. In recent years, PXRD has become more accessible to researchers due to advances in instrumentation and data analysis software. Modern PXRD systems can generate high-quality data quickly and accurately, making it an indispensable tool for researchers in a variety of fields. Unfortunately, more complex sample environments (liquids, electrochemical cells etc.) remain obstructing for laboratory X-rays.

4.2.2 High energy powder X-ray diffraction

The use of high-energy X-rays from brilliant synchrotron sources is a game-changer for *in situ* or *operando* X-ray powder diffraction. As discussed previously (chapter 3.1), high photon energies (in the range of 100 keV) provide better penetration power and the ability to probe a large fraction of the reciprocal space. In that sense, brilliant and high-energy X-rays meet the most desirable aspects of neutron scattering, while exceeding these by far in signal and temporal resolution properties. The increasing amount of high-energy beamlines at last-generation synchrotron sources around the globe has considerably accelerated the development and realization of *in situ* and *operando* powder diffraction experiments in numerous fields of material science. Considering the scope of the present review, we will briefly discuss the key aspects of powder X-ray diffraction, especially in the context of synchrotron *in situ* or *operando* experiments. Although beamlines do not necessarily use similar experimental setups (goniometer, detector geometry *etc.*), we will discuss the simplest case of a large flat 2D detector placed perpendicular to the incident beam. For a more comprehensive and

Table 1: Overview of X-ray scattering methods for *in situ* and *operando* studies, the samples they can be applied to, and the type of information provided by these methods (in-depth technical information is provide in the cited reviews).

technique	sample type	obtainable information
Bragg coherent diffractive imaging (BCDI) [74–77]	individual nanoparticles	3D displacement and strain fields, dislocations
crystal truncation rods (CTR) [5,6]	single crystal	3D interface structure
grazing-incidence small angle X-ray scattering (GISAXS) [78]	nanoparticle ensembles on planar surfaces, interfaces with nanoscale in-plane modulation	interface morphology, characteristic nanoscale dimensions
grazing-incidence X-ray scattering (GIXS) [5]	single crystals, planar surfaces, thin films	in-plane structure of 2D phases and 3D crystals, texture
high-energy surface X-ray diffraction (HESXRD) [79]	single crystal, ensembles of supported nanoparticles	3D interface structure, 3D crystallites on surfaces
X-ray atomic pair distribution function (PDF) [80]	ensembles of crystalline and/or amorphous nanoparticles	real space description of short-length structure
powder X-ray diffraction (PXRD) [81]	powders	lattice constants, crystalline symmetry, structural phase transformations
Ptychography [82]	larger particles, extended samples	3D displacement and strain fields, dislocations
resonant anomalous surface X-ray scattering (RASXS) [83,84]	single crystals, planar surfaces, thin films, liquid interfaces	distribution of selected element at interface, interface electronic structure
resonant anomalous X-ray scattering (RAXS) [83,84]	various samples	distribution of selected element
single-particle X-ray diffraction	individual nanoparticles	strain distribution, lattice mosaicity, phase transitions, particle rotation
small angle X-ray scattering (SAXS) [85,86]	ensembles of nanoparticles	size distribution, shape
surface X-ray diffraction (SXRD) [5,6]	single crystals	3D interface structure
X-ray reflectivity (XRR) [3]	single crystals, planar surfaces, thin films, liquid interfaces	surface-normal electron density profile

detailed coverage of the technique, notably its adaptation to contemporary laboratory powder diffractometers, the reader is referred to the excellent textbooks from R.E. Dinnebier and J.L. Billinge [87], V. K. Percharsky and P.Y. Zavalij [88], and a recent Primer from Kaduk et al. [26].

High-resolution powder X-ray diffraction experiments require optimization of X-rays beams, the detection system, and powder samples (among other parameters such as well-controlled geometrical configurations, such as a small sample size). The optimal X-ray beam is monochromatic, parallel (i.e., neither convergent or divergent), and has a beam size that exceeds by far the characteristic length of the crystals composing the sample. The detection system requires a high angular resolution and fast signal acquisition, which is particularly important for operando measurements. X-rays at synchrotron sources combined with large area detectors satisfy the requirements and are ideally suited for *operando/in situ* powder diffraction experiments. The ideal powder sample consists of an ensemble of completely randomly oriented crystals. The orientational average is the fundamental pillar of the powder diffraction technique.

As shown in Figure 10a, a hypothetical powder sample of crystals with identical orientation in space is equivalent to a pseudo single-crystal. When exposed to the monochromatic X-ray beam, diffraction peaks are only observed on the detector if the Laue conditions (Eq. 10) are fulfilled, which only is the case for selected

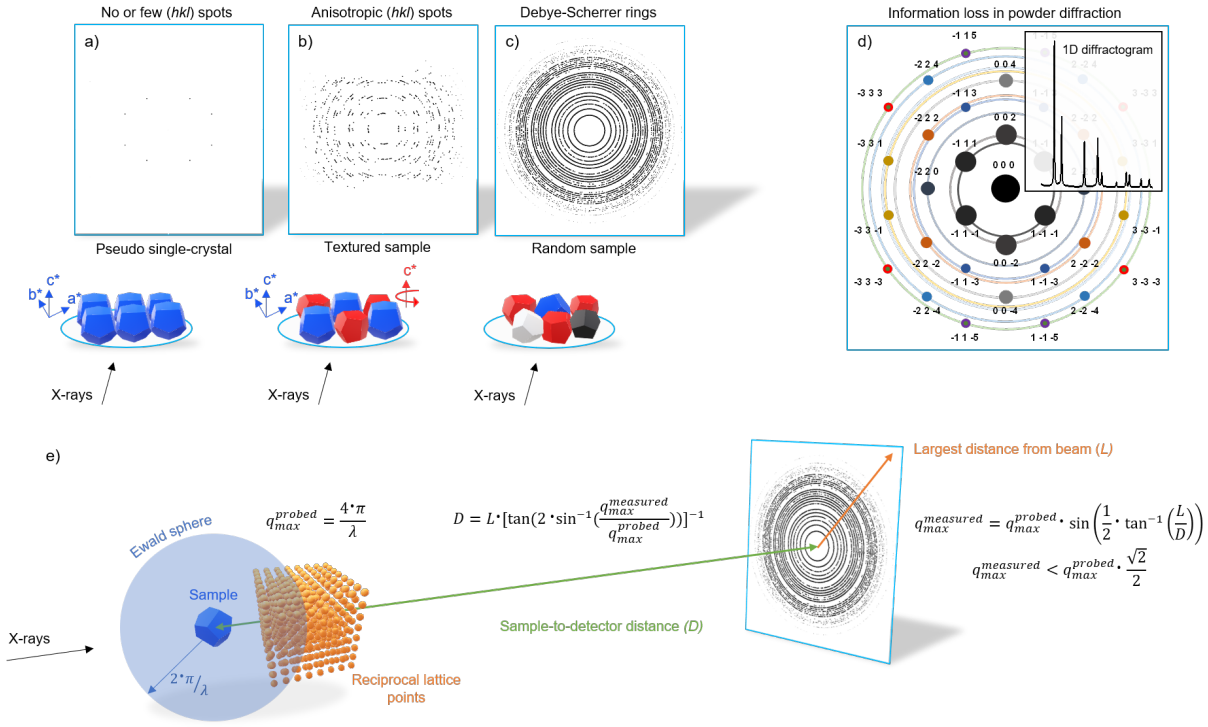

Figure 10: Key aspects of HE powder X-ray diffraction. Simulated diffraction pattern produced by (a) pseudo single-crystalline powder, (b) textured powder, and (c) randomly oriented powder. (d) Example of information loss in powder X-ray diffraction experiments for a face-centered cubic crystal powder. (e) Base parameters, controlling the q range to be effectively measured during a powder X-ray diffraction experiment in typical synchrotron experiment geometry involving forward scattering.

crystal orientations with respect to $\mathbf{k_i}$. Thus, without carefully rotating the sample into Laue condition no or only a few *hkl* reflections will be typically observed on the detector placed behind the sample. Solving such powder sample crystal structure would require the same approach as for single-crystals, meaning extensive sample alignment and rotations under the beam. For 'textured' samples in which the crystallites are rotated with respect to each other around a single axis that is aligned with a reciprocal lattice vector (**c*** in Figure 10b),[89], the Laue conditions can be more easily met and diffraction peaks will always be observed on the detector. Nevertheless, the distribution of these diffraction peaks on the detector will be highly anisotropic, resulting in a magnification of the scattered intensities for some families of reflections and a reduction of intensities for others. For a sophisticated structure analysis, a rotation of the sample would be required. In addition, it may be difficult to further disentangle the effects of such preferential orientation from those resulting from an anisotropic shape of the crystallites. Finally, if the crystallites are perfectly randomly oriented, the diffraction peaks merge into diffraction cones (i.e., a cone around the X-ray beam with a 2θ angle corresponding to the Bragg angle of a particular family of *hkl* plane spacing). All accessible Laue conditions are fulfilled without the requirement for a sample rotation and the detector shows characteristic Debye-Scherrer rings (i.e., the intersection of Debye-Scherrer cones with the flat surface of the detector). In other words, a fundamental advantage of powder X-ray diffraction compared to diffraction of single crystal and textured samples is that the sample 'aligns itself', and diffraction occurs systematically as long as X-rays reach the sample.

The experimental ease in powder diffraction measurements is paid for by a reduction of the information contained in the data. For example, during the transition from single crystal diffraction peaks to Debye-Scherrer rings, different (*hkl*) reflections from the same phase can become indistinguishable: they occur on the same ring if the lattice spacing of the different Bragg planes is identical (see the 333 and 511 rings for a face-centered cubic phase in Figure 10d). More generally, in the case of a multiphase sample, a ring describes an inter-planar distance, irrespectively of the original phase or (*hkl*) nature of this distance. Consequently, and as shown in Figure 10.d, 2D diffraction images of perfectly random powders measured on the large 2D detector can be reduced to conventional 1D diffraction patterns via azimuthal integration, without further loss of information. Note such 1D diffraction patterns still contain an extremely high amount of information (as detailed in the following), and that in the case of non-random powders such as textured powders, analysis can also be possibly performed on the 2D images.

As mentioned above, measuring diffraction from a powder sample that meets the condition of random crystallites orientation is quite straightforward. In the case of synchrotron setups using a flat 2D detector and tuneable X-rays energy, geometrical aspects of the experiment, such as X-ray wavelength and sample-to-detector distances must be set by the user according to the objectives of the measurement. Those parameters are summarized in Figure 10e. First, the energy of the incoming X-rays (i.e., their wavelength) must be chosen according to several key aspects including their penetration power, the possible absorption of the sample, its consequence on the beam flux, but also the maximal momentum transfers q that needs to be probed in the experiment. As the wavelength will set the radius of the Ewald sphere, the highest momentum transfers q_{max}^{probed} (or smallest interplanar distance d_{min}^{probed}) that can in principle be probed by the experiment (*i.e.*, that will produce diffraction) is given by Equation 41:

$$q_{max}^{probed} = \frac{4 \cdot \pi}{\lambda} = \frac{2 \cdot \pi}{d_{min}^{probed}} \tag{41}$$

This fundamental value cannot be reached in a typical synchrotron experiment that uses a large flat 2D detector because the geometry is restricted to forward scattering only (no backscattering). In practice, the highest momentum transfers q_{max}^{probed} to be possibly collected is given by Equation 42:

$$q_{max}^{measured} = q_{max}^{measured} \cdot \sin(\frac{1}{2} \cdot \arctan(\frac{L}{D})) \quad (42)$$

where L is the largest distance on the detector from the incident beam (supposed to impinge orthogonally on the detector) and D is the sample-to-detector distance (see Figure 10e). The user must naturally ensure that the interplanar distances of interest for the experiment exceed the minimum lattice spacing measured, controlled by the chosen wavelength and detector distance. At fixed detector dimensions L, $q_{max}^{measured}$ increases with decreasing D. Yet, excessively short distances D may result in a decrease of the pattern resolution at low angles if the thickness of the diffraction rings meets the detector pixel size. Because, contrary to some laboratory diffractometers, this geometry does not allow the measurement of diffraction angles 2θ higher than 90° the q-range is limited to $q_{max}^{measured} < q_{max}^{probed} \cdot /\sqrt{2}$. In practice, knowing the X-rays wavelength, the 'detector size' L and the desired q-range for the experiment, D is given by:

$$D = L \cdot [\tan(2 \cdot \arcsin(\frac{q_{max}^{measured}}{q_{max}^{probed}}))]^{-1} \quad (43)$$

Note that, L (and so $q_{max}^{measured}$) can be increased (L by positioning the detector in such a way that the incident beam hits one of the corners. Furthermore, the fraction of the recorded ring and thus the integrated scattered signal decreases for the rings with q values near $q_{max}^{measured}$, which has to be accounted for in the analysis. Finally, the above expressions must be considered carefully, as in practice (especially at high energies), the decreasing form factor strongly reduces the signal at high q values.

Figure 11 shows the exceptionally large amount of information on the sample structure that can be extracted from a powder diffraction pattern. Schematically, two main sources of information can be identified: the information located in the Bragg peaks (scattering by coherent domains, labeled in orange) and the information located 'underneath' the Bragg peaks (diffuse scattering from amorphous matter and/or extremely short coherence lengths, labeled in blue). Naturally, analytical methods used to extract the different information differ according to the information source. In the following, we will briefly present the Rietveld refinement method of the powder diffraction data and the pair distribution function analysis, related to the interpretation of the Bragg peaks and the total scattering, respectively.

4.2.3 The Rietveld method

Accessing quantitative information on the sample crystallographic structure, microstructure, and phases weight fractions through the Rietveld method[90] requires preliminary qualitative knowledge of the phases constituting the sample, such as their individual crystal space group and lattice constants. Taking only Bragg peak positions and intensities as input parameters, such qualitative information can be obtained by comparing experimental powder diffraction pattern and a database of reference patterns (manually or with the assistance of commercial software). For *in situ* or *operando* studies, the obvious starting point is the *ex situ* sample structure. Based on this qualitative information on the sample, the Rietveld method consists of a non-linear least-square fitting of the experimental data by the following model function:

$$y_{ci} = y_{bi} + \sum_{\phi=1}^{N} S_\phi \sum_{k=1}^{m} A_{\phi_k} \cdot |F_{\phi_k}|^2 \cdot \Omega_{i\phi_k} \quad (44)$$

where y_{bi} is the intensity of the background at point i, ϕ is the index of the structural phases, of which the sample constitutes, k is the index of the reflections contributing at point i, and S_ϕ is the scale factor of phase ϕ. A_{ϕ_k} is a corrective term applied to the intensity of the k^{th} reflection of phase ϕ, which takes into account the reflection's multiplicity, the Lorenz-polarization, possible preferred orientation, absorption, *etc.*. $|F_{\phi_k}|$ is the modulus of structure factor of the k^{th} reflection of phase ϕ and $\Omega_{i\phi_k}$ is the profile function of the k^{th} reflection of phase ϕ calculated at point i.

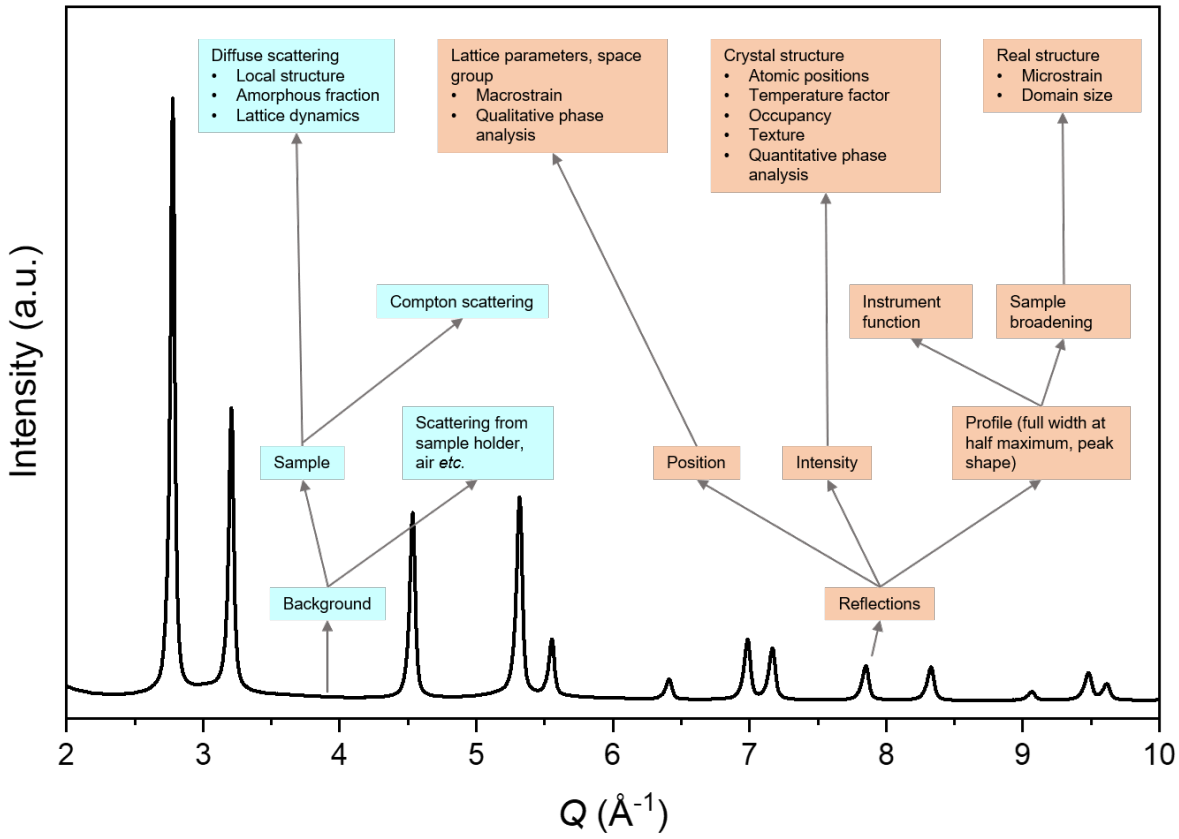

Figure 11: Information content of a powder diffraction pattern (Adapted from Ref.[26]. Copyright 2021 Springer Nature).

The variables adjusted during the refinement are those which determine the Bragg peak positions, shapes, and intensities. As shown in Figure 11, the positions of the Bragg reflections are determined by the lattice constants and crystal type of each phase. Their intensities can be derived from the structure factors, which depend on the atomic positions, displacements, and site occupancies. Complementary, the Bragg peaks shapes and broadening can be well-described by a Pseudo-Voigt (PV) function, which is the weighted sum of a Gaussian and a Lorentzian of the type $PV(2\theta, \eta, H) = \eta \cdot L(2\theta) + (1-\eta) \cdot G(2\theta)$ where θ is the Bragg angle, η ($0 \leq \eta \leq 1$) is the mixing parameter, $L(2\theta)$ and $G(2\theta)$ are respectively the Lorentzian and Gaussian contributions, and H the common FWHM of $PV(2\theta)$. Because PV is an analytical function, it can be easily least-square refined, giving the values of η and H. Moreover, it has been shown by Thomson, Cox, and Hastings[91] that the values of H_G and H_L (the widths of the Gaussian and Lorentzian components of the Voigt function, respectively) can be directly calculated from those of H and η. As shown in Figure 11, it is generally assumed that the Bragg peak profile (shape and width) can be described as the convolution of three main contributions: (i) the incident X-ray beam monochromaticity, (ii) the instrument optics (slit gaps and positions, detector pixel size, etc.), and (iii) sample-related broadening effects. Contributions (i) and (ii) can be unified as the 'instrumental resolution function' (IRF), while contribution (iii) can be further divided into two additional contributions, namely the finite size of the coherent domains (or grain size), and the presence of microstrain, which reflects the local variations of interplanar distances caused by some sort of stress (disorder, stacking fault, twins, grain boundaries, inhomogeneous alloying, etc.). H_G and H_L are directly linked to these different sources of broadening via:

$$\begin{aligned} H_G^2 &= H_{I,G}^2 + U_{strain,G}.\tan(\theta)^2 + \frac{I_{size,G}}{\cos(\theta)^2} \\ &= H_{I,G}^2 + H_{strain,G}^2 + H_{size,G}^2 \end{aligned} \tag{45}$$

$$\begin{aligned} H_L &= H_{I,L} + X_{strain,I} \cdot \tan(\theta) + \frac{Y_{size,L}}{\cos(\theta)} \\ &= H_{I,L} + H_{strain,L} + H_{size,L} \end{aligned} \tag{46}$$

where $H_{I,G}$ and $H_{I,L}$ are the Gaussian and Lorentzian instrumental contributions to broadening, $H_{strain,G}$ and $H_{strain,L}$ are the Gaussian and Lorentzian microstrain contributions from the sample to broadening, and $H_{size,G}$ and $H_{size,L}$ the Gaussian and Lorentzian size contributions from the sample to broadening. The IRF (*i.e.* $H_{I,G}$ and $H_{I,L}$) can be determined separately from the sample by refining the diffraction pattern of a standard powder of perfectly determined structure (CeO_2 or LaB_6 National Institute of Standards and Technology standards for example). However, the remaining parameters related to the sample can hardly be refined simultaneously due to strong correlation problems. In practice, simplifying hypotheses are commonly made, such as arbitrarily fixing the Gaussian or Lorentzian contribution(s) for the size and/or strain broadening to zero. This can of course impact the outcome of the refinement, as shown in Ref.[92]. The broadening derived from Equations 45 and 46 can be thus compared to the size and strain contributions from the sample. By derivation of Bragg's law, Scherrer demonstrated that this width ($\Delta_{size}(2\theta)$) depends on the domain size T as[93]:

$$\Delta_{size}(2\theta) = \frac{K \cdot \lambda}{T \cdot \cos(\theta)} \tag{47}$$

where $K \approx 1$. Alternatively, microstrain is characterized by the constant $\epsilon = \Delta d/d$. Using derivation of Bragg's law, one obtains:

$$\Delta_{strain}(2\theta) = 4 \cdot \epsilon \cdot \tan(\theta) \tag{48}$$

The above description refers to the isotropic case where the domain size is approximated by a sphere and the micro-strain is supposed to be the same in any direction. Although it often represents a good approximation, in some cases the micro-structure can be strongly anisotropic and the corresponding peak broadening will depend not only on the reflection Bragg angles but also on their Miller indices with respect to the

anisotropy of the microstructure. Overall, the Rietveld method is a powerful method to describe samples with crystallographic models in the reciprocal space. However, its application is naturally limited to crystalline materials.

4.2.4 X-ray atomic pair distribution function method

Crystallography has unambiguously powered the discovery and development of advanced functional materials over the past century. However, the last decades have seen a growing interest in non-crystalline materials, or in crystalline samples with pronounced local disorder. The pair distribution function (PDF) technique provides quantitative insights into the structure of materials where the coherence domains extend only over a few nanometers. In contrast to crystallographic methods such as the Rietveld method described above, PDF is based on the scattering theory outlined in section 2.3.4 and does not require assumptions of periodicity but can be defined directly in real-space in terms of static atomic coordinates. In the following, we briefly introduce the method and how it can be measured (for details see Ref.[80]). Basis for the analysis is the pair distribution function $g(\mathbf{R})$ defined according to Eq. 28 or, more typically, its isotropic counterpart, the radial distribution function $g(R)$. These functions have the advantage to be extremely intuitive and strongly emphasize the short range order, but they cannot be obtained experimentally with high accuracy, notably without assumptions on ρ_n.

Consequently, the reduced pair distribution function $G(R)$ is most widely used, which is defined as:

$$G(R) = 4\pi R\rho_n[g(R) - 1] \tag{49}$$

Inserting this function into Eq. 31, the total scattering structure function $S_t(q)$ is given by:

$$S_t(q) = 1 + q^{-1}\int_0^\infty sin(qR)G(R)dR \tag{50}$$

$G(R)$ can consequently be obtained by Fourier transformation of the experimentally observable quantity $S_t(q)$ via:

$$G(R) = \frac{2}{\pi}\int_{q_{min}}^{q_{max}} q[S_t(q) - 1]sin(qR)dq \tag{51}$$

where q_{min} and q_{max} define the q range in which the diffraction pattern is measured. $S_t(q)$ depends on the differential scattering cross section which is derived from the measured signal on the detector. The main advantages of $G(R)$ compared to the other related functions (besides being experimentally accessible from intensity data) are: (i) no assumption on underlying structure is required, (ii) random uncertainties of the intensity data 'spread' equally with R in $G(R)$ and (iii), the amplitude of the oscillations give a direct measure of the structural coherence in the sample[94].

Data acquisition for PDF is thus as straightforward as for high energy powder X-ray diffraction experiments, except that it is important to measure data over a wide range of momentum transfer, q. In fact, because the PDF is a Fourier transform, the q range and the resolution in q (δq) of the powder diffraction pattern will directly impact the quality of the PDF signal in real space, according to:

$$\delta R = \frac{2\pi}{q_{max}} \tag{52}$$

where δR is the resolution (or definition) of the PDF, i.e. the shortest real-space atomic oscillation to be possibly encoded in the data. The effective longest atomic pair distance probed by the PDF is:

$$R_{max} = \frac{2\pi}{\delta q} \tag{53}$$

With poor q resolution in reciprocal space, the PDF 'dampens' at high-R values. Importantly, however, the fine local structure (i.e. the PDF signal at low r values) is nearly nonsensitive to this parameter. Finally, the longest real-space oscillation present in the PDF data is given by:

$$\Lambda_{max} = \frac{2\pi}{q_{min}} \tag{54}$$

This parameter is particularly important for PDF on nanoparticles, as the shape function of

the nanoparticle is encoded in the low-q region of the diffraction pattern.

The procedure outlined above can also be applied to systems consisting of different types of atoms.[80] In this case, the different atomic form factors and concentrations of the involved species have to be considered.

4.3 Methods for studies of thin films

4.3.1 X-ray reflectivity

As any other electromagnetic wave, X-rays that impinge on a smooth surface or interface under an angle α_i split up into a reflected beam that leaves the interface under the same angle $\alpha_f = \alpha_i$ and a transmitted beam, entering the new phase under a different angle α_t due to the effect of refraction. The calculation of the refraction angle as well as the intensities of reflected and transmitted wave is fully possible within the classical theory of electromagnetic waves, but requires to go beyond the kinematic approximation, where we explicitly excluded refraction. Refraction depends on the dielectric properties of the phases at both sides of the interface, specifically on the complex index of refraction n. For X-rays n always is smaller 1, because the X-ray photon frequencies are higher than all electronic resonances of the atoms and molecules of the material. It therefore is commonly written in the form:

$$n = 1 - \delta + i\beta \tag{55}$$

Here the deviation from one for a homogeneous material with the total electron density ρ_e is given by[3]:

$$\delta = \lambda^2 r_e \rho_e / 2\pi \tag{56}$$

where $r_e = 2.82 \cdot 10^{-5}$ Å is the classical electron radius. δ is usually a very small quantity. For example, for a wavelength $\lambda = 1$ Å and Au, a material with very high electron density $\rho_e = 4.65$ Å^{-3}, this deviation is $\delta = 2.09 \cdot 10^{-5}$. The imaginary part of n, which describes the decay of the wave's amplitude due to absorption, is given by:

$$\beta = \lambda\mu / 4\pi \tag{57}$$

with μ being the linear absorption coefficient.

As a consequence of Snell's law, for an electromagnetic wave propagating from a region of higher to one of lower index of refraction total reflection occurs beyond a critical angle α_c. That is, the wave enters the low n material only in the form of an evanescent wave, whose intensity decreases exponentially with increasing distance from the surface, and the incident wave is completely reflected with almost identical intensity. This situation applies to the reflection of a wave entering into a sample with high electron density from the vacuum, where $n = 1$, or from a low-Z material (e.g. an electrolyte solution). In the latter case, the difference in the electron density of the two materials has to be used in the calculation of δ. For the case of a vacuum-Au interface, the critical angle, which is given by $\alpha_t = \sqrt{2\delta}$, is (at $\lambda = 1$ Å) 6.5 mrad or 0.37°, respectively. Such small critical angles are typical in surface X-ray scattering and justify the experimental needs for low divergent beams, highly planar surfaces, and precise positioning in these experiments. Since refraction and absorption effects are usually only relevant in the vicinity of the critical angle or of the Bragg peaks, they can be often ignored, justifying the restriction to the kinematic approximation in our derivation of scattering theory in chapter 3.3. Nevertheless, they are important at gracing incident angles, such as in reflectivity measurements at low q or grazing incidence X-ray diffraction (GIXRD).

To understand quantitatively the change in reflected intensity with the surface normal component of the scattering vector q_z, we first consider the case of reflection at a perfect interface between two materials described by the complex indexes of refraction n_1 and n_2, respectively. The reflectivity, defined as the ratio between the reflected and incident intensity, is then given by the Fresnel equations:

$$R_F \equiv \left|\frac{I}{I_0}\right| = \left|\frac{\alpha_i - \alpha_t}{\alpha_i + \alpha_t}\right|^2 \tag{58}$$

Expressing R_F as a function of the scattering

vector one obtains:

$$R_F(q_z) = \left| \frac{q_z - \sqrt{q_z^2 - q_c^2}}{q_z + \sqrt{q_z^2 - q_c^2}} \right|^2 \approx \left(\frac{2q_z}{q_c} \right)^{-4} \quad \text{for } q_z \gg q_c \tag{59}$$

where $q_t = 4\sqrt{\pi \rho_e r_e}$ is the critical scattering vector for total reflection. The behavior of $R_F(q_z)$ near q_c is illustrated in Figure 12a. For materials with low X-ray absorption coefficients, a sharp drop in intensity occurs at the critical angle; for strongly adsorbing materials this drop is slightly softened, but even here $\approx 70\%$ of the incident intensity is reflected at q_c. In parallel, the penetration depth Λ of the X-ray beam into the sample substantially increases and the transmitted intensity T directly at the interface exhibits a so-called Vinyard profile with a local maximum ("Yoneda peak") at q_c (Figure 12b,c).

For an interface where the total electron density does not change abruptly but varies gradually, the reflectivity differs distinctly from $R_F(q_z)$. In most cases, it is well described by the so-called master formula:

$$R(q_z) = R_F(q_z) \left| \int_{z=-\infty}^{\infty} \frac{d}{dz} \left(\frac{\langle \rho(z) \rangle}{\rho_\infty} \right) e^{-izq_z} \right|^2 \tag{60}$$

Here, $\langle \rho(z) \rangle$ is the electron density profile along the surface normal, obtained by averaging $\rho(\mathbf{r})$ within the plane parallel to the surface at each z value, and ρ_∞ is the difference in the electron densities, found in the bulk of the materials to both sides of the interface. Thus, the normalized curve $\langle \rho(z) \rangle / \rho_\infty$ is a smooth function that varies from 0 to 1 when crossing the interface region and describes the relative change in the refraction index n. The derivation of the master formula employs the kinematic approximation and is well justified for $q_z \gg q_c$. Since R is in many cases almost identical to R_F near the critical angle, it is usually well suited for describing the full reflectivity curve. A notable exception is the reflectivity of a sample, covered by a thin layer with much higher electron density and thus a larger critical angle.

As an example of the application of the mas-

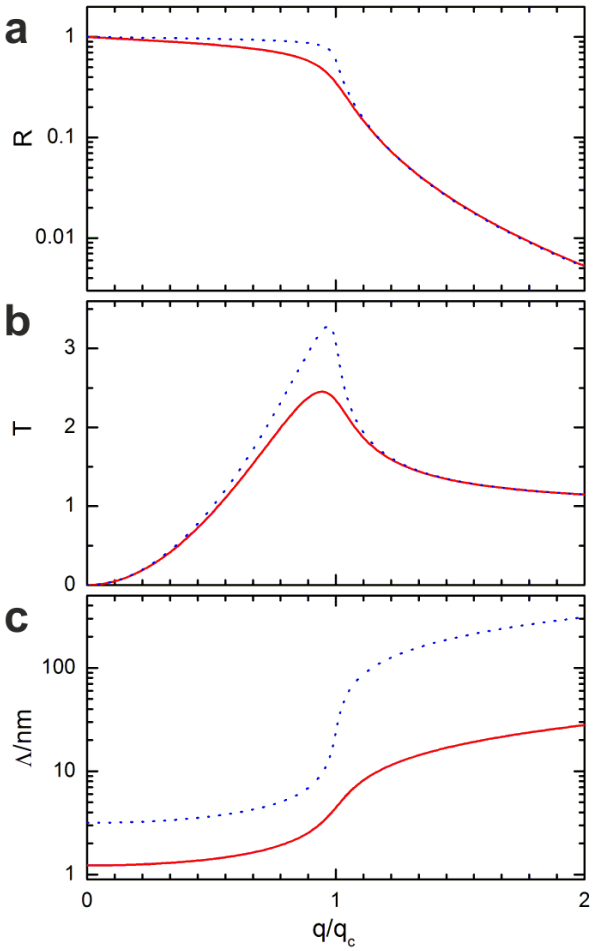

Figure 12: (a) Reflectivity R, (b) transmitted intensity T at the position of the interface, and (c) penetration depth Λ near the critical scattering vector q_c for perfectly terminated Au (red) and Si (blue) samples.

ter formula, we consider an interface where the density does not change abruptly, but gradually (Figure 13, inset, blue line). This type of density profile can be conveniently described by the error function $\langle\rho(z)/\rho_\infty = erf(z/\sqrt{2}\sigma)$; its derivation is a Gaussian. Fourier transform results in another Gaussian, resulting in a reflectivity curve described by:

$$R(q_z) = R_F(q_z)e^{-q_z^2\sigma^2} \tag{61}$$

The additional factor leads to a faster decay of R with q_z as compared to R_F (see Figure 13). This effect increases with the interface width σ, causing a decrease in the experimentally accessible q_z range (typically $\approx 10^{-8} \cdot I_0$). This is the reason why rather smooth surfaces are required for surface X-ray scattering studies.

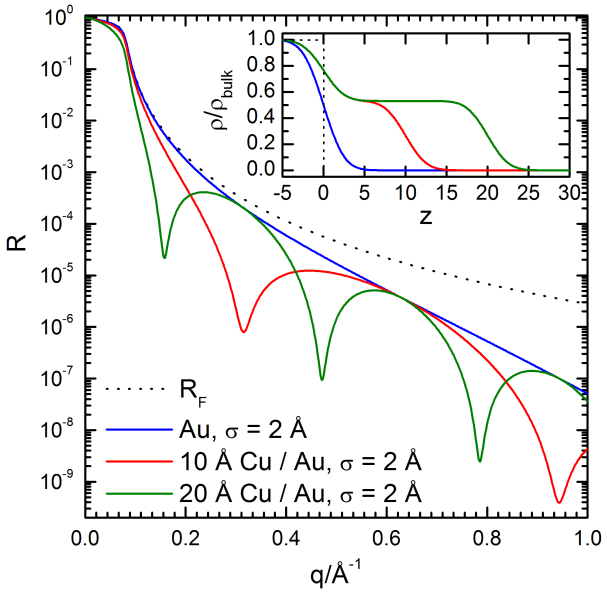

Figure 13: Calculated X-ray reflectivities and normalized density profiles (inset) for an Au surface exhibiting a gradual density change with a Gaussian width of 2 Å (blue) and a similar Au sample covered with a Cu layer of 10 Å (red) and 20 Å (green) thickness. For comparison, also the Fresnel reflectivity is shown (dotted line).

Because reflectivity does not involve any momentum transfer within the surface plane ($q_x = 0 = q_y$), it is insensitive to the lateral distribution of the electron density. Eq. (61) therefore describes equally the specular reflectivity of a surface with an inherent, spatially homogeneous density gradient, as e.g. caused by the gradual change in electron density within the ion core of the surface atoms, and that of an interface with an inhomogeneous density distribution in the surface plane, such as a (Gaussian) surface roughness. However, the latter induces additional diffuse scattering and leads to modifications along non-specular CTRs, which allows distinguishing these two cases.

As a second example, the influence of a thin layer of a different material on the sample surface is illustrated in Figure 13. Here, characteristic oscillations in the reflected intensity are observed (often denoted as "Kiessig fringes"). Their physical origin is identical to optical interference effects at soap bubbles: The coherent superposition of the waves reflected from the film surface and the film-substrate interface lead to constructive or destructive interference, depending on q_z. From the spacing of Δq_z of the interference minima, the layer spacing can be directly obtained as $2\pi/\Delta q_z$. The overall decay of the curve is determined by the decay in R_F and the widths of both interfaces, which provide an envelope for the interference fringes due to the adlayer.

More complex interface density profiles, consisting e.g. of several subsequent layers with different interface widths in between, can lead to reflectivity curves that exhibit a rich sequence of modulations. Such profiles can be determined by setting up a parametrized model of $\langle\rho(Z)\rangle/\rho_\infty$, calculating from those $R(q_z)$ via Eq. (61) or more precise approaches, and employing this in a numerical fit of the model to the reflectivity data. These fits are not fully unique, because of the loss of the phase information in the master formula, which can lead to indistinguishable reflectivity curves for rather different density profiles. For example, the reflectivity curves of a sample with an adlayer of density $x \cdot \rho_\infty$ and $(1-x) \cdot \rho_\infty$ are exactly identical. For these reasons, fits by models with a larger number of parameters can be difficult to obtain. Therefore, often additional physical information on the structure and composition of these interfaces is used to constrain the boundary conditions.

4.3.2 Grazing incidence diffraction

To obtain data on the crystal structure and the texture, i.e., the orientation distribution of the crystallites in the film, wide-angle diffraction is commonly used. Often, these experiments are performed in grazing incidence geometry, where the angle of the incident X-ray beam with respect to the surface is around the critical angle. In this scattering geometry the penetration of the X-ray beam into the substrate is minimized (see Figure 12c), reducing the substrate's contribution to the scattered intensity. In particular, this is important to lower the intensity of bulk Bragg peaks, which otherwise would provide orders of magnitude higher intensities. In addition, the enhancement of the transmitted intensity at the interface near the critical angle (see Figure 12b) can increase the diffracted intensity of the film's Bragg reflections. However, this effect only plays a role for very smooth films.

Depending on the type of texture, different types of diffraction patterns are observed. This is schematically illustrated in Figure 14a, where the distribution in reciprocal space is shown for different textures. For thin films in which the individual crystallites are randomly oriented, i.e., powder-like samples, the Bragg peaks are distributed over a spherical surface. The condition for scattering is met where this sphere intersects with the Ewald sphere (green), which is on a ring, resulting in the typical powder rings. In contrast, the Bragg peaks of epitaxial films on a single crystalline substrate are located at well-defined reciprocal space positions, similar as those of a single crystal. Here, diffraction peaks are only observed for orientations of the crystal relative to the incoming beam, in which one of the Bragg reflections lies on the Ewald sphere. An important intermediate case are films where the crystallites have a defined orientation along the surface normal, but a random in-plane orientation. The Bragg reflections of films with such fiber texture reside on rings around the surface-normal axis. These rings always intersect the Ewald sphere at a well-defined point, resulting in an intensity peak that is independent of the in-plane sample orientation.

An example of the scattering by such fiber-textured films is given in Figure 14b. Here, *in situ* grazing incidence diffraction data is shown that was recorded at a liquid Hg - electrolyte interface after electrodeposition of a PbFBr film. The PbFBr crystals are oriented with their c-axis along the surface normal but have arbitrary orientations within the interface plane due to the liquid metal substrate. Various intensity peaks can be found on the 2D detector images, which can be attributed to PbFBr Bragg reflections. Enlarged detector areas around these reflections (top panels) show that these peaks consist of small individual peaks of different crystals. The intense peaks in the center are located precisely on the Ewald sphere, and the peaks to both sides of that gradually decrease in intensity reflecting the decreasing match with the diffraction condition.

4.4 Methods for studies of single crystals

We will now discuss experimental X-ray scattering techniques for studies of single-crystal interfaces, using predominantly electrochemical systems as examples. Figure 15a gives an overview of the characteristic features in reciprocal space as well as of several typical modes of measurements for the case of a (100) surface of an fcc metal. As discussed in textbooks of solid state physics the face-centered unit cell results in systematic extinctions of Bragg reflections, leaving only the reflections with h, k, and l all even or all odd intact. Hence the lowest-order CTRs are the (0 0 l), (0 2 l), the (2 0 l), and the (1 1 l) rod. In addition, an additional layer with a $c(2 \times 2)$ in-plane superstructure is included in Figure 15a, which is a very common adlayer arrangement on this type of surface. This 2D superstructure lattice gives rise to additional (h k l) rods at all integer h and k in between the CTRs. As shown in chapters 3.3.3 and 3.3.4 the intensity of the superstructure rods is approximately independent of l, whereas that of the CTRs exhibits strong variations with maxima at the Bragg peak positions. First information on the presence of ordered superstructures at

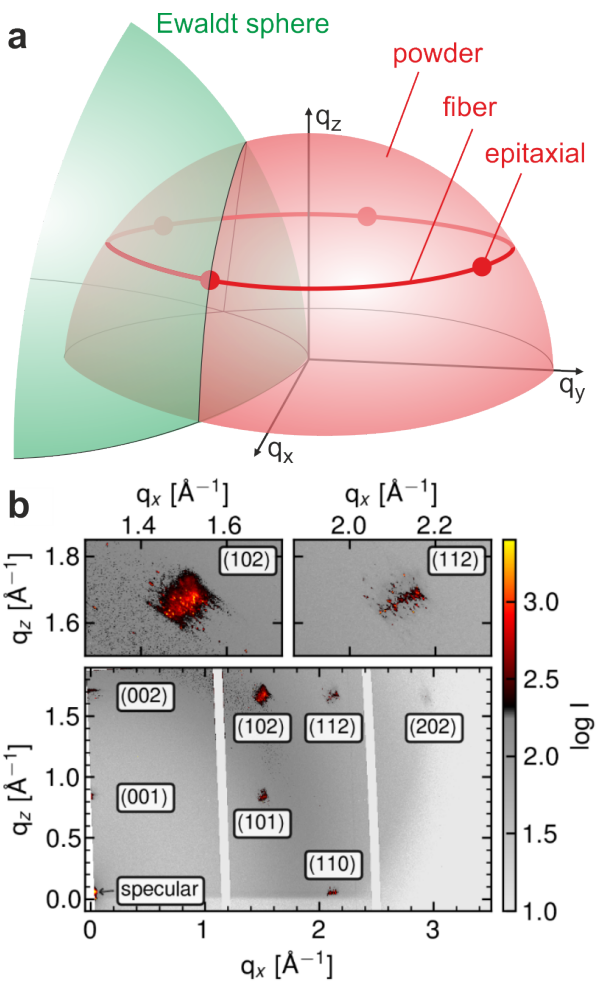

Figure 14: (a) Reciprocal space scheme illustrating wide-angle scattering in grazing incidence geometry from a film with epitaxial, powder, and fiber texture. (b) Example of the scattered intensity distribution from a thin film with fiber texture. The bottom panel shows a detector image (projected into the q_x-q_z plane) that was obtained at an incidence angle of 0.135° on an electrodeposited c-axis oriented PbBrF film on a liquid Hg electrode. The top panels show selected parts of the detector in the vicinity of the (102) and (112) PbFBr Bragg peaks (reproduced for Ref.[95]. Copyright 2020 American Chemical Society).

the interface is usually obtained by studies at small l, i.e., under gracing incidence and exit angles α_i and α_k, respectively. Because of the small wave vector transfer q_z normal to the surface, this GIXRD selectively probes the lateral positions of atoms within the surface plane but is insensitive to their positions in the surface normal direction, e.g., vertical modulations or their spacing to the atomic layer underneath. In contrast, measuring the (0 0 l) CTR, which is identical to a specular reflection of the beam at the crystal surface, only provides data on the in-plane averaged structure along the surface normal. Full crystallographic data on the 3D arrangement of atoms at the interface requires the measurement of specular and non-specular CTRs as well as potential superstructure rods. All three types of measurements will be discussed in detail in the chapters below.

To give an impression of the strength of the various contributions to scattering from electrochemical interfaces, actual SXRD data for Cu(100) in Cl-containing perchlorate solution is shown in Figure 15b. At the employed potential of 0.2 V the surface is fully covered by an ordered Cl adsorbate layer with $c(2\times2)$ structure, i.e., the structure is identical to that in Figure 15a. The displayed in-plane scan along the h axis exhibits two sharp peaks that correspond to the diffraction rods at (1 0 l) and (2 0 l) and sit on a slowly varying background, caused predominantly by the bulk liquid scattering. However, the peak intensity at the $h = 2$ position, which is close to the (2 0 0) Bragg peak, is orders of magnitude higher than that of the superstructure peak (at $h = 1$) or of the CTRs close to the anti-Bragg position (not shown), who have a signal-to-background ratio in the range of one. As a rule of thumb, this is a typical situation in *in situ* SXRD studies, although signal-to-background ratios from more than 10:1 down to immeasurably small signals are possible – depending on the material (due to the $\approx Z^2$ dependence of the atomic form factor), the domain size (via $I \propto N_x N_y$), and the surface roughness (see below). We note that the same considerations apply to the case of epitaxial multilayer films with well-defined orientation relative to a single crystalline substrate

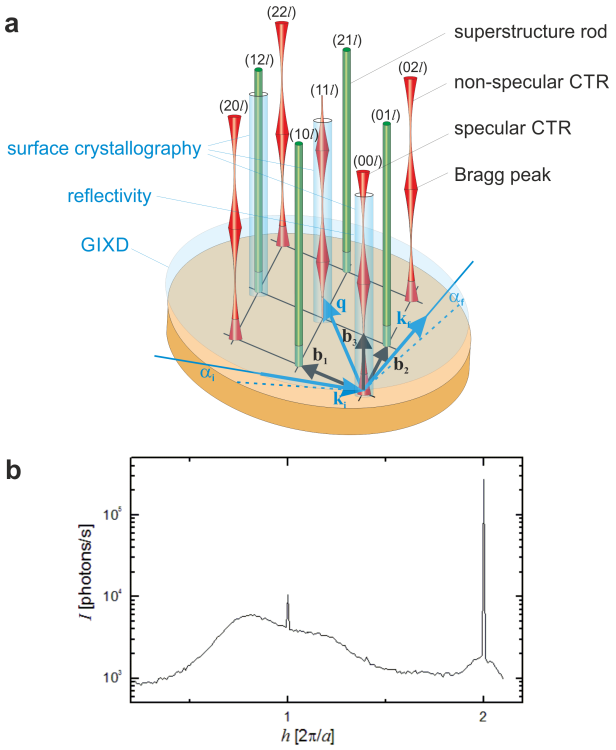

Figure 15: (a) Overview over surface X-ray scattering techniques, shown exemplarily for a $c(2 \times 2)$ adlayer on an fcc(100) surface. (b) *In situ* surface X-ray scattering data for a Cu(001) surface in Cl-containing electrolyte, illustrating the various contributions to the scattered intensity. The scan was performed along the $\mathbf{b}_1$ axis at small $q_\perp (l = 0.1)$ and is scaled in units of the reciprocal lattice. Visible are sharp peaks at the positions of the CTR at (2 0 0.1), i.e., close to the (2 0 0) Bragg peak, and of a superstructure rod at (1 0 0.1), that indicates the presence of an ordered $c(2 \times 2)$ Cl adlayer, as well as the broad distribution, caused by scattering of the bulk liquid electrolyte.

(see section 6.2.4 for an example).

4.4.1 In-plane surface diffraction

In gracing incidence X-ray diffraction, the crystalline order within the surface plane is probed. Prime applications are studies of surface reconstructions and adsorbate layers. In these measurements, the incident X-ray beam impinges on the surface under a small incident angle α_i and the intensity scattered under similarly small exit angles α_k is recorded. Under these conditions, the wave vector lies almost in the surface plane, i.e., $q_\parallel \approx q$ whereas the out-of-plane component $q_z \ll q$ (see Figure 1a). By varying the scattering angle 2θ, the radial component q can be changed; by rotating the sample around its surface normal, the azimuthal orientation of the wave vector relative to the surface lattice is altered.

In typical grazing incidence X-ray scattering (GIXS) experiments the incident angle is chosen to be close to the critical angle for total reflection, i.e., $\alpha_i \approx \alpha_c$. Under these conditions, the transmitted intensity at the interface is enhanced by up to a factor 4 (see Figure 12b), resulting in a corresponding enhancement of the X-ray scattering (the height of this maximum decreases with increasing X-ray absorption of the material, as illustrated in the figure for the case of Si and Au surfaces). A similar enhancement effect is also found for exit angles $\alpha_f \approx \alpha_c$. The increase in intensity leads to the amplification of the weak scattering by 2D crystalline layers, such as adsorbates. However, in *in situ* studies of electrochemical interfaces often substantially larger angles are used, in particular, if the experiments are performed in thin layer cells of the type shown in Figure 8a. Here, the gain in intensity due to this enhancement can be easily overcompensated by the longer X-ray path length in the electrolyte, which increases proportionally to α_i and α_f.

A second advantage of choosing angles near the critical angle is the small penetration depth Λ, which reduces the contributions from the bulk material. As shown in Figure 12c, Λ increases in a strongly non-linear way from values of a few 10 nm at angles clearly below α_c to sev-

eral 100 nm up to several μm, depending on the X-ray absorption coefficient. Thus structural properties of the material in the near-surface region and in the bulk can be probed in the same experiment, simply by a small variation of the incident angle. For example, this allows the determination of surface strain or an increased defect density near the interface. Such experiments are only possible with samples of very high surface quality, however. In reality, even metal single crystal electrodes often do not exhibit a sufficient planarity to realize a (within $\approx 0.1°$) defined incident angle, required for utilizing these effects.

Typical applications of *in situ* and *operando* GIXS are studies of surface reconstructions and chemisorbed adlayers on electrodes (see section 5.1.1 and 5.2.1), which form ordered 2D atomic layers with unit cells that differ from those of the underlying substrate lattice. GIXRD measurements allow to determine these superstructures with high precision. To illustrate how the in-plane surface structure is obtained by GIXS measurements, we consider typical adlayer structures found on substrates with a hexagonal surface lattice (lattice spacing a), such as the (111) surface of fcc metals (Figure 16a-b). One of the most simple types of superstructures formed by adsorbates on these surfaces is a simple commensurate $(\sqrt{3} \times \sqrt{3})$R30° superlattice (red symbols), where all adsorbates sit on identical adsorption sites, separated by the next-nearest neighbor spacing $\sqrt{3}a$. The presence of this 2D superstructure gives rise to additional diffraction rods, which are located at q that are a factor $1/\sqrt{3}$ further inward and 30° rotated with respect to the CTRs of the substrate lattice. In a simple picture, these superstructure peaks may be considered as Bragg reflections at regular rows of the adsorbates (e.g., at the close-packed rows of neighboring adsorbates for the first-order peaks). For this commensurate structure, some of the adlattice peaks are located at the in-plane positions of the substrate CTRs and therefore will not be directly visible. However, they will modify the intensity distribution of the CTRs, and thus adlayer formation may manifest in the form of sudden intensity changes at those peaks.

Furthermore, incommensurate structures are observed in many electrochemical systems, where one or two of the adlattice's unit cell vectors cannot be described as a rational fraction of substrate lattice vectors. Such structures are frequently found for simple atomic or ionic adsorbates and usually exhibit potential-dependent lattice parameters. We illustrate GIXS studies of incommensurate structures by two examples, found on hexagonal surfaces. In the first case – a uniaxially incommensurate superstructure denoted as $c(p \times \sqrt{3})$ (Figure 16a-b, blue symbols) – the adlattice maintains the commensurate $\sqrt{3}a$ spacing along one of the main lattice directions but is slightly compressed in the perpendicular direction. As a consequence of this compression, the superstructure peaks shift outwards from the positions of the $(\sqrt{3} \times \sqrt{3})$R30° structure. Because the adlattice can be compressed along any of the three symmetrically equivalent main directions of the hexagonal substrate, a splitting in three adsorbate peaks is observed at each position, corresponding to the three rotational domains of this phase. Concretely, the full diffraction pattern is obtained by rotating the pattern corresponding to a single domain by $\pm 60°$.

A typical 2D incommensurate superstructure on hexagonal substrates exhibits a hexagonal lattice, which has a different spacing a_{ad} than the substrate lattice and is rotated to the latter by an angle $\pm\phi$(Figure 16a-b, green symbols). Consequently, the GIXS diffraction pattern is obtained by scaling the in-plane pattern of the substrate's CTRs by a factor a/a_{ad} and rotating it appropriately, leading to pairs of peaks separated by 2ϕ. Such a structure is formed for example by bromide adsorption on Au(111) electrodes. Typical *in situ* GIXS data at the superstructure peaks, obtained by measuring the X-ray intensity while rotating the sample (azimuthal scans) or changing q (radial scans) are shown in Figure 16c-e. The rotation angle of $\phi = 3.7°$ relative to the $\sqrt{3}$ direction (i.e., $h = k$) and the spacing a_{ad} of 4.24 to 4.03 Å, depending on potential, can be directly obtained from such scans with a precision of $\approx 0.1°$ and sub-picometer, respectively. The

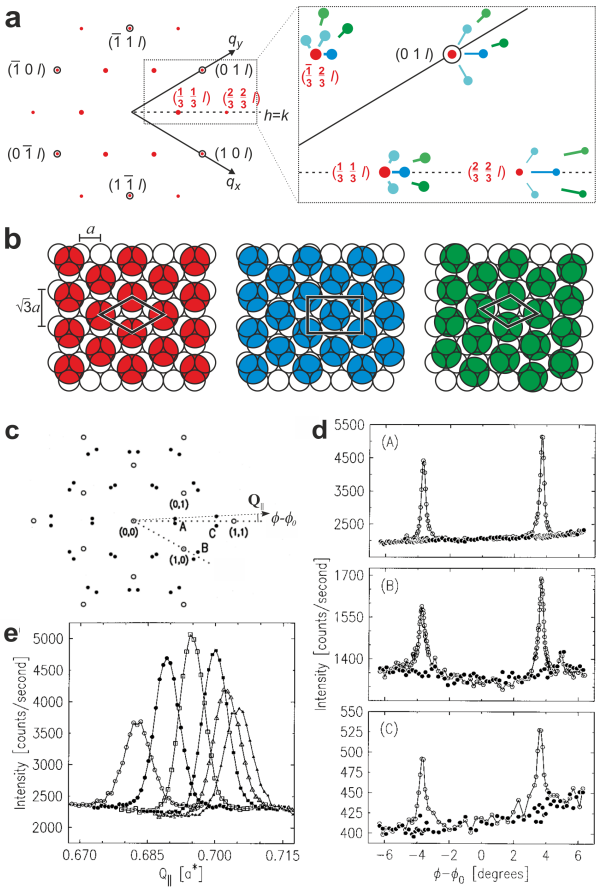

Figure 16: Schematic (a) in-plane diffraction pattern and (b) real space structure of a commensurate $(\sqrt{3}\times\sqrt{3})$R30° superstructure (red), a uniaxially incommensurate $c(p\times\sqrt{3})$ superstructure (blue), and a 2D incommensurate hexagonal-rotated superstructure (green). 1st, 2nd, and 3rd order peaks are indicated by circles of decreasing size; open black circles indicate the CTRs of the substrate. In addition to the superstructure domains shown in (b), the diffraction spots of other rotational domains are shown in lighter colors. The shift of the diffraction peaks of the incommensurate structures upon compression are indicated by the blue and green lines. For clarity, the peaks of the incommensurate phases are omitted in the full diffraction pattern (a, left side). (c) In-plane geometry and (d-e) *in situ* GIXRD data for an incommensurate hexagonal-rotated Br adlayer, formed on Au(111) in 0.1 M $HClO_4$ + 10 mV NaBr. (d) Azimuthal scans at the positions of the 1st (top), 2nd (center), and 3rd (bottom) superstructure peak, obtained at 0.2 (filled circles) and 0.6 V (open circles) vs. Ag/AgCl, where the superstructure is present and absent, respectively. (e) Radial scans through the 1st order peak at various potentials between 0.48 and 0.68 V, showing the outward shift of the peaks with increasing potential (Reproduced from Ref.[96]. Copyright 1996 American Chemical Society.

accuracy in the determination of these lattice parameters surpasses other methods, such as scanning probe microscopy, by orders of magnitude, which is a major strength of this technique. In particular, it allows precise measurements of the potential-induced compression of the adlattice – a phenomenon that is typical for incommensurate adlayers at electrochemical interfaces.

As visible in Figure 16d, the 1st order Bragg peaks are of equal intensity as the background scattering of the bulk electrolyte, the intensity of the 3rd order peaks is a factor of ≈ 20 lower and only slightly above background. Nevertheless, even those weak peaks can be clearly identified and associated with the Br adlayer by shifting the potential to more negative values, where the adlayer becomes disordered, resulting in a disappearance of these peaks. As expected, the scattering of the bulk electrolyte (as well as of X-ray windows and other contributions to the background) remains constant and thus can be removed by such potential-dependent measurements. If the peak position does not shift with potential, as e.g. in the case of commensurate adlayers or CTRs, the potential-dependence and kinetics of the in-plane adlayer order can be directly monitored by measuring the peak intensity during cyclic voltammograms, often denoted as "X-ray voltammogram" (XRV), or during potential steps, which provides a powerful tool for studying structural transitions at electrode surfaces.

The decrease in the peak intensities from the 1th to the 3rd order Bragg peaks is caused by the q-dependence of the atomic form factors and Debye-Waller factors, i.e., the displacements due to thermal motion or in-plane disorder. Such static disorder may arise from the occupation of different adsorption sites in such adlayers. Specifically, adsorbates may be displaced toward energetically favored sites (e.g., hollow sites) and away from unfavorable sites (e.g., top sites), leading to a modulation of the adlattice. In the most extreme case, a periodic network of commensurate domains, separated by domain boundaries of higher or lower surface density may be formed. A well-known example of such a network is the Au(111) surface reconstruction, discussed in chapter 5.1.1. In such a case, one will still observe diffraction peaks at the positions corresponding to the average spacing in the adlayer, but also additional weaker "satellite peaks" separated from each other and the main peaks by a small Δq that corresponds to the size of the domains. If the network is not well ordered or the surface density changes rather gradually across the domain boundary, the satellite peaks intensity often becomes too weak to be distinguished from the background – a situation found in most studies of electrochemical systems.

Also, the peak width contains information about the adlayer. According to chapter 3.3.3, the full width at half maximum of the peak in the radial direction is given by $2\pi/L$, where L is the characteristic size of (incoherently scattering) adlayer domains. In the experiment, the actual peak width is convoluted by the instrumental resolution function. However, for experiments at typical surface scattering beamlines of modern synchrotron sources, the latter has typical widths in the range of 10^{-3} Å^{-1} and thus often can be neglected for many electrochemical systems. The azimuthal peak width is determined by both the domain size and the rotational dispersion. These effects can be deconvoluted by measuring the width of peaks with different q. (the q width due to the domain size is identical for all peaks, whereas that caused by the rotational dispersion scales with q).

All the above is valid for 2D ordered structures with single atoms in the primitive unit cell as well as more complex surface structures, formed by periodic ensembles of different atoms. In the latter case, the interference between the atoms within the unit cell gives rise to a structure factor $F(q)$, which leads to a modulation of the peak intensities.

4.4.2 CTR measurements

For a full surface crystallographic determination of both the lateral and the vertical positions of the atoms at the interface, the CTRs of the sample have to be measured. As demonstrated in Figure 17, the intensity distribution along the CTRs is highly sensitive to

the structural arrangement at the crystal surface. Even rather small deviations from a perfectly truncated crystal lattice can give rise to $|S_{CTR}(\mathbf{q})|^2$ distributions that strongly differ from that given by Eq. (20). For example, an expansion or contraction of the spacing between the topmost and second atomic layer at the crystal surface can lead to pronounced asymmetry in the decay of the intensity to both sides of the Bragg peaks and a corresponding shift and deepening of the minimum in intensity in between. At selected reciprocal space positions, the intensity can change by orders of magnitude, providing a highly sensitive tool for measuring surface relaxations of the lattice. Changes in the electron density of the surface layer, e.g., due to surface reconstructions or a pseudomorphic adlayer formed by a different atomic species, likewise result in clear changes of the intensity in between the Bragg peaks. Specifically, the intensity increases for a higher and decreases for a lower density, respectively. A similar decrease is found, if the displacement amplitude of the atoms along the surface-normal direction increases or if the sample exhibits roughness. However, in these cases, the effect increases with a larger L, i.e., increasing q_z. Displacements parallel to the surface obviously cannot affect the specular CTR (see chapter 4.3.1), but lead to intensity decreases in the non-specular CTRs.

In real interface systems typically a combination of changes in layer density, spacing, and displacement amplitudes occurs. These can often be disentangled, because of the different effects they have on the CTRs. Furthermore, one may have to consider structural deviations from the bulk lattice structure in more than one atomic layer as well as layers of adsorbed species, including laterally disordered layers of water or hydrated ions in the double layer. Just as in the crystallographic analysis of bulk crystals, the structure determination becomes more precise with an increasing number of independent reflections measured, i.e., larger numbers of (symmetrically non-equivalent) CTRs and an extended range of l values.

As demonstrated in section 5, CTR measurements are capable of providing very detailed in-

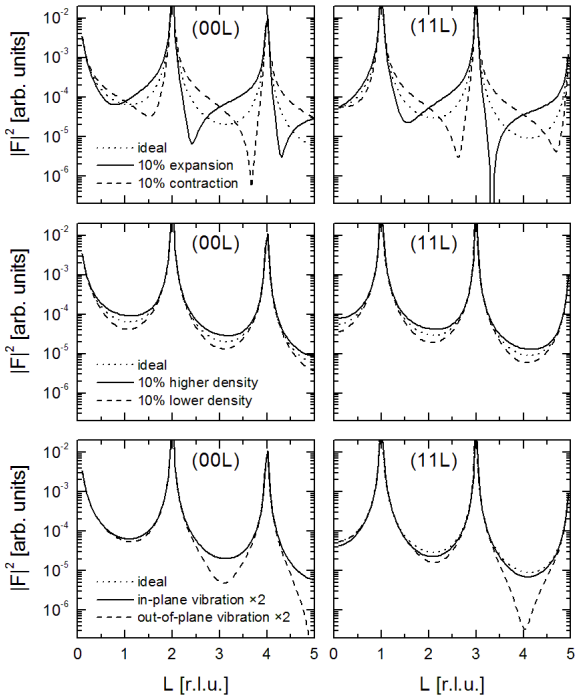

Figure 17: Influence of changes in the structure of the topmost atomic layer at an fcc(001) crystal surface on the specular (left) and a non-specular (right) CTR. The effect of a change in the vertical spacing between this layer and the underlying lattice (top), an increase or decrease in the layer density (center), and an increase in the in-plane or out-of-plane vibrational displacements of the atoms in this layer (bottom) are illustrated. For reference, the CTRs of an ideally terminated crystal are shown in all figures (dotted lines).

sight into the interface structure. However, one should keep in mind that high-quality *in situ* CTR data can only be obtained by experiments at synchrotron sources that employ single crystal samples of high crystallinity and with very smooth surfaces. In addition, recording a full set of CTRs typically requires hours, even at X-ray sources of high brilliance, since it requires sequential recording of the intensity at different angles of the detector and the sample. In studies where time resolution is critical, e.g., *in operando* studies of structural changes at electrodes under reaction conditions, the measurements are therefore often confined to locations in reciprocal space that are particularly sensitive to the surface structure, e.g., the "anti-Bragg" positions between two Bragg peaks of the substrate and the locations of superstructure rods.

4.4.3 High energy surface diffraction

Modern hard X-ray synchrotron sources can deliver beams with sufficient intensity for surface scattering experiments up to photon energies of 150 kV, i.e., very small wavelengths λ. HESXRD has recently been introduced as a new method for *operando* studies of heterogeneous catalysts in the gas phase[79,97] and of electrochemical interface processes.[98–101] Employing very high photon energies has several advantages: First, the linear X-ray absorption coefficient becomes very small. This allows penetration of large amounts of condensed matter without significant attenuation of the beam, which is highly beneficial for *in situ* studies of electrochemical interfaces. Secondly, because of the small λ, the same q values are reached at much smaller scattering angles 2θ. In other words, X-ray scattering at high energies occurs predominantly in directions close to that of the incident beam. This forward scattering can be measured simultaneously with a 2D X-ray detector (Figure 18a). The latter collects the intensity for all scattered beams with outgoing wave vectors $\mathbf{k}_f$ in a certain solid angle. This allows direct imaging of a fraction of the Ewald sphere. At high photon energies, the curvature of the Ewald sphere is low and a nearly planar slice through reciprocal space is imaged by the detector. Under grazing incident angles, this allows projecting a large section of a CTR onto the detector, enabling rapid acquisition of the surface structural data. By taking detector images while rotating the sample around the surface normal, a large reciprocal space volume can be collected within a few minutes, enabling subsequent quantitative analysis of CTRs and superstructure rods as well as other scattering features, e.g., Bragg peaks of deposited materials. The strong Bragg peaks of the substrate have to be blocked by absorbers to avoid damage of the detector. Because of the large Ewald sphere volume, the accessible reciprocal space in HESXRD measurements can be several times larger than that in conventional SXRD. This leads to considerable improvements in the structural resolution and allows more precise and more complex modeling of the interface structure. Nevertheless, these data sets can be obtained in a much shorter time than in conventional SXRD, opening up possibilities for time-resolved surface crystallographic studies, e.g., *operando* measurements of transient interface structures. HESXRD measurements require extremely precise alignment, because the angle of incidence should be kept near the critical angle, which is very small ($\approx 0.1°$) at small λ. This make the experiments technically challenging. Specialized high-precision diffractometers and samples with very high bulk crystal quality and surface planarity are needed. A further disadvantage is the lower resolution in reciprocal space, although the latter can often be compensated for by moving the detector further away from the sample.

As a variant of this method, high energy X-ray scattering may also be performed in a geometry, where the beam impinges approximately perpendicular onto the interface (Figure 18b).[102] X-ray beams with photon energies in the range 70 to 150 keV can even penetrate several hundred micrometers of high-density materials such as Au, allowing experiments where the beam passes through a thin single crystal, a layer of electrolyte, and an X-ray window. In this transmission geometry, the detector images a slice that is almost parallel to the surface and

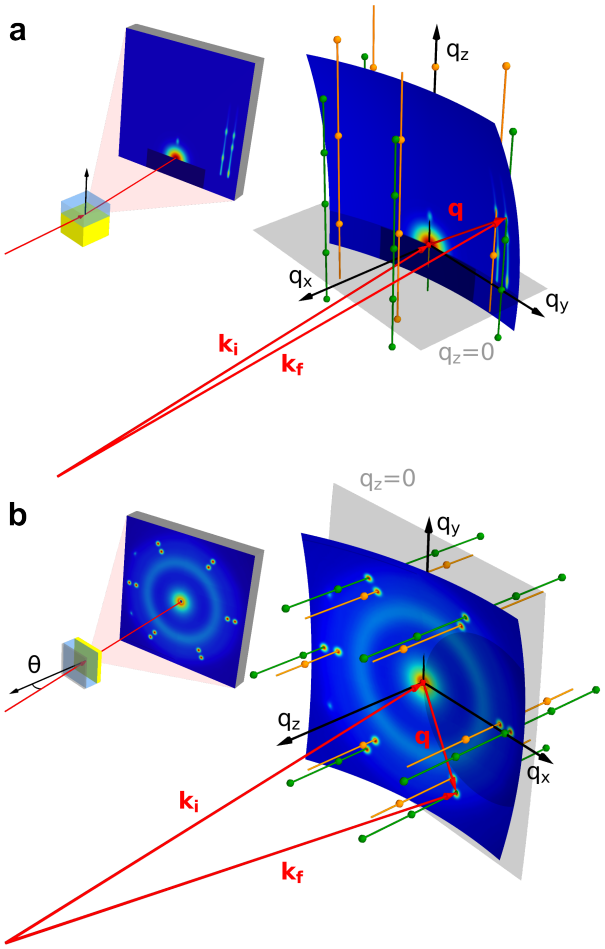

Figure 18: High energy surface diffraction (a) in grazing incidence and (b) in transmission geometry, shown in real space (left) and reciprocal space (right), respectively. X-ray diffraction peaks are located at the intersections of the CTRs and adlayer rods with the Ewald sphere (Reproduced from Ref.[102]. Copyright 2014 American Chemical Society).

thus can record the in-plane intensity distribution. The obtained structural information is similar to that of a GIXRD experiment, but in contrast to the latter can be recorded in a single shot. As a further advantage as compared to studies under grazing incident conditions, only a surface area of the size of the beam diameter is probed, which can have (sub-)micrometer dimensions. This enables studies with corresponding spatial resolution in real space, which can be used e.g. for the local mapping of the atomic scale interface structure on the μm scale or for studying the surfaces of materials that cannot be grown as large single crystals.[102,103]

4.5 Methods for studies of nanoscale morphology

4.5.1 Small angle X-ray scattering

Small-angle X-ray scattering (SAXS) allows to determine the inhomogeneities in materials on the order of tens to hundreds of Å. It is therefore an appropriate technique to look at the morphology of electrode materials and electrolytes (both solid and liquid). As the SAXS probe lengths are substantially larger then the atomic distances, the medium is typically treated as a continuum of electronic density. Consequently, the scattering is described as scattering of electron density embedded in a matrix of different electron density (see chapter 2.4).

While wide-angle scattering measures the atomic scale structure of a material, small-angle scattering probes structural correlations between larger units. For simplicity, we consider a nanoscale object of homogeneous density (e.g., a metal nanoparticle) and of a characteristic size R_0 (e.g., the particle's radius). Inside this object, the electron density has a constant value ρ_e (neglecting the atomic structure); outside the density is assumed to be 0. If the particle is embedded in another medium, the difference in electron density has to be used here instead of ρ_e. This is called a 'contrast'. The scattering amplitude and the scattered intensity of such an object can be calculated from Eq. (1) and (2) in chapter 2.2, respectively (explicit examples for simple object shapes can be

found in the more advanced literature, e.g., in Ref.[3]). This procedure is completely analogous to that used in the calculation of the atomic form factor $f(\mathbf{q})$ and leads to similar decay at q values larger than $2\pi/R_0$. For this reason, the resulting $P(\mathbf{q})$ is called the form factor of the particle. The main differences to $f(\mathbf{q})$ are the shift of the decay to smaller q and the appearance of characteristic oscillations. The latter is caused by interference effects due to the abrupt change in density at the particle boundary.

In the second step, we consider now an ensemble of such objects. Even in the absence of interactions between them, short-range order will emerge at sufficiently high number densities ρ_n of the objects, because the particles cannot overlap. This situation is analog to the local order in a liquid and thus can be described by the same formalism as that discussed in chapter 2.3.4. The scattering by the ensemble is consequently described by a structure factor $F(\mathbf{q})$ with the relevant q range being now in the small-angle regime. The most prominent feature in $F(\mathbf{q})$ is a peak that corresponds to the correlations between neighboring objects – analogous to the first peak in the structure factor of real liquids. Given the above, the total scattered intensity is therefore given by

$$I(\mathbf{q}) = I_0 N (\Delta\rho)^2 V^2 P(\mathbf{q}) F(\mathbf{q}) \qquad (62)$$

, where I_0 is proportional to incident X-ray flux, N is the number of nanoscale objects in the volume of the sample intersected by the beam, $\Delta\rho$ is the contrast, and V is the volume of one object. For uncorrelated particles, $F(\mathbf{q}) = 1$ and $I(\mathbf{q})$ contain only information about the size, shape, and internal structure of the particle. For correlated objects, $F(\mathbf{q})$ characterizes the type of order. The separation of these two contributions is a challenge and good knowledge of the model helps with this task.

Because the SAXS signal increases very strongly with the particle volume (e.g., for spherical particles the SAXS signal increases with a power of six with the radius), the particle size distribution determined from the SAXS pattern is weighted by the particle size. As an example, SAXS intensity from one 10 nm particle is the same as the SAXS intensity from 10^6 1 nm particles. This is important to keep in mind when comparing the size of nanocatalyst particles measured by different techniques, as the determined average size is often not the same even for the same sample. Eq. 62 also shows that the SAXS signal is proportional to squared contrast, so the sign of the contrast does not play a role. Voids in the matrix, therefore, result in the same scattering as material particles in the matrix.

The assumption that all N particles in the probed volume of the sample have the same size is typically not correct. Usually, the particles have a distribution of sizes (polydisperse) or different shapes (polymoprhous). The scattering curves can be then seen as a sum of all N form factors $P(\mathbf{q})$ from each particle and the result is an averaged form factor with no sharp minima. In contrast, an experimental profile with sharp minima is a sign of a monodisperse sample.

The typical shape of SAXS patterns, if plotted on a double logarithmic scale, is a plateau at low q followed by a decreasing intensity with a transition at λ^* defined by the average size of the objects (Figure 19a). It can be shown that at low q the particle form factor can be approximated by $P(q) \simeq exp[-(qR_G)^2/3]$ where R_G is the radius of gyration.[3] This is known as Gunier law and provides an independent way of size determination as R_G is closely related to the size and from the plot of $ln(I(q))$ versus q^2 it is straight forward to find R_G. In practice, however, this analysis can be challenging for composite materials, such as nanocatalyst used in electrochemical systems, due to the strong small-angle scattering from the carbon-based supports (or any other fractal materials). The shape of the SAXS curve at high q typically follows $I \simeq C/q^{-\alpha}$, which is easily observed in the scattering curves (Figure 19). The q^{-4} relationship is known as Porod law and it is universal to all structures with a sharp interface (Figure 19 a,b,c). Smeared interfaces or fractal structures lead to exponents larger than -4 and are typical for materials used as supports for electrocatalysts (Figure 19 d.). The constant C in the Porod law relates to the specific surface

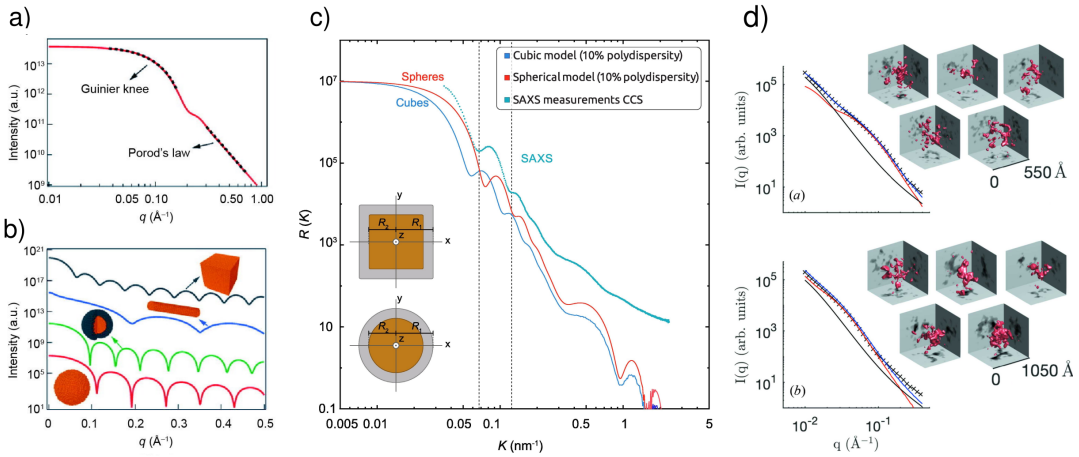

Figure 19: Representative SAXS patterns. (a) Guinier approach and Porod's law for obtaining the sizes and surface areas of particles/voids, respectively, and (b) SAXS curves for different nanostructures (Adapted from Ref.[104]. Copyright 2020 Elsevier). c) Scattering curves obtained from SAXS measurements on cubic silica shells. The cyan curve is the measured scattering profile while the blue, green, and red curves are obtained from models of, respectively, a cubic 14 nm shell, a cubic 13 nm shell, and a spherical 14 nm shell (Adapted from Ref.[105]. Copyright 2020 Elsevier). (d) Fitting of the SAXS of (a) the fresh and (b) the spent ORR electrocatalyst with a stochastic model. The crosses are the data and the blue line is the best fit, with the contributions of the solid support in black and of the particles in red. In each case, five realizations of the particle model are shown, together with their projections. (Reproduced from Ref.[106]. Copyright 2021 International Union of Crystallography).

area and can be therefore used for its determination, provided that the contrast of the system is well known. This type of analysis can be useful in determining changes in the porosity of materials in electrochemical systems. The full SAXS curve can also be analyzed by combining various models for nanoparticle form factors and structure factors and fitting those models to experimental SAXS data (Figure 19b,c,d). This is typically done by using specialized software which contains a library of possible models. Prior knowledge of particle size and shape is often needed to properly select the model and extra caution has to be taken not to overinterpret the fitted values, as the final interpretation heavily depends on the model chosen for analysis.

SAXS can be measured on both lab instruments and at synchrotron beamlines. Currently, several companies offer specialized instruments capable of SAXS/WAXS/USAXS (Ultra SAXS) combination with variable X-ray sources and flexible detection systems. These are suitable mainly for ex-situ measurements due to lower X-ray flux and often *in-vacuum* detection, but can be also used for slow *in-situ* and *operando* experiments. Such experiments are regularly performed at synchrotron beamlines, which sometimes provide the possibility to combine various scattering techniques within one experiment (e.g. SAXS, WAXS, XAS and imaging). The beamline choice and setup depend on the planned experiment. The use of high-energy probes allows to use more relevant electrochemical cells, but limits the q-range and maximum size of probed objects. On the other hand, lower energies provide possibilities to measure lower q-values and thus larger objects, but the cells need to be optimized for X-ray transmission. Both transmission and grazing incidence geometries are used, each of them having advantages and disadvantages. Transmission geometry (X-ray beam perpendicular to the sample) allows to measure with small beams and achieve good in-plane spatial resolution in the scanning mode. However, the signal-to-background ratio is low, and electrodes with high loading need to be used. This limits the

electrochemical performance and can lead to misleading results, as parts of the electrode might not be active. Grazing incidence geometry (X-ray beam parallel to the electrode) permits the use of low-loading electrodes and superior resolution in the direction perpendicular to the electrode but does not provide in-plane resolution. The detector is typically positioned far from the sample (1-10 m) and an evacuated or helium-filled tube between the sample and the detector is used to reduce the background. Ideally, this tube is equipped with a beamstop before the exit window to block the direct beam before the detector. The beam is often focused on the beamstop to further lower the background.

4.5.2 Grazing incidence small angle X-ray scattering

The same ideas as for general SAXS scattering hold true for a spatial distribution of objects on a surface, such as deposited nanoparticles or islands formed by a growth process. This 2D distribution can be probed by an X-ray beam impinging on the surface under grazing incidence (Figure 20a). Because the curvature of the Ewald sphere can be neglected in the small angle regime, the intensity distribution of this scattering in a plane perpendicular to the incident beam direction $I(q_y, q_z)$ can be directly recorded by a 2D X-ray detector. This scattering is much weaker than that of the reflected beam, which has to be masked by a beam stop. However, *in situ* measurements at electrochemical interfaces are still feasible, since the background scattering by the electrolyte is low at small angles.

Typically, this grazing incidence small angle X-ray scattering technique is used for studying nano- and mesoscale structures in the range between one and several hundred nanometers. As an example, we discuss the case of a Pt(111) surface, which has been roughened by repetitive potential cycles into the potential range of Pt surface oxidation (Figure 20b,c). Such oxidation/reduction cycles result in the formation of 3D Pt islands with characteristic distances of a few nm (see chapter 6.2.1. The *in situ* GISAXS data obtained from this surface exhibit wings at reciprocal space positions $\pm 2\pi/\zeta$, where ζ corresponds to characteristic distances between the islands. This scattering represents a specific case of diffuse surface scattering, which originates from the deviation of the surface from a perfect plane. Along q_z, the intensity reaches a maximum at $q_z = q_c$, caused by the enhancement effect discussed in chapter 4.3.1, and then decays. The diffuse peaks intensity increases with increasing scattering volume of the islands; their width is a measure of how well-defined the short-range order is. For epitaxial systems, $S_L(\mathbf{q})$ is not necessarily isotropic, but may reflect the sample symmetry. For example, anisotropic island growth on surfaces with a uniaxial symmetry will result in GISAXS images that depend on the in-plane orientation of the sample relative to the incident beam.

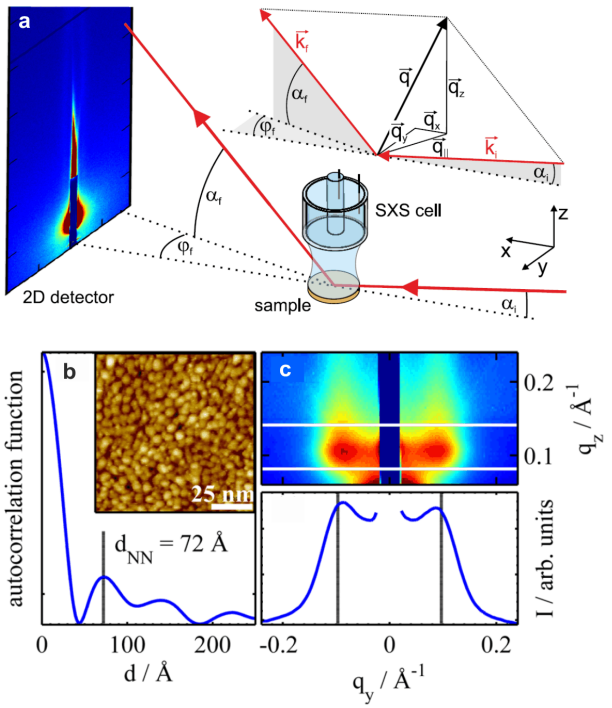

Figure 20: (a) Scattering geometry of a GISAXS experiment. (b) STM image and corresponding autocorrelation function and (c) *in situ* GISAXS data obtained on a Pt(111) electrode that was roughened on the nanometer scale by potential cycling into the oxide formation regime (Adapted from Ref.[107]. Copyright 2017 American Chemical Society).

Because GISAXS images can be obtained within seconds, this technique is well suited for time-resolved *in operando* studies of the nanoscale evolution of the surface structure during interface reactions. Studies of that type have been performed for electrochemical and other interface processes. Furthermore, since GISAXS is insensitive to the crystal structure, it does not require single-crystal surfaces but can be performed on any sufficiently planar interface, including amorphous and liquid substrates. It thus fills an important niche between *in situ* atomic-scale characterization methods and *ex situ* studies by techniques such as electron microscopy.

A more recent variation of GISAXS is transmission small angle X-ray scattering (TM-SAXS).[108] Here, the measurements are performed with high photon energy beams at incidence angles above the critical angle, and the scattering of the transmitted X-ray beam is measured. Analysis of the data obtained in this geometry is substantially simplified, because refraction of the X-rays can be neglected.

4.6 Locally resolved measurement techniques

4.6.1 X-ray nanodiffraction

The advent of spatially coherent X-ray sources and sophisticated X-ray optics enabled the focusing of the hard X-ray beams to 10 nm and below[109–111]. Step-wise scanning these small beams across the specimen and recording scattering signal at every position allow imaging that is reminiscent of dark field microscopy conventionally used with light or electrons. Nanodiffraction, which is possible with X-rays and electrons, yields direct access to the crystal structure and distortions thereof. While electron nanodiffraction typically works in transmission geometry on thin membranes, X-ray nanodiffraction often finds application in reflection geometry and has extensively been used to image nanoscale heterogeneity in thin crystalline films epitaxially attached to substrates. In X-ray nanodiffraction, one records diffraction profiles of sample volumes that are only a few tens of nanometers across all directions. Recent research focused on interpreting these diffraction profiles and forming images of coexisting phases during phase transitions[112,113], domains in poled ferroelectrics[114], and local crystal distortions[115]. While early work focused on manual interpretation of diffraction profiles, for example by choosing regions on the detector corresponding to different structural phases, more recent approaches use unsupervised machine learning for interpreting the data[115,116]. The high penetration depth of hard X-rays makes X-ray nanodiffraction an appealing approach to studying electrochemical systems *operando*. In addition, the sample geometry potentially allows forming of an *operando* electrochemical cell on top of the thin film supported by the substrate.

4.6.2 Bragg coherent diffraction imaging

Many electrochemical systems comprise active crystalline particles ranging in size from a few nanometers in electrocatalytic systems to up to a micrometer in battery electrodes. Often, it is desirable to study fundamental processes inside these nanoparticles under real operating conditions. For particles of the order of 50 nm and larger, high-quality diffraction data can be collected at the modern X-ray synchrotron sources, which includes the Bragg peak and the interference fringes surrounding it[74,75,117–119]. The 3D diffraction profile can be recorded by using an area detector, which records 2D slices of the Ewald sphere through the reciprocal space, and rocking the crystal through the diffraction condition (typically tens of angles within about 1 degree of total rotation)[117].

As shown in 2.3.2, one can readily calculate the scattering amplitude from an arbitrarily shaped and strained particle via a Fourier transform. The Fourier transform is invertible, yet the notorious phase problem – one can only measure X-ray photon intensities, not their phases – prevents a direct inversion of the coherent X-ray data into a real-space structure. Bragg Coherent Diffractive Imaging is a tech-

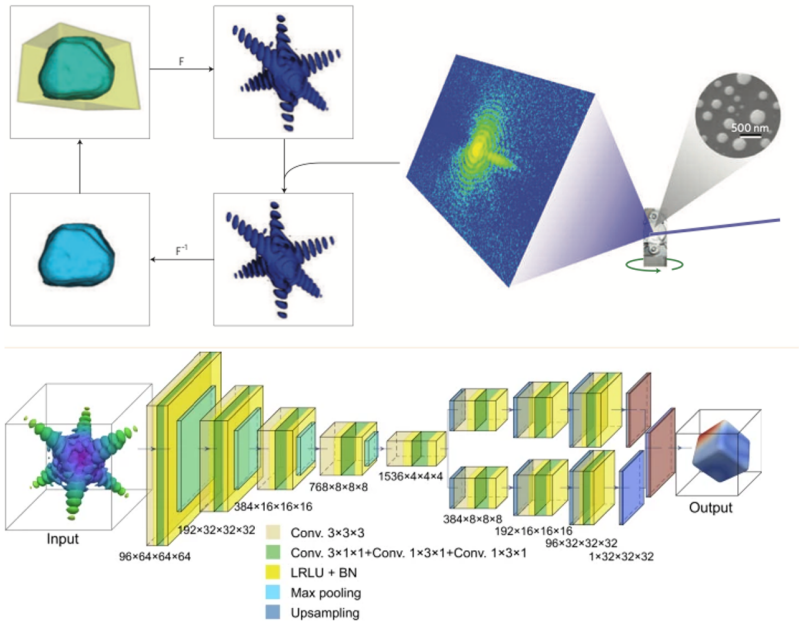

Figure 21: (Top) The schematic illustration of an iterative phase retrieval algorithm: the forward and inverse Fourier transforms are complemented by real space and reciprocal space constraints. The iterative procedure retrieves the shape of the nanocrystal and the displacement field projected on the reciprocal lattice vector within the crystal (reprinted from Ref.[75]. Copyright 2009 Springer Nature). (Bottom) The schematic of a 3D neural network comprised an encoder network and two decoder networks. In the network, the amplitude of a 3D coherent X-ray diffraction pattern in reciprocal space is used as input, and the output is the complex structure information (i.e., amplitude and phase) of the particle in real space. (reprinted from Ref.[120]. Copyright 2021 Springer Nature).

nique that uses phase retrieval[121] to find the lost phases of the intensity profile $I(Q)$ and thereby invert the diffraction profile into a 3D image of the nanocrystal. The method generates the density of Bragg planes (allowing to determine the shape of the nanocrystal) and displacement field (allowing a study of the internal displacement field inside the nanocrystal). The conventional BCDI uses iterative phase retrieval algorithms. One starts with a randomized guess of what the crystal might look like, typically a phase object where in 3D, every voxel receives a random phase. The algorithm consists of four steps (see figure 21): (1) Fourier transform, (2) reciprocal space constraint, (3), inverse Fourier transform, and (4) real space constraint. In the reciprocal space constraint, the modulus of the complex X-ray field is replaced with the square root of the measured intensity. Often, a low-pass filter is applied at the beginning of the procedure and gradually eliminated towards the end: this is believed to determine the overall shape first and subsequently achieve a higher resolution while taking higher Q values into account. More recently, convolution networks have been used to invert the coherent diffraction data[120]. One advantage of the approach is the ability to invert the data within a single step, avoiding the tedious iterative procedure. The network is trained on simulated data and can continuously be improved.

BCDI combines a spatial resolution on the order of 10-50 nm (excellently suited to image the long-range displacement fields due to crystalline distortions) with sub-picometer sensitivity to displacements (excellently suited to resolve the minute lattice displacements due to defects). Through a numerical differentiation, the displacement field can be converted into a local strain field or local crystal inclination[122]. Importantly, the local displacement, strain, and crystal-plane inclination are all measured on the crystal planes that are normal to the reciprocal lattice point G_{hkl}. Measuring the full strain tensor is possible by combining BCDI measurements on multiple Bragg peaks[123,124]. Furthermore, the X-ray interference of all parts of the crystal is critical for detecting clear interference fringes and therefore is a key requirement for capturing the distortions in the coherent diffraction profile, although small deviations from perfect coherence can be accommodated[125,126]. The size of the nanocrystal is limited from below by the amount of scattering signal: too small particles will generate insufficient intensity in the interference fringes and make the inversion impossible. The size of the crystal is limited from above by experimental geometry (interference fringes become too small to be resolved) and more importantly by the breakdown of the kinematic approximation[127]. While the experimental geometry limitation can be overcome by larger sample-detector distance or smaller detector pixels, the latter requires an interpretation of the diffraction signal in terms of dynamical diffraction theory. The limit for the validity of kinematical approximation is about 1 μm for Au nanocrystals[127]. An interpretation of BCDI data from intermediately sized crystals is possible within the quasi-kinematical approximation[128].

4.6.3 Ptychography

Ptychography is another method that uses iterative phase retrieval to form an image of the specimen under study[82]. Ptychography combines raster scanning during the experiment with iterative phase retrieval during the analysis. Specifically, the early works on X-ray ptychography[129] showed that the overlap of illumination regions during a raster scan leads to a robust conversion of the iterative phase retrieval algorithm. In the last decade, X-ray ptychography matured and is widely used to study biological systems[130,131], X-ray optics[132,133], magnetic structures[134], or the structure of integrated circuits at nanoscale[135]. Ptychography can be used to image extended objects, which is a major advantage as compared with other diffractive imaging approaches such as BCDI. Finally, X-ray ptychography is appealing to studying electrochemical systems: the method is applicable *operando* due to the high penetration depth of hard X-rays, enables studying extended objects, and leads to a robust inversion of scattering data.

4.7 Determination of composition and electronic structure

4.7.1 Resonant anomalous X-ray scattering

Resonant anomalous X-ray scattering (RAXS) combines X-ray diffraction techniques with X-ray absorption spectroscopy (XAS). It allows to probe the long-range structural order and, in addition, to provide element-specific structural information for atoms of a selected element within this structure. The theoretical foundation for RAXS and its applications in experiments at modern synchrotron X-ray radiation sources was reviewed comprehensively by Walker and Specht.[136] RAXS is based on the analysis of the scattering near an X-ray absorption edge, where the atomic form factor of the corresponding element exhibits a pronounced, so-called anomalous dependence on photon energy (see chapter 2.5). By quantitatively analyzing the scattered X-ray intensity distribution as a function of the energy, the position of the atoms of this element in the structure can be located. This principle can be applied to every X-ray scattering method.

RAXS experiments have to be performed at synchrotron X-ray sources, where the energy can be scanned with a resolution of at least 1 eV through the absorption edge of the studied resonant element. During this energy scan, the scattering vector $\mathbf{q}$ must be maintained. The scattering intensity at a specific $\mathbf{q}$ as a function of energy is called a RAXS spectrum. Its variation near the absorption edge energy contains both structural and electronic information about the resonant element, which can be retrieved by modeling.

The general mathematical equation for computing the RAXS intensity is given by combining Eq. 4, 5, and 40, resulting in

$$\begin{aligned} F_{TOT}(\mathbf{q},\varepsilon_{Ph}) &= F_{NR}(\mathbf{q}) + F_R(\mathbf{q},\varepsilon_{Ph}) \\ &= \sum_j \theta_j f_{0,j}(\mathbf{q}) e^{i\mathbf{q}\cdot r_j} e^{-M_j} \\ &+ (f'(\varepsilon_{Ph}) + if''(\varepsilon_{Ph})) \sum_k \theta_k e^{i\mathbf{q}\cdot r_k} e^{-M_k} \end{aligned} \tag{63}$$

According to Eq. 63, the RAXS structure factor $F_{TOT}(\mathbf{q},\varepsilon_{Ph})$ can be split into two contributions, one (F_{NR}) from the non-resonant Thomson scattering described by the q-dependent form factors $f_{0,j}(\mathbf{q})$, and the other (F_R) from the resonant contributions of the selected element caused by the dispersion corrections (f' and f''), which vary with X-ray energy ε_{Ph}. F_{NR} is a sum over all atoms in the sample's unit cell, which are described by their position $\mathbf{r_j}$, their site occupancy θ_j, and their Debye-Waller factor M_j. The sum in F_R only includes the atoms of the resonant element. This calculation requires *as priori* knowledge of the dispersion corrections f' and f'' as a function of photon energy. f'' can be obtained experimentally by X-ray absorption near edge spectroscopy (XANES), f' is computed from f'' through a Kramers-Kronig transformation. In addition, the non-resonant structure factor $F_{NR}(q)$ is needed for fitting the RASXS spectra. The latter is usually obtained from scattering data recorded at an energy far away from the absorption edge, where the resonant scattering factor can be ignored. Once the non-resonant total structure factor is known, the RAXS can be fitted by optimizing the occupancy, position and Debye-Waller factor for the resonant atoms.

Besides this traditional fitting approach based on a structural model, F_R can also be obtained from a model-independent approach, where the structure factor for the resonant atoms is expressed as

$$F_R(q,\varepsilon_{Ph}) = [f'(\varepsilon_{Ph}) + if''(\varepsilon_{Ph})] A_R(q) e^{i2\pi P_R(q)} \tag{64}$$

This expression is independent on the structural parameters of resonant atoms and introduces instead two new fit parameters, the coherent occupancy $A_R(q)$ and coherent position $P_R(q)$.[84] If F_{NR} is known, each RAXS spectra can now be fitted separately with one pair of coherent parameters. Using this approach for multiple RAXS spectra recorded at different q values, the obtained $A_R(q)$ and $P_R(q)$ values can be employed in a discrete Fourier synthesis to regenerate an electron density profile for the resonant element. Due to the fi-

nite number of **q** positions where RAXS spectra are recorded, the resonant element peak in the deduced electron density profile is broadened, but the peak positions correctly represent the positions of the associated resonant atoms. The atomic positions determined by this model-independent approach can then be used as constraints in further fits of the RAXS data by conventional modeling, which then provides the full structural parameters, including position, occupancy, and Debye-Waller factor. This procedure can be iterated until a self-consistent structural model is obtained where the positions from model-independent fitting and the deduced electron density profile of the resonant element are in agreement with the total electron density distribution derived from non-resonant CTR fitting.

Because of the strongly increasing X-ray absorption with decreasing photon energy, most *in situ* RAXS studies of electrochemical or solid-liquid systems employ hard X-rays (> 5 keV). Studies at lower photon energy ("tender X-rays") typically have to be performed under vacuum, as even air leads to pronounced absorption. Light elements are therefore difficult to access by *in situ* RAXS. Nevertheless, first *ex situ* RAXS studies of electrochemical materials that studied Bragg reflections at the Cl and S L edges using tender X-rays have recently emerged.[137] Similar *in situ* studies seem feasible but will require adapting cell designs and approaches from *in situ* X-ray absorption and photoelectron spectroscopy.

4.7.2 Resonant anomalous surface X-ray scattering

Even though the theory of RAXS was established by Walker and Specht as early as 1994, its wide application to surfaces and interfaces was only realized one decade later. Park et al.[83] employed RAXS in pioneering anomalous X-ray reflectivity studies to resolve two species of outer-sphere adsorbed $Pt(NH3)_4{}^{2+}$ above a quartz (100) surface. In that work, the mathematical basics for modeling resonant anomalous surface X-ray scattering (RASXS) data were provided, which laid the foundation for many follow-up studies. Most *in situ* RASXS measurements focused on the surface sorption chemistry of ions or nanoparticles at different mineral-water interfaces under open circuit conditions. Applications of RASXS in the field of electrochemistry and energy science are still scarce. Nevertheless, this technique is of great interest here as well, as it's element sensitivity can significantly help to unambiguously resolve the location of species of interest at the solid-fluid interface.

In a RASXS experiment, the resonant anomalous scattering at **q** values along the specular and non-specular CTRs (see chapter 4.4.2) is recorded. These data are analyzed using the methodology described in the previous chapter, i.e., by applying Eq. 63 to the structure factors of the CTRs. As an example, data obtained from an *in situ* RASXS study of Zr_xO_y aggregation on muscovite (001) surface in aqueous NaCl solutions is shown in Figure 22.[138] Here, the evolution of the aggregate on the surface was investigated as a function of ionic strength. The measurement in each solution included recording the specular reflectivity (Figure 22a) at a photon energy of 16 keV (figure 22) and collecting 21 RAXS spectra (example shown in Figure 22b) at different q positions along the specular axis by scanning the photon energy through the Zr K-edge (17.998 keV). The modeling of the reflectivity data provided the total electron density profile (solid lines in Figure 22c), while the vertical distribution of the electrons associated with the Zr atoms was obtained from independent fits of the RAXS spectra (filled area in Figure 22c). In combination, these data revealed together, with complementary AFM measurements, a multistep growth process with increasing ionic strength. Here, the primary building units first aggregated into nanosheets, which then grew laterally and, finally, became stacked vertically, resulting in 3D nanoparticles. RAXS played a key role in unraveling this complex mechanism, as it allowed to unambiguously separate the contribution of the Zr atoms from that of other interfacial species in the total energy density distribution. This example illustrates the value of element-sensitive data in determining complex

interface processes on a molecular scale.

4.7.3 Determination of electronic structure by RAXS

By combining RAXS with *ab initio* theory calculations, information about the electronic structure can be obtained, for example, on electron transfer and electric orbital hybridization during covalent bond formation. To understand how this works in principle, we first revisit the conventional approach for fitting RASXS spectra described in chapter 4.7.1. Here, the dispersion corrections to the form factor ($f' + \mathrm{i}f''$) are obtained from experimental XANES data, using the assumption that all resonant atoms are structurally equivalent in terms of geometrical surrounding, symmetry, and electronic state. This constraint works well in many cases, for example, in RASXS studies of systems where the resonant atoms are present as adsorbates above a substrate. However, problems arise if the resonant atoms are present in different environments, e.g., at the interface and in the substrate itself, since those structural nonequivalent atoms of the resonant element should respond differently to the energy scan through the absorption edge. In this case, the resolved distribution of the minority species of the resonant atoms, i.e., the adsorbed atoms at the interface, could be faulty, because the experimental dispersion corrections used in the fits by the structural model are only average values. This limitation can be overcome by using dispersion corrections f' and f'' that are calculated by density functional theory (DFT). This method became practically feasible only recently with the advent of advanced self-consistent *ab initio* software for the simulation of X-ray absorption and X-ray resonant scattering spectroscopy,[139] which allows the simulation of the CTR intensity for a known surface structure (to be resolved by fitting CTR data) at any specified momentum transfer $\mathbf{q}$ and X-ray energy ε_{Ph}). In these simulations, the structurally nonequivalent resonant atoms can be described by different resonant form factors, depending on their geometrical surroundings and symmetry. In addition, also the polarization dependence of RAXS spectra can be simulated. As a result, a full picture of the local environment of the resonant absorbing atoms can be obtained, including both geometrical surroundings and electronic parameters. This allows geting insights into changes of the electronic orbitals due to interface processes, such as electron transfer and orbital hybridization. Although the application of this DFT-assisted approach to the electrochemical interface is still in its early stages, some interesting results have recently been published by Soldo-Olivier, Grunder and coworkers.[140,141] In this work, pioneering experimental results on the charge distribution at metal-electrolyte interfaces, specifically platinum and Br-covered copper electrodes, were reported. These studies found that, contrary to common belief, the surface charge is not located directly at the metal surface but spread out over the two outermost atomic planes. Such data can be directly compared to *ab initio* molecular dynamics simulations. RAXS is unique in its ability to probe simultaneously geometric and electronic structures and expected to play an important role in future fundamental studies of electrochemical interfaces.

5 Fundamental electrochemical interface structure

Insight into the atomic-scale structure of electrodes in an electrochemical environment is an important prerequisite to the fundamental understanding of reactions at these interfaces. *In situ* surface X-ray diffraction methods have provided detailed structural data on the electrode surface structure. In particular, these methods have revealed surface structural changes as a function of potential as well as differences in the surface structure found under UHV conditions. In this section, we review results on the interface structure in the absence of electrochemical reactions, i.e., in the double layer potential regime. Because many of these studies have already been described in previous reviews,[142–153] we keep this section brief. We first discuss *in situ* SXRD studies of structural transitions at metal electrodes, both of the metal itself and of

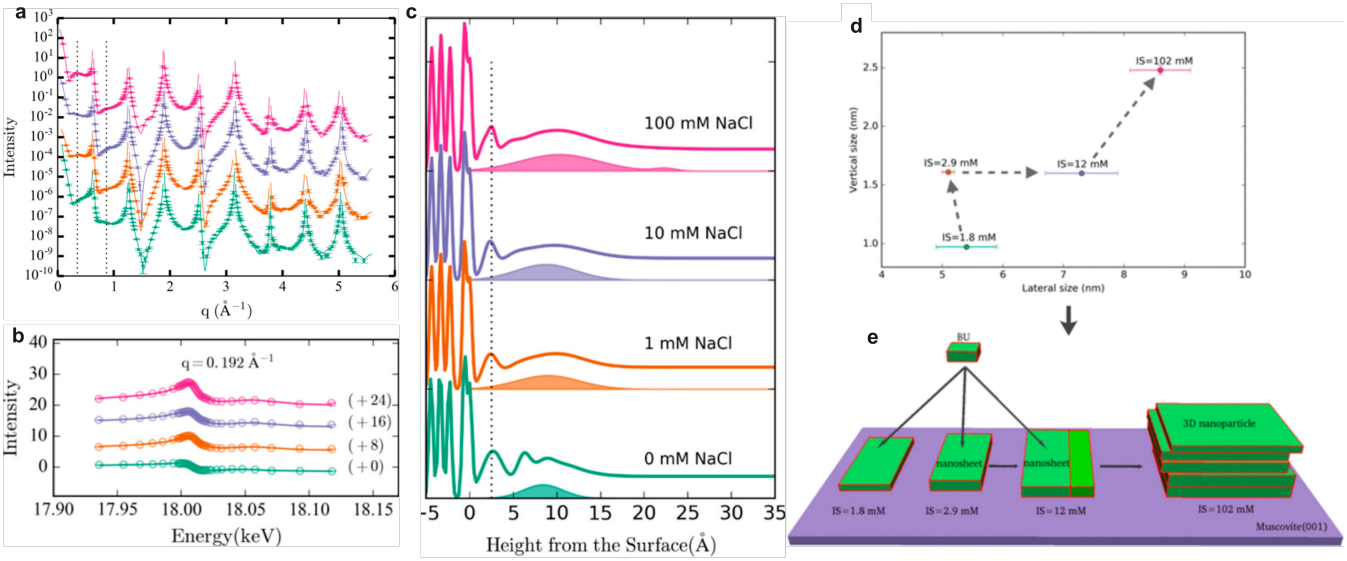

Figure 22: *in situ* RASXS measurements of Zr_xO_y nanoparticle aggregation on the muscovite (001) surface in NaCl solutions of different ionic strength. (a) CTR profiles, (b) exemplary RASXS spectra collected at q = 0.192 Å^{-1}, and (c) total electron density distribution along the surface normal direction obtained from CTR modeling (solid lines) together with Zr electron density distribution derived from the RASXS modeling (filled area). (d) Lateral and vertical Zr_xO_y size obtained from the RASXS modeling and (e) proposed aggregation mechanism as a function of ionic strength. (reprinted from Ref.[138]. Copyright 2018 American Chemical Society).

adsorbate layers on top of the metal, and then provide an overview of the interface structure at non-metallic electrodes, especially oxides.

5.1 Metal electrode structure

5.1.1 Surface reconstruction

Surface reconstruction is a well-known phenomenon in UHV surface science. It denotes the case where the atoms in the materials' surface layer(s) form a 2D ordered arrangement that deviates from that of the ideally truncated crystal lattice. In the following, we adopt this traditional definition of surface reconstruction. However, we note that in the more recent literature, often a less stringent wording is employed, where any restructuring at the surface of a material, including morphological changes (e.g., surface roughening), the formation of disordered structures, and chemical phase changes (e.g., surface oxidation), is called surface reconstruction.

Under UHV conditions, surface reconstructions are found on the clean surfaces of certain metals, e.g., Au, Pt, and Ir, but also can be induced by adsorbates. They originate from the different chemical environments of the surface atoms and result in a reduced surface energy. Typically, the 2D unit cell describing the periodicity of the reconstructed surface is larger than that of the unreconstructed surface and has a defined orientation with respect to the underlying bulk lattice. This results in additional superstructure rods in between the CTRs, which are well accessible to surface diffraction measurements. Indeed, GIXRD studies and surface crystallographic analysis of CTR data played a central role in determining the structure of the reconstructions of Au and Pt at the metal-vacuum interface.[154–158]

Surface reconstructions can also be observed on Au and Pt single-crystal surfaces in an electrochemical environment, where their stability usually depends on the potential.[159] Specifically, the reconstructed surface is usually only stable below a critical potential, which is determined by the electrolyte composition. Positive of this critical potential, a surface phase transition to an unreconstructed surface oc-

curs. Direct evidence for the presence of surface reconstruction in electrolyte solution was first provided by *in situ* GIXRD measurements of Ocko et al. for the case of Au(100) electrodes in $HClO_4$ solution.[160] They demonstrated that, similar to the surface structure found in UHV, the reconstruction of the Au(100) electrode consists of a densely-packed hexagonal Au surface layer on top of the square substrate. Upon increasing the potential, the reconstruction was found to disappear above the potential of zero charge but recovered upon changing the potential back to values below -0.3 $V_{Ag/AgCl}$, albeit with some hysteresis. Similar *in situ* GIXRD were performed by Ocko and coworkers for Au(111)[161,162] and Au(110)[163] in acidic and neutral electrolyte solutions, revealing a qualitatively similar potential dependence. Au(111) electrodes exhibit at negative potentials a $(23 \times \sqrt{3})$ reconstruction, consisting of dislocation stripes. The reconstructed Au surface layer is 4% uniaxially compressed along the [100] direction and exhibits the same local order as in the herringbone reconstruction found on well-annealed Au(111) single crystals but has a more disordered arrangement of the 3 differently oriented domains. Upon increasing the potential, the phase transition between the reconstructed and unreconstructed surface at the critical potential occurs gradually via a gradual change in the average separation of the reconstruction stripes. Furthermore, the transition potential was found to strongly depend on the anion species in the electrolyte. This was attributed to the effect of the surface charge on the electrode surface but may also be caused by the onset of anion chemisorption, as both are closely correlated and cannot be easily separated (see Ref.[164,165] for a discussion of this still controversially discussed topic). In the case of Au(110), a mix of a (1×2) and (1×3) reconstruction was found in $HClO_4$, whereas in alkali halide solutions only a (1×3) reconstruction was observed.[163] Also here, highly reversible transitions between reconstructed and unreconstructed surfaces occurred. Furthermore, a similar structural behavior was observed for the Au(111) and Au(100) reconstruction in sulfuric acid solution[166] and alkaline electrolyte.[167–169] All these results were in good agreement with data obtained by complementary surface-sensitive methods, such as *in situ* scanning tunneling microscopy (STM).[170–172,172–175]

In contrast to the very detailed studies of reconstructions of Au single crystals, data on the reconstruction of other metals is scarce. For platinum electrodes, only the thermally prepared (1×2) reconstruction of Pt(110) was observed by *in situ* SXRD.[176,177] This structure was remarkably stable over a wide potential range and found to persist on the surface even in the presence of adsorbed CO, which under vacuum conditions induces a lifting of the (1×2) phase on Pt(110). The reconstructed Pt(100) surface does not survive immersion into the electrolyte according to *in situ* STM observations, resulting in an unreconstructed surface covered by 0.25 monolayer (ML) of Pt monolayer islands.[178] In contrast to Au, potential-induced transitions from the unreconstructed to a reconstructed surface were not observed on Pt electrodes. This is probably related to kinetic limitations of the required long-range surface mass transport, because the surface mobility of Pt is much lower than that of Au. Similar reasons may be responsible for the inability to observe surface reconstructions on the electrodes of other high melting point metals, such as Ir. These limitations do not exist for metals such as Cu and Ag, which have very high surface mobilities at room temperature. Although the clean metal surfaces of Cu and Ag do not reconstruct, surface reconstructions can be induced by adsorbates. Such reconstructions were observed by *in situ* STM and AFM on all three low-index Cu surfaces in the presence of adsorbed anions, hydrogen, and hydroxide.[179–185] However, *in situ* SXRD studies of these systems have not been reported up to now.

In addition to the steady-state surface structure, also the dynamic behavior of surface reconstructions was assessed by *in situ* X-ray scattering techniques. The kinetics of the structural transitions between reconstructed and unreconstructed surfaces were already addressed in the early studies of Au(111) by Wang et al, where the $(23 \times \sqrt{3}) \leftrightarrow (1 \times 1)$ transition was

studied during potential sweeps and steps by monitoring the intensity at selected reciprocal space positions along the CTRs and $(23 \times \sqrt{3})$ superstructure rods.[161,162] Lucas and coworkers extended such *in situ* SXRD studies to elevated temperatures and found faster kinetics of the surface phase transitions, which could be attributed to the faster surface mass transport.[186,187] You and coworkers pioneered the use of coherent surface scattering techniques to study equilibrium fluctuations on Au(100) electrode surfaces.[188,189] Using *in situ* X-ray photon correlation spectroscopy (XPCS), they investigated fluctuations between reconstructed and unreconstructed areas on the partly reconstructed surface. These studies showed that the electrochemical environment leads to increased dynamics as compared to Au(100) surfaces under UHV conditions and that the dynamics increase further in the presence of halides, as expected on the basis of studies by *in situ* scanning probe microscopy.

5.1.2 Surface relaxation

Even in the absence of surface reconstruction, the symmetry break at the surface of a crystal leads to changes in the bond distances. This surface relaxation results in deviations of the spacings between the topmost atomic layers as compared to the bulk spacing, which are typically on the order of a few percent or lower. Specular and non-specular CTRS are highly sensitive to such changes in the layer spacings (see Figure 17). Surface relaxations are significantly affected by the presence of chemisorbed species,[190] which provides an indirect probe of the latter, even for very weak X-ray scatterers such as hydrogen. On the other hand, the effect of surface relaxation as well as increased surface vibrations (i.e., Debye-Waller factors) has to be taken into account in any quantitative surface crystallographic analysis.

Surface relaxation at a metal electrode was first reported by Wang et al., who found on the $(23 \times \sqrt{3})$ reconstructed Au(111) a 3.3% relaxation of the topmost layer whereas on the unreconstructed, halide-covered surface no surface relaxation was observed.[162] More detailed studies of the potential-dependent surface relaxation were reported by the group of Ross, focusing on Pt electrodes. For Pt(100), an expansion of the top layer spacing was observed when the potential was shifted 400 mV negatively, from the region of hydroxide adsorption to a potential where the surface was covered by a hydrogen monolayer.[191] Similar results were obtained for (1×2) reconstructed Pt(110), revealing a complex relaxation of the topmost 4 Pt layers and an additional expansion in the presence of both hydrogen and hydroxide adsorbates.[176] An outward surface relaxation was also induced by adsorbed CO[192] or halides[193] on Pt(111) electrodes. The amount of vertical relaxation can depend strongly on the local adsorption geometry. For example, the atoms in the surface layer of Pt(111) covered by a $(\sqrt{(19)} \times \sqrt{19})$ adlayer of CO exhibit a very large expansion of 0.28 Åunder near-top-site CO molecules, but only 0.04 Åunder near-bridge-site CO.[194] Similar local relaxation effects were also observed on halide-covered Cu electrodes[195,196] and will be discussed in more detail in the next chapter. Surface relaxation effects were also observed in SXRD studies of bimetallic electrode surfaces[197–200] and in non-aqueous electrolytes.[201] Furthermore, a close correlation between the vertical surface relaxation and the surface stress was found, which could be rationalized by their dependence on the metal's electronic structure.[202,203]

5.2 Adsorbates at metal electrodes

Adsorption of electrolyte species at the electrode surface, such as anions, cations, neutral chemisorbed species, and solvent molecules, is a ubiquitous phenomenon in electrochemical systems. These adsorbates can either directly participate in electrode reactions or be present as spectator species that influence the reactions. Clarifying the precise arrangement of these species at the interface is thus of central importance for understanding the electrochemical reactivity. Together with *in situ* scanning probe microscopy, *in situ* surface X-ray scattering methods have played a central role

in such data on the adlayer structure. First attempts at investigating adsorption phenomena by *in situ* XRD were made by Fleischmann and coworkers, who employed a laboratory X-ray anode for studies of potential-dependent changes in the scattering of polycrystalline and thin film electrodes.[204–206] However, unambiguous surface structural data was only obtained in studies by Melroy, Toney, and coworkers, where synchrotron radiation was used for *in situ* GIXRD studies of metal monolayers formed by underpotential deposition (UPD) on single crystal electrodes.[207–210] Indeed, these studies represent the very first direct determination of the atomic-scale structure at an electrode-electrolyte interface. Many similar studies of adlayer structure have been performed since then, revealing a complex, potential-dependent surface phase behavior of the adsorbed species. In the following chapter, a short overview is given, focusing on the results from SXRD measurements. For a more detailed discussion of adlayer structures at electrode surfaces, we refer to Ref.[148,149,211].

5.2.1 Anion adlayers

In situ SXRD studies of anion adlayers focused on halides adsorbed on coinage metals and platinum electrodes.[145,148] Here, various ordered adlayers were found positive of a critical potential. The structure of these adlayers depends on the in-plane order of the substrate and the coverage, which in electrochemical systems is determined by the potential. On the (111) surface of Au, Ag, and Cu, incommensurate structures were dominant, in which the halide packing density continuously increased with increasing potential (see Figure 16c-e).[96,145,212–216] At the most positive potentials, prior to the onset of halide-induced metal dissolution, Au(111) and Ag(111) are covered by close-packed 2D incommensurate adlayers. In the case of iodine, this 2D adlayer is preceded by an uniaxially-incommensurate $c(p \times \sqrt{3})$ phase and, on Ag(111), a commensurate $(\sqrt{3} \times \sqrt{3})$R30°.[145] On Cu(111), GIXS measurements were only performed for Cl, finding a 2D incommensurate adlayer.[215,216] On Pt(111) disordered adlayers or commensurate structures with larger unit cells were observed, usually with more than one adsorbate in the superstructures unit cell. Examples are a (3×3) and $(\sqrt{7} \times \sqrt{7})$R19° superstructure of iodide on Pt(111)[145,193] Apart from GIXS studies, also *in situ* CTR studies were performed for Cl and Br on Au(111), which provided similar adlayer coverages as the in-plane studies and a vertical spacing between the halide and the Au surface layer of 2.4 Å, indicating chemisorption of these species.[162]

On (100) and (110) surfaces, predominantly commensurate structures are observed, reflecting the higher energetic corrugation of the (100) as compared to the (111) lattice. Incommensurate adlayers were only found on Au(100) electrodes, namely a $(\sqrt{2} \times p)$R45° structure, which undergoes a 2D phase transition to a commensurate, quasi-hexagonal $(\sqrt{2} \times 2\sqrt{2})$R45° adlayer,[145,148,217] and for iodide coadsorbed with alkali cations on Au(110).[218] The most commonly observed structure on (100) surfaces is a $c(2 \times 2)$ adlayer with a coverage of 0.5 ML (Figure 23a), which has been observed for Cl and Br on Ag(100) and Cu(100).[146,195,196,219–224] This particularly simple type of adlayer is highly suited for in-depth studies of anion adsorption. Ocko et al. studied by *in situ* GIXS the potential-dependent transition between the disordered and the $c(2 \times 2)$ ordered Br adlayer on Ag(100).[219,220] They found that the formation of the $c(2 \times 2)$ phase occurred in a second-order phase transition at a coverage of 0.35 ML as determined from chronocoulometric measurements, in good agreements with simulations.[225,226] Detailed *in situ* CTR measurements were performed for Cl and Br on Cu(100), revealing the detailed adsorption geometry.[195,196,221–224] As in UHV,[227] the halide ions adsorb in fourfold-hollow sites. However, in-depth SXRD studies and corresponding DFT calculations revealed subtle but distinct differences to adsorption from the gas phase, caused by the adjacent electrolyte.[195,196,221,223,228,229] Specifically, the Cl-Cu bond length is noticeably increased, the spacing between the two topmost Cu layers is contracted, and the buckling of the Cu atoms in the second layer is

reversed in the presence of the electrolyte as compared to UHV. On the basis of DFT calculations, these effects could be assigned to the influence of water and cations in the outer Helmholtz plane of the electrochemical double layer.

In a similar way, also the influence of "specifically adsorbing" cations that interact more strongly with the adlayer has been assessed. On Ag(100) and Cu(100) surfaces that are fully covered by a $c(2 \times 2)$ halide adlayer a partial coverage of coadsorbed (hydrated) K^+ and Cs^+ cations was found by SXRD (Figure 23b).[223,228–230] These coadsorbed cations were proposed to be located in fourfold coordinated sites with respect to the halide anions underneath. They were bound to those via bridging hydration water and gradually desorbed towards more positive potentials (Figure 23b,c). In an intermediate coverage range, the anion and cation mutually promoted their adsorption on the electrode surface.[228] This cooperative adsorption manifests in an enhanced Br adsorption as compared to electrolytes with non-specifically adsorbing Li^+ cations and a corresponding maximum in Cs^+ coverage near the potential of the 2D phase transition between disordered and $c(2\times2)$ adlayer. Recently, also adsorbed Cs^+ on the (1×2) reconstructed Pt(110) was reported.[231] These measurements illustrate that also the outer parts of the electrochemical double layer are accessible to *in situ* SXRD studies, making it possible to probe the subtle interplay of the molecular interactions in this part of the interface region. Furthermore, Nakamura et al. demonstrated for the same system that the dynamics of adsorption processes can be studied on sub-millisecond time scales by fast time-resolved SXRD measurements, allowing to detect short-lived transient states.[229] Based on these experiments they proposed that the Cs^+ ions were in a first step accumulated in the outer Helmholtz plane, followed by a slight vertical relaxation towards the surface (Figure 23c). These time-resolved studies required averaging over $\approx 10^5$ potential cycles and thus require highly reversible systems. However, with the increasing availability of 4th generation synchrotron sources and XFELs, also dynamic studies of less reversible processes may get into reach. Finally, also the electronic interface structure of halide-covered electrodes has been recently probed by pioneering studies of Grunder et al., using resonant surface X-ray diffraction.[141,232] Together with *ab initio* calculations, these measurements allowed to determine the charge distribution at $c(2 \times 2)$ - Br covered Cu(100) electrode. They showed that the bonding of the chemisorbed adsorbate to the metal leads to a rearrangement of the charge and a shift of the surface dipole moment into the metal electrode.[141]

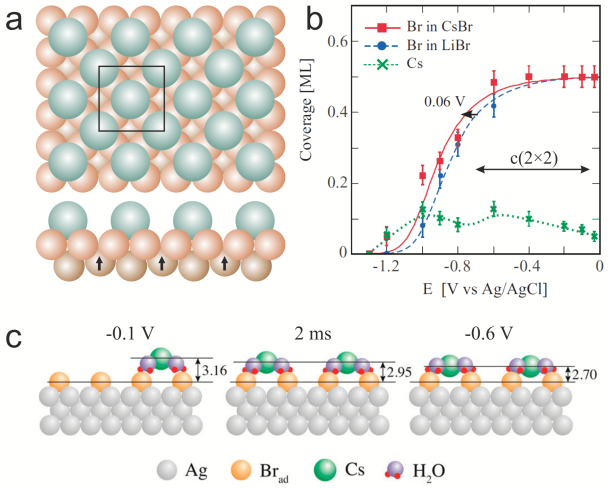

Figure 23: (a) Structural arrangement in the $c(2 \times 2)$ halide adlayer on (100)-oriented fcc metal surfaces. (b) Influence of alkali cations on the Br adlayer coverage on Ag(100) (reprinted from Ref.[228] with the permission of the APS). (c) Temporal changes of the adlayer structure in Cs-containing solution during a potential step from -0.1 to -0.6 V, derived from *in situ* XRR measurements with 100 μs time resolution (Reprinted from Ref.[229]. Copyright 2014 American Chemical Society).

5.2.2 Metal adlayers

The formation of metal adlayers via underpotential deposition (UPD) is an extensively studied phenomenon in interfacial electrochemistry.[233,234] *In situ* surface X-ray scattering technique have contributed greatly in resolving the atomic-scale structure of these adlayers. From the initial *in situ* GIXS studies

on, UPD adlayers of heavy metals, such as Pb,[177,193,207–210,235,236] Tl,[236–243] and Bi,[244–247] were studied on the (111) and (100) surfaces of Ag, Au, and Pt. For Pb and Tl on Ag(111) and Au(111), hexagonal close-packed adlayers with 2D incommensurate structures were found that were continuously compressed with decreasing potential.[207–210,236] This electrocompression effect is similar as found for halide adlayers, but much smaller in magnitude. For Tl on Au(111) in alkaline electrolyte, in addition, an incommensurate aligned-hexagonal phase was found at more positive potentials.[238,239] Tl UPD layers on Au(100) and Ag(100) form $(p \times \sqrt{2})$, which compress uniaxially.[240,241] A particularly rich structural phase behavior was observed for Bi UPD layers. On Au(111), first a (2×2) and then a uniaxially incommensurate $(p \times \sqrt{3})$ structure forms with decreasing potential.[245,246] The latter structure was also observed for Bi on Ag(111).[244] On Au(100), a sequence of even three ordered adlayer phases is observed: a (3×3)R45° structure consisting of square Bi quadrumers, a $c(\sqrt{2} \times 3\sqrt{2})$ structure, where the Bi adatoms are arranged in zigzag chains, and a quasi-hexagonal close-packed $c(p \times 2)$ adlayer, which is uniaxially incommensurate and compressible.[247] In contrast, UPD layers of these metals on Pt electrodes had commensurate structures or were disordered. Pb forms a $(3 \times \sqrt{3})$ structure on Pt(111), whereas it is disordered on Pt(100) and Pt(110).[235] Bromide anions have a strong influence on the Pb adlayer, inducing on Pt(100) a $c(2 \times 2)$ ordering[248,249] and on Pt(111) a $p(2 \times 2)$ structure, which was attributed to a PbPt surface alloy.[250] SXRD studies of irreversibly adsorbed Bi found a disordered adlayer with a coverage of ≈1/3 ML on Pt(111)[251] and a $c(2 \times 2)$ structure on Pt(100).[252]

The arguably best-studied system is the UPD of copper. In this case not merely a metal monolayer is formed, rather Cu coadsorbs with specifically adsorbing anions. A key system here is Cu UPD on Au(111) in sulfuric acid solution where a with decreasing potential first a $(\sqrt{3} \times \sqrt{3})$R30° superstructure is formed, which in a second surface phase transition changes to a full Cu monolayer with adsorbed sulfate on top. The arrangement in the $(\sqrt{3} \times \sqrt{3})$R30° phase was clarified in detailed surface crystallographic studies and shown to consist of a Cu honeycomb lattice with 2/3 ML coverage, in which 1/3 ML of sulfate ions were adsorbed in the honeycomb centers, bound via 3 of their oxygen atoms.[253,254] An identical behavior was found for the Cu UPD adlayer in sulfuric acid on Pt(111).[255] The influence of the anion on the adlayer structure increases for more strongly coadsorbing ions, such as halides. For Cu UPD on Pt(111) in Cl or Br containing solution stoichiometric bilayers with a hexagonal incommensurate structure are formed, in which the 2D Cu and the halide lattices were in registry with each other, but not with the substrate.[256–258] This type of arrangement, which was determined using anomalous surface scattering, resembles that found in the (111) plane of CuCl and CuBr salts, respectively. Cu UPD on Pt(100) was found to occur always in form of a pseudomorphic (1×1) layer, but the potential range and formation kinetics significantly increased in the bromide-containing solution.[249,259,260]

The mutual stabilization of anions and cations on metal electrodes is not restricted to Cu UPD, but has been observed in a number of systems. Particularly insightful are *in situ* X-ray surface scattering studies of Wang and coworkers that reported the presence of salt-like adlayers of halides coadsorbed with Tl or Pb on Au(111) electrodes in acidic electrolyte.[242,243,261] These systematic studies reported a complex potential-dependent sequence of differently ordered adlayer structures. With increasing potential, the stoichiometry changes stepwise from a purely metallic adlayer to a pure halide layer. In an intermediate potential range, various salt-like phases are found, including phases with a square 1:1 arrangement of halide and metal. The halide is either coadsorbed with the metal species on the Au surface or resides on top of the adsorbed metal layer. In both cases, the ad-metal is stabilized on the electrode surface at much more positive potentials as in halide-free electrolyte. For Pb in Br-containing solution, the transition between the different mixed adlayer phases was found to

be slow, resulting in the long-term coexistence of those phases.[261]

Among the other UPD systems studied by *in situ* SXRD methods, the most interesting cases are Ag and Pd UPD. Ag UPD on Au and Pt is unusual in that respect that not only monolayer but also bilayer phases are formed prior to the onset of bulk Ag deposition. According to SXRD measurements on Pt(111), the initially formed Ag monolayer is pseudomorphic, despite the large lattice mismatch to the Pt substrate, whereas the bilayer adapts an expanded hexagonal lattice to partly release the associated surface stress.[262,263] This commensurate to incommensurate transition is accompanied by a substantial decrease of the Ag-Pt spacing and an expansion of the vertical spacing between the two Ag layers as compared to bulk Ag, which was attributed to charge transfer from Ag to Pt and results in enhanced adsorption of sulfate anions and CO on the Ag top layer. Pd UPD is of interest for electrocatalysis and hydrogen storage (see section). It was studied on Pt(111) and Pt(100) by the Markovic group, who reported a pseudomorphic growth behavior.[198,264,265]

5.2.3 Molecular adsorption

Adsorbed molecular species play a central role in electrochemical reactions, e.g. as intermediates, inhibitors, or accelerators. Although these molecular adsorbates often only contain low-Z elements (C, O, H) and thus scatter X-rays only weakly, their in-plane order often could be detected successfully. The reason for this is the local relaxation of the substrate lattice, induced by the chemisorbing molecule. This relaxation leads to a periodic modulation of the (strongly scattering) atoms in the substrate's surface layer(s) with the same in-plane periodicity as that of the adlayer structure, which can provide a strong and often dominant contribution to the diffraction signal.[194]

The by far most studied molecular adsorbate is CO, owing to its importance as a catalyst poison and reaction intermediate. Especially CO on Pt(111) is a key model system in interfacial electrochemistry and has been studied in detail by *in situ* surface diffraction.[194,266–270] *In situ* STM studies showed that CO adlayers formed by adsorption from CO-saturated solution adapt at potentials near the onset of hydrogen evolution a $(p2 \times 2)$ structure with a coverage of 0.75 ML, which undergoes a transition to a $(\sqrt{19}\times\sqrt{19})$R23.4° adlayer with 13 CO in the unit cell (13/19 ML coverage) upon increasing the potential into the "pre-oxidation" range.[271,272] This adlayer phase behavior was confirmed by *in situ* SXRD measurements, which allowed not only to clarify the structure but also to study the adlayer kinetics during potential sweeps.[194,267–270,273] These studies revealed that the stability of the two phases and the surface phase transition depend strongly on the CO partial pressure in the solution as well as on the anion species in the electrolyte. Furthermore, temperature-dependent SXRD studies of the $p(2\times2) \leftrightarrow (\sqrt{19}\times\sqrt{19})$R23.4° transition showed that the ordering of the $(p2\times2)$ CO adlayer has a maximum near room temperature and that $(\sqrt{19}\times\sqrt{19})$R23.4° ordering increases with temperature.[149] The $(p2 \times 2)$ CO adlayer was also studied by *in situ* resonant anomalous surface X-ray scattering, from which the Pt-C binding distances were determined.[274]

On Pt(100) electrodes, CO induces surface relaxation, but no ordered CO adlayers were observed in SXRD studies,[275] in contrast to reports by *in situ* STM.[276,277] No ordered CO adlayers were also found on Au(111), Au(100), and Au(110) electrodes, however, in alkaline electrolyte the presence of CO in the electrolyte stabilized the surface reconstruction in these systems over a wide potential regime.[169,278] In addition, bimetallic systems of Pt and other metals have been investigated, owning to the interesting electrocatalytic properties of Pt alloys. Lucas et al. studied the interaction of CO with metal UPD layers adsorbed on Pt single-crystal surfaces. Cu and Pb adlayers on Pt(111) and Pt(100) were found to be displaced by CO, whereas the $(c2 \times 2)$ Bi UPD layer on Pt(100) was unaffected.[197,279] Pd monolayers on Pt(111) exhibited a reversible vertical contraction of the Pd-Pt spacing upon CO adsorption and transformed into a Pd oxide phase in the CO oxidation region.[280] Ag mono- and bilayers

on Pt(111) were found to adsorb and oxidize CO, contrary to Ag(111) electrodes, which was attributed to Pt-induced changes in the electronic structure.[263]

A second type of molecular adsorbates that are of great importance in fundamental electrochemistry and electrocatalysis are oxygen species, such as OH, water, and H_3O^+. For Pt(111) in $HClO_4$ solution, Kondo et al. reported a continuous increase in the coverage of oxygen species and a concomitant relaxation of the spacing of the topmost Pt layer in the entire double-layer regime.[281] In accordance with results for Pt(111) oxidation in the gas phase and DFT calculations, they reported a p(2×2) phase in their *in situ* SXRD studies and assigned it to a mixed layer of OH_{ads} and H_2O. Furthermore, they observed in potential-dependent measurements of the non-specular CTR a distinct two-step process. This behavior was attributed to random adsorption in the broad region, followed by the formation of a transient p(2×2) adsorbate phase and a subsequent phase transition to a p(1×1) adlayer at the sharp butterfly peak. In addition, SXRD studies by Liu et al. found the formation of a buckled top Pt layer in the butterfly region,[282] in good agreement with DFT predictions.[283] In both SXRD studies, the CTR data was modeled with the oxygen atoms in fcc or hcp hollow sites, on the basis of results from theory and oxygen adsorption in the gas-phase. Nakamura et al. reported a pronounced cation effect on OH adsorption on Pt(111) in alkaline electrolytes.[284] Whereas Li^+ ions were found to stabilize OH_{ad}, no such stabilization was observed in the case of Cs^+ ions. A similar cation-induced stabilization of OH_{ad} was also reported for Ag(111) in an alkaline solution.[285] Furthermore, *in situ* X-ray reflectivity studies of Ru(0001) in H_2SO_4 solution revealed that the (bi)sulfate adlayer is partially replaced by adsorbed oxygen species between 0.6 and 1 V vs. reversible hydrogen electrode (RHE).

The structure of water near metal electrodes has been a topic of some controversy. Toney et al. performed detailed CTR measurements of Ag(111) in NaF solution.[286,287] According to their analysis, the orientation of the water dipoles flips upon reversal of the electrode's polarity and the density of the interfacial water layer significantly exceeds that of bulk water. While the water layering and orientation reversal are undisputed, the strongly enhanced water density was not found in other X-ray surface scattering studies and molecular dynamics (MD) simulations of water at metal surfaces. For Ag(100) in NaF electrolyte[288] and Au(111) in halide solutions,[162] the CTRs were well described with water layers that corresponded to the bulk water density. MD simulations as well as more recent AIMD simulations of water at Ag, Hg, and Pt electrodes also found water layers with bulk-like density at the interface.[289–292] Furthermore, the interfacial water at multilayer graphene on SiC was studied by SXRD.[293,294] Although the electron density contrast between water and the solid is more favorable here than in the case of metals, the intrinsic heterogenity of these electrodes leads to additional difficulties in the data analysis. Zhou et al. studied this interface at open circuit conditions and reported a slight hydrophobic gap between graphene and the first water layer, as predicted by AIMD simulations.[293] However, the water-graphene interactions depended strongly on the number of epitaxial graphene layers and defects. Hayashi et al. performed potential-depend measurements and proposed an ice-like water bilayer at the interface without adsorbed ions in the double layer.[294]

More recently, these studies of the near-surface structure of the electrolyte near the solid surface were extended to non-aqueous systems, in particular ionic liquids (ILs). First, *in situ* XRR studies of these types of interfaces were performed for ILs at a sapphire single crystal surface and revealed strong stratification into alternating cationic and anionic layers, with the layering decaying into the bulk on length scales of 1-2 nm.[295] Studies of electrochemical interfaces to Au(111)[296,297], graphene on SiC,[298,299], $SrTiO_3$,[300], boron doped diamond,[301], and Si.[302] These studies found similar interface layering, as well as a reversal of the anion and cation layers with potential. In some cases, substantial crowding, i.e., accumulation of more than a single layer of one of the ion

species at the electrode surface, was observed at potentials far away from the pzc.[300,303] Very recent studies of mixtures of ILs with carbonate solvents reported at positive potentials several nanometer thick layers, in which the anion concentration was 3 to 5 times higher than that of the cations.[302] Furthermore, very slow interfacial dynamics on time scales from 10 to 1000 s were reported.[297–299,304]

Overall, these studies illustrate the unique capabilities of X-ray surface scattering methods for probing not only species that are directly chemisorbed at the electrode surface, but also the molecular arrangement within the outer parts of the electrochemical double layer. However, precise measurements are challenging, and clarification of the detailed structure of the electrolyte near the electrode and its dependence on the potential will require further efforts.

5.3 Interface structure of oxides and minerals

Metal oxides have received increasing attention in many research fields, including catalysis, gas sensing, and contaminant removal. In the context of electrocatalysis, oxides have become of great interest in recent years, in particular as catalysts for oxygen evolution and reduction. Furthermore, oxide films and oxide-electrolyte interfaces are of great interest in electrochemical materials science and corrosion, especially if they exhibit sufficiently high electric conductivity. Most studies of oxide interface structure have been driven by questions coming from geochemical and environmental science and focus on common minerals, such as calcite, barite, quartz, corundum, hematite, rutile, and muscovite. Although these are, with the exception of hematite, good electric insulators and the state of their interfaces is, thus, controlled by the solution chemistry rather than the potential, the results obtained here are still relevant for electrochemical systems. First, general insight on oxide-electrolyte interactions is obtained that can be transferred to oxidic electrode materials. Second, (ultra)thin films of such oxides or related species may form during electrochemical reactions, e.g., due to passivation, and affect the latter. We, therefore, included this work in this and the following chapter.

Oxides and other minerals typically have multiple energetically stable crystallographic planes of different terminations that would expose a rich combination of different surface oxygen groups. The latter are potential binding sites and are involved in a range of interfacial processes. For example, they may facilitate the surface complexation of metal ions, modulate the H-bonding network of interfacial water, and induce the aggregation of small molecules to form nanoparticles at the surface. Similar to metals, oxide surfaces may reconstruct as a function of potential and electrolyte conditions. Obtaining insight into the atomic-scale oxide-electrolyte interface structure is thus of substantial importance for an improved understanding of oxide surface chemistry. In this chapter, we will discuss *in situ* SXRD results on the surface structure of oxides and minerals in aqueous solutions.

5.3.1 Surface termination and surface reconstruction

Because of the more complex bulk structure, also the surface and interface structure of oxides is much more complex than those of metals, as shown in extensive studies of clean oxide surfaces under UHV conditions.[305,306] Different crystal facets on oxides and minerals can have very different stability. For oxides in contact with the vacuum, a key aspect is surface polarity. Surfaces that are charge-neutral (nonpolar surfaces), i.e., carry identical anionic and cationic charges in the top layer, are typically thermodynamically stable. In contrast, surfaces that carry an excess charge (polar surfaces) are unstable. Here, stabilization is achieved either by reconstruction of the surface or adsorbates, in particular the replacement of surface oxygen species by OH. The latter stabilization mechanism is easily accessible in aqueous solutions. Furthermore, in electrochemical systems, the surface charge and, thus, the degree of surface hydroxylation can be varied by the potential.

Most oxide interfaces found in natural (aqueous) environments correspond to low-index crystallographic facets. High-index surfaces can usually only be obtained through specific synthesis procedures and are typically very reactive. Although the latter is often desired in electrocatalysis, such high-index surfaces are unstable and tend to undergo structural reconstruction. In addition, different surface terminations may coexist on surfaces with the same crystallographic orientation, depending on the preparation conditions. For example, an r-cut hematite ($1\bar{1}02$) surface tends to terminate with a stoichiometric crystallographic plane (Figure 24a) upon annealing at 500°C,[307] whereas preparation via a chemical mechanical polishing procedure resulted in a partial transformation of this stoichiometric surface termination into a so-called half-layer termination.[308]. Considering that in all oxide crystal lattices multiple atomic layers with different surface symmetries exist, different surface termination patterns are likely to occur in other oxide materials as well.

On well-prepared oxide single-crystal surfaces in ultrahigh vacuum, often ordered surface reconstructions are observed. Whether similar reconstructions exist also in an electrochemical environment is largely not clear, because of the challenges to prepare oxide electrode surfaces of similar quality. A first *in situ* GIXD study on this topic was recently performed by Grumelli et al. for the case of the (100) surface of magnetite.[309] This surface exhibits a characteristic $(\sqrt{2}\times\sqrt{2})R45\,\mathrm{deg}$ reconstruction, in which the presence of subsurface Fe vacancies and interstitials leads to a modified structure where the top four atomic layers exclusively contain Fe^{3+} cations.[310,311] By exposure to pure water vapor, this reconstruction is quickly lifted.[311] Nevertheless, the work by Grumelli et al. revealed that the $(\sqrt{2}\times\sqrt{2})R45\,\mathrm{deg}$ structure remained at least partly stable in 0.1 M NaOH, if the potential is kept above 0.8 V vs RHE. Only at more negative potentials, where the magnetite surface starts to be reduced, irreversible removal of the $(\sqrt{2}\times\sqrt{2})R45\,\mathrm{deg}$ superstructure rods occurred. Considering that the reconstruction corresponds to an oxidized state of the surface, these results indicate that sufficiently oxidizing conditions are required to maintain the reconstruction. Similar may be true for other reconstructed oxide surfaces in an aqueous environment.

5.3.2 Surface relaxation

Similarly as in the case of metals, the atomic layers at oxide surfaces tend to relax at surfaces and interfaces, i.e., the bonds to neighboring atoms expand or contract as compared to the bulk lattice. This relaxation depends on the oxidation state of surface species and the protonation of the surface and, thus, on the solution pH. The associated displacements from the bulk lattice positions are in the sub-angstrom range and can be easily resolved by surface X-ray diffraction measurements. Schlegel et al. applied X-ray reflectivity to probe the structure of quartz (100) and (101) surfaces in water.[312] The vertical relaxation of terminal oxygen was found to be as large as 0.4 Å, and the relaxation observed for atoms in deeper layers were decreasing quickly within a slab of 14 Å. A similar surface relaxation was observed on barite (001) and (210) surfaces, which showed a larger displacement of 0.4 Å for the outermost SO_4 ions.[313] In addition, the second and third SO_4 ion group was significantly rotated with respect to the surface normal direction by 8° and 19°, respectively. The relaxation of Ba ions is negligible (≈0.07 Å), and the relaxation extended to a much lower depth (≈3 Å) much smaller than that observed on quartz.[312] The solution chemistry can influence surface relaxation as well. Zhang et al. compared the relaxation of the rutile (110) surface in deionized water with that in Rb^+ solution at pH 12.[314] Interestingly, the surface Ti atoms are displaced from their bulk positions by up to 0.05 Å when exposed to deionized water, whereas this relaxation is largely suppressed in Rb^+ solution. Lee et al. studied by X-ray reflectivity the surface relaxation of the muscovite (001) surface in solutions containing different alkali ions, including Li^+, Na^+, K^+, Rb^+ and Cs^+.[315] They reported systematic trends in the vertical atomic displacements within a region up to 40 Å from the surface. These involved a general

<0.1 Å shift of the interlayer K^+ cations toward the interface and an expansion of the tetrahedral–octahedral–tetrahedral layers, except for the top layer in contact with the solution. This cation-dependent relaxation was found for the distortion of the top tetrahedral sheet as well as its tilting angle.

5.4 Adsorption on oxides and minerals

5.4.1 General aspects

In situ surface X-ray scattering methods have played a central role in determining the binding geometry of adsorbed species on oxide surfaces, which is considerably more complex than in the case of metal surfaces. On oxides, surface functional groups, namely under-coordinated oxygen species, are reactive surface sites responsible for a variety of interface reactions, including adsorption of surface complex species. In an aqueous solution, metal atoms at oxide surfaces are coordinated with aqueous O species (OH^-, H_2O, H_3O^+). Those groups are under-saturated, i.e., containing unoccupied orbitals that enable surface complexation reactions. In addition, lattice O atoms may be under-coordinated as well due to the presence of broken metal-O bonds at the surface, e.g., at surface defects. Consequently, surface complex species can be bound to different types of surface functional groups, giving rise to numerous binding configurations. Traditionally, surface binding is categorized into two large groups, inner-sphere (IS) and outer-sphere (OS) binding mode, which correspond to species in the inner and outer Helmholtz layer in electrochemical nomenclature.

In IS binding mode, the adsorbate forms at least one covalent bond with a surface O group, resulting in a comparably short distance of the complex from the surface. The binding configuration is then further distinguished by the number of formed covalent bonds to the surface. Common configurations are monodentate (MoD), bidentate (BD), tridentate (TD), and tetradentate (TeD) binding corresponding to adsorption via one, two, three, and four covalent bonds, respectively. Apart from the number of covalent bonds, the origin of the surface O species that are involved in the surface complexation reaction can be different. One distinguishes mononuclear (MN), binuclear (BN), and trinuclear (TN) surface complex species, depending on whether the complexing oxygen groups belong to the same structural motif in the oxide lattice, i.e., are coordinated to the same metal cation, or belong to two or three structural motifs, respectively. Furthermore, involved O atoms can share the edge or face of the same structural motif (called edge-sharing and face-sharing, respectively) or, on polynuclear complexes, binding O atoms can be located at the outer corners of the structural motifs (corner-sharing). In combination, these classifications are commonly used to describe the adsorption geometry of species that bind covalently to oxide surfaces.

In the OS binding mode, the adsorbate is surrounded by a complete coordination shell of oxygen species (OH^-, H_2O, H_3O^+) from the solution, and the complex species adsorbs through electrostatic attraction or hydrogen bonding. Accordingly, this binding mode is structurally less defined and the binding strength is sensitive to the surface net charge. Furthermore, OS complex species are located further away from the oxide surface and are described by a broader density distribution along the surface normal direction. In some high-resolution X-ray reflectivity studies,[316] it was found that OS species could be further classified into two sub-types according to the distance of the species from the substrate surface, namely adsorbed OS species and extended OS species. Adsorbed OS species are located directly above the substrate surface with one or two water layers confined between the surface complex species and the oxide surface. In contrast, the extended OS species is located further away, typically >1 nm from the surface, and exhibits a broader density distribution.

5.4.2 Metal cation adsorption

Cation complexation on oxide and mineral surfaces has been extensively addressed by *in situ*

SXRD methods. Here, we briefly summarize those studies, starting with calcite ($CaCO_3$), the most stable polymorph of calcium carbonate. Calcite is ubiquitous in natural water and has a significant impact on the environment due to its ability to buffer pH and scavenge trace metals. In SXRD studies, both As(IV)[317] and Pb(II)[318] were found to associate with the calcite (104) surface in an IS mode, where the cation adsorbate substitutes the structural Ca atoms (also called incorporation process). The bound Pb species were vertically displaced by 0.2 Å compared to the unrelaxed Ca positions, which was related to the larger size of Pb. In contrast, U(VI), which has a similar size as Pb(II), was found to not bind to calcite(104) through isomorphic substitution but via the formation of covalent bonds with O groups originating from surface carbonate groups.[319] Similar studies on barite($BaSO_4$) showed both Pb(II)[320] and Sr(II)[321] to be able to incorporate into the barite surface structure through substitution. Interestingly, in the case of Pb(II) on barite(001), these incorporated species were found to coexist with IS binding species and, at the highest Pb concentrations (200 μM), OS species.

Hematite (α-Fe2O3) is a common natural mineral as well as a widely studied material for electrochemical water oxidation.[325] It has a corundum-type structure and a hexagonal unit cell with two-thirds of the sites filled with Fe atoms. As mentioned in section 5.3.1, the r-cut hematite ($1\bar{1}02$) surface can be prepared with different types of surface terminations (Figure 24a), containing a mixture of different surface O groups. The adsorption of different metal cations on r-cut hematite has been studied using *in situ* X-ray reflectivity and X-ray standing wave (XSW) measurements. The associated binding structure was found to depend on the type of studied cation. Se(IV) was found to form a surface complex species via a bidentate binuclear binding.[326] XSW studies of arsenate adsorption on r-cut hematite suggested a bidentate bound As species, bridging two terminal O groups.[327]. In subsequent RAXS measurements, evidence of additional OS-bound species was also found (Figure 24b).[322] In detailed surface crystallographic studies, Qiu et al. investigated the Pb(II) binding mechanism on r-cut hematite ($1\bar{1}02$), treated by different procedures to prepare different types of surface termination.[323,328] The best fit of the CTRs was obtained by a structural model in which Pb(II) is bound in bidentate binuclear edge-sharing sites. On a half-layer terminated hematite surface two types of such sites were shown to be occupied (Figure 24c,d). In contrast, on a stoichiometrically terminated surface Pb(II) selectively binds to only a single type of these sites whereas the other site was not occupied. The latter was attributed to the structural mismatch between the binding species and the surface sites. The same group also investigated Sb(V) adsorption on a half-layer terminated hematite surface.[324] Here, the SXRD results indicated a tridentate binding structure that bridged two terminal O groups and another type of O group that is coordinated with two lattice Fe atoms (Figure 24e).

A key oxide system that has been studied extensively in the past is titanium dioxide, especially in the rutile structure.[329] Surface complexation of metal ions on the rutile (110) surface has been widely studied using surface X-ray diffraction. Rutile (110) has a well-defined surface structure with two alternating rows of oxygen atoms, one composed of terminal O groups binding to one Ti atom (^{I}O) and one in which the O atoms are coordinated by two adjacent Ti atoms (^{II}O). This configuration enables multiple binding modes, such as bidentate binuclear corner-sharing and tetradentate trinuclear corner-sharing/edge-sharing binding geometries. A comprehensive study of metal binding occurring at rutile (110) surface in contact with Rb^{+}, Sr^{2+}, Zn^{2+} and Y^{3+} solutions was conducted by Zhang et al. using a range of different techniques, including X-ray reflectivity and X-ray standing wave measurements, *ab initio* calculations, molecular dynamics simulations, and classical macroscopic surface sorption experiments.[330] The molecular structure derived from the X-ray data suggests that all cations are bound to rutile (110) via a tetradentate binding geometry which bridges four adjacent surface functional O groups, except for

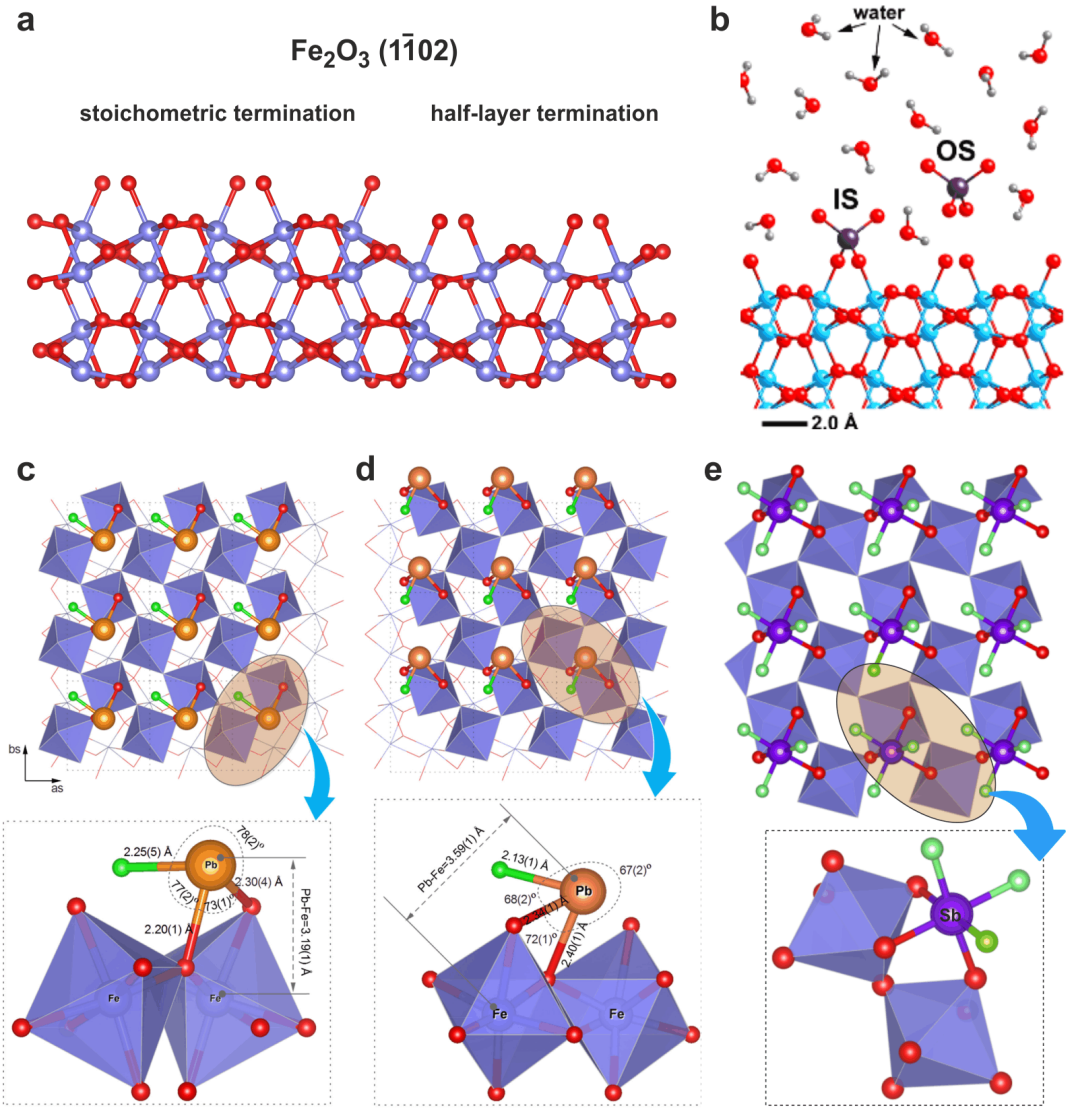

Figure 24: Adsorption of different species on the r-cut hematite (1$\bar{1}$02) surface. (a) Molecular structure of the hematite (1$\bar{1}$02) surface with stoichiometric and half-layer termination. (b) Simultaneous IS and OS binding geometry of As(V) on the stoichiometrically terminated surface (reprinted from Ref.[322]. Copyright 2008 Elsevier). Binding structures of Pb(II) on (c,d) half-layer terminated hematite (1$\bar{1}$02) at two different surface sites (reprinted from Ref.[323]. Copyright 2018 American Chemical Society). (e) Binding structure of Sb(V) on half-layer termination hematite (1$\bar{1}$02) (adapted from Ref.[324]. Copyright 2018 American Chemical Society)

Zn^{2+}, which dominantly adsorbs in a bidentate mode above two ^{II}O and, to a smaller extent, ^{I}O groups (Figure 25a). Similar results were reported by Predota et al., who studied the binding geometry of different ions (Rb^+, Na^+, Sr^{2+}, Zn^{2+}, Cl^-) by molecular dynamics simulations, X-ray standing waves and CTR measurements.[331] Also here, a bidentate geometry of Zn^{2+} was found, as opposed to the other cations which displayed a tetradentate binding configuration. The difference in the binding geometry observed for Zn^{2+} compared to the other cations was attributed to the difference in ionic radii of the studied cations (Figure 25b). Interestingly, a more recent work by Zhang et al. proposed Zn^{2+} to be bound in addition in a monodentate mode to a single ^{II}O group.[332] This study also showed that the pH (pH 8 and 6) has no effect on the adsorption geometry but favors the bidentate surface species at pH 6. The same group also studied the binding geometry of Rb^+ on rutile (110) in an alkaline solution at pH 12 and found the same binding mode as in earlier reports, *i.e.*, a tetradentate binding geometry.[314] Using RAXS, the adsorption heights of Rb^+ (3.72 $\pm$ 0.02 Å) and Sr^{2+} (3.05 $\pm$ 0.16 Å) relative to the first Ti layer was determined and identified as the average height of surface species with both bidentate and tetradentate binding modes.[333] Such a multi-site adsorption mechanism was not proposed in those studies mentioned above, and further work is necessary to reach a consensus on the metal binding mechanism at rutile (110) under different conditions.

Muscovite has been widely used as a model substrate for studying interfacial chemistry using surface X-ray diffraction techniques since it has a cleavable (001) surface that is atomically flat. The muscovite (001) surface has a fixed structural charge (0.34 C/m^2), independent of solution pH, and thus differs from the oxides described above, which carry a surface charge that depends on the protonation of surface functional groups and thus on solution pH. X-ray reflectivity studies on cation sorption on muscovite (001) were first performed by Park et al., who compared the binding geometry of Rb^+ and Sr^{2+} cations in pH 5.5 solution.[334] The structural modeling of these data suggested simultaneous IS and OS binding for Sr^{2+}, but only IS binding of Rb^+. However, in a later study also for Rb^+ an extended OS species at a distance of 7 Å was reported and attributed to a diffuse ion profile with a large vertical mobility.[315] In addition, the IS Sr^{2+} species was found to disappear upon decreasing the pH to 3.5.[335] Schlegel et al. investigated by XRR the adsorption geometry of K^+, Cs^+, Ca^{2+} and Ba^{2+}.[336] The derived electron density profiles revealed two solution layers adjacent to the muscovite surface, corresponding to IS surface complex species with a partial hydration shell and completely hydrated OS species. In a systematic *in situ* XRR study of the sorption behavior of alkali ions (Li^+ , Na^+ , K^+ , Rb^+ , Sr^{2+}) on muscovite (001), it was found that the speciation of adsorbed ion could be understood by the difference of the associated hydration energy of the alkali ions[315]. It was proposed that metal ions of smaller hydration energy (K^+ , Rb^+ , Sr^{2+}) tend to form IS species in which the hydration layer is partially replaced by surface oxygen, whereas for metal ions of larger hydration energy (Li^+ , Na^+) OS-binding geometry with an intact hydration shell energetically more favorable. Similar studies of divalent cations (Cu^{2+}, Zn^{2+}, Sr^{2+}, Hg^{2+}, Pb^{2+}) indicated a more complex adsorption geometry.[316] Here, the proposed binding configuration consists of an IS species, an adsorbed OS surface complex species close to the surface, and an extended OS complex species further away (Figure 25c). RAXS modeling allowed to determine the relative proportions of those three surface complexes species (Figure 25d). The results could be explained by the energy balance of cation hydration, interfacial hydration, and electrostatic attraction. The introduction of competing ions can alter the surface complexation speciation in different ways. For example, the introduction of NaCl background electrolyte does not alter the binding speciation of Y(III), which can be described by one IS species, one adsorbed OS species, and another extended OS species, but rather suppressed the surface overcharging.[337]. The influence of fulvic acid (FA) on the adsorption

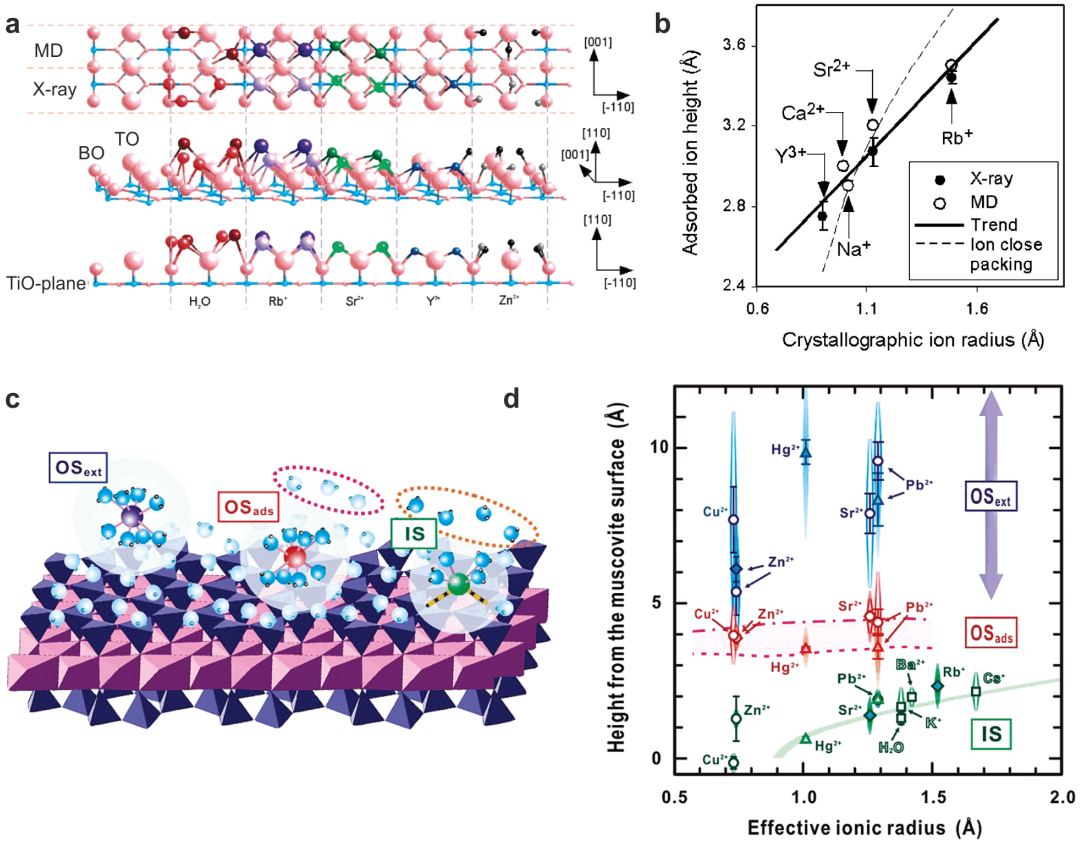

Figure 25: Systematic trends in cation sorption on oxides. (a) binding geometry of different cations on the rutile (110) surface, as obtained from SRXD measurements and MD simulations, and (b) corresponding dependence of the adsorbates' height over the TiO surface plane on the ion radius. (reprinted from Ref.[330]. Copyright 2004 American Chemical Society). (c) Schematic illustration of three surface binding species on muscovite (001), including IS species, adsorbed OS species, and extended OS species, and (d) relationship among measured heights of these complexes of divalent metal cations adsorbed at the muscovite (001)-water interface vs the effective ionic radius.(reprinted from Ref.[316]. Copyright 2004 American Chemical Society).

of Ba^{2+} [338], Hg^{2+} [339] and Sr^{2+} [340] on mucvovite (001) was investigated by Lee et al. by RAXS. FA was found to decreased the IS/OS ratio of Sr^{2+} surface species, suggesting the competitive adsorption of FA for IS binding sites. In the case of Ba^{2+}, the binding geometry, dominadomainsted by IS mode, is not affected by the presence of FA, if Ba^{2+} is premixed with FA before exposure to the muscovite surface. However, if muscovite is first exposed to FA first and then to Ba^{2+} solution, the IS Ba^{2+} species was found to be more broadly distributed and present also in the FA layer, suggesting an enhanced uptake of Ba^{2+} in the presence of FA. In contrast, in Hg solution premixed with FA the uptake of Hg^{2+} was enhanced and exhibited an additional broader distribution. The difference in competitive adsorption of Ba^{2+} and Hg^{2+} with FA may reflect the intrinsic difference in the binding strength of these cations on the muscovite (001) surface. In addition, surface-induced nanoparticle aggregation and accumulation, another surface-induced reaction on a charged oxide mineral surfaces, was commonly observed for tetravalent cations, such as Zr^{4+} [138,341] and numerous actinide ions (Pu^{4+}, Th^{4+}) [342–344]. It was proposed that nanoparticle aggregation starts with the oligomerization of simple structural monomers to form species of larger polymer structure, such as dimers, trimers, and tetramers, which then form nanoparticles. This nanoparticle aggregation mechanism was attributed to the presence of surface charges, as it should not occur in a pure solution system according to speciation predicted from the thermodynamic model.

Surface complexation of ions represents an important surface process on all mineral-fluid interfaces. The described studies by *in situ* SXRD methods showed the surface binding geometry to be determined by a range of different factors, such as cation hydration energy, surface charge, solution chemistry, and availability/reactivity of surface binding sites. Many of these factors are coupled and interrelated to each other, and thus defy up to now a uniform thermodynamic description of the heterogeneous surface adsorption process over a wide range of external conditions. Deeper insights into these complex issues will require systematic studies by a combination of different structure-sensitive and computational methods such as in the work of Zhang. [330] These complexation phenomena are also of high relevance in the context of electrocatalysis on oxide surfaces, where adsorbed species may significantly alter the catalyst activity. A well-known example of this is the strongly activating influence of small amounts of adsorbed Fe ion impurities on the oxygen evolution reaction on transition metal catalysts. [345] Future *in situ* SXRD studies may provide a structural basis for explaining this important phenomenon.

5.4.3 Interfacial water structures at oxide surface

The importance of interfacial water at the oxide surface has been realized for decades. *In situ* X-ray reflectivity studies allowed its structural characterization, showing that the interfacial water ordering depends on the surface chemistry of the studied substrate. As for other liquid interfaces, interfacial water forms a layered structure, consisting of one or two near-surface layers with strong structural ordering and subsequent quick decay of the layering within a few nanometers. The layered water structure typically has weak lateral structural order, but well-defined vertical positions. It manifests in the scattering along the surface-normal direction, as described in section 2.3.5, and thus can be probed by XRR. Pioneering XRR studies of the water structure on muscovite (001) surface were performed by Cheng et al. [346] In that work, the proposed water layering included a near-surface oscillatory region with a layer spacing matching the size of the water molecule and a more broadly distributed extended structure.

For some substrates, a water layering structure is not observed. Instead, adsorbed water species either directly bind to surface cations to complete their coordination shell or form H-bonds to surface oxygen groups, resulting in both lateral and vertical ordering. For example, the derived positions of bound water molecules on both barite (001) and (210) surfaces reacting with pure water are consistent with the satura-

tion of broken Ba-O bonds at the surface without additional water layering structures.[313] Recent CTR studies on barite (001) surface gave a more detailed picture of the water structure, revealing four distinct water species in addition to those required to complete the broken Ba-O bonds.[347] It should be noted that in the latter study, not pure water but a solution containing a mixture of different ions was used, including Ba^{2+}, Na^{+}, and $SO_4{}^{2-}$. Therefore, the observed difference may reflect an effect of the solution chemistry on interfacial water speciation. Different from barite, a single-layer water structure was found above quartz (100) and (101) surfaces[312] and on brushite (010).[348] From modeling of the reflectivity data and two non-specular CTRs, it was deduced that the deduced water layer only exhibits ordering in the vertical direction but no lateral ordering. Interestingly, the adsorbed water species on the rutile (110) surface exhibits both vertical and lateral ordering at three distinct sites, according to CTR measurements by Zhang et al.[314] Similarly, on calcite (104) surface the derived water structure has two interfacial water species at distinct heights of 2.3(1) Å and 3.5(2) Å without extended layering structure.[349] The derived water structure is consistent to that reported later in an X-ray reflectivity experiment[350]. A more extended water structure including two sites of adsorbed water and an additional layering was reported on the hematite (110) surface (Figure 26a,b).[351] The water structure on hematite (110) was compared to that on the $(1\bar{1}02)$ surfaces reported earlier by the same group (Figure 26c),[352] showing differences in the vibrational amplitudes or positional disorder of the adsorbed water molecules and in the average spacing of near-surface layered water. In that earlier work, Catalano et al. also studied the difference of the water structure on the $(1\bar{1}02)$ plane of two isostructural oxides (hematite and corundum). The obtained water structure is similar on the studied oxide surfaces, except for a less pronounced structural ordering on the hematite surface(Figure 26d). These studies highlight the importance of surface composition and structure on the induced interfacial water network. Subtle differences observed in the interfacial water structure may reflect different oxygen exchange rates from surface functional groups or the structural match of water adsorption sites on the terminated surface. Furthermore, Rao et al. studied by various *in situ* techniques the interface structure of (100),(101), and (110) RuO_2 surfaces in the context of electrochemical water splitting (see chapter 6.2.3).[353–356]

The interfacial water structure has an important influence on the surface complexation of foreign ions. A strong hydrogen bonding network will hamper the inner-sphere binding of ions, which requires breaking the hydrogen bonding network. For a charged surface, such as muscovite, the orientation of water dipoles affects the water polarization properties, which in turn can influence the transport of ions, biomolecular self-assembly, and surface chemical reactions. However, because H atoms are almost invisible to X-rays, a full picture of the water network at the surface is hard to achieve by XRD methods alone.

5.5 Liquid-liquid interfaces

Interfaces between immiscible liquids are particularly difficult to access by surface-sensitive probes. X-ray scattering techniques can provide unique insights into these interfaces, especially into the average structural arrangement along the surface-normal direction, which can be directly determined by XRR. Because of the three-phase boundary between the two liquids and the containment vessel induces curvature (see Figure 27a, inset), large sample diameters of several centimeters are required. Thus, the X-ray beam is strongly absorbed and the measurements are only possible with beams of high brilliance and high photon energies > 20 keV. Furthermore, specialized liquid surface diffractometers are required that allow to tilt the beam down on the liquid interface.[12,29]

The most well-known type of liquid-liquid interface in electrochemistry is the boundary between a liquid metal and a liquid electrolyte solution. This type of interface has historically been of great importance for developing a fundamental understanding of the electrochemical

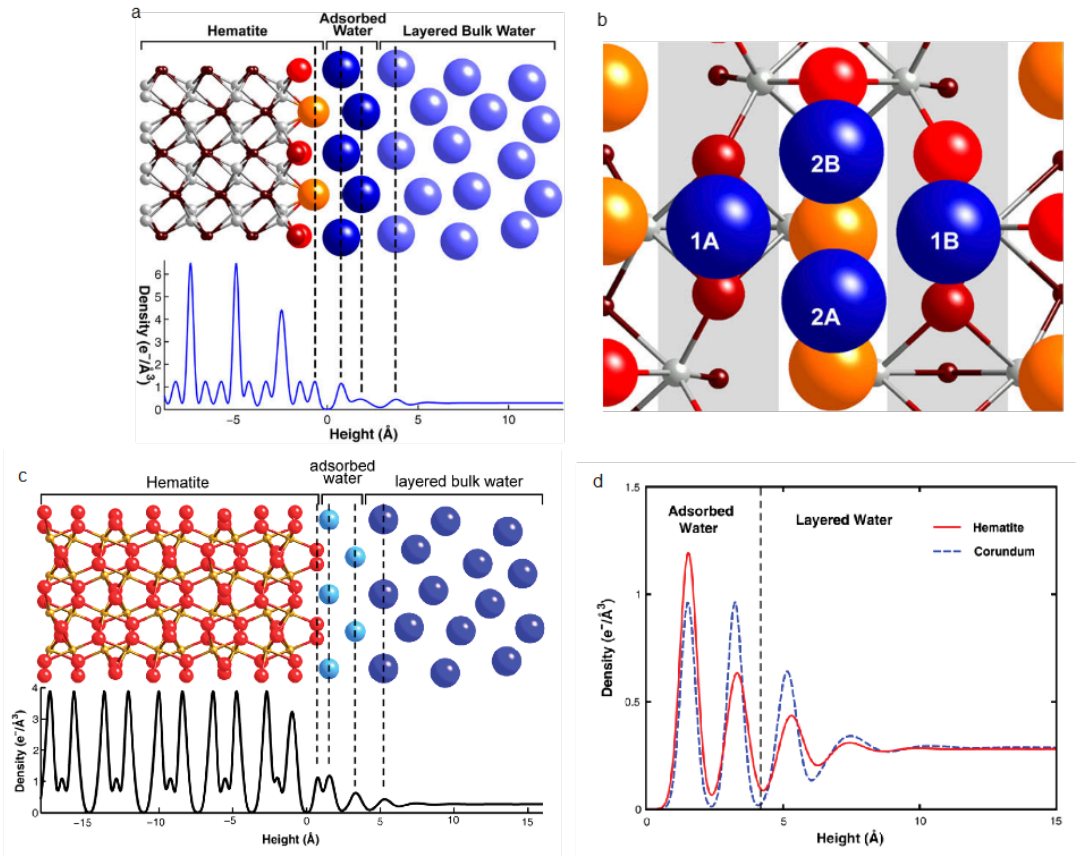

Figure 26: (a) Structural model and total electron density distribution of the hematite (110)-water interface and (b) corresponding molecular structure in a top view showing two specific adsorbed water species (Reprinted from Ref.[351]. Copyright 2009 by Elsevier). (c) Structural model and total electron density distribution of the hematite ($1\bar{1}02$)-water interface. (d) Comparison of water structures on the hematite and corundum ($1\bar{1}02$) surfaces (Reprinted from Ref.[352]. Copyright 2007 by Elsevier).

double layer structure, adsorption phenomena, and electroanalytical methods, but has recently received new interest because of applications in electrochemical materials synthesis,[357] materials processing,[358] and electrocatalysis.[359] The structure of liquid metal-electrolyte interfaces has first been determined by Elsen et al. for the case of liquid Hg, the most prominent liquid metal electrode, in NaF solution.[360] *In situ* XRR studies indicate a low surface roughness and a shallow peak at $q_z = 2.15\,\text{Å}^{-1}$, where the reflectivity increases above the Fresnel reflectivity (Figure 27a,b). This peak has been found before in studies of the Hg-vapor interface and results from an atomic layering in the Hg near the interface that exponentially decays into the bulk.[13] The corresponding electron density profile and interface structure is illustrated in Figure 27c. This type of structure was found over the entire double-layer potential range. Variations in the profile with potential could be explained by a combination of surface roughness, induced by electrocapillary effects, and changes in the intrinsic interface profile due to the electronic polarization at the liquid metal surface.[360] Later temperature-dependent studies allowed to separate these contributions in more detail and confirmed this picture.[361]

Surface layering has been shown to be a general property of liquid Hg and other liquid metals[362,363] and was also observed in other electrolytes, including electrolytes that contain chemisorbing species.[364–368] In the latter studies, also insight into the adlayer structure could be obtained. Specifically, measurements in solutions containing Pb and halide ions revealed the formation of salt-like layers at the interface,[365,368] similar to those observed on solid electrodes.[242,243,261] As an example, the electron density profile and interface structure of Hg in $PbBr_2$-containing NaF solution is shown in Figure 27d, where the formation of a defined layer of crystalline c-axis oriented PbFBr with a thickness of one unit cell was observed.[365]

A second class of liquid phase boundaries that have been studied by *in situ* XRR are interfaces between immiscible electrolyte solutions. Seminal studies of such interfaces were performed by Schlossman and coworkers, who investigated the ion distribution at the interface between water and nitrobenzene containing a common tetrabutylammonium cation.[369,370] They found clear deviations from the predictions of the classic Gouy-Chapman theory, but good agreement with MD simulations. In these initial experiments, the measurements were performed under open circuit conditions and the ion distribution was controlled via the concentration. Later studies analyzed the distribution as a function of potential and arrived at similar conclusions.[371–373] Together with DFT calculations, the obtained results revealed the role of ion–ion correlations and ion–solvent interactions in the structure of these interfaces. More recently, these studies were extended to interfaces between aqueous electrolytes and ionic liquids (IL).[374,375] Here, anion/cation multilayers were observed in the IL's near-surface region, an effect known also for the free surfaces of ILs and their interfaces to solids. The polarity of these layers was inverted upon changing the sign of the applied potential. Finally, also phospholipid monolayers at liquid-liquid interfaces were studied at variable potentials as a model for biomembranes and shown to be highly stable in the range of typical membrane potentials.[376]

6 Electrocatalysis

Driven by seminal results from model surfaces science which established activity descriptors of metallic surfaces for numerous reactions in the framework of the Sabatier principle[377,378], the development of commercial electrocatalysts follows a 'catalyst-by-design' approach, in which both catalysts activity and stability on the long-term are tailored by their crystallographic structure and chemistry[379]. In that framework, *operando* X-ray scattering methods are powerful tools for monitoring relationships between structure, activity, and stability in electrochemical environments. As detailed in the following, *operando* X-ray diffraction allows not only the identification of the active phase present in the system, which often differs from the as-prepared or post-reaction states observed in *ex situ* studies, but also enables tracking of the structural

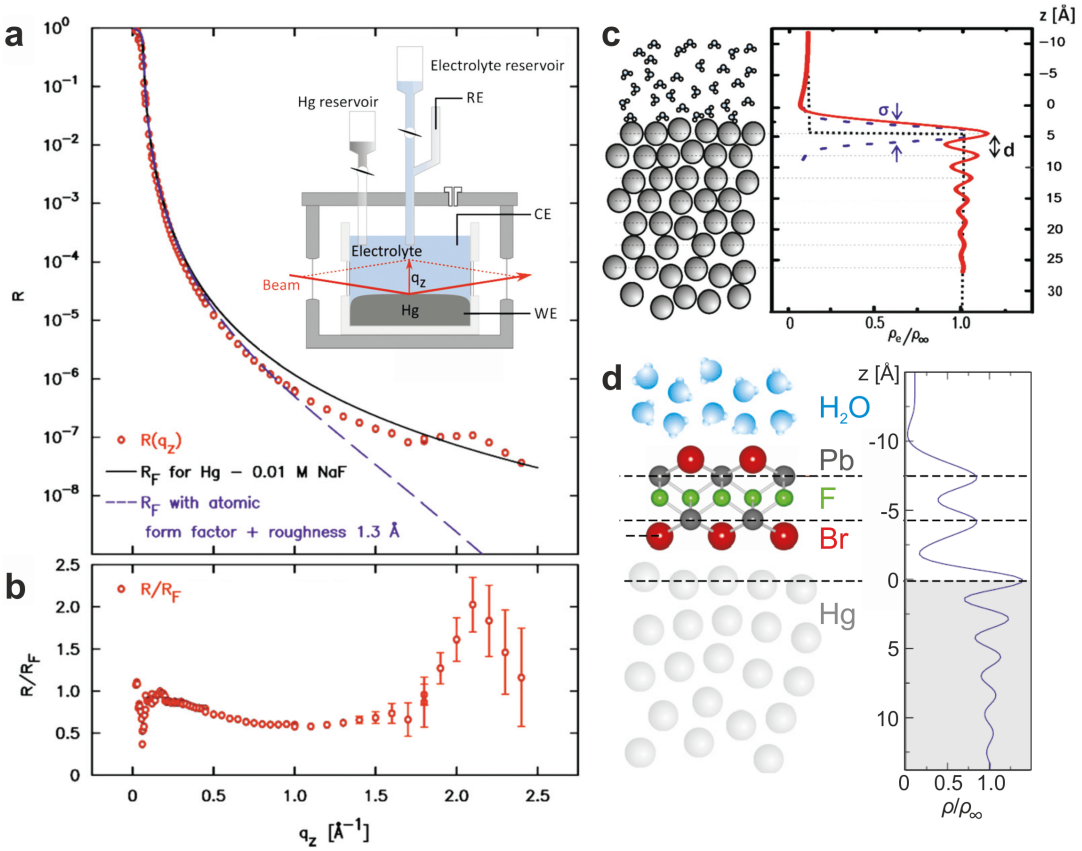

Figure 27: (a) X-ray reflectivity $R(q_z)$ of the interface between liquid Hg and 0.01 M NaF solution at 0.28 V above the pzc. For comparison, the Fresnel reflectivity of an ideally sharp interface and the reflectivity of an interface with a simple Gaussian density profile are shown. The inset presents a scheme of the experimental geometry. (b) Corresponding Fresnel-normalized reflectivity, showing the quasi-Bragg peak at $q_z = 2.15\,\text{Å}^{-1}$. (Adapted from Ref.[360]. Copyright 2010 American Physical Society) (c,d) Electron density profile and schematic presentation of (c) the Hg/NaF interface structure (Reprinted from Ref.[366]. Copyright 2016 Royal Chemical Society) and (d) the PbFBr adlayer formed at this interface in Br containing electrolyte (Adapted from Ref.[365]. Copyright 2013 National Academy of Sciences).

evolution during catalyst operation. This holds true for both single crystal model catalysts and nanoparticulate electrodes.

6.1 Hydrogen oxidation, evolution, and absorption

6.1.1 Hydrogen oxidation and evolution

Hydrogen oxidation (HOR) and hydrogen evolution (HER) are central electrochemical reactions and are commonly investigated due to their relevance to energy technologies, such as electrolysis and fuel cells. Platinum is typically used as an efficient catalyst for both HOR and HER , because of its unrivaled electrocatalytic performance. However, the high price and scarcity of Pt push research to find less noble alternative materials. Furthermore, whereas Pt is an excellent HER/HOR catalyst in acidic media, its activity in an alkaline solution is lower and depends on the cation species in the electrolyte. Tanaka et al. investigated this cation effect by *operando* SXRD studies of Pt(110) in Li^+ and Cs^+ containing solution.[231] They found that the (1×2) surface reconstruction remained stable during the HER, but that the interface structure on the solution side could substantially rearrange, dependent on the cation species. In Li^+ containing solution, the dense interfacial water layer was maintained, resulting in high activity, whereas the Cs^+ adsorbed in a bilayer on the Pt surface, which inhibited the HER. Chattot et al. systematically studied the structure of Pt nanoparticulate catalyst during HER in alkaline electrolyte[60]. Besides the change of lattice parameter due to the H_{UPD} before the onset of HER, no structural differences were observed at potentials in the HER regime.

Whereas the internal structure of platinum catalysts does not significantly change under HOR/HER reaction conditions, this is not the case for many non-noble catalysts. For the latter, reaction-induced phase transformations have been studied by *operando* XRD. In the case of Nickel based selenides, Zhai et al. showed that the original $NiSe_2$ cubic phase is rapidly transformed into the hexagonal NiSe phase in the first several hours of HER (Figure 28).[380] The formed NiSe phase has an enhanced catalytic activity and is the active phase under HER conditions. Theoretical calculations based on this observation suggested that the charge transfer from Se to Ni site during this phase transition leads to an increase in conductivity, shifting up the d-band center and overall enhancement of activity.

Multimodal *operando* characterization employing XRD was also used to determine the phase transformations of a phosphide-based bifunctional catalyst (CoP) for hydrogen/oxygen evolution.[381] Two catalysts, pristine and Fe-doped CoP, were studied. Upon polarization in an alkaline electrolyte, Fe-doped CoP retained its structure under HER conditions, whereas undoped CoP transformed first to a mixture of hydroxides and subsequently to an amorphous Co metal phase. This two-step transformation was found to be detrimental to catalytic activity.

Electroreduction of Iridium and Ruthenium oxides under HER conditions was thoroughly studied by XRD and SXRD on polycrystalline thermally prepared RuO_2 and IrO_2[382,383] and on ultrathin $RuO_2(110)/\,Ru(0001)$ and $IrO_2(110)/\,TiO_2(110)$ films[384–386] respectively. According to Pourbaix diagrams, both metals should first reduce to a hydroxide phase and then further reduce to their metallic phase under HER conditions[387]. The first step was confirmed in the basic environment (0.1M NaOH) by an early *in situ* SXRD study, where the formation of hydroxide on a $RuO_2(110)$ single crystal surface was clearly observed[388]. In acidic conditions, (0.5M H_2SO_4) the situation is not as obvious and polycrystalline RuO_2 is neither transformed to the corresponding hydroxide nor to the metallic phase. Instead, it undergoes lattice expansion at HER conditions, which was attributed to proton incorporation[383]. However, further experiments on ultrathin RuO_2 films provided clear evidence of a full transformation from Ru^{4+} oxide to Ru^0 via transformation of lattice oxygen to OH^- and water[384]. Even though IrO_2 should behave in a similar manner, it was shown to be very stable under reductive potentials, at least down to

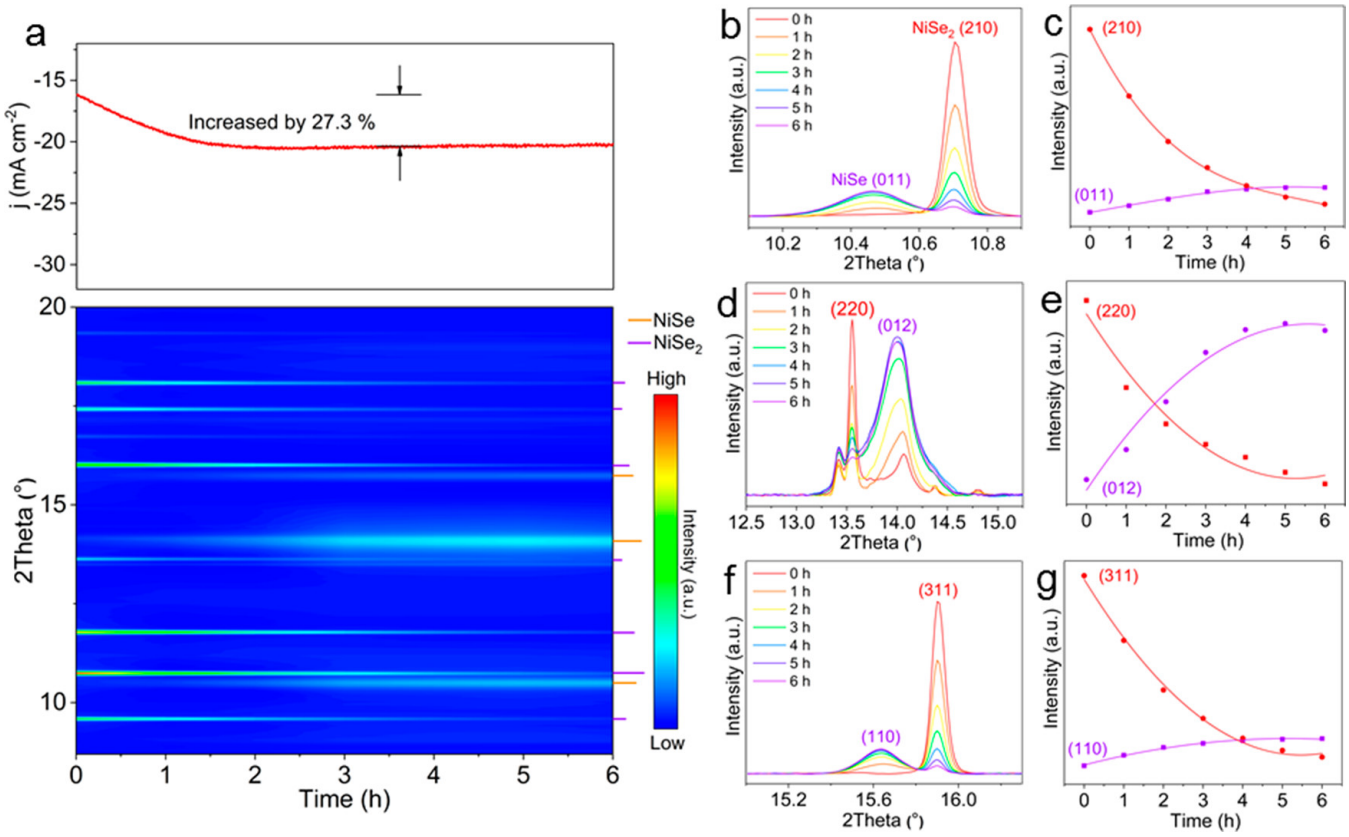

Figure 28: (a) Chronoamperometric curve of the $NiSe_2$ at -0.18 V for 6 h and the corresponding *operando* XRD patterns ($\lambda = 0.495\,47(1)$ Å). (b–g) Enlarged characteristic peaks of the $NiSe_2$ and NiSe phases and the corresponding intensity variations (Reprinted from Ref.[380]. Copyright 2020 American Chemical Society.

cathodic potentials of -1.2V vs. RHE. Studies using IrO_2(110) ultrathin layers found no evidence of swelling or loss of crystallinity under these conditions.[386] Such extraordinary stability of both polycrystalline RuO_2 and IrO_2(110) can be traced to a hindered kinetics of the reduction reaction. Such *operando* diffraction experiments play a prominent role in assessing the structural transformation of electrodes during HER and provide important insight into degradation mechanisms.

6.1.2 Electrochemical hydrogen loading of Pd

Beyond its excellent electrocatalytic properties for various fuel cell devices[389], the peculiar ability of Pd to absorb large volumetric quantities of hydrogen in the form of hydrides (PdH_x) enables its application in numerous other hydrogen technologies, such as hydrogen purification, storage, and detection[390]. In all cases, a detailed understanding of the physico-chemical parameters ruling the onset and amount of hydrogen insertion into Pd is pivotal to the further development of these applications. In the gas phase, it has been established for a long time that at low hydrogen partial pressure, H_2 molecules dissociate on the Pd surface and occupy the surface, subsurface, and octahedral interstitial lattice sites of the bulk.[391–394] As the hydrogen partial pressure is increased, the hydrogen content first increases in the Pd metal phase, referred as PdH_x-α. Below a critical temperature, a certain gas pressure can be reached at which the hydrogen chemical potential in the PdH_x-α phase equals the one of a PdH_x-β phase, thus triggering the phase transition. This phase transition manifests as a plateau in the pressure-composition isotherm. As the phase transition continues to the PdH_x-β phase, further increase in hydrogen partial pressure increases the hydrogen content in the PdH_x-β phase. Importantly, the existence of a microscopic energy barrier for the phase transition results in a hysteresis, and the phase transition from PdH_x-β to PdH_x-α occurs at lower hydrogen partial pressure.

Because this phase transition consists in a sharp lattice expansion of the Pd lattice, the latter is easily monitored by *in situ* and *operando* XRD techniques. Numerous studies investigated the hydrogen pressure-composition isotherms in the gas phase[395–398], where the hydrogen partial pressure controls the hydrogen chemical potential. Electrochemistry, however, represents a convenient and straightforward alternative to such an approach, as the chemical potential of hydrogen can be controlled by mild polarization of a Pd electrode. Thermodynamically, only about 100 mV polarization should induce hydrogen content in Pd equivalent to that obtained with pressures in the GPa range[399,400] at room temperature. The versatility of electrochemical hydrogen insertion opens an avenue to numerous applications for Pd, (including the highly controversial case of cold fusion[401]), but requires a better understanding of the enabled fast insertion dynamics in nanoparticulate Pd under an electrochemical environment, which makes adapted characterization methods necessary.

The electrochemical loading of Pd foil cathodes with deuterium and hydrogen in LiOH (H_2O) or water LiOD (D_2O) electrolytes, respectively, has been investigated *in situ* via energy dispersive X-ray diffraction by Felici *et al.*[402] and Knies *et al.*[403] The authors estimated the Pd loadings from its lattice parameter, measured by XRD, and the relationship between composition and lattice parameter at 77 K[404], which they extrapolated to room temperature. They demonstrated that this approach was more accurate than other *in situ* methods, such as the electrical resistance ratio measurement technique[405,406]. Moreover, they confirmed the possibility to reach a H:Pd ratio close to 1 at room temperature by electrochemical loading. However, the nature and temporal resolution ($>$ 5 min) of the energy-dispersive X-ray diffraction method employed did not allow to obtain mechanistic insights on the hydride formation. X-ray diffraction was also used by Jisrawi et al. to assign particular cathodic or anodic peaks in the adsorption and desorption of hydrogen to specific layers in thin film multilayered electrodes (Pd, Pd-capped Nb and Pd/Nb)[407]. These authors re-

ported an anisotropic lattice expansion along the *c*-axis, which was interpreted as a consequence of a film-substrate interaction. Using *in situ* surface X-ray diffraction, Ball and co-workers followed the morphology of electrochemically deposited Pd films on Pt(001) electrode surface in the presence of CO[198]. They reported the formation of larger Pd islands following a pseudomorphic Stranski–Krastanov (SK) growth. The effect of adsorbed CO was found to enhance hydrogen permeation into the Pd film only at low electrode potential below the H_{UPD} region. Similar SXRD studies were performed by Lebouin et al., who investigated the hydrogen insertion into a 3 ML thick electrodeposited Pd film on Pt(111)[408]. The results showed overall good reversibility of the insertion-desorption processes in the thin film. However, a high resistance to hydration of the two first atomic Pd layers closest to the Pt substrates was deduced from observed changes of the corresponding interlayer distances. The strong effect of the Pt(111) substrate thus explains the low H:Pd ratio that can be achieved in such films up to 14 MLs[409].

More recently, Benck et al.[400] used high-energy powder X-ray diffraction to investigate the electrochemical insertion of hydrogen into Pd foils and thin films via aqueous liquid, solid polymer and solid ceramic electrolytes. In their seminal contribution, the authors employed three different electrochemical cells for *operando* XRD, and provided important new insights on the H:Pd ratios possibly achieved in the different systems investigated. As shown in Figure 29a-b, they could reach a temporal resolution below 10 min for powder XRD pattern collection. However, the quality of the signal was highly dependent on the nature of the electrochemical cell. Importantly, using a collection of data from past literature, they proposed an updated calibration of the PdH_x-β lattice parameter (a) as a function of H:Pd ratio (c) at 25 °C and 1 atm (Figure 29c), namely $a[\text{Å}] = 3.9321 + 0.179 \cdot c \pm 0.0034$. Employing this calibration, Benck et al. showed that a H:Pd ratio in Pd thin films of up to 0.96 ± 0.02 could be obtained in room temperature aqueous 0.05 M H_2SO_4 at a cathode potential of -1.5 V *vs.* RHE. As shown in Figure 29d, faster insertion rates and shorter stabilization times were observed for thin films compared to thicker foils. Also, the liquid electrolyte was found to possibly produce higher H:Pd ratios than polymeric or ceramic electrolytes. In general, achieving a higher H:Pd ratio was found to be limited by competition with the hydrogen evolution reaction (HER) and electrochemical damage due to significant volume changes in the Pd layer during hydrogen absorption.

Using the recently upgraded Extremely Brilliant Source of the European Synchrotron Radiation Facility (ESRF-EBS, Grenoble, France), Chattot *et al.* investigated the mechanism of electrochemical hydrogen absorption in commercial carbon-supported Pd nanoparticles (Pd/C) in alkaline aqueous electrolyte (0.1 M NaOH)[60]. The unprecedented temporal resolution (333 ms) and signal-to-noise ratio achieved during these *operando* high energy powder X-ray diffraction experiments enabled the continuous recording of diffraction patterns during cyclic voltammograms and potential steps experiments (Figure 29e-f). This allowed capturing the transient core-shell mechanism of the PdH_x phase transition and showed that it involved supersaturated and undersaturated hydrogenated phases, in agreement with previous theoretical predictions and observations from the gas phase[394,396,397,410,411]. Finally, the onset and end potentials for hydride formation in various PdM alloys was found to depend on the second M metal in studies by Lee et al.[412]

6.2 Oxygen reduction and evolution

The oxygen reduction reaction (ORR) and the oxygen evolution reaction (OER) are undoubtedly the most studied electrocatalytic reactions in recent decades. These reactions have large overpotentials, which contribute significantly to the limited efficiency of electrolysers and fuel cells. To improve the kinetics, the elementary reaction mechanisms have to be understood, which requires knowledge of the atomic-scale interface structure of the electrocatalyst under reaction conditions. Furthermore, ORR

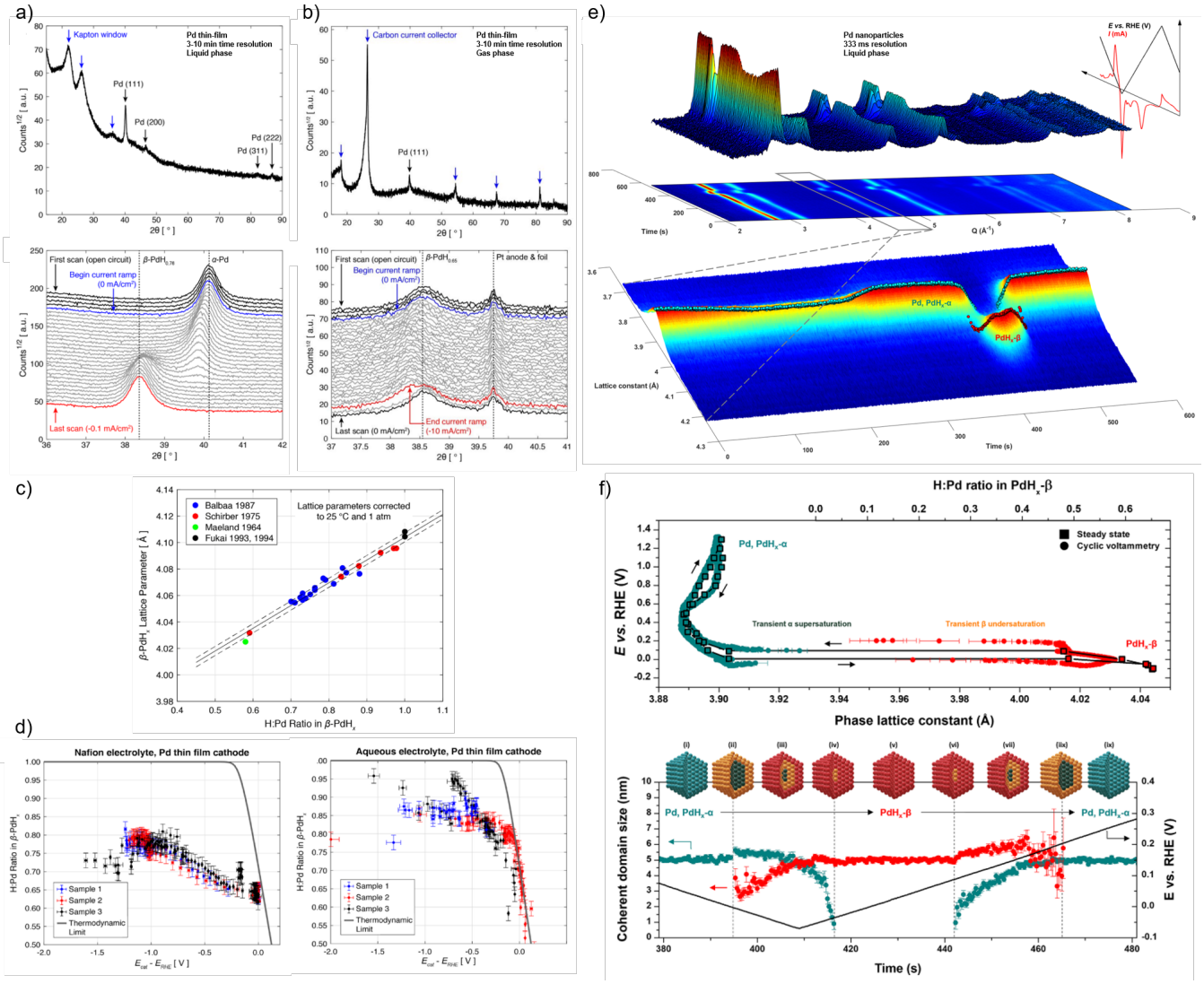

Figure 29: Understanding electrochemically-induced Pd hydride formation with *operando* XRD. Studies were performed on Pd thin-film cathode mounted in (a) an aqueous electrolyte cell and (b) a Nafion electrolyte cell. Shown are (top) representative XRD pattern and (bottom) the evolution during electrochemical H insertion. (c) Calibration of PdH_x lattice parameter vs H/Pd ratio and (d) PdH_x composition as a function of the cathode potential for Pd thin film in (left) Nafion and (right) aqueous electrolyte (Adapted from Ref.[400]. Copyright 2019 American Chemical Society). (e) 3D representation and corresponding 2D projection of WAXS patterns intensities recorded during Pd cyclic voltammetry experiment in N_2-purged 0.1 M NaOH electrolyte at room temperature. (f) (top) Change of the lattice constants during the PdH_x $\alpha \leftrightarrow \beta$ phase transition in the steady state (square symbols interpolated by black lines), measured after 60 s hold at various potentials, and during a cyclic voltammogram at 5 mV s^{-1} (circles) and (bottom) evolution of the coherent domain sizes as a function of time for the transition from the PdH_x α to the β phase and back during the cyclic voltammogram (adapted from Ref.[60]. Copyright 2021 American Chemical Society).

and, especially, OER occur at very positive potentials, i.e., under highly oxidizing conditions. This poses significant challenges for catalyst stability, which is a main issue for technological applications. Knowledge-based approaches to improve stability require insights into the precise mechanisms of electrocatalyst degradation and dissolution under ORR/OER conditions. *Operando* X-ray scattering methods played an important role in addressing these issues.

6.2.1 Platinum group metal based single crystals

In recent years, Pt electrochemical oxidation has received renewed interest, triggered by the relevance of this process for the stability of Pt-based oxygen reduction catalysts. Detailed studies by state-of-the-art *in situ* X-ray scattering techniques and *ab initio* theory provided an atomistic picture of the surface during oxidation and new insight into the elementary mechanisms of oxidation/reduction and its detailed connection to Pt dissolution. The basic understanding of the surface structure at potentials relevant to oxygen reduction and evolution for Pt(111) surface is depicted in Fig. 30, mostly determined by a combination of SXRD techniques with electrochemical measurements and DFT.[413] The relevant potential range for ORR and OER starts in the "butterfly" region, 0.60 to 0.95 V in the case of $HClO_4$, which consists of two parts: the sharp peaks at 0.80 V and the broader region leading up to them. The broad regions were associated with OH and H_2O adsorption into a transient disordered $p(2\times2)$ adlayer, while the sharp peaks are attributed to a phase transition into a $p(1\times1)$ phase.[281] These transitions are accompanied by Pt surface buckling.[282] In the case of H_2SO_4, the phase transition in the "butterfly" region is from disordered bidentate (bi)sulfate to an ordered $(\sqrt{3}\times\sqrt{7})$ overlayer of tridentate (bi)sulfate with coadsorbed water.[281] Most of this information has been found by careful analysis of CTR profiles acquired during *in situ* measurements, providing the exact position of substrate Pt atoms as well as adsorbate molecules.

The anodic peak at ≈1.06 V is traditionally assigned to the further oxidation of OH_{ads} to O_{ads}. However, first *in situ* SXRD measurements on the structure of the oxidized Pt(111) surface by You et al. showed that place exchange, in which a Pt surface atom exchanges with an oxygen species, occurs in the potential region of this peak.[147,414] In addition, early *in situ* RASXS experiments by the same group verified the oxidation of Pt surface atoms in this process.[415,416] The place exchange process is structurally reversible on Pt(111), i.e., cycling returns the Pt atoms to their original state, as evidenced by SXRD measurements. Thus, the voltammogram is stable for many cycles at typical sweep rates. The main structural motif responsible for this rather unusual behavior is the particular location of extracted (place-exchanged) atom (Pt_{ex}) on Pt(111) surface. For low Pt_{ex} coverages, this atom is located exactly above the vacancy, stabilized by three oxygen atoms adsorbed in close vicinity.[417] This stabilization allows Pt_{ex} atoms to return to the original position in the Pt lattice upon the subsequent reduction. This unusually stable atomic arrangement is also responsible for the overall stability of Pt(111) surface against dissolution, as shown by combined *operando* HESXRD and inductively coupled plasma mass spectrometry (ICP-MS) studies by Fuchs et al.[98] Furthermore, similar SXRD measurements performed in O_2 containing electrolyte did not show any major influence of O_2 presence on the place exchange process.[418]

Time-resolved studies of Pt(111) oxidation indicated a complex kinetics of Pt surface extraction with a fast initial process and a subsequent slower logarithmic growth law.[99,417,418] In addition, recent studies where SXRD data were obtained during voltamogramms at sweep rates up to 1000 mV/s indicated a very fast Pt_{ex} formation whereas the corresponding charge transfer in the O_{ads} peak was much slower.[100] This behavior suggests that the extraction is driven by the potential rather than the O_{ads} coverage, indicating fundamental differences of electrochemical oxidation as compared to oxidation in the gas phase. HESXRD studies employing very slow sweep rates to thermodynamically stabilize the surface structures showed

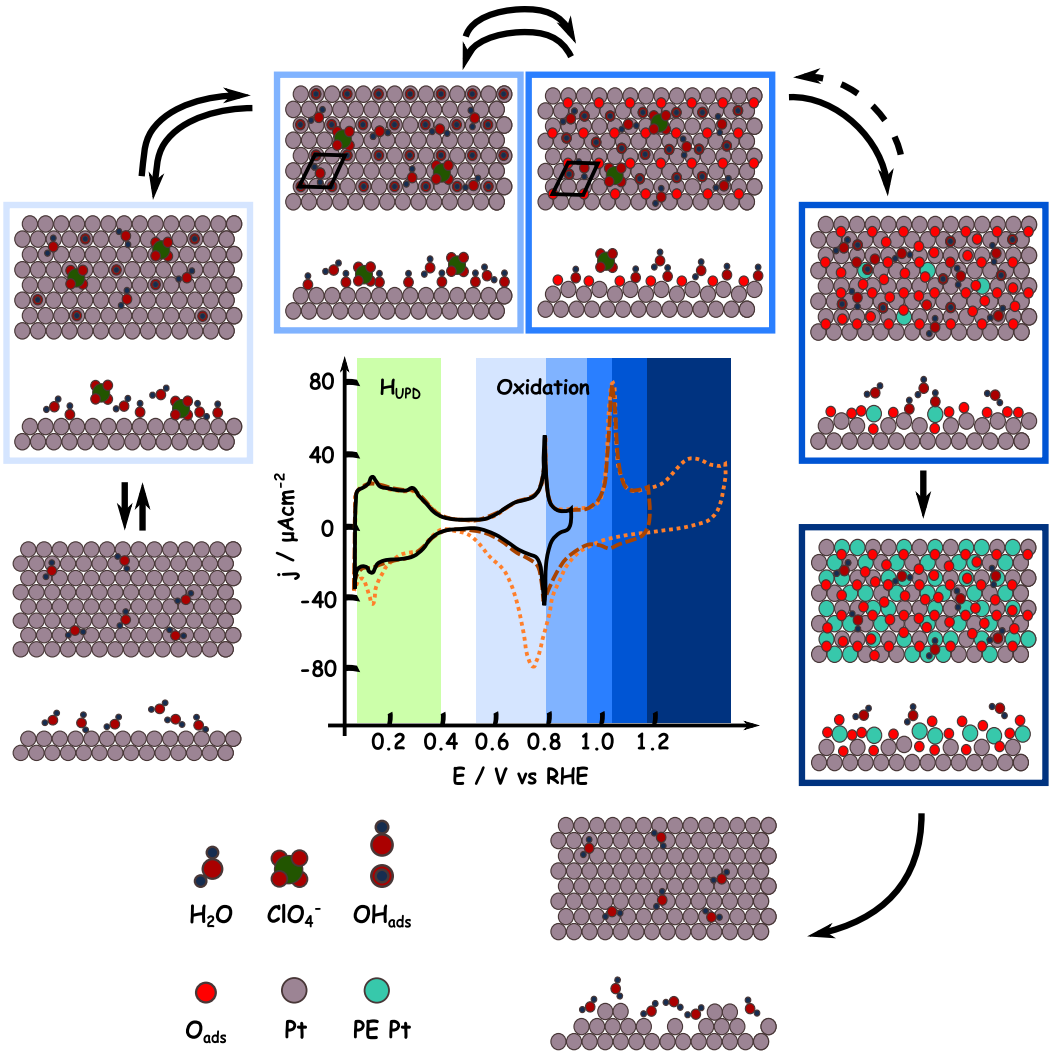

Figure 30: Typical cyclic voltammograms of Pt(111) in 0.1 M $HClO_4$ together with a schematic illustration of the atomic-scale surface structures in the different potential regions (Reproduced from Ref.[413]. Copyright 2017 by Elsevier).

that increasing the potential beyond the place exchange onset (>1.2 V) leads to the formation of a mixed oxide structure, where about 20% of atoms remain on the stable place exchanged sites, 30% occupy regular sites away from the original vacancy, and the remaining 50% are incorporated in the rather disordered oxide.[101] This severe restructuring of the surface leads to less stable arrangements, where Pt atoms are more prone to dissolution and surface migration during the reduction. The structural reordering of these less stable atoms induced by oxidation/reduction cycles was studied in detail by *in situ* GISAXS.[107,419] This approach allows quantitative characterization of the nanoscale surface morphology as a function of the upper potential limit and the number of cycles. The results indicate a continuous increase in the height of the nanoscale islands and an increasingly homogeneous island distribution with an increasing number of cycles, whereas the characteristic distances between the islands predominantly depend on the potential limit.

According to the combined *in situ* HESXRD and ICPMS studies, oxidation of the Pt(100) surface exhibits a strikingly different behavior.[98,99] In this case, cyclic voltammetry shows irreversible behavior from the very onset of the place exchange process and the surface degrades much faster at the potentials relevant to the oxygen reduction reaction. This rapid degradation is linked to the different place exchange mechanisms, where the oxide grows in rows along the main lattice directions and the O-stabilized Pt_{ex} are shifted by 1/2 of the unit cell distance from the corresponding vacancies. These rows cannot accommodate all the extracted atoms which leads to unstable Pt species on the surface and enhanced anodic dissolution (Figure 31). At potentials of $\geq$ 1.2 V, the coverage of this stripe-like oxide saturates and the amount of anodic dissolution starts to decrease again.[99] In parallel, a more disordered, second Pt oxide phase is observed that linearly increase in coverage with increasing oxidation potential and can be linked to the cathodic dissolution during oxide reduction.

The structure of bimetallic surfaces, and its relation to ORR catalysis, have also been thoroughly investigated by SXRD on model single crystal surfaces in the last decade. The studies on most relevant systems, such as Ni/Pt(111),[420,421] $Pt_3Co(111)$,[422],$Cu_3Pt(111)$,[423] Zn/Pt(111),[424], and Gd/Pt(111),[425] paint a similar picture. Independently of the initial surface composition and structure of the crystal, a Pt-skin evolves rapidly upon contact with the electrolyte. This skin is then the active surface for ORR and its electronic properties, which are significantly affected by the underlying alloy layer, determine the overall electrocatalyst activity.[420,423,425] The structure of the surface further changes upon cycling to oxidative potentials, similar to that of the Pt(111) surface, but in these cases, the transformation is mainly characterized by the surface roughening and the dissolution of the less noble metal. The thickness of the resulting skin depends strongly on the upper potential limit and the number of cycles.[423,425] Furthermore, the out-of-plane relaxation of the skin layer's uppermost atomic layer also changes with its thickness and the most active surfaces show compressive strain in this direction.[423,425] This effect can be explained by the weakening of surface OH bonding, which affects not only the electrocatalytic performance but also the stability of the surface through suppression of the oxide formation.[420]

6.2.2 Platinum group metal based nanoparticles

Platinum group metal (PGM)-based catalysts are extensively used in the most developed PEMFCs and water electrolyzer systems for hydrogen conversion and production. However, considering the price and scarcity of such materials (Pt, Pd, Ir, etc.), the viability of PEMFC systems relies on dramatic constraints in terms of PGM catalysts performance and stability. For both PEMFCs and electrolyzers, ensuring efficient and durable oxygen electrocatalysis is the current major bottleneck notably because of the poor reaction kinetics and highly corrosive environments. In this context, tuning the nanocatalysts structure, size, morphol-

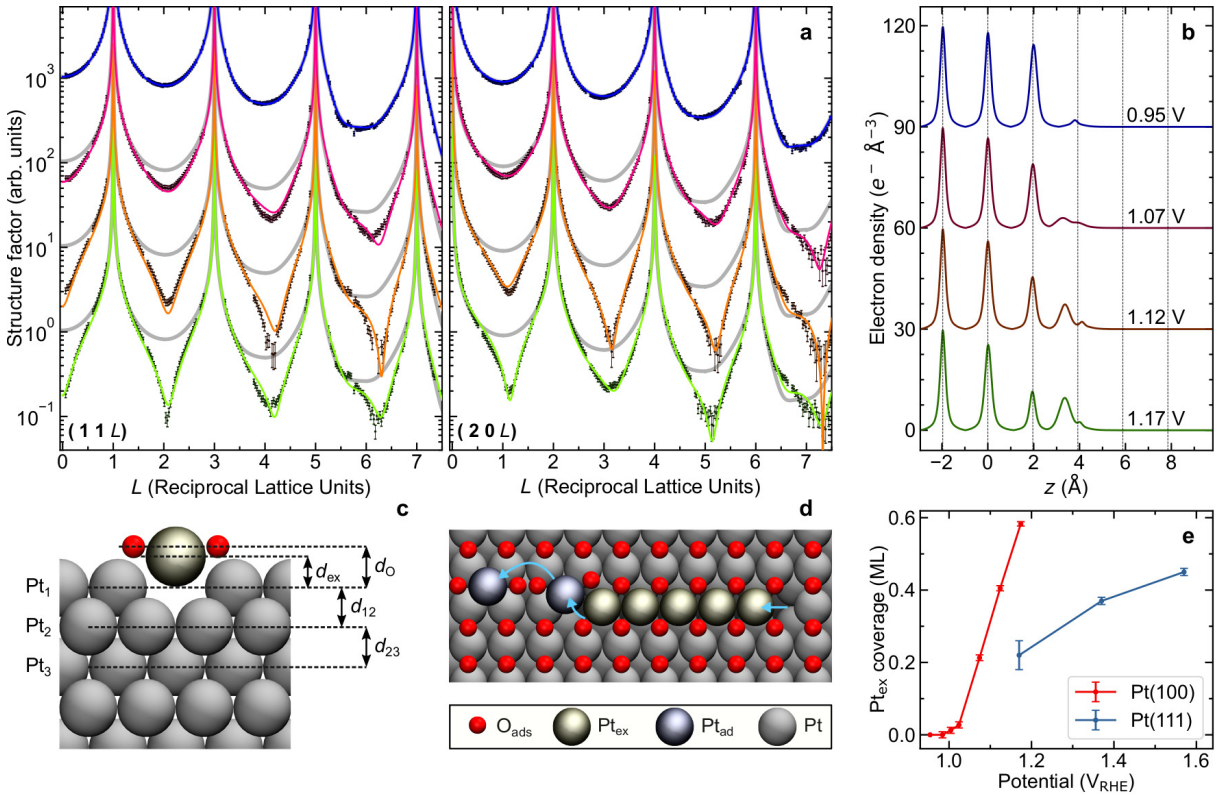

Figure 31: Atomic structure of the Pt(100) surface during electrochemical oxidation. (a) Two CTRs of Pt(100), obtained by *in situ* HESXRD measurements (68 keV) at different potentials. The best fit (coloured lines) and the CTR fits for the smooth surface at 0.95 V (grey line) are shown. (b) Corresponding electron density profile along the surface normal, obtained from the quantitative modeling of the CTRs. Bulk Pt lattice positions are indicated by dashed vertical lines. (c,d) Atomic arrangement of the extracted Pt atoms. (e) Potential-dependent coverage of extracted Pt surface atoms on oxidized Pt(100) and Pt(111) (Adapted with permission from Ref.[98]. Copyright 2020 Nature-Springer).

ogy, and chemistry are the main parameters to optimize their initial performance and long-term stability. As reviewed in the following, *operando* X-ray diffraction methods are powerful in monitoring such parameters successful implementation at the device level, also with their evolution during operation. Due to the powder nature of practical catalyst layers, powder X-ray diffraction-based techniques (WAXS, SAXS, PDF) are particularly suited.

A convenient metric of activity for PGM-based catalyst materials is the metal mass-normalized current density associated with a given reaction reported at application-relevant electrode potential. The mass activity can be seen as the product of the catalyst electrochemically active specific surface area (ECSA, in m^2 g_{PGM}^{-1}) and the surface-normalized current density (SA, in A m^{-2}). At fixed chemical composition, the ECSA is mostly a consequence of the catalyst particle size and morphology, which should aim at maximizing the atomic surface-to-volume ratio. Complementarily, at fixed particle size, the SA is mostly controlled by the surface fine structure and chemistry. As summarized in Figure 11, all those pivotal characteristics are more or less directly accessible from *operando* powder X-ray diffraction.

Implementing and maintaining the smallest particle size possible during operation is probably the most straightforward but still challenging approach to ensuring the long-term performance of heterogeneous catalyst materials. In fact, if the smallest nanoparticles feature the highest ECSA, they are particularly prone to dissolution in the environment of oxygen electrocatalysis[98,426–435] favoring the Oswald electrochemical ripening and redeposition processes[436–439]. In addition, corrosion of the carbon or metal oxide supports is known to favor nanoparticle motion, aggregation and coalescence[440]. In other words, nanoparticles' size increase is symptomatic of various degradation mechanisms, with a direct detrimental impact on the cell performance. Using anomalous small angle X-ray scattering (ASAXS) on commercial carbon-supported Pt nanoparticles mounted in an electrochemical liquid cell, Haubold et al. demonstrated during the late 1990ies the possibility of investigating Pt nanoparticle size distribution evolution *in situ*[441,442]. By combining *in situ* ASAXS and XANES, the authors showed the apparent size of oxidized Pt nanoparticle increases due to the formation of a 1 nm thick oxide shell at high electrode potential (1.1 V vs. Ag/AgCl compared to 0.25 V vs. Ag/AgCl in 1 M H_2SO_4). Complementarily, the method was shown to be powerful in separating the scattering of the nanoparticles from the porous carbon background scattering even at low Pt loadings (5 wt.%)[443]. If ASAXS allows the obtention of strong scattered signal from Pt, this is to the detriment of temporal resolution since each measurement must be performed at two distinct X-ray energies. In 2008, Smith et al. achieved high quality *in situ* SAXS of carbon-supported Pt nanoparticle in 0.1 M $HClO_4$ with 30 s temporal resolution[444]. This seminal work revealed the incomplete size dynamics reversibility during electrode cycling (Figure 32.a). The continuous size increase of the Pt nanoparticles even at the reduced state was interpreted as the first *in situ* observation of the Ostwald ripening process. From this point, ASAXS was extensively used (possibly in combination with XAS)[445] to monitor the particle size distribution evolution during accelerated stress test procedures (electrode potential cycling). In a liquid electrochemical cell, Gilbert et al. first evidenced the strong correlation existing between the maximum surface oxide coverage produced by different potential cycle profiles and the resulting particle size growth during ageing[20]. However, while constant potential holds at 1.0 or 1.1 V vs. RHE resulted in only minimal changes in Pt nanoparticles size, cycling to these same upper potential limits in a high-frequency fashion was shown to trigger significant particle growth. The fundamental role of Pt oxide formation and subsequent reduction in Pt dissolution and redeposition processes according to the place-exchange mechanism was further evidenced by means of on-line ICPMS[434]. The complementary effects of potential cycle profile[20], upper potential limit[446], particles' chemistry[447], particles' initial size distribution[448] or catalyst layer thickness[449] on the particles' size evolution were also investigated

with *in situ* SAXS.

If the nanoparticle size distribution derived from SAXS measurements meets the intuitive definition of particle size, such as those observed in the transmission electron microscope (TEM) images, another interesting parameter is the coherent domain size possibly obtained by WAXS. Contrary to the SAXS-derived size which is independent of the particle's crystallinity, WAXS only captures the characteristic size of the crystalline domains from the Bragg peaks broadening. One of the main advantages of the WAXS technique at high X-ray energy considering *in situ* studies is its ability to provide signal from the catalyst at high diffraction angle virtually free from the cell environment and background, with higher temporal resolution compared to SAXS. Contrary to the previously discussed SAXS observations, Sasaki et al.[450] showed the formation of the oxide shell during the potential step from 0.41 V vs. RHE to 1.51 V vs. RHE leads to a decrease of the coherent domain size of the Pt nanoparticles from 2.6 nm to 2.1 nm, thus demonstrating the amorphous nature of the as-formed Pt oxide layer (Figure 32.b). By combining WAXS and time-resolved quick scan X-ray absorption fine structure (QXAFS), Sekizawa et al., captured the key structural transformations kinetics of Pt nanoparticles in PEMFC during fast potential steps[452,453]. These authors evidenced the Pt oxidation process being composed of a quick Pt-O bond formation followed by subsequent slower subsurface events, such as the formation of subsurface oxygen leading to Pt crystal disordering[452]. Interestingly, the kinetics trends were found inversed during oxides reduction, with fast removal of subsurface oxygen and slow desorption of oxygenated species. Also using WAXS, Martens et al. later evidenced the scale factor (i.e. the intensity of scattered signal) a powerful descriptor of Pt oxidation in close relation with the particles' size but with better sensitivity[454]. Beyond the oxidation-dependent size dynamics, WAXS has also been extensively used to investigate the long-term stability of Pt-based catalysts in the environment of electrochemical cells. Taking the nanoparticles' coherent domain size increase as an indicator of catalyst degradation, the influence of the catalyst support material chemistry such as doped metal oxides[455–457] or carbon functionalization[458,459], the initial particles 'size distribution[448,449], the liquid vs. solid electrolyte[460], the upper potential limit during accelerated cycling[54], or the post-mortem cyclic voltammetry experiment[461] on the material stability were investigated by means of *in situ* WAXS.

The PDF can also provide insights on the size of the nanoparticles, by probing the longest atomic pair distribution distances. Compared to the ASAXS and WAXS approaches, the PDF combines the advantages of not being dependent on particle crystallinity nor the periodicity of their distribution on the support. *in situ* monitoring of the growth of Pt/C and various PtCo/C catalysts in PEMFC was successfully performed by Redmond et al, and the largest PtCo/C sample was found more resistant to particle growth among the different samples[462].

Finally, because the different X-ray scattering techniques can provide insights into the nanoparticles size evolution with some subtle differences in the definition of size, their comparison can be of high interest. For example, it was proposed by Martens et al. to compare the sizes obtained during simultaneous WAXS and SAXS *in situ* measurements. Because SAXS does not distinguish between aggregated (polycrystalline) or coalesced (single crystalline) nanoparticles but WAXS does, the distinct evolutions of the SAXS and WAXS sizes allowed the authors to decorrelate catalyst aggregation, ripening, and coalescence processes inside operating PEMFC[451] (Figure 32.c). Contrary to previous reports which used only one of these techniques, nanoparticle aggregation, and coalescence sequential steps during ageing were revealed as major causes for particles' size increase, likely more significant than the Oswald ripening process.

Nanostructured, or shape-controlled nanocatalysts are used in various fields of electrocatalysis as they feature highly desirable catalytic properties[463]. However, the as-implemented preferential-shape is subject to changes during catalysis long-term operation. Post mortem, *ex situ* TEM imaging is by far the most

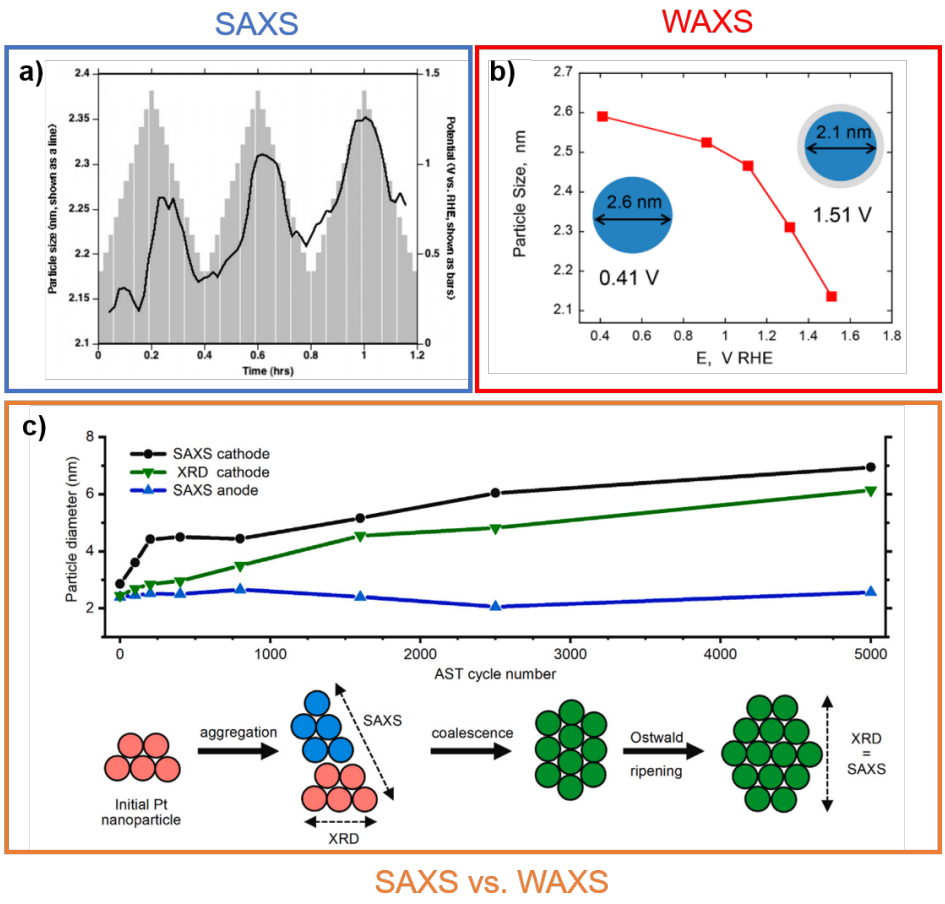

Figure 32: : Monitoring nanoparticles' size evolution during oxidation or long-term stability test using *in situ* (a) SAXS (Reprinted from Ref.[444]. Copyright 2008 American Chemical Society), (b) WAXS (Reprinted from Ref.[450]. Copyright 2016 American Chemical Society), and (c) combined SAXS and WAXS (Reprinted with permission from Ref.[451]. Copyright 2121 Elsevier).

powerful and widely used method to monitor such changes (albeit the development of ETEM)[464–469], but X-ray scattering methods can also provide valuable *operando* insights. While tracking nanoparticles' size from WAXS can be performed using simple anisotropic description of the particles (spherical shape), refinements of X-ray scattering data can also be performed by introducing anisotropy. Schmies et al. used this approach to better describe the anisotropic ellipsoidal shape of Pt nanocrystallites synthetized on various carbon or oxide support materials, and could correlate *in situ* the shape of the particles with their resistance to oxidation and dissolution[457]. A more versatile description of the particle shape is possible with SAXS. Using a model of hollow nanoparticles to fit SAXS data, Asset et al. could monitor *in situ* the shape evolution of hollow PtNi/C nanoparticles during mild and harsh accelerated stress tests[54]. The distinct evolution of the inner and outer diameters of the PtNi shell captured the partial collapse of the hollow structure, triggered by enhanced restructuring during the harsher test (upper potential limit of 1.1 V vs. RHE compared to 1.0 V vs. RHE). Following this study, Gommes developed a versatile stochastic model of dense or hollow nanoparticles to fit SAXS data, which was demonstrated to be powerful in capturing the morphological changes that occurr during accelerated stress testing of hollow PtNi/C catalyst in operating PEMFC[106].

The main advantage of X-ray scattering techniques is undoubtedly their ability to probe the nanoparticles' structure and (to some extent) chemistry, which controls their intrinsic catalytic properties. A particularly convenient and well-established structural descriptor of Pt-based catalysts activity is the lattice strain[463,470,471], easily accessible from XRD during *operando* measurements. Using WAXS, the lattice strain dynamics of Pt nanoparticles during oxidation were largely investigated[60,450,452,454,457,472], and it was generally observed that the Pt lattice expands during adsorption of oxygenated species, prior to the formation of Pt oxides. Consequently, the lattice strain was recognized as a parameter sensitive to the adsorption of electroactive species, providing fundamental insights on adsorbate surface coverage. Regrading Pt-based nanoalloys, the direct application of Vegard's law from lattice constant measurements during catalyst operation can inform on possible dealloying. Such an approach can be performed either in the reciprocal space by analysis of the Bragg peaks or in the real space from PDF analysis.

Asset et al. used the Rietveld refinement of *operando* WAXS patterns to track the progressive losses of both global and local strain in hollow PtNi/C catalysts caused by Ni leaching and restructuring during accelerated stress tests[54]. More recently, Hornberger used the same approach to investigate the stability of quaternary RhMo-doped PtNi/C octahedra nanocrystals[474]. The presence of Rh and Mo was found to enhance structural integrity of the particles by suppressing the migration of Pt surface atoms. In general, it can be stated that the reciprocal space analysis has been surprisingly underused in the field for *in situ* and *operando* studies of PGM materials in PEMFC than the real-space analysis (PDF). In fact, PDF analysis has been extensively used notably by Petkov, Chuan-Jian Zhong and coworkers. In 2018, these authors used high energy XRD coupled with PDF analysis to investigate the structural evolution of carbon-supported PdSn/C and PdNiCu/C nanoalloys of various compositions in an X-ray transparent PEMFC during electrochemical cycling[56]. This study nicely showcases the power of *operando* XRD technique, as combined *operando* insights on the sample-dependent crystal phase transitions (between orthorhombic, hexagonal and face-centered cubic PdSn) and strain relaxation in direct comparison with electrochemical performance in PEMFC were obtained (Figure 33.a-b). Whereas similar information could have been probably reached from Rietveld refinement of the WAXS patterns, Petkov later further exploited the capabilities of the PDF on trimetallic PtNiCo/C PEMFC cathode catalysts[473]. Using 'large box' models of various PtNiCo nanoparticles' type-structures (sandwich, janus, intermixed or core-shell) to fit the PDF data, it was possible to resolve the var-

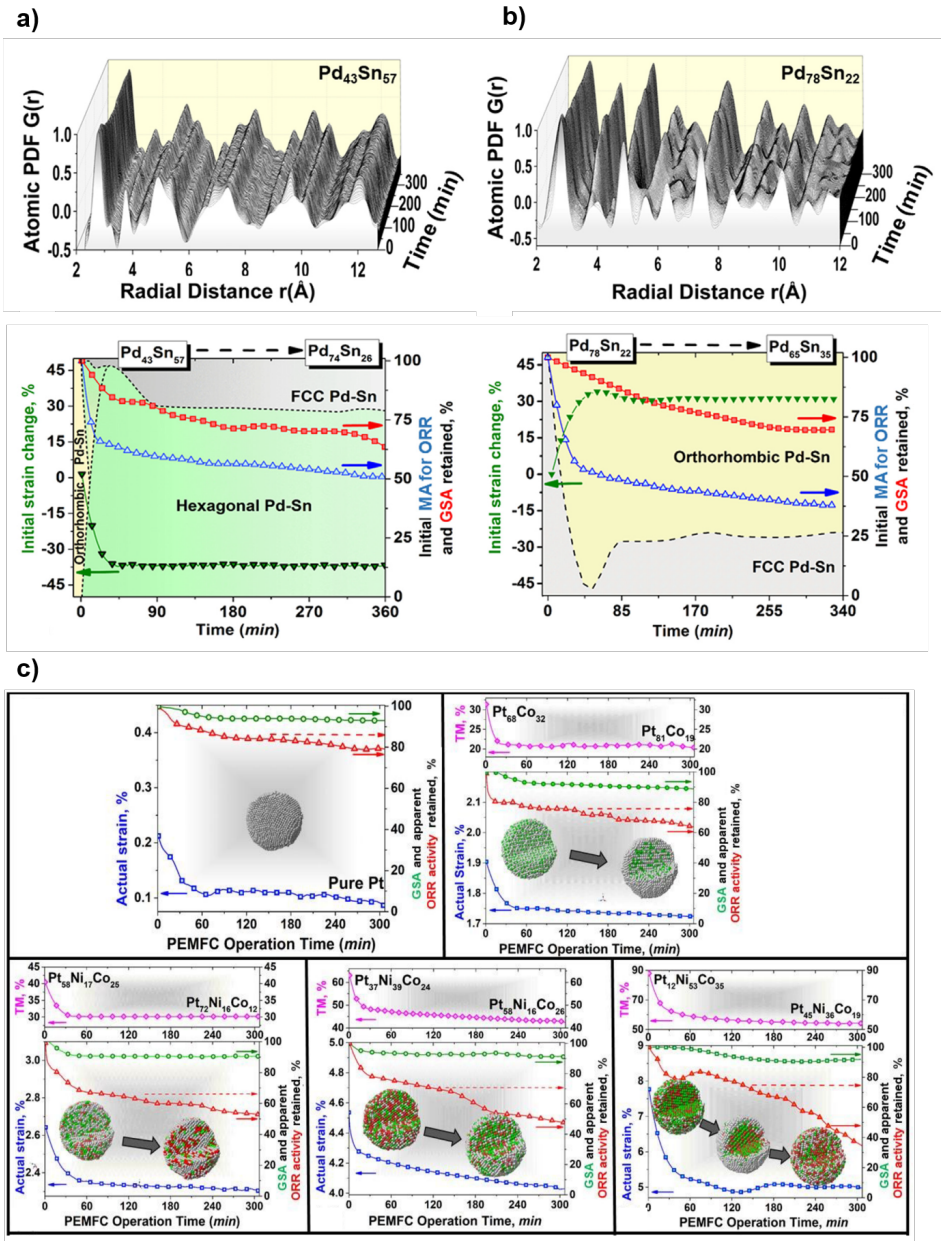

Figure 33: Probing the atomic scale structure of nanocatalysts during operation in PEM fuel cell by means of high energy X-ray diffraction coupled with PDF analysis. (Top) representative PDF curves and (bottom) color maps of the phase content of (a) $Pd_{43}Sn_{67}$ and (b) $Pd_{78}Sn_{22}$ alloy NPs vs time of electrochemical cycling; c) Evolution of the atomic-level, chemical composition, and apparent ORR activity for different nanoalloy catalysts deposited on the cathode of an operating PEMFC. Panels a-b are adapted with permission from Ref[56]. Copyright 2018 Elsevier. Panel c) is adapted with permission from Ref[473]. Copyright 2019 Royal Society of Chemistry.

ious particles' compositional profiles reached *in situ* during the segregation of the various metals during catalyst accelerate stress test (Figure 33.c). A similar approach was previously used for *post mortem*, ex situ analysis of PtNi/C catalysts[447]. More recently, Chuan-Jian Zhong's group applied this PDF approach to the investigation of PtFe nanowires[475] and PtPdCu/C[476] catalysts. Especially, in the case of PtPdCu/C, the authors introduced the concept of alloying-realloying, by probing the absence of pronounced segregation (maintaining the disordered homogeneous alloy) even after extended electrode cycling for this class of multimetallic materials. Very recently, Altan et al. used in situ electrochemical BCDI to probe the potential-dependent strain evolution of a single Pt nanoparticle in a liquid electrolyte. Their study directly maps the adsorbate-induced surface train field initiating at edge and corner sites and propagating toward the facets, thus providing important insights for the design of strain-engineered catalysts[477].

6.2.3 Ir and Ru oxide electrodes

Iridium and Ruthenium-based oxides are the best-performing materials for the oxygen evolution reaction in an acidic environment, and currently, there are no substitutes. In this respect, these materials have got substantial attention in recent decades, and our understanding of the activity/stability relationships improved considerably[387]. While RuO_2 is one of the most active of the known oxides in an acidic environment, stability is an issue. Contrary, IrO_2 is much less active but has better stability. Several studies concluded that the stability and activity of these materials are coupled: more active materials are typically less stable and vice-versa[429,478–480]. This spurred research into the structural aging of the catalysts using *operando* techniques, in which SXRD and XRD play a prominent role. The atomistic picture of the degradation process has been elucidated for both anodic and cathodic corrosion. The anodic corrosion was studied on a model $IrO_2(110)-RuO_2(110)/\,Ru(0001$ surface by Weber et al. using SXRD and XRR techniques[481]. The anodic corrosion for this system starts already at 1.48V vs. SHE via pitting through the $IrO_2(110)$ layer. Once the pits reach the $RuO_2(110)/\,Ru(0001$ interface, the corrosion is accelerated due to the low stability of both $RuO_2(110)$ and Ru(0001). In addition, evolving O_2 disrupts the cohesion of $IrO_2(110)$ leading to further degradation by lifting some of the weakly bonded $IrO_2(110)$ flakes. The residual $IrO_2(110)$ seems to remain stable up to 1.98V vs. SHE. To better understand the stability of $IrO_2(110)$, the thin film was also deposited directly on the $TiO_2(110)$ substrate to circumnavigate the problem of preferential $RuO_2(110)$ corrosion. Such $IrO_2(110)-TiO_2(110)$ films were studied in *operando* by high energy SXRD and XRR, and separately with supercritical fluid chromatography ICPMS[482]. The results unambiguously showed that such film is very stable (at least for 26 hrs) during galvanostatic hold in the OER range ($50\,mA/cm^{-2}$) and that indeed the instability of $RuO_2(110)$ is the main degradation pathway in $IrO_2(110)-RuO_2(110)/\,Ru(0001$ films (Figure 34 a). Interestingly, the dissolution rate seems to depend on the operation conditions: under steady-state conditions the film is more stable than under dynamic conditions (variable currents), pointing to the importance of catalyst design when a water electrolyzer is coupled with intermittent sources of energy. The SXRD and XRR measurements were also performed at lower X-ray energies (21.5 keV vs. 67.15 keV) for the same system[483]. In the studies at 21.5 keV, the researchers observed X-ray induced delamination of $IrO_2(110)$ film due to the detoriation of the $IrO_2(110)-TiO_2(110)$ interface (Figure 34 b). This serves as a reminder that damage induced by X-ray radiation can severely affect the outcome of the experiment and suitable condition for measurements have to be found prior to the experiment. The activity-stability relationship of high surface area IrO_2 at OER conditions was studied by Povia et al. using *operando* ASAXS and XAS techniques, probing both oxidation state and morphology changes[484]. In agreement with previous results, the lower oxidation extent of as-synthesized sample (IrO_2-AS)

correlated well with higher mass- and surface-specific activity when compared with the high-temperature treated sample (IrO_2−HT). On the other hand that was accompanied by lower stability. ASAXS measurement reveal that the IrO_2−AS sample is composed of less stable configurations of disk-shaped particles assembled in a 2D structure, causing the change of the ASAXS signal (Figure 34 c). In contrast, ASAXS studies of IrO_2−HT showed that the sample stays stable during the aging test, disclosing excellent mechanical stability. This work is an important step to understand the relative contributions of different degradation mechanism, in this case, morphological stability. Rao et al. studied the nature of the active site and the influence of their coordination on the activity of (100),(101) and (110) RuO_2 surfaces by surface scattering techniques[353–356]. Based on a combination of SXRD and DFT, they proposed specific adsorption sites of OOH species at different potentials in 0.1 M $HClO_4$ and elucidated the rate-determining step for each surface. However, some skepticism about the analysis of the SXRD data in this work renders the current interpretation open[387].

6.2.4 Fe, Co, and Ni oxide electrodes

First-row transition-metal oxides and (oxy)-hydroxydes containing Fe, Co, or Ni have been identified as promising OER catalysts in alkaline to neutral electrolytes, since they are earth-abundant, scalable, highly efficient, and stable without a serious degradation of catalytic performance.[485–489] Accordingly, extensive efforts have been devoted to study the OER mechanism on these catalysts. Because these material systems exhibit a rich potential and pH dependent structural phase behavior,[490] structural transformations under reaction conditions are likely. The atomic-scale composition and structure of the OER active phase at the catalysts' surface and the nature of the active sites is still controversially discussed and the subject of much current research. There is increasing evidence from *operando* scattering and spectroscopy studies that the as-prepared oxide materials (often denoted "pre-catalyst") is

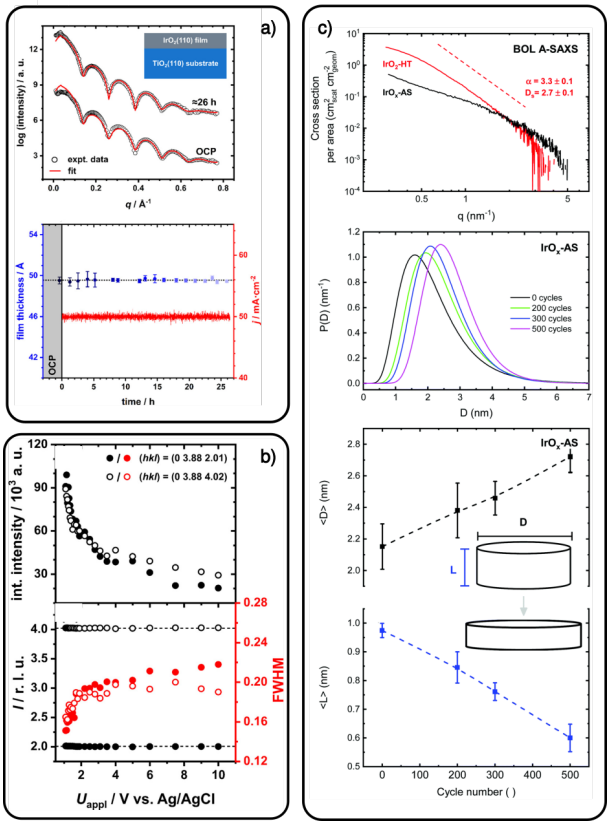

Figure 34: (a) Comparison of experimental (black hollow circles) and fitted (red lines) XRR data at OCP and after 26 h of galvanostatic hold at 50 mA cm^{-2}. Film thickness as derived by the fitting of the XRR data and applied current density as a function of polarization time (Adapted with permission from Ref.[482]. Copyright 2021 American Chemical Society). (b) Analysis of the IrO_2(110) Bragg reflections at (h, k, l) = (0, 3.88, 2.01) and (0, 3.88, 4.02): integrated intensities of the specified reflections as a function of the applied potential and the reflection positions and FWHM values. Adapted with permission from Ref.[483]. Copyright 2022 American Chemical Society. (c) BOL, *in situ* ASAXS curves obtained (at 1.0 V vs. RHE) on the IrOx-AS and IrO2-HT catalysts, diameter's log-normal distribution, the corresponding variation of the oxide disks' average diameter (<D>) and thickness (<L>) (Reproduced from Ref.[484]. Copyright 2019 by the Royal Society of Chemistry).

structurally transformed in a near-surface region due to chemical interaction with the electrolyte or the OER itself.[491,492] In contrast to the 2D-ordered surface reconstructions described in section 5, the phases formed by this restructuring are often amorphous or highly disordered.

A key example for the dynamic restructuring of iron-group metal oxides under OER conditions are Co oxides, which are the most active single-metal oxides of this class of materials. Especially Co_3O_4 has been addressed in several *operando* X-ray scattering studies, which allows comparing the merits of the different approaches. Bergmann et al. studied polycrystalline Co_3O_4 films in a neutral electrolyte by powder diffraction under grazing incidence angles.[491] Because of the employed thin layer cell, these studies were limited to potentials in the double layer range up to the onset of the OER. At the most positive potential, a broadening of the Co_3O_4 Bragg peaks was observed, which indicated a decrease in the average crystal size by $\approx$ 1 nm, followed by a reversal of his broadening in diffractograms recorded *ex situ* after the OER (Figure 35a,b). Based on these changes and corresponding variations in complementary X-ray adsorption spectroscopy data, the authors concluded that the OER induces a reversible and highly dynamical structural transition of the near-surface region, where an amorphous Co (oxy)hydroxide skin layer without long-range ordering is formed. In parallel to this work, similar grazing incidence powder diffraction studies in neutral and alkaline electrolytes were performed by Tung et al., who employed as samples cubic Co_3O_4 nanoparticles with (100) surfaces, which were coated by an $\approx$ 1 nm thin epitaxial layer of CoO with (100) orientation and were supported on a fluorine-doped tin oxide substrate (Figure 35c,d).[493] At the onset of the OER, new peaks that were assigned to β-CoOOH and, at somewhat higher potentials, a further α-CoOOH phase was observed. Although the ultrathin CoO surface layer could not be detected by XRD, it was proposed that it was reversibly transformed into CoOOH under OER conditions. The authors did not analyze the coherent crystal size, but the large intensity of the CoOOH peaks suggests that the average thickness of these phases clearly exceeds that of the original CoO layer. These measurements were performed up to currents of 30 $mAcm^{-2}$, which required high overpotentials, because of the high ohmic drop within the thin layer geometry. Similar *in situ* XRD measurements were performed by Wang et al. on calcinated Co_3O_4,[494] but in this case, no new crystal phases were detected.

More recently, *operando* X-ray diffraction studies of the oxide's structural transformation were performed using thin epitaxial Co oxide films with well-defined orientation on metal single crystals ((Figure 35g)).[53,495] The use of such model systems has several advantages. First, the roughness of these highly planar samples is small, i.e., the ECSA is close to the geometric electrode area, and the oxide film has a defined surface orientation. Second, all oxide crystallites have the same macroscopic lattice orientation. For this reason, their Bragg peaks are located at identical locations in reciprocal space, rather than on the surface of a sphere as in powder diffraction. This provides a gain in scattered X-ray intensity of several orders of magnitude, which allows structural studies with $\leq$ 1 s time resolution (as compared to $\approx$ 1 min in the powder diffraction studies[493]). Furthermore, the defined reciprocal space location allows easy separation of the oxide peaks from the isotropic background scattering of the electrolyte and the sample environment. The measurements therefore can tolerate the higher background, which are concomitant with the use of transmission cells as in Figure 8b. Such cells enable studies under extensive gas evolution conditions, i.e., deep into the OER regime, as well as simultaneous high-quality measurements of current density and XRD scattering, which allows direct correlation of the electrochemical and X-ray data.

Reikowski et al. applied this approach to *operando* studies of well-defined epitaxial Co_3O_4(111) and CoOOH(001) thin film model catalysts in 0.1 M NaOH under OER conditions.[53] There, changes in the position and width of one of the oxide's Bragg peaks were continuously imaged with a 2D detector as il-

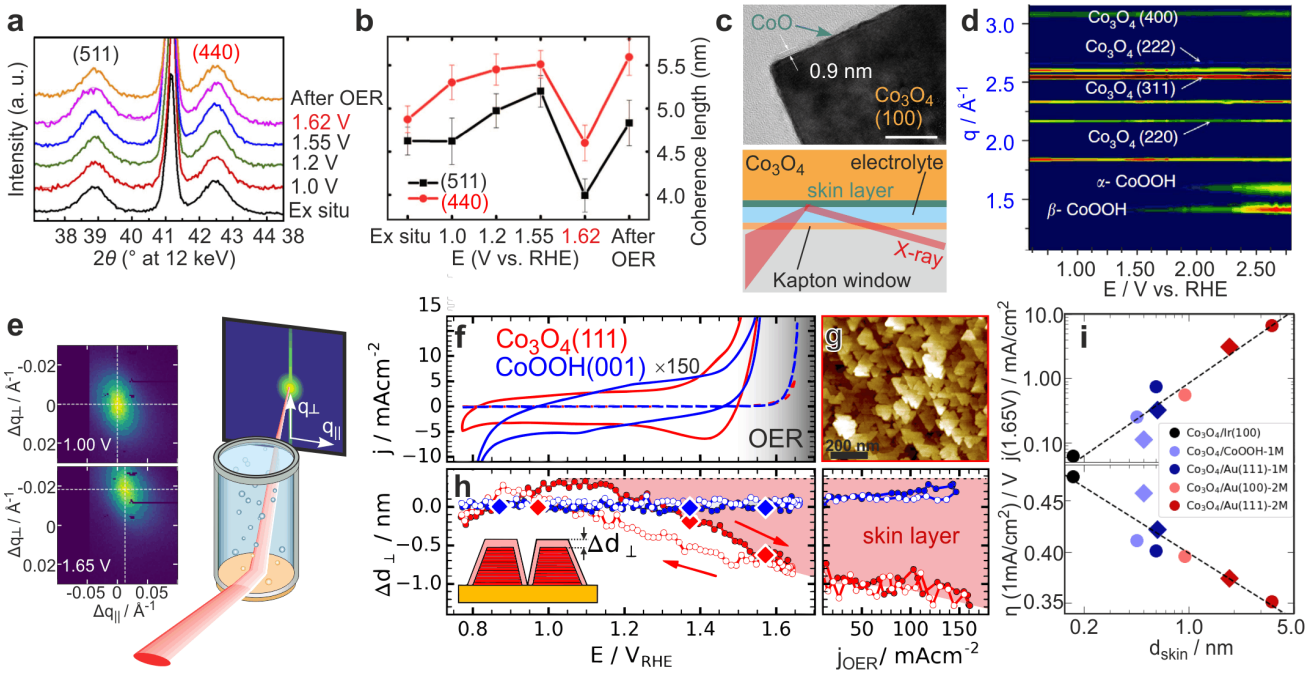

Figure 35: *Operando* X-ray scattering studies of Co_3O_4 OER catalysts. (a) Powder diffraction data of polycrystalline Co_3O_4 and (b) corresponding coherence length at potentials in the pre-OER range and at 1.62 V, above the onset of the OER, showing a reversible decrease in Co_3O_4 crystal size (Reproduced from Ref.[491]. Copyright 2015 Springer Nature). (c,d) GIXRD studies of cubic (100)-terminated Co_3O_4 nanoparticles that are coated by an ultrathin CoO layer in 0.5 M KOH. Shown are (c) a TEM image of the nanoparticle structure (scale bar 10 nm) and the scattering geometry as well as (d) the diffraction data, which reveals the emergence of CoOOH phases at the onset of the OER (Reproduced from Ref.[493]. Copyright 2015 Springer Nature). (e-i) *Operando* SXRD studies of epitaxial Co oxide thin films. (e) Scattering geometry and 2D detector images of the Co_3O_4(440) Bragg peak at 1.00 and 1.65 V vs. RHE. (f) CVs and (h) corresponding vertical grain size change of electrodeposited Co_3O_4(111) (red) and CoOOH(001) films (blue) on Au(111) in 0.1 M NaOH, showing the formation of a skin layer on Co_3O_4 (indicated by pink shading). (g) AFM image of the Co_3O_4(111) film (Reproduced from Ref.[53]. Copyright 2019 American Chemical Society). (i) Correlation between average skin layer thickness and OER activity, obtained on 5 different types of epitaxial Co_3O_4(111) films. (Reproduced from Ref.[495]. Copyright 2022 American Chemical Society).

lustrated in Figure 35e. These changes provide data on changes in lattice strain and average coherent width of the oxide film's grains, with changes in vertical and lateral direction corresponding to structural changes normal to and within the surface plane. By this method, the oxide structure could be monitored during cyclic voltammograms into the OER regime (Figure 35f). The obtained data indicate a profoundly different behavior of the two types of catalysts (Figure 35h). The CoOOH samples were perfectly stable during potential cycles into the OER regime. In contrast, the studies of Co_3O_4 films confirmed the reversible formation of (sub-)nanometer thick skin layers with an amorphous structure, reported by Bergmann et al.,[491] and showed that it is accompanied by a contraction of the remaining Co_3O_4 lattice. However, the higher time resolution allowed to verify that this transformation of the oxide surface already started at a potential well before the OER onset, indicating that the skin layer forms because of the intrinsic Co redox chemistry rather than a product related to the OER process, and demonstrated a fast reversible back-transformation in the cathodic potential sweep. Furthermore, the employed transmission cell allowed to extend these studies to high OER current densities (Figure 35h, right panel), revealing a continuous thickening of the surface skin layer.

Employing the same strategy, Wiegmann et al. recently performed more systematic studies of a variety of epitaxial $Co_3O_4(111)$ films, prepared by electrodeposition or physical vapor deposition on different single crystal substrates.[495] Despite the identical oxide lattice structure, the deposit morphology and the extent of skin layer formation differed on these samples. By correlating the simultaneously obtained structural and electrochemical data, a clear scaling of the OER activity with the effective skin layer thickness could be shown. This indicates that the entire skin layer is a 3D OER-active region.

Similar structural transformations were also found in X-ray diffraction studies of other Fe, Co, and Ni-containing oxides. Hsu et al. performed *in situ* powder diffraction studies of ferrite nanocubes (MFe_2O_4 with M = Fe, Co, Ni, Zn) in alkaline electrolyte.[496] On the highly active $CoFe_2O_4$ and $NiFe_2O_4$ catalysts the formation of new phases was observed near the onset of the OER, which were assigned to oxyhydroxides of Co and Ni, respectively. In contrast, no additional phases were found for Fe_3O_4 and $ZnFe_2O_4$ up to potentials high in the OER range, together with a lower OER activity. These observations suggest that the formed oxyhydroxide phases are active phases in the OER. Furthermore, similar XRD measurements found a structural phase transformation and high OER current densities in $CoCr_2O_4$ but not in $ZnCo_2O_4$, indicating that phase transformations involving the divalent Co^{2+} ions have an important influence on the OER activity. The same group also studied Co and CoFe phosphides and found first conversion into crystalline $Co(OH)_2$ upon immersion into the KOH electrolyte, followed by a gradual transformation into an amorphous state near the onset of the OER.[381]

Strong evidence for dynamic restructuring of the near-surface region into an amorphous interphase has been also found for perovskites, another important class of OER catalyst in alkaline and neutral media.[497–502] In many cases, this restructuring results in thin transition metal oxide layers, which constitute the actual catalyst. As an example, Wan et al. reported the irreversible amorphization of a 2.3 nm thick region at the surface of $SrIrO_3$ films during cycling into the OER range, using *ex situ* XRR, CTR measurements, and complementary X-ray absorption spectroscopy.[502] Detailed *operando* X-ray scattering studies of these structural transitions are still missing, however.

Studies of single crystalline model electrocatalysts of Fe, Co, and Ni oxides are largely lacking. Many of these oxides have a limited electric conductivity, which impedes the use of large bulk crystals. A notable exemption is magnetite(Fe_3O_4), which is sufficiently metallic for electrochemical studies. Although the OER activity of magnetite is moderate, it exhibits the inverted spinel crystal structure found also in other more active phases. A first *operando*

SXRD study of the OER on magnetite was performed by Grumelli et al., who investigated UHV-prepared $Fe_3O_4(100)$ by GIXRD.[309] Interestingly, the $(\sqrt{2} \times \sqrt{2})R45\,\mathrm{deg}$ reconstruction of this surface was found to be moderately stable at potentials deep in the OER regime, showing that this system is highly suitable for studying the OER reaction at a highly defined transition metal surface.

6.3 Other electrocatalytic reactions

6.3.1 Electrochemical reduction of CO and CO_2

The electrochemistry of the carbon monoxide reduction reaction (CORR) and the carbon dioxide reduction reaction(CO_2RR) has become a subject of great current interest, as it may enable direct electrochemical formation of valuable chemical compounds by a one-step electrolysis process.[503,504] Most of the research in this area focuses on copper and copper alloys, which have the unique capability to reduce CO_2 to multi-carbon products. A key challenge here is to identify parameters that steer the reaction toward specific products. It was found that the reactivity and selectivity of CO_2RR strongly depend on the catalyst material, on the interface structure and composition, and on the catalyst's nanoscale morphology.[505]

Particularly strongly debated has been the question of whether, despite the very negative potentials, Cu oxides and subsurface oxygen species are present on the electrode under reduction conditions and whether these influence the catalytic reactions. *In situ* GIXRD studies of CORR on polycrystalline Cu electrodes in CO-saturated 0.1 M KOH indicated a full reduction of Cu_2O surface oxide at potentials below 0.3 V vs RHE as well as evidence for the formation of Cu(100) facets.[506] Similar studies in 0.1 M $KHCO_3$ provided very similar results and showed that Cu faceting occurs only in the presence of CO_2 but not in Ar-saturated solution.[507] Furthermore, the ratio of the Cu(100) to the Cu(111) Bragg peak increased with more negative potentials, indicating an increasing tendency towards faceting. *Operando* powder XRD studies with a laboratory source were used to study Cu oxide and hydroxide on carbon paper during CO_2RR.[508] For all samples full reduction to metallic Cu was observed, albeit with different kinetics. Furthermore, the Cu samples derived from Cu hydroxides exhibited considerable tensile strain with corresponding increases in CO_2RR reactivity, whereas those derived from CuO were strain-free.

In contrast to studies under stationary reaction conditions, recent time-resolved *operando* XRD and XAS measurements of reduced Cu_2O nanocubes under pulsed CO_2RR conditions by Timoshenko et al. found clear evidence for transient oxide species and correlations of its presence with the catalyst's selectivity.[509] At the anodic potential of the pulse a sub-nanometer thick region of the Cu nanoparticle was converted into a Cu_2O surface oxide on timescales of $\approx$ 10 s. This oxide phase was removed within 1-2 s after the cathodic potential was applied. The strain in the Cu_2O lattice was found to evolve on similar time scales and to be anisotropic, whereas the Cu lattice strain changed more rapidly to a steady-state value. Comparison with electrocatalytic measurements indicated an enhanced selectivity towards ethanol formation in the regime of cathodic pulses of intermediate length, which was attributed to an optimal balance between oxidized and reduced Cu surface species and a high fraction of Cu(II) species.

Very recently, first *operando* SXRD results of the Cu surface structure under CO_2RR conditions were reported for the case of Cu(100) in CO_2-saturated 0.1 M $KHCO_3$.[510] Here, CTR measurements were combined with *operando* STM and Raman spectroscopy studies, showing the formation of CO-induced Cu nanoclusters below -0.2 V vs. RHE. These clusters were stable down to -1.1 V and decayed into Cu adatoms upon increasing the potential back into the double layer range. These results indicate that irreversible formation of low-coordinated Cu surface species even occurs, if the Cu oxidation range is avoided.

In addition, CO_2RR on CuAg bimetallic

catalysts was studied, as those have an enhanced selectivity towards multi-carbon products. *Operando* GIXRD studies of Ag-coated Cu nanowires reported that the Cu Bragg peaks irreversibly broadened for CO_2RR below -0.55 V vs. RHE for materials containing 32% Ag and attributed this change to alloy formation.[511] As Cu and Ag are immiscible in the bulk, it was proposed that intermixing occurs during the reduction of Cu surface oxide, as the latter results in a highly defective Cu phase. Studies of CuAg metallic foams found that oxidation of these catalysts enhances the selectivity towards ethanol and propanol formation.[512] Here, *operando* XRD studies indicated a full reduction of the Cu oxide at -0.2 V vs RHE, showing that the activation of the catalyst before the onset of the CO_2RR.

X-ray scattering studies of CO_2RR catalysts other than Cu are rarer. Medina et al. employed XRR to investigate the structure of bismuth thin film electrodes during CO_2 electroreduction in electrolytes containing ionic liquids.[513,514] They found that these electrodes originally correspond to a mixture of Bi and Bi oxide, but are fully reduced to metallic Bi under CO_2RR conditions. Furthermore, extensive surface restructuring was observed at a potential near the onset of CO_2 reduction in a imidazolium-based electrolyte that promotes CO formation, but not in electrolytes containing electrochemically inactive tetrabutylammonium cations. Thus, surface restructuring processes seem to play in general a critical role in steering the catalyst selectivity under these highly reducing conditions.

6.3.2 Nitrogen reduction

The electrochemical N_2 reduction reaction (NRR) has recently attracted significant attention as an mild and viable alternative to ammonia synthesis through Haber-Bosh process. Among others, Li-mediated, non-aqueous NRR systems seem to be a promising route. In this process, Li electrodeposition is followed by a reaction with N_2 forming a Li_3N intermediate, which subsequently reacts with a proton source to form NH_3. Using *in situ* XRD, Gao et al. clarified the role of good electrocatalysts for NRR. They showed that catalysts with higher Li affinity, in this case Au plated carbon paper, ease the first step of Li reduction and therefore speeds up the overall process[515]. The role of the solid electrolyte interface (SEI) was investigated by *in situ* neutron reflectometry by Blair et al.[516]. They demonstrated that the SEI layer consists mainly of carbonaceous electrolyte degradation products. Current-cycled NRR allows to limit the growth of the SEI, which has positive effects on the NRR rate. While this report uses a neutron technique, the X-ray equivalent could also provide the same level of information, and may be a valid approach to assess the SEI growth and composition in future studies. In the case of a $1\,T-MoS_2-Ni$ catalyst, Li has a different role. *In situ* XRD revealed intercalation of Li^+ ions in $0.1\,M$ $LiClO_4$ at $-0.3\,V$, which results in structural distortions, lowering the energy barrier for N_2 fixation and higher NRR activity[517].

Other materials for NRR have been also investigated by *in situ* X-ray techniques. Covalent organic frameworks (COF) show an interesting behavior, where the as synthesized material is less active than the electrochemically activated equivalent[518]. The amorphization of the structure, as revealed by *in situ* XRD and Raman spectroscopy, has a positive effect on the accessibility of active sites as well as a strong affinity to N_2. A low overpotential during the NRR was found to provide the optimal configuration with high NRR activity.

6.4 Electrocatalytic devices

Conditions inside commercial electrochemical reactors diverge from typical laboratory cells in terms of temperatures, pressures, gas vs. liquid phases, flowing vs. static electrolytes, pH, fouling, reagent purity, and more. These factors influence the kinetics, thermodynamics, and mass transport of reactions inside the cell. In many cases, such as CO_2 reduction, where a diverse array of product distributions are possible, the reactions that occur inside the cell are a strong function of coupled mass transport and electrokinetics conditions. Therefore, studying

complex multistep processes such as PEMFC catalyst aging, benefits from probing actual devices, instead of laboratory model systems.

6.4.1 Proton exchange membrane fuel cells

Platforms for *operando* X-ray scattering measurements on complete PEMFC devices have been developed at several synchrotrons. The first-generation cells repurpose sample environments from early spectroscopy efforts, modifying commercial cell designs by thinning down flow field plates, and operating in transmission mode.[462] This strategy allows *operando* scattering to be combined with simultaneous imaging, fluorescence,[519,520] absorption spectroscopy, and other complementary techniques.[453] In transmission mode, the thin sample minimizes parallax distortion[521] in the scattering signal while providing a relatively constant background and a wide angular range. These advantages allow for high-quality *operando* pair distribution function analysis of catalyst aging inside complete fuel cell membrane electrode assemblies, as pioneered by the Petkov group.[473,475,522] Studies across a diverse family of alloy catalysts reveal how strain and local disorder in the alloy change due to corrosion over the life cycle of the device[476], as well as reveal the microstructural evolution, e.g, of the crystallite size[462].

Unfortunately, transmission geometry designs that accumulate X-ray damage in a single spot, do not allow probing of many heterogeneous locations inside the device, and provide a very low signal-to-background ratio signal, necessitating a sparse number of slow measurements per sample. Grazing incidence designs offer a solution to these problems without compromising the device performance[57], but require a high-energy, microfocused beam, and preclude spectroscopy or high angular resolution diffraction. Grazing incidence geometry allows correlative XRD and SAXS computed tomography (XRD/SAXS-CT) experiments with sufficiently high spatial resolution, which can reveal interesting heterogeneities during PEMFC operation. Using this combination Martens et al. showed that the catalyst degradation in the cell is more severe under the land of the flowfield and it is correlated with the increased water content in the membrane in these areas[460]. The same cell was later used to decouple the catalyst degradation mechanisms in the operating fuel cell by combined WAXS/SAXS measurements[451]. This has been achieved by comparing the NP size measured by both techniques. From the WAXS data the size of coherent domains, i.e., the individual crystallites, was determined and the SAXS data provided the size of aggregated particles, given that aggregation occurs during the aging of the catalyst. Furthermore, Chattot et al. also characterized in *operando* the anomalous aging of the Pt catalyst after accelerated stress test (AST)[461]. Interestingly, the catalyst fully degrades only when the potential is swept below the AST's low potential limit, which removes the surface oxygen from oxophylic sites and causes sintering of the catalyst particles and increase of the electrochemical surface area. These findings are only obtainable by performing *operando* measurements in industrially relevant, high-performance devices.

6.4.2 Solid oxide fuel cells

The major challenge of solid oxide fuel cell (SOFC) engineering is their high operating temperature, 500 °C to 1000 °C, which is necessary for oxide ion conduction. This difficulty is even more acute for *operando* cell design[59], and therefore relatively few studies have investigated microstructure and phase transitions of the ceramic and metallic composites used in the anode, cathode, and solid electrolyte *in situ* with X-ray scattering.

SOFCs are relatively durable and typically operated under steady-state conditions when fed with hydrogen. This complicates *operando* aging studies, particularly those requiring synchrotrons, since the dynamics are very slow and require hundreds to thousands of hours for substantial performance loss. The Hardy group has run several long-term investigations into the degradation of cathode microstructure, showing that the occupancy of different sites in the ceramic lattice is altered over time by diffu-

sion.[523,524] Specifically, XRD is suited for tracking changes in strain, cation migration, and depletion of O atoms, which are well understood to be linked to conductivity loss, interdiffusion/poisoning, and other deleterious reactions.[525]

Startup/shutdown phenomena and side reactions with fuel gases and impurities[526] can occur much faster. Korjus et al. investigated the *in situ* activation of the metallic Ni anode catalyst from NiO.[527] Obvious strain effects on both the Ni and the ceria-based support appeared as a function of operating potential and fuel pressure, indicating considerable structural sensitivity to redox conditions of the conductive oxides. Li and coworkers used high resolution *operando* XRD-CT in a microtubule SOFC to image the stability of the ceramic/metallic phases during thermal cycling. The homogeneous strain of the Ni catalyst is observed throughout the whole device, which is correlated with the quality of gas distribution and local ionic/electronic conductivity.[528]

6.4.3 Electrolysers

The clear need for *operando* investigations of materials functioning at high current densities during electrolysis led recently to the development of an electrochemical XRD cell able to achieve high performance in membrane electrode assembly (MEA) configuration[58]. This cell has been used to study anion exchange membrane-based CO_2 electrolyzers[529,530]. In those studies, XRD was used together with reaction product analysis by gas and liquid chromatography, to quantify the amount of electrolyte and salt in the gas diffusion layer (GDL) during the electrolyzer operation. Both GDL flooding and carbonate precipitation phenomena play important role in the performance of the device, because they block the access of the CO_2 feed to the electrode, leading to switching between CO_2RR and HER. It was found that the carbonate salt from the anode side transfers through the membrane to the cathode causing salt precipitation and electrolyte buildup, shifting the reaction to HER. HER accelerates H_2O transport through the membrane, dissolving the blocking salt deposits and allowing CO_2 to reach the cathode, which switches the reaction back to CO_2RR. The cycle then repeats itself[529]. The key parameter is the solubility of the carbonate salt, where the key to circumventing salt precipitation is to use highly soluble alkali cation salts as the anolyte (e.g. $CsHCO_3$) along with an optimal salt concentration between 0.01 and 0.1 M[530].

7 Electrochemical phase formation

The formation of materials by electrochemical growth or structural changes in a material due to electrochemical dissolution or phase change processes are key application areas of scattering techniques. Such processes play an important role in the context of (electro-)chemical material synthesis, electrodeposition, etching, and corrosion. XRD has been employed for a long time as a standard method for the *ex situ* characterization of the resulting materials. However, also the processes itself can be investigated in *operando*, often on the atomic scale, which can provide detailed insights into the growth mechanisms and kinetics.

7.1 Electrodeposition and dissolution

Electrodeposition and electrochemical etching are widely used in industry, e.g., for electroplating, electrorefinement, and electropolishing. Applications range from the production of functional coatings to chip metallization in the microelectronics industry and the preparation of nanomaterials. The latter ones require to improve our understanding of the underlying processes, which currently is still largely phenomenological, on the atomic and nanometer scale. As will be shown in the following, *in situ* and *operando* XRD methods are well suited tools for this.

7.1.1 Homoepitaxial electrodeposition

The conceptually most simple type of growth process is the growth of a material on a single crystal substrate of the same material. Such homoepitaxial growth has been studied extensively in the gas phase.[531,532] Here, studies that monitor the scattering of electrons, ions, or X-rays as a function of deposition time have played an important part in determining the temporal evolution of the surface morphology during deposition. In particular, these methods allow to identify the kinetic growth modes, which are determined by the flux of the deposited atoms to the surface, the intralayer transport on atomically flat terraces of the crystal surface, the interlayer transport across steps between neighboring terraces, and the probability for island nucleation on the terraces (Figure 36a). If the flux is sufficiently low and the surface diffusion of the deposited adatoms high, all deposited atoms are rapidly transported to existing step edges, where they are incorporated into the crystal. During this step-flow growth the surface morphology is maintained and, thus, the scattered intensity at reciprocal positions along the specular and non-specular CTRs does not change with time. Upon increasing the flux, the surface concentration of deposited adatoms increases until the nucleation threshold for the formation of monolayer islands on the terraces is reached. If adatoms can easily descend from these islands, island growth and subsequent coalescence to a new layer occurs, on which then the next layer islands nucleate and grow (layer-by-layer growth), that is, the occupation of the topmost layer oscillates between zero and a full monolayer. The partially filled top layer results in destructive interference of the scattered beam, which manifests particularly clearly at reciprocal space positions that are halfway between two Bragg peaks along a CTR ("anti-Bragg position"). Consequently, the scattered intensity varies periodically in the form of so-called growth oscillations, where each intensity maximum corresponds to a newly deposited layer. At very high flux or if the Ehrlich-Schwoebel barrier for the diffusion of adatoms across steps is high, new nuclei are formed on existing islands before they coalesce to a closed layer. This results in a 3D growth mode, in which multilayer islands are formed. This results in a gradual roughening of the growing surface, leading to a continuous decay in the scattered intensity along the CTRs.

In the gas phase, such studies are comparably simple, because the deposition process can be easily switched on and off. However, this is not the case in homoepitaxial electrodeposition, where either electrochemical deposition or dissolution occurs. These processes proceed even at the equilibrium potential, making it difficult to start the growth on a defined surface. For these reasons, most studies of electrodeposition have focused on heteroepitaxial growth. Furthermore, the flux of deposited species and the deposition potential, which influences the interface structure and the dynamic behavior of adsorbed species, cannot be easily controlled independently due to the mass transport in the electrolyte: Under potentiostatic conditions, the deposition current will vary with time; under galvanostatic conditions, changes in the deposition potential will occur. To circumvent these problems, first *operando* XRD studies of homoepitaxial electrodeposition used low concentrations of the deposited ions and performed the studies under diffusion-limited conditions. Krug et al. employed this strategy to study Au electrodeposition on Au(100) in Cl-containing electrolyte and showed that the kinetic growth behavior depends strongly on potential Figure 36b,c).[52,533] At the most positive potentials, no changes in the scattered intensity with time were found, indicating step flow growth. Subsequently, the potential was step-wise changed from this range to a more negative value. This resulted first in the characteristic growth oscillations of layer-by-layer growth and, at even lower potentials, rapid intensity decay due to step-flow growth. As the Au flux to the surface was constant, these transitions indicate a strong increase in the Au surface mobility with increasing potential, which is in good agreement with results from scanning probe microscopy.[535,536] Interestingly, the growth reverted to layer-by-layer mode at even more negative potentials, where the Au(100) surface reconstructs, which

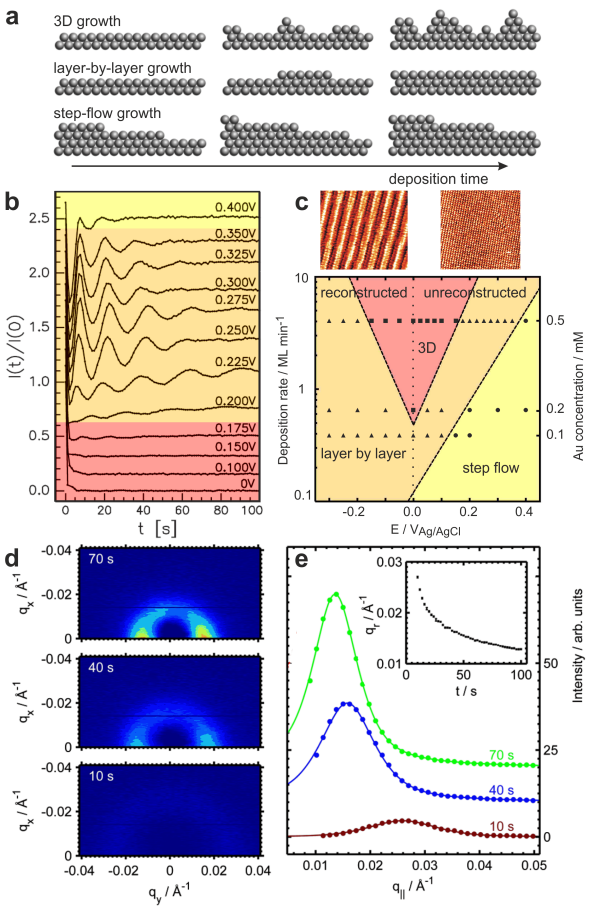

Figure 36: (a) Schematic illustration of the three kinetic growth modes. (b) Time-dependent scattered intensity during homoepitaxial Au deposition on Au(100) in 0.1 M HCl + 0.5 mM $HAuCl_4$, indicating a crossover from step-flow (yellow) to layer-by-layer (orange) to 3D growth (red) with decreasing deposition potential, and (c) the regions of different growth modes as a function of potential and deposition rate (Adapted from Ref.[533]. Copyright 2006 American Physical Society). (d) Selected GISAXS data and (e) corresponding intensity distributions as a function of in-plane momentum transfer, showing the temporal evolution of mounds during 3D deposition on Au(100). The inset shows the change of the peak position with deposition time (Adapted from Ref.[534]. Copyright 2014 American Physical Society).

may be caused by a higher Au adatom mobility on the hexagonally ordered top layer of the reconstructed surface as well as quasi-collective transport mechanisms.[537]

In a subsequent study such step experiments were performed systematically at different positions along the specular CTR, which allowed measuring the latter with sub-100 ms time resolution.[538] Fits of these CTRs in the initial stages of growth showed that deposition at 0.35 V vs Ag/AgCl is well described by nucleation and growth of Au monolayer islands, whereas at -0.2 V first the hexagonal reconstruction is formed, followed by layer-by-layer growth. The formation of the Au(100) reconstruction was found to occur two orders of magnitude faster than in the absence of Au deposition, which can be attributed to the enhanced surface mass transport under growth conditions. A similar influence of Au electrodeposition on surface reconstruction was found in SXRD studies of Au(111).[539] Here, the compression of the Au surface layer did not saturate at a $(23 \times \sqrt{3})$ superstructure, but linearly increased with potential. This behavior resembles the electrocompression effect found for UPD metal adlayers and can be explained by lower kinetic limitations for surface restructuring under growth conditions.

The evolution of the Au(100) surface morphology during 3D growth was studied by Ruge et al. via *operando* GISAXS.[534] The authors monitored peaks in the small angle regime, which result from the scattering by nanoscale mounds that are formed on the surface by the electrodeposition process (Figure 36d,e). With increasing deposition time, the peak intensity increased and the peak position shifted to smaller angles, indicating vertical growth and lateral coarsening of the mounds, respectively. The coarsening followed a well-defined scaling law with an exponent that shifted from 1/4 to 1/3 in the potential range of -0.1 to 0.2 V. In the context of 3D growth theory,[532] this behavior may be explained by a crossover from mounds without defined slope to mounds with faceted side walls.

Analogous SXRD studies were performed for Cu electrodeposition, which is a process of

tremendous importance, especially because of its applications in the microelectronics industry. These measurements were performed in an Cl-containing electrolyte at growth rates up to 38 ML per minute. Interestingly, the growth behavior changed from 3D to layer-by-layer to step-flow growth with increasingly positive potential, i.e., in the opposite order as in the case of unreconstructed Au(100).[216,540,541] This surprising effect was attributed to the influence of adsorbed Cl, specifically the formation of an ordered $c(2 \times 2)$ Cl adlayer, on the Cu surface mobility. *Vice versa*, the Cu deposition process was found to significantly slow down the kinetics of Cl adlayer ordering.[541] Furthermore, the measurements indicated an oscillatory strain in the surface layer, which was tentatively attributed to surface stress induced by island step edges and Cu adatoms. Furthermore, the influence of polyethylene glycol (PEG), which is an important additive in the Cu damascene plating process, was studied by the same group.[542] CTR and superstructure rod measurements revealed that the polymer interacts more strongly with the partially $c(2 \times 2)$ covered surface than with the close-packed Cl adlayer. However, the growth-inhibiting properties of the PEG-Cl complex are more pronounced in the latter regime according to time-resolved SXRD studies. In addition, the presence of PEG in the solution shifted the crossover from layer-by-layer to 3D growth to significantly more negative potentials.

7.1.2 Electrochemical and chemical dissolution

We first discuss dissolution at the crystalline surface of a simple elemental metal, which is the inverse process to homoepitaxial deposition. This process was studied for the case of Au(111) and Au(100) electrodissolution in Cl-containing electrolyte using the same methodology as in the electrodeposition experiments above.[543,544] That is, the dissolution mode was analyzed by time-resolved measurements of the X-ray intensity near anti-Bragg positions and simultaneous measurements of the electrochemical current density. Because the dissolution process is rather irreversible, these studies could only be performed as single-shot experiments. Nevertheless, a time resolution of down to 2 ms could be obtained, which allowed studying the etching of the surface at technologically relevant rates of up to 20 ML/s. During the dissolution of Au(100), the characteristic intensity oscillations of a layer-by-layer mechanism were observed.[544] However, at the most positive potentials, the oscillating intensity rapidly decayed, indicating an increasing surface roughening at higher dissolution rates. Studies of Au(111) at lower dissolution rates ($\leq$ 20 ML/min) found a transition from step-flow to layer-by-layer dissolution prior to surface passivation via gold oxide formation.[543] From a quantitative analysis involving both the X-ray intensity transients as well as the current transients the dissolution behavior could be shown to be described by a smooth multilayer growth model. Here, progressive vacancy island nucleation occurs in the whole active dissolution regime with next-layer nucleation occurring at rather low critical top layer coverages between 0.29 and 0.44 ML.

Furthermore, detailed studies were performed on the dissolution of alloys, in particular dealloying. Here, the less noble component dissolves selectively, leaving behind the matrix of the more noble metal. Pioneering work in this area was performed by Renner et al., who studied this process by *in situ* SXRD and anomalous GIXRD on alloy single crystals.[545–553] Studies of (111)-oriented Cu_3Au, an important model system for dealloying, in sulfuric acid solution revealed in the first stage of this process the formation of a 2-3 ML thick passivation layer with depleted Cu content (less than 40 %).[545,548] Interestingly, the stacking sequence of the atomic planes in this passivation layer was inverted relative to the fcc stacking sequence in the underlying Cu_3Au substrate (Figure 37. In the later stages of the dealloying process, the passivation layer transformed into a thicker layer consisting of Au-rich islands. This transition heralds the onset of the nanoporous Au formation and confirms predictions by Monte-Carlo simulations.[554] Subsequent systematic studies of the effect of halides on $Cu_3Au(111)$ dealloying,[546,549,550] found for Cl and Br very similar

behavior as in pure H_2SO_4 solution, apart from a negative shift in the potential of the transition between passivation layer and island formation. These results suggest that the transition is not thermodynamically driven but a kinetic effect, caused by the (potential-dependent) rate of surface diffusion, which is higher in the presence of halides. In iodide-containing solution, no stable passive film was observed. Instead, precipitation of an epitaxial CuI(111) film was found, which partly inhibited the dealloying, resulting in the formation of a bimodal pore size distribution in the resulting Au layer. In addition, functionalization on $Cu_3Au(111)$ electrodes by thiols resulted in an inhibition of the dealloying.[552,553] Other Cu alloy electrodes exhibit a similar dissolution behavior, i.e., the formation of an epitaxial metallic passivation layer composed of islands of the noble alloy component that suppresses massive Cu dissolution. On $Cu_3Au(100)$, a layer of islands with (111) facets was observed.[547] Dealloying of (111) and (100) oriented Cu_3Pd lead to the formation of epitaxial passivation layers of Pd on both surfaces.[547,551]

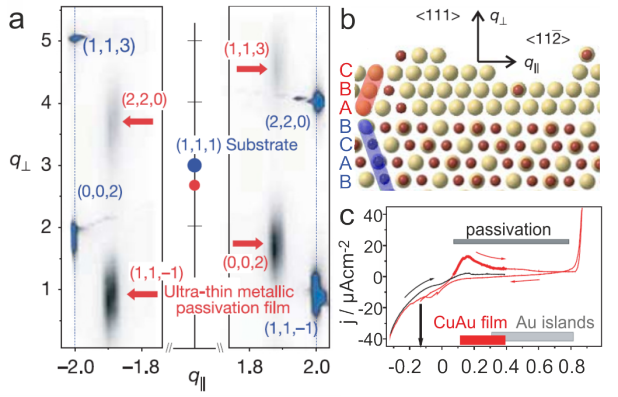

Figure 37: Dealloying of $Cu_3Au(111)$ electrodes. (a) Reciprocal space map showing the Bragg reflections from the passivation layer (red) and the Cu_3Au substrate (blue). (b) Schematic illustration of the electrode structure in the passivated state. (c) CV of the dealloying process (Adapted from Ref.[545]. Copyright 2006 Springer Nature).

More recently, dealloying has become of interest for the formation of nanoporous metals, especially nanoporous gold. A prototypical system here is the dealloying of AuAg in nitric acid solution under open circuit conditions. This process was first addressed by *in situ* XRD in a study of polycrystalline $Au_{30}Ag_{70}$ dealloying by Van Petegem et al..[555] They observed the evolution of a broad component in the Bragg peaks over several hours and revealed a decrease in the coherent grain size by a factor of four and a parallel build-up of tensile stress in the residual Au lattice. More detailed *in situ* SAXS and XRD studies by Toney and coworkers at different acid concentrations, performed using AuAg thin film samples to achieve more uniform dealloying, revealed several characteristic stages of this process.[556] After an initial fast dealloying, in which a random distribution of pores and compressively strained Au ligaments were formed, coarsening of the morphology was observed. In the latter, first a bicontinuous morphology with quasi-periodic character emerged, which then coarsens in a self-similar manner. Furthermore, both of these studies deduced the presence of directional strain anisotropies in the Au ligaments. More recent studies investigated the influence of temperature on the dealloying process by *in situ* SAXS[557,558] and determined the structural changes in isolated AuAg nanocrystals that were induced by 10 s of dealloying by *ex situ* BCDI.[559] The latter work provided detailed strain distributions within the nanoparticle that showed the formation of nanopores near the surface induced compressive strain 60-80 nm deep beneath, but weak tensile strain deeper within the particle. This coexistence of differently strained areas is in agreement with previous averaging XRD studies[555,560] and demonstrates the potential of coherent imaging techniques in resolving structural transformations in complex materials.

In addition, the chemical dissolution of oxides has been addressed. The surface dissolution of orthoclase (001) has been studied using X-ray reflectivity by Teng et al., who looked at the dissolution process of orthoclase (001) at two extreme pH conditions (pH 1.1 and pH 12.9).[561] It was found the dissolution process in an acidic solution proceeded nonstoichiometrically and is accompanied by terrace roughening. In an alkaline solution, the dissolution is mostly stoi-

chiometric and occurs via a step-flow mechanism. The dissolution mechanism at two different pH was thought to be controlled by surface reactions at distinct reactive sites. Fenter et al. studied the same system and identified two dominant reactive sites, namely bridging oxygen between Al and Si sites (site A) and bridging oxygen between Si surface sites (site B).[562] Those two reactive sites are responsible for dissolution occurring at pH>0.5 and pH <0.5, respectively. The terrace roughening at pH 1.1 observed by Teng et al. may correspond to the surface reaction occurring dominantly at site B with a smaller portion of surface dissolution occurring at site A. In contrast, the step flow motion at pH 12.9 should be related to surface reactions occurring solely at site B. Besides solution pH, the crystal orientation can also play a role in the dissolution kinetics on orthoclase surfaces.[563] In addition, NaCl background electrolyte was found to enhance the surface dissolution of orthoclase.[564] This effect was assigned to a higher terrace reactivity in the presence of NaCl that leads to more 3D dissolution, resulting in faster dissolution rates.

7.1.3 Heteroepitaxial electrodeposition

The evolution of the deposit's lattice structure and morphology during electrochemical nucleation and growth on a substrate of a different material is a complex process, which has been studied extensively by a variety of *in situ* methods.[565] Commonly, a well-defined relationship between the orientations of deposit and substrate lattice exist, which is denoted as epitaxial growth and depends on the mismatch of the in-plane lattice geometries at the interface. A specific case is pseudomorphic growth, where the deposit adopts the in-plane lattice of the substrate, but this is usually only observed in systems with very small lattice mismatch. The interplay of interface energies and strain in the deposit results in structural transitions with increasing thickness of the deposit that can be probed well by XRD methods.

In situ X-ray scattering studies of heteroepitaxial electrodeposition originally focused on metal-on-metal deposition in aqueous electrolytes. In particular, the crossover from UPD (see section 5.2.2 to multilayer growth was addressed. Early SXRD studies of Pb electrodeposits on Ag(111) found a disruption of the Pb UPD layer at coverages ≥5 ML and the formation of (111)-textured but randomly oriented islands.[209] In contrast, bulk electrodeposition of Tl on Ag(100) and Au(100) proceeded epitaxially on top of the Tl UPD bilayer and monolayer, respectively, in form of well-defined 3D islands of (0001) hcp Tl.[240] The stability of the UPD layers underneath the bulk deposit was explained by the low interface energies, resulting from the similar (quasi-)hexagonal in-plane lattices. Several *in situ* SXRD studies investigated the electrodeposition of Pd on single crystal substrates, because of its interest in electrocatalysis and hydrogen storage. Pd growth on Pt(111)[265] and Pt(100)[198] was found to proceed via a Stranski–Krastanov growth mode, in which first a pseudomorphic Pd monolayer formed, followed by the growth of 3D islands. For Pd electrodeposition on Au(111), the first two layers are deposited via a non-ideal layer-by-layer pseudomorphic growth, on which subsequently relaxed 3D islands form.[566] The important influence of interface energy and deposit strain was illustrated in SXRD studies of Cu bulk electrodeposition on Au(100)[567,568] and Ag(100).[569] In both cases, the large lattice mismatch enforces an initial layer-by-layer growth in form of body-centered cubic (bcc) Cu up to 10 ML. However, at larger film thickness, this bcc-like structure becomes unstable, resulting in a buckling transition. The resulting phase exhibits a uniaxial periodic modulation, in which local orthorhombic regions are formed, reminiscent of martensitic distortions in Fe alloys.

The electrodeposition of thin magnetic films, a topic of substantial interest for industry, has been studied likewise on defined single crystal substrates. Co and Fe electrodeposition on Cu(100) was investigated using simultaneous *in situ* XRD and magnetooptical Kerr effect (MOKE) measurements.[570,571] For Co, the growth of a pseudomorphic fcc Co deposit was found up to 15 ML, together with the formation of an in-plane relaxed component, which

was attributed to Stranski-Krastanov growth of 3D islands. In the case of Fe, a transition from pseudomorphic fcc Fe to a bcc Fe(110) film was observed at coverages $\geq$7 ML. In this transition, the fcc lattice was reoriented. In parallel, the MOKE measurements indicated a reorientation of the easy axis of magnetization from out-of-plane to in-plane. *In situ* SXRD and STM studies of electrodeposited Co layers on Au(111) indicated that the growth started with the formation of an hcp Co(001) bilayer, followed by a smooth layer-by-layer growth.[572] Interestingly, the presence of the Co film was found to restructure the $(23 \times \sqrt{3})$ reconstructed top Au layer into an isotropically compressed arrangement, demonstrating the unique capability of XRD methods to access such deeply buried metal/metal interfaces. Subsequent studies demonstrated the epitaxial electrodeposition of Pd(111) capping layers onto Co/Au(111) and showed that the in-plane strain in the Pd film upon H absorption was coupled into the underlying Co film.[573]

Only a few *in situ* XRD studies have addressed epitaxial electrodeposition on semiconductors. The main problem here is the strong photoelectrochemical effects induced by the X-ray beam.[574,575] Zegenhagen and coworkers performed a series of *in situ* SXRD and X-ray standing wave measurements of noble metal deposition on Si and GaAs electrodes from aqueous electrolytes.[574,576–579] Characteristic for these systems is a 3D cluster growth of the deposit. Studies of the electroless deposition of Au and Pb on H-terminated n-Si(111) indicated wetting of the semiconductor substrate by Au at sub-monolayer coverages, followed by growth of epitaxially aligned (111)-oriented clusters.[576,577] A similar epitaxy was found for electrodeposited Au films on this surface by *ex situ* XRD.[580] Cu electrodeposition on H-terminated n-Si(111) proceeded via the growth of Cu clusters, in which the (111), (110), and (100) planes were oriented parallel to the Si(111) surface (with the first two orientations being dominant) but only the Cu(110) clusters had defined in-plane orientations relative to the substrate lattice.[574,575] For Cu electrodeposits on UHV-prepared GaAs(100) a splitting of the Cu diffraction pattern into 8 Bragg peaks was found, indicating an unusual epitaxial relationship, in which the Cu(100) planes were rotated by $\approx$5° and tilted by $\approx$9° with respect to the substrate lattice.[578,579] In addition, diffuse intensity streaks extending from the Cu(022) peak were observed, indicating that the sides of the Cu clusters were terminated by (111) facets.

Non-aqueous electrolytes and, in particular, room-temperature ionic liquids (ILs) allow to deposit a wider range of materials and have accordingly received much attention. SXRD studies of Zn electrodeposition from ILs found in the initial stages formation of epitaxial Zn and $Au_{12}Zn_{88}$ films.[581] More extensive deposition, studied on polycrystalline Au films by powder diffraction under grazing incidence angles, resulted in stronger alloying with the parallel formation of Zn and several Zn intermetallic phases. XRR studies of Si electrodeposition in ionic liquids reported the formation of an intermediate polymer-like Si chloride layer, which subsequently was further reduced to the Si deposit.[582] Of particular interest in this field are studies of alkali and second row metal electrodeposition as anode processes in advanced batteries, as performed e.g. by Renner et al. for Li[583] and Ebenshade for Mg[584] (see also chapter 8).

Electrodeposits of non-metallic materials have been frequently characterized using *ex situ* XRD methods, but *in situ* studies of the corresponding electrodeposition processes themselves are still scarce. A challenge for these studies may be the more complex growth conditions and, especially, the higher temperatures often required for these studies. A rare example was published by Ingham et al., who studied ZnO electrodeposition on Au(111) under conditions where growth was limited by Zn ion diffusion.[585] The XRD measurements showed that a (002) texture develops in the nucleation stage, followed by anisotropic growth of ZnO nanorods along this axis.

Apart from wide-angle scattering studies of the deposit crystal structure and epitaxial orientation, also the nanoscale evolution of the morphology during nucleation and growth have been studied by *in situ* SAXS. Such studies are well established for studies of chemical and

physical deposition processes[78] and have also been applied to electrodeposition.[586–591] Ustarroz et al. employed SAXS to determine the evolution of the nanoparticle size during Ag nucleation and growth on HOPG and found good agreement with the growth behavior deduced from electrochemical measurements.[586] Combination of *in situ* SAXs and *ex situ* electron tomography allowed to monitor the electrochemical growth of dendritic aggregates of Pt, showing that the deposition potential influenced the aggregation and coalescence of the primary nanoclusters.[587] In similar SAXS and WAXS measurements, lateral and orientational ordering during Pt electrodeposition in 3D ordered lipid templates was studied.[588,592] SAXS is not only sensitive to the deposited particles, but can also provide insight into the surrounding electrolyte, as indicated by detailed studies of Hammons et al. on Pb and Zn nanoparticle growth in deep eutectic solvents.[589,590] For Pb, mesoscale anisotropic scattering was observed in SAXS measurements at different incidence angles, which was attributed to strong potential-dependent perturbation of the solution structure around the Pb particles. The latter was described in a simplified model by a layered structure, similar to that found for ionic liquids at planar interfaces (see section 5.2.3), that extended several 10 nm into the solution. The evolution of the porous growth morphology of electrodeposited MnO_2 was followed by *in situ* SAXS in studies by Dupont and coworkers, revealing a gradual change in pore size with deposition time.[593,594] In principle, also GISAXS should be highly suitable for such nanoscale studies, but up to now has been employed only for *ex situ* characterization of electrodeposits.[595]

All the SXRD studies above provided information about the average film structure over macroscopic surface areas, owing to the large footprint of the beam on the sample surface. However, this problem can be overcome at modern synchrotron beamlines, which typically allow the focusing of the beam to micrometer or even sub-micrometer dimensions. Such microdiffraction studies can be performed by employing focused high photon energy beams in transmission geometry, as illustrated schematically in Figure 18b. This allows to map structural heterogeneities of the deposit, as has been shown in *in situ* studies of electrodeposited Co[102] and Bi films.[103] Similar as in low-energy electron diffraction, this transmission surface diffraction method provides at each point on the sample 2D detector images that show the in-plane reciprocal space geometry over a wide $q_{\parallel}$ range (Figure 38a). The sensitivity of this method is sufficient to resolve single atomic layers, e.g., the Au(111) surface reconstruction or the Bi UPB superstructures. By performing such measurements at different locations on the sample and automated quantitative analysis of the diffraction peaks, the local variation of characteristic structural properties of the local deposit can be investigated. This is illustrated in Figure 38b where maps of the local thickness, in-plane grain size, and strain in the Co electrodeposit as well as induced strain in the Au substrate are presented, revealing clear correlations of these properties.[102] Similar correlations were also found in analog measurements of Bi electrodeposition within a microfluidic cell.[103] Such locally resolved measurements will benefit strongly from the emerging fourth-generation synchrotron sources. However, the very high local X-ray intensity in such experiments will lead to increased problems with beam damage effects.

Finally, *in situ* X-ray scattering techniques also offer unique capabilities to study electrodeposition at liquid-liquid interfaces. Such deposition processes have received renewed interest, because they offer a substrate that is free of defects and strain, enable growth from both sides of the interface, and thus open up opportunities for the electrodepositon of a wide range of materials, including semiconductors.[357] Only hard X-rays allow to probe the atomic-scale structural studies of these deposition systems directly. Several studies investigated electrochemical growth at liquid metal electrodes by *in situ* XRR and GIXRD. Specifically, the nucleation and growth Pb halide films on liquid Hg were studied in detail.[95,365,366,368] It was shown that ordered salt-like adlayers, formed initially on the Hg surface (see section 5.5), pro-

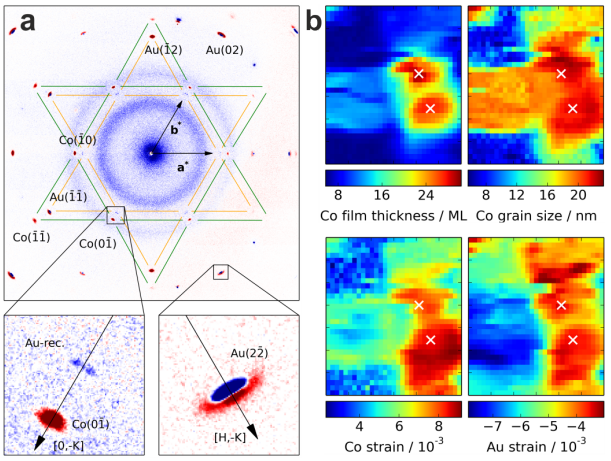

Figure 38: Structure of electrodeposited Co this films on Au(111), studied by HESXRD at 40 keV in transmission geometry. (a) Difference in the scattered X-ray intensity, obtained by substracting the 2D detector images recorded prior and after Co deposition. Sixteen Au CTRs and 12 Co CTRs are visible, with peaks that emerge after deposition depicted in red and peaks that disappear in blue, respectively. (b) Maps showing the micrometer-scale variation of the deposit thickness, lateral grain size, and strain in Co deposit and Au substrate, derived from a quantitative analysis of the Bragg peaks in detector images recorded at each point of the map. (Adapted from ref.[102]. Copyright 2014 American Chemical Society).

vide a template for the subsequent growth of a strongly textured bulk deposit. Detailed studies of PbBrF growth indicated with increasing overpotential a crossover from the slow growth of a small number of large crystals to the formation of a compact film with a saturation thickness of 25 nm.[95] In the context of studies of the electrochemical liquid-liquid-solid deposition of Ge on Hg and HgIn alloys, *in situ* XRR was used to determine the influence of the interface structure on the growth process.[367,596] *In situ* X-ray scattering techniques have also been applied to study growth at interfaces between other immiscible liquids, e.g., between aqueous and non-aqueos solutions,[597–601] but corresponding studies of electrodeposition in such systems have not been reported yet.

7.2 Passivation and corrosion

The ability of *in situ* X-ray scattering methods to obtain insight into buried interfaces has proven to be highly valuable in corrosion science, especially for the structural investigation of passive layers and for monitoring the structural evolution of the surface morphology during metal dissolution. This section will focus on the more classical subjects of corrosion science, such as Cu, iron-group metals, and valve metals. Related studies on electrocatalyst degradation and noble metal dissolution can be found in sections 6 and 7.1.2, respectively.

Detailed *in situ* SXRD studies of passivation processes, performed on single crystal electrodes, showed that passive film in many cases grows epitaxially on the underlying metal and typically consists of nanoscale islands separated by grain boundaries. Toney et al. reported such epitaxial films, consisting of Fe_3O_4 on Fe(001) and Fe(110) electrodes and showed them to exhibit significant numbers of cation vacancies and interstitials.[602,603] SXRD studies of Ni(111) passivation in sulfuric acid solution indicated the presence of an epitaxial crystalline NiO(111) inner layer and a more porous and probably amorphous outer layer of Ni hydroxide, supporting the duplex model of passive film growth.[604,605] The thickness of the crystalline inner layer was found to increase lin-

early with potential from 1.0 to 2.0 nm. A very similar passive film structure was observed on Ni(111) electrodes in pH 14 KOH solution.[606] Studies of thin epitaxial Co(001) films in 0.1 M NaOH indicated a stepwise oxidation mechanism, starting with the rapid growth of an ultrathin $Co(OH)_2$ layer, followed by the slower formation of 3D $Co(OH)_2$ crystallites at grain boundaries in the Co film.[607] On Cu(111) in pH 4.5 solution, phases with the same cuprite structure and orientation as the air-grown native oxide film were found, but exhibited strong differences in growth behavior and strain.[608] In particular, the experiments revealed the formation of an initial monolayer oxide phase, which was also found in independent *in situ* STM measurements.[184] In general, *in situ* SXRD and STM results on the initial stages of passivation in the above systems have been in excellent agreement and found to provide highly complementary information on the underlying atomic-scale mechanisms.[609]

In addition to these model systems, *in situ* X-ray scattering methods have also been used to study passivation and corrosion in more realistic systems, typically on polycrystalline materials. Early studies of thin Cu films on Si by *in situ* XRR and diffuse scattering found in borate buffer solution the formation of ≈ 2.5 nm thick Cu_2O layers after anodic oxidation, whereas in bicarbonate solution evidence for pitting corrosion was reported.[610–612] Powder diffraction studies under grazing incidence conditions of the anodic oxidation of lead in sulfuric acidic electrolytes, an important process in Pb acid batteries, allowed to identify several crystalline products, such as Pb sulfate, PbO_2, and tribasic Pb sulfate hydrates.[613]

Several studies addressed the structure and evolution of passive films on steel, a key topic in corrosion science. Sinha and coworkers determined by anomalous XRR the passive film on type 430 stainless steel in pH 8.4 borate buffer.[614] In the regime of passivity, the film was shown to consist of an inner layer consisting of insoluble Cr_2O_3, which acted as a barrier to oxygen anion incorporation, and a Fe/Cr oxide outer layer. In the transpassive regime, the entire film consisted of a mixed Fe/Cr oxide. Ingham and coworkers performed systematic *in situ* SAXS and WAXS studies of the formation of protective scales during the corrosion of carbon steels in CO_2-saturated brine at temperatures up to 90° C, a problem of practical interest in oil and gas pipelines.[615–623] The protective phase was identified as crystalline siderite ($FeCO_3$). It was shown to form at high supersaturation via a complex reaction, which involved the spreading of a colloidal amorphous precipitate over the metal surface, followed by the formation of pre-nucleation clusters and finally the nucleation and growth of the crystalline phase. This process was strongly affected by the presence of Cr and Mo in the steel, the solution pH and flow conditions, the nature of cations in the solution, the presence of trace amounts of oxygen, and the presence of organic scale inhibitors.

Related to passivation and corrosion is anodization, a technologically important process in which the metal is electrochemically oxidized in a controlled way. Conventional anodization results in films of defined thickness that increases linearly with potential, as also confirmed by *in situ* XRR.[624] However, most research in this area focused on the self-organized growth of oxides with well-defined ordered arrays of cylindrical pores, especially the growth of porous anodic aluminum oxides.[625] Various groups investigated the structural evolution of the pores during anodic aluminum oxidation by *in situ* SAXS,[626,627] GISAXS,[628] and grazing incidence transmission small angle X-ray scattering (GTSAXS),[629,630] coming to similar conclusions. SAXS measurements can only provide data on the in-plane ordering. In contrast, GISAXS and GTSAXS provide information about the in-plane nanoscale morphology as well as the film structure vertical to the surface, as illustrated in Figure 39a. The in-plane ordering was found to proceed via a power law and could be described by domain structure formation and Ostwald ripening of domains. The pore has a well-defined vertical length, and manifests in oscillations along the q_z direction at the in-plane peak positions (Figure 39b). The vertical growth of the pores, determined from the periodicity of these oscillations, pro-

ceeds at a constant rate, which depends on the substrate orientation (Figure 39c). In addition, *in situ* GTSAXS has been employed to monitor the filling of these pores by electrodeposition of Sn.[631,632]

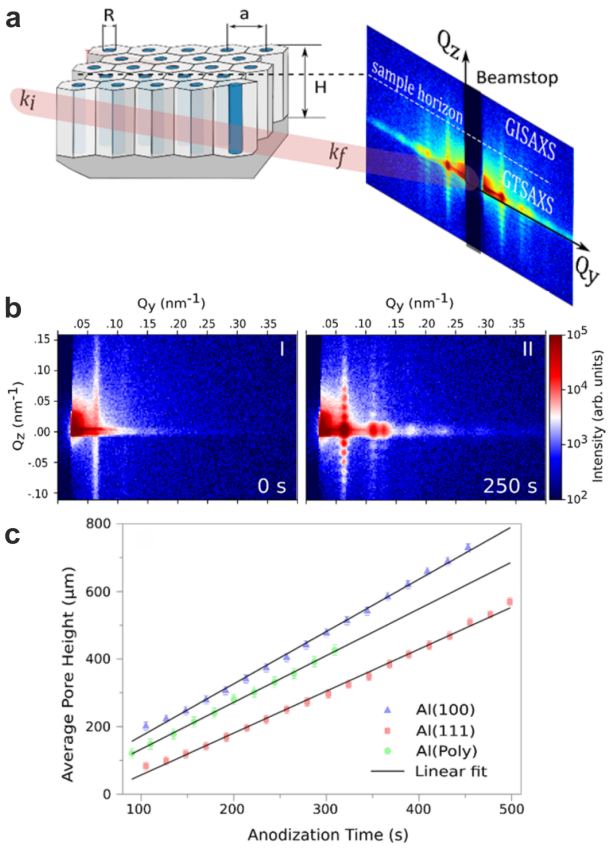

Figure 39: *In situ* GTSAXS measurements of the formation of porous anodic alumina oxides. (a) X-ray scattering geometry. The intensity distributions along q_y and q_z provide information about the in-plane and out-of-plane structure, respectively. (b) Detector images illustrating oxide growth during 2nd anodization in oxalic acid solution. (c) Increase in pore length, obtained from the period of the oscillations along q_z (Reproduced from ref.[629]. Copyright 2018 American Chemical Society).

7.3 Synthesis of electrocatalysts

Another interesting utilization of *in situ* X-ray scattering techniques for electrochemistry and electrocatalysis purposes, beyond the study of electrode materials during electrochemical operation, is to monitor how the electrode materials' properties emerge during their fabrication. This aspect is essential in the 'electrode-by-design' approach largely adopted in the field, as desirable catalyst structure and chemistry must be tailored mostly during their synthesis. Early uses of this possibility were made in the 1980ies to investigate the formation of Pt-alumina reforming heterogeneous catalysts in high-temperature chambers under different gas atmospheres,[633–635] where guiding strategies toward the preparation of targeted Pt alloy phase(s) were established. In electrocatalysis, a similar approach was used to monitor the formation of binary intermetallic PtM (M=Co, Fe or Ni) ORR catalysts during thermal annealing. In the case Pt_3Co particles, Xiong et al. investigated the impact of a variety of annealing conditions on the degree of ordering that could be obtained.[636] It was found that an annealing temperature of 750 °C maximizes the catalyst ordering (30 %) and so the long-term durability of the material in practical PEMFC tests. Recently, Zeng et al. extended the study to PtCo, PtFe, and PtNi materials.[637] Using powder diffraction, they monitored the structural evolution during heating/cooling cycles and extracted the degree of structural ordering (Figure 40a-c). This allowed to develop rational annealing processes that maximized the ordering degree for the three materials by sequential alloying-ordering steps. *In situ* WAXS and SAXS were also used to investigate the sol-gel formation of FeOx, Fe_3N, and Fe_3C ORR catalysts.[638,639] Here, it was found that the transition from oxides to carbide was strongly size-dependent, having important consequences on the resulting catalyst morphology, while the intermediate nitride form was highly unstable and difficult to isolate. The combination of *ex situ* electron microcopy and *in situ* SAXS and WAXS with PDF analysis also allowed to understand the formation and growth of hollow PtNi/C ORR catalysts during a one-pot synthesis, which was found to result from the sequential nucleation of NiB nanoparticles, the galvanic displacement of Ni by Pt, and the nanoscale Kirkendall effect (Figure 40.e-f).[640]

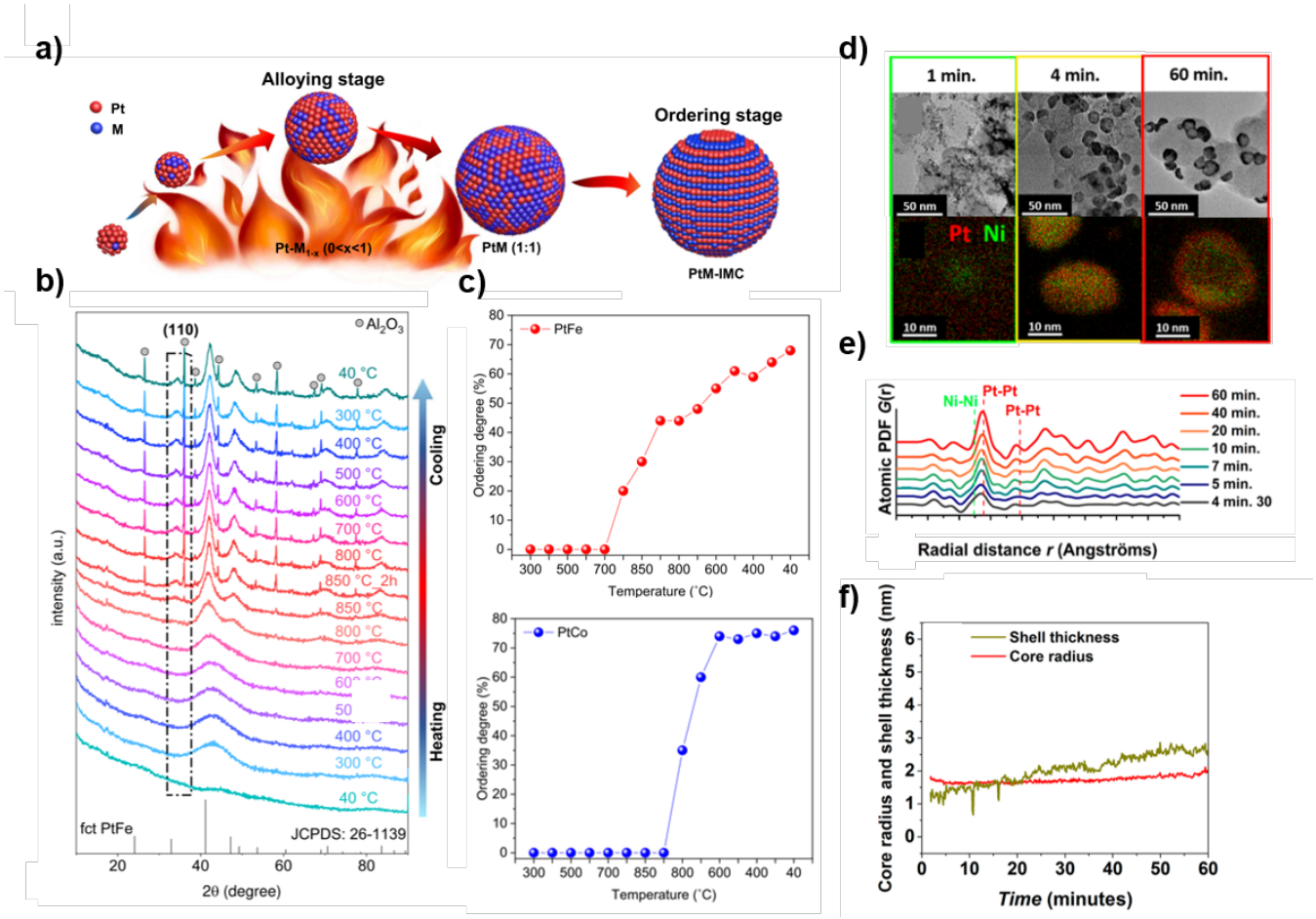

Figure 40: Monitoring nanostructure formation and tailoring for electrocatalysis using *in situ* X-ray scattering. (a) schematic illustration of the synthesis of structurally ordered Pt–M (M= Fe, Co, and Ni) intermetallic compounds, (b) *in situ* HT-XRD results on PtFe structural evolution during heating and subsequent cooling, and (c) calculated ordering degrees of PtFe and PtCo obtained from the *in situ* HT-XRD experiments (Adapted from Ref.[637]. Copyright 2022 by Nature -Springer). Time-resolved formation and growth of hollow PtNi/C nanoparticles as revealed by (d) electron microscopy, (e) PDF analysis, and (f) SAXS. (Adapted from Ref.[640]. Copyright 2017 American Chemical Society.)

8 Intercalation batteries

8.1 Introduction to battery intercalation

Intercalation materials have been ubiquitous in rechargeable batteries since the commercialization of lithium-ion batteries. The intercalation mechanism involves the reversible insertion of ions (ie. lithium) into a host structure, such as graphite or $LiCoO_2$, which results in long-lasting and energy-dense batteries. Key to the development of higher performing electrode active materials and cell designs has been the use of *in situ* and *operando* X-ray techniques to deepen our understanding of intercalation material dynamics at a wide range of length scales. This section will cover *in situ/operando* cell design considerations and review a range of *in situ* and *operando* techniques used to study intercalation materials in battery systems.

While X-ray techniques can offer better penetration depth than other forms of characterization, the structural stainless steel cases of commercial batteries are often too great of an obstacle for X-ray to penetrate adequately. Therefore, X-ray windows are important to the design of an *in situ/operando* cell. Beryllium, the most X-ray transparent material, is a clear option for use as a cell window. However, cost and toxicity of beryllium windows are concerns. Beryllium is also electrochemically reactive in lithium-ion systems[645], so further design elements must be implemented to prevent interaction, such as an air gap.[646] Glassy carbon is also commonly used as an X-ray window for *in situ/operando* battery cells. Glassy carbon provides decent X-ray transparency while being electrically conductive and rigid,[647] but the cell must be designed to prevent lithium intercalation into glassy carbon.[648] Polymer films are another option for a cell X-ray window. Films like Kapton (polyimide) and Mylar (polyethylene terephthalate) are fairly X-ray transparent, durable, and electrochemically inert[649]. Thin metal foils are also an option for X-ray windows due to their ductility and electrical conductivity. Aluminum foil, in particular, has been successfully used as both a current collector and an X-ray window.[650] Another consideration is that polymer films and thin metal foils are less mechanically stiff than the metal cases of a cell. This can lead to less than ideal electrochemical performance in the cell due to inhomogeneous stack pressure.[648]

Since batteries come in a wide range of formats and sizes, *in situ/operando* cells reflect this diversity in designs (see Figure 41). Coin cells are extremely common in battery research due to their small scale and ease of assembly, and are mainly used to study material performance. Coin cells have been modified with windows in the top and bottom cases for use in a variety of *in situ/operando* X-ray applications.[641,651–653] More customized cells serve to reduce a shortcoming of the modified coin cell while maintaining a similar format, such as the Argonne multi-purpose *in situ* X-ray (AMPIX) cell which aims to improve electrochemical performance by reducing pressure inhomogeneity in the cell.[648] Swagelok cells are another type of cell common in research due to their small scale and reusability. They are often designed with non-metallic cases to allow for X-ray penetration and with the electrodes of interest parallel to the X-ray beam, increasing the amount of material being probed.[642] Pouch cells straddle the line between research and commercial applications due to their intermediate size. They can be made with just one layer of electrodes similar to coin cells or with multiple layers similar to commercial cells. For *in situ/operando* X-ray applications, windows are made on the front and back side of the pouch using polymer films or metal foils due to their mechanical similarity with the laminated aluminum pouch.[643,654] Cylindrical and prismatic cells are common commercial battery formats for electric vehicles and stationary energy storage. They are larger in size and contain up to hundreds of electrode layers. Due to their use in commercial applications, cylindrical and prismatic cells are studied with *in situ/operando* X-ray techniques mainly to understand the role of microstructure and degradation mechanisms such as electrode swelling.[655,656]

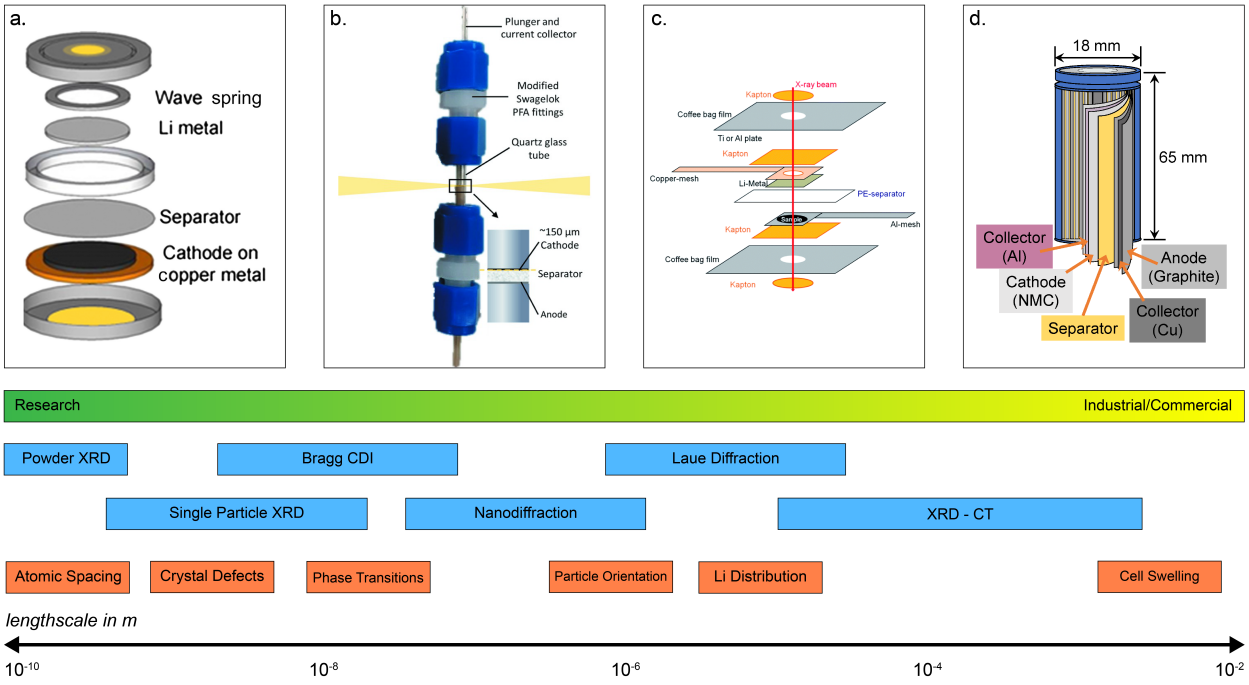

Figure 41: *Operando* battery cell designs and X-ray scattering techniques. (a) Schematic of *operando* coin cell with Kapton windows (Adapted from Ref.[641]. Copyright 2016 Elsevier). (b) Schematic of *operando* Swagelok cell (Adapted from Ref.[642]. Copyright 2020 Wiley). (c) Schematic of *operando* pouch cell with Kapton windows (Adapted from Ref.[643]. Copyright 2014 Royal Society of Chemistry). (d) Schematic of cylindrical cell (Adapted from Ref.[644]. Copyright 2019 MDPI).

8.2 Powder Diffraction

The vast majority of *operando* X-ray scattering studies in batteries utilize powder diffraction. This is due to the wide availability of powder diffraction instruments and familiarity with the principles of this technique, in addition to the structural sensitivity noted above.

The first *in situ* powder diffraction experiments on lithium-ion batteries date back to 1978, when Chianelli and colleagues used a cell with a beryllium window in reflection geometry to study structural transformations in the Li_xTiS_2 cathode during intercalation and deintercalation of lithium[657]. Subsequently, Dahn and colleagues improved the cell design to allow a better correlation between electrochemistry and powder diffraction: the former measured reactions at the cathode particle surface while the latter is a bulk technique. Their study on Li_xTiS_2 by using laboratory X-ray diffractometer[658] and expanded the understanding of structural changes in the cathode material introduced by S. Whittingham.*In situ* X-ray diffraction was extended to other cathode materials, notably Li_xNiO_2[658] and Li_xCoO_2[645]. Particularly the study in Li_xCoO_2 - the cathode material introduced by J. Goodenough - generated significant interest because Li_xCoO_2 is the cathode material of most of today's batteries in portable electronics. *In situ* powder diffraction revealed transitions between three distinct phases as x was varied between 1 and 0.4, and distinguished between order-disorder transitions and first-order phase transitions.

Commercial sample environments for laboratory instruments are available from several manufacturers, almost exclusively based on a windowed coin cell design. Windows of Be or thin polyimide are needed for X-ray transmission. These windows often produce either electrochemical incompatibility (e.g. Be corrosion), small leaks, or inhomogeneous electrode compression, which lead to poor long-term cycling and voltage gradients across electrodes[659]. With modern 1/2D detectors, the time required for simple measurements (1-3 hrs) is appropriate for slow cycling cells. Despite these limitations, laboratory PXRD is both common and valuable for probing the mechanism of phase transformations in active materials. Intercalation commonly follows either a solid solution mechanism, where ion insertion is continuously variable in stoichiometry, or a phase-segregated model, where ions are intercalated at fixed stoichiometries, separated by phase transitions. An idealized solid solution mechanism produces only peak shifts in the powder pattern, while phase-segregated transitions produce new peaks or different patterns entirely. Sharp phase transitions create large strain gradients inside active materials, which generally results in accelerated degradation and poor cyclability. Changes in doping, coating, and growth conditions of active materials can produce dramatic changes in the intercalation chemistry and phase transitions.

The extension of *in situ* powder diffraction to synchrotron sources[660] significantly improved the signal to noise ratio, as well as the temporal, spatial, and angular resolution, as well as penetration depth, which are all useful for *operando* PXRD battery experiments. The increased signal enabled experiments in transmission geometry where the material throughout the thickness contributes to the diffraction signal. Higher flux allows for PXRD measurements down to the ms scale, which permits the same measurements described above, but over cycling rates relevant to battery operation. Spatially resolved PXRD allows for linescan or imaging experiments where lithiation heterogeneity across electrodes can be evaluated.[661] Measurements scanning the plane of the electrode to explore gradients at the mm and cm level require minimal focusing, while focusing towards the 1 um level allows reactions gradients through the thickness of conventional electrode films to be evaluated. High angular resolution PXRD allows for accurate peak shape analysis.

While most *in situ* powder diffraction focused on transition metal oxide cathodes, which generate a high signal, *in situ* diffraction on graphitic anode[662], silicon[663,664] and lithium-sulfur systems[665] have also been reported. Following this pioneering work, *in situ* powder diffraction is a pillar of today's structural char-

acterization of battery materials and has been extensively reviewed[666].

The increased penetration depth of higher energy X-rays is transformative for *operando* battery PXRD. By utilizing high-energy X-rays, commercial cells can be measured *operando* with no concessions in cell performance.[667] The thick steel casing of cylindrical cells requires photon energies of at least 60keV, preferably 90keV.[668] PXRD in pouch cells can be measured at lower energies and has been demonstrated on laboratory instruments with Mo radiation (18 keV). The ability to perform measurements inside conventional cells is important for two key reasons. First, it enables measurements on highly aged cells, which is essential to understand degradation and cycling stability in active materials.[669] Secondly, battery performance and aging phenomena are well known to be intrinsically linked to the form factor of cells.[670] Failure mode analysis including the growth of irreversible phases, Li inventory loss, and consequently the cell's state of health can be directly inferred from PXRD measurements.

Operando SAXS is an emerging technique for batteries. Most active materials are crystalline, and therefore more easily probed with traditional PXRD. However, several promising next-generation chemistries involve amorphous materials, and more suitable for SAXS.[671] When used as an anode, Si becomes amorphous, and determining the lithiation state of the electrode is challenging, but important for optimizing these electrodes.[672] Lithiation of Si drives expansion and changes in electron density, altering the SAXS pattern. Solid-state electrolytes are currently being studied intensely for high-energy density batteries. The microstructure of polymer and glassy electrolytes can be analyzed with SAXS, towards optimizing their microstructure and understanding their complicated solid state chemistry.[673]

Under the right conditions, the pair distribution function of battery materials can be calculated from the PXRD pattern. This technique has proven useful for understanding disorder inside amorphous or poorly crystalline materials, and how short-range and long-range ordering inside active materials can differ. The ability to probe the structure of amorphous and disordered materials overlaps with SAXS. Pair distribution function measurements are preferably performed at very high photon energies to obtain a large angular range. The added value of real-space analysis using PDF has been demonstrated in battery applications, most commonly exploiting differences between the short range and long range ordering in cathode materials, where doping, vacancies, and nonstoichiometric compounds are ubiquitous. Wiaderek et al. showed how PDF can determine the phase transition mechanism of O-doped FeF_3, which undergoes a partial, irreversible amorphization, invisible in the conventional powder pattern.[674] The extreme data quality requirements for useful PDF have until recently limited broad adoption of operando measurements. Advances in cell design now allow structure dynamics of very complex materials to be probed *in situ*, such as defect-rich, mechanochemically synthesized $Li_4Mn_2O_5$[642] or Cu/CuF_2 nanocomposites with extremely small crystallites (0.5-1.0 nm).[675] A combined real space and reciprocal space analysis revealed the formation of a weak superlattice induced by local ordering. Anode materials are frequently amorphous alloys, with poorly understood intercalation mechanisms. These systems are particularly amenable to PDF structure analysis, ranging from the Si anode,[676] which is well-known for irreversible first-cycle disordering, to the more exotic Na3P system,[677] where the sodiation/desodiation reactions follow different pathways.

PXRD can be used complementary in neutron powder diffraction, which is much more sensitive to Li atoms, and therefore very useful in *operando* battery measurements.[678] In comparison to PXRD, neutrons have exceptional angular resolution, good penetration depth, and moderate speed, but have several specific drawbacks, such as the need for deuterated electrolytes, and the challenge of instrument access.[679]

8.3 Single Particle Diffraction

While *in situ*/*operando* powder X-ray diffraction is an extremely powerful technique to study

crystalline structure dynamics in intercalation materials, it is limited to only probing many electrode particles at once. To observe structural details like lattice tilting and strain gradients in individual particles, single particle diffraction is needed. The focusing optics of a synchrotron X-ray source allows for a small beam diameter which reduces the scattering volume in an *in situ/operando* cell. A smaller scattering volume results in a spotted rather than complete Debye-Scherrer ring on a 2D detector. Each spot along the ring is the diffraction peak associated with a single particle of electrode material, and peak width and movement along the ring (χ rotation) is now resolvable. This unlocked resolution allows for the observation of phenomena like crystal mosaicity, particle rotation, and phase transition mechanisms in intercalation materials[651,652,680,681].

Single particle *in situ/operando* X-ray diffraction has been used to study multiple different battery intercalation materials. In Singer et al.[652], disordered $LiNi_{1/2}Mn_{3/2}O_4$, a spinel intercalation Li-ion cathode material, was studied using *operando* single particle XRD. They are able to resolve single particle peaks and report about particle rotation and lattice expansion and contraction. In addition, single particle diffraction revealed nonequilibrium dynamics of a structural phase transition in $LiNi_{1/2}Mn_{3/2}O_4$ where upon charge, the phase transition is facilitated by a solid solution of the two phases, but during discharge, the two phases are distinct and coexist in nanoparticles[652].

Single particle diffraction was also used to study a layered sodium-ion battery cathode material in Huang et al.[651]. Nanoparticle peaks of $Na_{2/3}[Ni_{1/3}Mn_{2/3}]O_2$ were resolved along the Debye-Scherrer ring using *operando* single particle XRD. From the dynamic peak width behavior of the single particles, increasing layer distortions were observed during charge. They also reported an aligning of crystalline layers just prior to the P2-O2 phase transition which revealed that the P2-O2 phase transition proceeds through an intermediate phase[651].

Work by Zhang and van Hulzen[680,681] also utilized small X-ray beam size to study single particle behavior in lithium iron phosphate (LFP) and lithium nickel manganese cobalt oxide (NMC) lithium-ion battery intercalation materials. By following single particle diffraction peaks, they were able to observe a variety of phase transition mechanisms. Specifically, they observed a rate dependent phase transition within single nanoparticles of LFP[680], first-order and solid solution phase transitions in LFP, and a solid solution phase transition in NMC[681].

8.4 Operando Bragg Coherent Diffractive Imaging

Bragg coherent diffraction imaging is excellently suited for studying electrochemical systems operando. The high penetration depth of hard X-rays (typically around 10 keV) allows collecting data from fully operational, multi-component devices, for example rechargeable battery coin cells in transmission geometry. Moreover, the high angular sensitivity of Bragg diffraction enables one to isolate signal from a specific crystal structure by tuning the scattering angle 2θ to the Bragg angle of that structure. Finally, the nanoparticulate systems often comprise of randomly oriented nanoparticles: most of the illuminated particles of the same crystal structure will generate no signal generating sparse diffraction profile on the Ewald sphere and allowing to isolate signal from a single nanocrystal buried in the electrode.

Operando BCDI has been extensively used to characterize the changes inside positive electrodes of rechargeable lithium-ion batteries[76,77,682–684]. The initial developments were led by Shpyrko, Meng and coauthors[682]. Typically, an *operando* coin-cell consists of a Lithium anode, separator, and cathode. As in commercial rechargeable lithium-ion batteries, the cathode is made of mostly active material (nanocrystals), mixed with carbon black for improved electrical conductivity, and a polymer matrix. The polymer binder creates space between the crystalline particles, which otherwise would degrade mechanically due to their swelling and shrinking during charge and discharge. After the electrode slurry is cast on the current collector, baking introduces pores,

which will later be filled with electrolyte providing access to the active nanocrystals. The electrode thickness is typically 50-100 μm, similar to conventionally created electrodes for electrochemical characterization. Prior to coin-cell assembly, openings in the stainless-steel coin-cell casting are made and covered with X-ray transparent kapton[685]. The transmission of the whole device at 10 keV is on the order of 50 %, with the cathode absorbing the most. In one *operando* BCDI study, the authors study 3D strain evolution of a single $LiNi_{0.5}Mn_{1.5}O_4$ $(500nm)^3$ nanocrystal in a fully operational coin cell battery under *operando* conditions during charge/discharge cycles[682]. *operando* strain imaging revealed a stripe morphology due to phase coexistence and coherency strain at the interface between the two phases. The authors were able to determine the stripe size and estimate the interface energy based on Cahn-Hilliard formalism[686]. Because BCDI maps the strain field inside a single nanocrystal, one can directly calculate the strain energy of the crystal by numerically integrating the strain field. The authors in[682] found a strain energy on the order of few femtojoules.

Point defects, such as Lithium vacancies, naturally occur during intercalation due to a change of the lithium-ion concentration and can be well characterized using average measurements and equilibrium modelling[687]. The importance of linear and planar defects in the properties of crystalline electrochemical systems is indisputable. Yet because extended defects are metastable, studying materials properties in their proximity remains challenging because it requires *operando* measurements. Therefore, recent BCDI studies focused on defect dynamics in individual nanoparticles operando. Shpyrho, Meng and co-authors reported *operando* 3D imaging of dislocation dynamics in individual battery cathode nanoparticles using BCDI[76] (see Figure 42, top). The defects were only mobile during charge or discharge, suggesting ionic diffusion as the driving force behind dislocation migration. Furthermore, the local displacement field around dislocations allowed the authors to map the local elastic constants around the defect. In

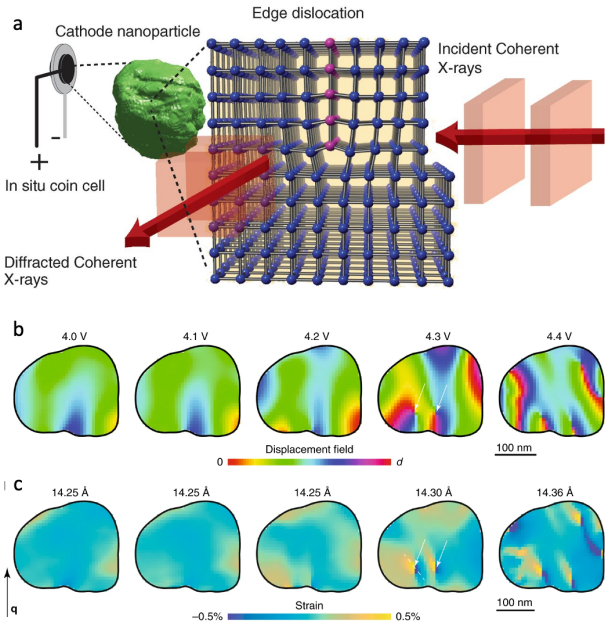

Figure 42: (a) Schematic of an *operando* Bragg Coherent Diffractive Imaging experiment. Coherent X-rays (red) are incident on a cathode nanoparticle (green) embedded in a fully operational coin-cell. A schematic of an edge dislocation for a cubic unit cell structure is shown with the extra half-plane colored purple. The diffracted X-rays carry information about the 3D density of Bragg planes and their atomic displacement along the reciprocal lattice vector. The latter allows identifying the type of dislocation. (Reprinted from Ref.[76]. Copyright 2015 American Association for the Advancement of Science). (b) The changes in the displacement field of a Li-rich layered oxide nanocrystal during charge (shown on a 2D slice through 3D particle). The voltage versus Li^+ is indicated. Two edge dislocations emerge at 4.3 V. (c) Strain calculated from the displacement field in (b). White arrows indicate the position of the edge dislocations at 4.3 V. (Reprinted from Ref.[77]. Copyright 2018 Springer Nature.)

a subsequent study, the same groups reported nucleation of dislocations inside a previously dislocation-free nanocrystal of a lithium-rich layered oxide material[77] (see Figure 42, bottom). The dislocations were also mobile and were associated with the notorious voltage fade in the high energy-density material. The authors used the results from *operando* BCDI to design and execute an annealing experiment, which led to the voltage recovery. Subsequent *operando* BCDI work showed the presence of 2D domain boundaries during a phase transformation[683] and a metastable antiphase-domain boundary during dislocation pair formation[688].

The BCDI method is a unique, powerful tool for studying lattice distortions inside individual nanocrystals. Yet due to the limited spatial resolution, the retrieved density of Bragg planes, i.e., the Ewald function, is generally not atomically sharp at the boundary. Therefore, a user-defined threshold (typically around 0.2 when the maximum of the Ewald function is 1) is used to somewhat arbitrarily define the particle boundary. To overcome the arbitrariness, some authors, when calculating properties such as strain energy, average over multiple threshold values[77]. Because of the slight ambiguity of where the particle boundary is, BCDI has lower surface sensitivity than other approaches, and *operando* BCDI was initially thought to be inapplicable for studying electrocatalytic reactions at the surface. Initial *operando* studies at open circuit conditions have revealed that structural rearrangements in bulk can occur[689], especially during dealloying[690] and thermal annealing[691].

Very recently, *operando* BCDI studies on electrocatalysts under potential control have been reported in different configurations. Sheyfer and coauthors imaged a nanograin of Pt inside of a polycrystalline Pt foil, which mechanically stabilizes the particle under intense irradiation.[692] A carefully positioned nanopipette supplied liquid electrolyte and reference/counter electrodes for high quality, low background diffraction, at the cost of complexity and poor quality electrochemistry. Atlan et al. imaged a more traditional Pt/C catalyst using a flow cell.[477] In both cases, substantial strain evolution on the exposed facets, corners, and edges is observed as a function of potential, attributed to electrolyte adsorption and surface oxidation. Comparison of the experimentally reconstructed nanoparticles with DFT or molecular dynamics simulations allows surface and bulk strain to be more confidently assessed. Furthermore, BCDI of nanoparticle electrocatalysts allow strain effects on dozens of facets with different surface crystallography to be analyzed simultaneously[477,691], along with edges and corner features which cannot be probed using single crystal approaches. The advent of fourth-generation X-ray synchrotron sources with highly spatially coherent beams and much-increased brightness will improve the spatial resolution and enhance the capability of *operando* BCDI to bulk and surface structural rearrangements inside smaller nanocrystals, which are relevant for electrocatalysis, and investigate phenomena next to their surface.

8.5 Operando Surface Scattering in Intercalation Batteries

Interface reactions critical for intercalation compounds. Therefore, X-ray surface scattering and diffraction have been used extensively for investigating the formation of solid-electrolyte-interphases and interfaces in both anode and cathode materials. In early work, Hirayama and others have developed an *in situ* cell for conducting *operando* surface studies in solid oxide cathodes[693–695]. They developed a cell with two modes alternating during the measurements: mode 1 with liquid electrolyte inside the cell for electrochemical reactions and mode 2 with liquid electrolyte out of the cell for X-ray measurements. Specifically, the work investigated the formation of the solid electrolyte interface on the layered oxides $LiCoO_2$ and $LiNi_{0.8}Co_{0.2}O_2$ and spinel oxide $LiMn_2O_4$. A critical development for these studies was synthesizing epitaxial thin films with surface roughness below 1 nm on electrically conducting substrates (for example, Nb-doped $SrTiO_3$), required for high-quality reflectivity data and quantitative fits for the present layers and their densities. Subsequent work on lithium-ion in-

tercalation hosts also included surface diffraction and bulk diffraction from thin films[696,697].

In situ X-ray surface scattering was also used for studying interfaces at the anode. For example, small and wide-angle scattering in epitaxial graphene on SiC showed LiF crystal growth with (002) planes parallel to graphene layers and the presence of other amorphous species in the solid-electrolyte interphase[698]. *In situ* X-ray reflectivity in CrSi multilayers revealed a predominant lithiation at interfaces[699]. Subsequent work used *operando* X-ray reflectivity to study interface roughness and propagation in conversion reactions and alloying in multilayers[700–704]. *Operando* GISAXS on patterned electrodes were used to elucidate dynamics during conversion reactions[705].

Toney and colleagues have used *in situ* X-ray reflectivity to investigate the electrochemical lithiation of silicon anodes, elucidating the formation process, structure, and behavior of the SEI layer in lithium-ion batteries[706–711]. They presented a mechanistic model of the first two (de)lithiation processes of a silicon wafer, highlighting the differences in reactions of Li ions with crystalline and amorphous structure and providing insights into the formation and evolution of the SEI layer on native oxide-terminated silicon anode[706]. They proposed a three-stage lithiation mechanism, with mechanistic insights into the SEI growth process revealing two well-defined inorganic SEI layers next to the Si anode[707–709]. Additionally, they used a model system combining electrochemical experiments with X-ray reflectivity measurements to quantitatively link capacity-fading mechanisms to electrochemical and chemical processes in lithium-ion batteries, identifying SEI growth as the major contribution to capacity fading and providing insights into the factors affecting SEI growth[710]. Overall, *operando* X-ray surface scattering contributed to a better understanding of the formation, structure, behavior, and growth mechanisms of the SEI layer.

9 Conclusions

In the past decades, *in situ* and *operando* X-ray scattering techniques have been developed into highly flexible tools for experimental research in electrochemistry and energy science. As shown above, these techniques can be applied to a large variety of sample materials and sample types, allowing to bridge the material gap between well-defined model systems and the complex systems employed in technological applications. Furthermore, they can provide structural information on length scales from the atomic to the micrometer scale, enabling characterization of complex, hierarchically structured materials, and on time scales from milliseconds to days. This allows to study a wide range of phenomena. The scope of these studies reaches from work aiming at a deep fundamental understanding of the atomic arrangement at electrochemical phase boundaries to the determination of structural changes of materials in actual devices.

X-ray scattering methods can be readily combined with other methods, allowing multimodal analysis. Obtaining simultaneously X-ray scattering and electrochemical data is routine in current *in situ* and *operando* studies. Furthermore, parallel probing the sample in other regions of the electromagnetic spectrum, e.g., by optical reflectivity[53,712,713], has already been demonstrated. On the horizon are experiments where X-ray scattering is performed together with spectroscopic characterization of the sample. Currently, such studies are performed via independent measurements by different techniques, but parallel data acquisition is in principle straightforward. An obvious extension would be combined studies by X-ray scattering and spectroscopic methods, such as X-ray fluorescence and X-ray absorption spectroscopy, as these signals are anyway generated by the incident beam. These would provide simultaneous structural data and information about the chemical composition and the oxidation states of relevant species, respectively. Also feasible is a combination with vibrational spectroscopy, specifically infrared absorption or Raman spectroscopy. These could provide parallel data

on molecular species, e.g., adsorbed intermediates. Such experiments would allow an unambiguous correlation of the electrode structure with data that pertain the electrode's reactivity, which would justify the higher experimental efforts required with such studies. As such multimodal characterization is also of interest in many fields outside of electrochemistry, the permanent installation of suitable setups is an emerging trend at high-end synchrotron sources.

Other future developments in this field are linked to the emergence of XFELs and fourth-generation synchrotron sources, which offer X-ray beams of unprecedented brilliance. With the first of these machines in the hard X-ray regime up and running and more of them on the horizon, X-ray scattering methods are developing into even more powerful tools. This development is still ongoing and will advance the more widespread use of these techniques as well as the development of even more sophisticated X-ray scattering methods and their applications to electrochemical systems. In particular, these new sources deliver beams that can be highly focused, have a high coherent fraction, and provide short X-ray pulses for ultrafast time-resolved measurements. These properties are advantageous for imaging material systems with high local resolution. One route here is mapping of the structure and other properties with nanobeams, the other is based on coherent imaging, which may now be applied to much smaller objects, such as nanoparticles with diameters of a few 10 nm or lower. The short pulses may be employed to address fundamental questions on the structural dynamics of electrochemical systems on femto- to nanosecond time scales. Such ultrafast X-ray scattering studies have already been demonstrated for molecular systems and thin films.[714–718] They necessarily employ pump-probe approaches and thus will require systems that allow highly repeatable measurements.

The new experimental capabilities pose on the other hand new challenges for *in situ* and *operando* studies. To avoid severe radiation effects when using intense, highly focused X-ray beams, novel approaches with regards to sample and cell geometry will be required. These may involve new methods of radiation product removal via fast electrolyte exchange, e.g., turbulent flow cells, scavenger molecules, or schemes for minimizing local exposure, such as rapid translation of the beam across the sample. For studies of individual nanoparticles, methods for strong anchoring on suitable substrates have to be developed. In addition, the application of *in situ* and *operando* X-ray scattering methods has to be extended to a wider range of systems, including highly reactive or uncommon electrode materials. For a fundamental understanding of the interfaces in such systems, studies of suitable model systems will be necessary. The latter will require setups that allow electrode preparation and characterization under UHV conditions and controlled transfer into electrochemical environment.

The high brilliance at high energies of 4th generation synchrotron sources also opens up possibilities to study in detail larger electrochemical devices, and materials within, typically used in industrial applications. Beside the fact that such experiments generate large amount of data due to the large probed volume, they also suffer from complicated diffraction patterns as many different materials are probed at the same time. Therefore significant effort still needs to be put forward to develop fast algorithms for data analysis, dealing with effects such the parallax, and employing machine learning to overcome the problem of large datasets. We also foresee that the upcoming instrumentation upgrades will allow X-ray scattering techniques to be part of of the artificial intelligence assisted materials discovery workflows by enabling high throughput *operando* and *in-situ* studies.

Overall, *in situ* and *operando* X-ray-based methods employing synchrotron radiation have tremendous capabilities for in-depth characterization of electrochemical systems. Together with computational methods, the results obtained by these methods can lead to crucial insights into the structure and properties of the involved complex materials and phase boundaries under reaction conditions. These provide a knowledge base for further developments in

energy science and many other areas of high technological relevance. However, the potential of synchrotron-based methods is still not fully tapped by the community, mainly because these approaches are considered technically challenging and time-consuming in terms of beam time acquisition and data analysis. The management of many synchrotron sources has realized this and is starting to initiate remedies. These range from support in data analysis by high-level software and experienced personnel to quick-access schemes for pressing research matters. *In situ* and *operando* studies are by nature more complex experiments than routine sample characterization and thus have been performed in the past predominantly by specialist groups that design dedicated setups for electrochemical research on their own. Such setups are now starting to be offered directly at the beamlines, making *in situ* and *operando* more accessible. We hope that the introduction to these techniques given in the present review helps to encourage the electrochemistry and energy science community to make larger use of these powerful tools and employ them for their research.

Table 2: Acronyms used in the text.

Acronym	Full name
1D	one-dimensional
2D	two-dimensional
3D	three-dimensional
AFM	atomic force microscopy
AIMD	ab initio molecular dynamics
AMPIX	Argonne multi-purpose in situ X-ray
ASAXS	anomalous small angle X-ray scattering
BCDI	Bragg coherent diffractive imaging
BD	bidentate
BN	binuclear
CMOS	complementary metal-oxide semiconductor
CO_2RR	carbon dioxide reduction reaction
COF	covalent organic framework
CORR	carbon monoxide reduction reaction
CS	corner-sharing
CTR	crystal truncation rod
CV	cyclic voltammetry
DCM	distorted crystal model
DFT	density functional theory
ECSA	electrochemically active surface area
ES	edge-sharing
ETEM	environmental transmission electron microscope
FA	fulvic acid
FS	face-sharing
FWHM	full width at half maximum
GDL	gas diffusion layer
GISAXS	grazing incidence small angle X-ray scattering
GIXRD	grazing incidence X-ray diffraction
GIXS	grazing incidence X-ray scattering
GTSAXS	grazing incidence transmission small-angle X-ray Scattering
HER	hydrogen evolution reaction
HESXRD	high energy surface X-ray diffraction
HOR	hydrogen oxidation reaction
ICP-MS	inductively coupled plasma mass spectrometry
IL	ionic liquid
IRF	instrumental resolution function
IS	inner sphere
LFP	lithium iron phovsphate
LPTEM	liquid phase transmission electron microscope

Table 2: Acronyms used in the text. (cont.)

Acronym	Full name
MD	molecular dynamics
MEA	membrane electrode assembly
ML	monolayer
MN	mononuclear
MoD	monodentate
NMC	lithium nickel manganese cobalt oxide
NRR	N_2 reduction reaction
OER	oxygen evolution reaction
ORR	oxygen reduction reaction
OS	outer sphere
PDF	pair distribution function
PEEK	polyether ether ketone
PEG	polyethylene glycol
PEM(FC)	proton exchange membrane (fuel cell)
PGM	platinum group metal
PV	pseudo-Voigt
PXRD	powder X-ray diffraction
QXAFS	quick scan X-ray absorption fine structure
RASXS	resonant anomalous surface X-ray scattering
RAXS	resonance anomalous X-ray scattering
RHE	reversible hydrogen electrode
SAXS	small angle X-ray scattering
SOFC	solid oxide fuel cell
STM	scanning tunneling microscopy
SXRD	surface X-ray diffraction
TD	tridentate
TeD	tetradentate
TEM	transmission electron microscope
TMSAXS	transmission small angle X-ray scattering
TN	trinuclear
UHV	ultrahigh vacuum
UPD	under potential deposition
WAXS	wide angle X-ray scattering
XANES	X-ray absorption near edge spectroscopy
XAS	X-ray absorption spectroscopy
XFEL	X-ray free electron laser
XPCS	X-ray photon correlation spectroscopy
XRD	X-ray diffraction
XRD-CT	X-ray diffraction computed tomography
XRR	X-ray reflectivity
XRV	X-ray voltammogram
XSW	X-ray standing wave

Table 3: Symbols used in the text.

α_c	critical angle
α_f	exit angle
α_i	incident angle
α	phase factor
$\bar{n}$	density functional operator
δ_{ij}	Kroneker delta
ϵ_{ph}	photon energy
ϵ	wave field vector
η	mixing parameter
$\hbar$	reduced Planck constant
λ	X-ray wavelength
Λ	penetration depth
μ	attenuation coefficient
Ω	profile function
ϕ	phase
ρ_e	electron density
$\rho(r)$	pair density function
σ_0	layer width
θ	Bragg angle
2θ	scattering angle
θ_j	occupancy of site j
a_1, a_2, a_3	lattice vector
b_1, b_2, b_3	reciprocal space vector
$f_{0,j}$	atomic form factor of atom j
f',f''	dispersion corrections
F	structure factor
$F_N R$	non-resonant structure factor
$F_N R$	resonant structure factor
G_{hkl}	reciprocal lattice point
$g(R)$	pair distribution function
$G(r)$	reduced pair distribution function
h, k, l	Miller indices
H	peak width
I	scattering intensity
k_f	scattered wave vector
k_i	incident wave vector
k	wave vector
M	Debye Waller factor
N_n	number of unit cells
n	index of refraction
P	particle form factor
q	scattering vector
Q	momentum transfer
R_G	radius of gyration
r	distance vector
$\mathbf{R}$	difference vector
R	distance vector
s_{hkl}	density of hkl Bragg planes
$S(\mathbf{Q})$	scattering amplitude
$S_t(Q)$	total scattering structure function
$S_L(Q)$	liquid structure factor
T	domain size
$\mathbf{u}$	displacement vector
V_c	unit cell volume

10 Biographies

Olaf Magnussen is a full professor of solid state physics at Kiel University, Germany, since 2001. He obtained his PhD from Ulm University, Germany, in the group of Prof. Jürgen Behm in 1993. After a Postdoc with Dr. Ben Ocko at Brookhaven National Laboratory he returned to Ulm, where he obtained his habilitation in 2001. Focus of his research are studies of the atomic-scale structure and dynamics of electrochemical interfaces. He has been employing synchrotron-based *in situ* and *operando* X-ray scattering techniques for the past 30 years to studies of electrode surface structure, adsorbate layers, liquid-liquid interfaces, electrodeposition, corrosion, and electrocatalytic processes. His current research focuses on *operando* studies of electrocatalysts for energy conversion, in particular, by employing high-energy surface scattering methods.

Jakub Drnec obtained his PhD degree at University of Victoria, Canada, in the field of surface electrochemistry. Currently he is a beamline scientist at European Synchrotron (ESRF) in Grenoble (France), developing new high energy X-rays experimental techniques to study materials for energy conversion and storage. His main goal is to probe materials in their working environment in order to better understand their functioning. His current projects involve *operando* investigations of fuel cells and batteries, fundamental studies of electrocatalyst's degradation and structure-activity relationships, and development of *operando* electrochemical cells and data analysis routines.

Canrong Qiu received his Ph.D. degree in 2016 from University of Alaska Fairbanks, USA in the field of environmental chemistry under the supervision of Prof. Thomas P. Trainor. After his Ph.D., he moved to Germany and worked as a postdoc with Dr. Moritz Schmidt at Helmholtz Zentrum Dresden Rossendorf and Olaf Magnussen at Kiel University. Since November 2022, he has been working as a staff scientist at the P25 beamline of PETRA III at Deutsches Elektronen-Synchrotron (DESY) in Hamburg. His research interest includes resolving and characterizing molecular-scale interfacial processes of different adsorbates on environment or energy relevant substrates using modern synchrotron X-ray techniques. In addition, he is also developing Python-based high performance data analysis software, in particular, the open-source DaFy software package (https://github.com/jackey-qiu/DaFy) for processing and modeling surface X-ray diffraction data.

Isaac Martens recieved his B.Sc. in Biochemistry from the University of Calgary, before completing his Ph.D. studies at the University of British Columbia on in situ electrochemistry under supervision of D. Bizzotto and D.P. Wilkinson. He recently completed a postdoctoral appointment at the European Synchrotron Radiation Facility developing operando techniques for battery studies.

Jason Huang is a Ph.D. candidate at Cornell University in the lab of Prof. Andrej Singer where he studies the dynamics and defect mechanisms of electrochemically active crystalline materials using advanced in situ and operando X-ray scattering techniques. Previously, he received his B.S. (2019) in Nanoengineering from the University of California, San Diego. There, he worked in the lab of Prof. Ping Liu and studied materials for Li-ion and Li-metal batteries. Jason is interested in understanding how active materials change under electrochemical environments and applying those findings to develop the next generation of energy materials.

Raphaël Chattot obtained his Ph.D. in Electrocatalysis from the University of Grenoble-Alpes in 2017 under the direction of Dr. Frédéric Maillard and Dr. Laetitia Dubau. After an 18-month period as a postdoctoral researcher between the Laboratory of Electrochemistry and Physicochemistry of Materials and Interfaces (LEPMI, Grenoble, France) and the European Synchrotron Radiation Facility (ESRF, Grenoble, France) he joined the ESRF as a Junior Scientist at the ID31 beamline (Jakub Drnec and Veijo Honkimäki's group). Since 2021 he is a permanent researcher of the French National Center for Scientific Research (CNRS) at the Institute Charles Gerhardt (ICGM, Montpellier France). His research focuses notably on exploring the funda-

mental role of nanoscale structural disorder in electrocatalysis for energy conversion systems such as fuel cells and water electrolyzers by means of advanced *in situ* and *operando* X-ray scattering techniques.

Andrej Singer received his Ph.D. (2012) in Physics from the University of Hamburg, Germany in the lab of Prof. Edgar Weckert and Prof. Ivan Vartanyants, following a Physics diploma from the University of Muenster, Germany. He studied the properties of new X-ray sources, particularly their ability to generate interference patterns, similar to lasers in optics. He then worked as a Postdoc in the lab of Prof. Oleg Shpyrko at the University of California, San Diego. Dr Singer's group uses coherent X-ray scattering techniques at synchrotrons and free-electron lasers to study a wide range of materials, spanning from quantum materials to applied energy materials in operando dbtained his PhD degree at University of Victoria, Canada, in the field of surface electrochemistry. He is a beamline scientist at European Synchrotron (ESRF) in Grenoble (France), developing new high energy X-rays experimental techniques to study materials for energy conversion and storage. His main goal is to probe materials in their working environment in order to better understand their functioning. His current projects involve operando investigations of fuel cells and batteries, fundamental studies of electrocatalyst's degradation and structure-activity relationships, and development of operando electrochemical cells and data analysis routines.evices. Dr. Singer is interested in understanding the fundamental properties of energy materials and quantum materials out-of-equilibrium.

Acknowledgement O. M. M. and C. Q. acknowledge financial support by the German Federal Ministry of Education and Research (BMBF) via Project 05K19FK3. R.C acknowledge financial support from the French National Research Agency through the HOLYCAT project (grant number n○ ANR-22-CE05-0007). Work at Cornell University was supported by the Center for Alkaline-based Energy Solutions, an Energy Frontier Research Center funded by DOE, Office of Science, BES under Award # DE-SC0019445.

References

(1) Kolb, D.; Rath, D.; Wille, R.; Hansen, W. An ESCA study on the electrochemical double layer of emersed electrodes. *Ber. Bunsenges. Phys. Chem* **1983**, *87*, 1108–1113.

(2) Kolb, D. Surface science aspects of interfacial electrochemistry. *J. Vac. Sci. Technol. A* **1986**, *4*, 1294–1391.

(3) Als-Nielsen, J.; McMorrow, D. *Elements of modern X-ray physics*; Wiley, NY, 2001.

(4) Feidenhans'l, R. Surface structure determination by X-ray diffraction. *Surf. Sci. Rep.* **1989**, *10*, 105.

(5) Robinson, I. K.; Tweet, D. J. *Surface X-ray diffraction*; IOP Publishing, 1992; Vol. 55; p 599.

(6) Vlieg, E. In *Surface and interface science*; K.Wandelt, Ed.; Wiley-VCH, NY, 2013; Vol. 1; pp 375–425.

(7) Ewald, P. P. X-ray diffraction by finite and imperfect crystal lattices. *Proc. Phys. Soc.* **1940**, *52*, 167–174.

(8) Vartanyants, I. A.; Robinson, I. K. Partial coherence effects on the imaging of small crystals using coherent x-ray diffraction. *J. Phys.: Condens. Matter* **2001**, *13*, 10593.

(9) Vlieg, E. Characterization of solid-liquid interfaces using X-ray diffraction. 2004; p 31.

(10) Chaikin, P. M.; Lubensky, T. C. *Principles of condensed matter physics*; Cambridge University Press, Cambridge, 1995.

(11) Keen, D. A comparison of various commonly used correlation functions for describing total scattering. *Journal of Applied Crystallography* **2001**, *34*, 172–177.

(12) Pershan, P.; Schlossman, M. *Liquid surfaces and interfaces*; Cambride University Press, Cambridge, 2012.

(13) Magnussen, O.; Ocko, B.; Regan, M.; Penanen, K.; Pershan, P.; Deutsch, M. X-ray reflectivity measurements of surface layering in liquid mercury. *Phys. Rev. Lett* **1995**, *74*, 4444–4447.

(14) Guinier, A.; Fournet, G. *Small-angle scattering of X-rays*; Structure of matter series; Wiley, 1955.

(15) Gommes, C. J.; Jaksch, S.; Frielinghaus, H. Small-angle scattering for beginners. *J. Appl. Crystallogr.* **2021**, *54*, 1832–1843.

(16) Sun, Y. Anomalous small-angle X-ray scattering for materials chemistry. *Trends Chem.* **2021**, *3*, 1045–1060.

(17) Bazin, D. Anomalous wide angle X-ray scattering (AWAXS) and heterogeneous catalysts. *Appl. Catal., A* **2002**, *226*, 87–113.

(18) Bazin, D.; Lynch, J.; Ramos-Fernandez, M. X-ray absorption spectroscopy and anomalous wide angle X-ray scattering: Two basic tools in the analysis of heterogeneous catalysts. *Oil Gas Sci. Technol.* **2003**, *58*, 667–683.

(19) Yu, C.; Koh, S.; Leisch, J. E.; Toney, M. F.; Strasser, P. Size and composition distribution dynamics of alloy nanoparticle electrocatalysts probed by anomalous small angle X-ray scattering (ASAXS). *Faraday Discuss.* **2009**, *140*, 283–296.

(20) Gilbert, J. A.; Kariuki, N. N.; Subbaraman, R.; Kropf, A. J.; Smith, M. C.; Holby, E. F.; Morgan, D.; Myers, D. J. In Situ anomalous small-angle X-ray scattering studies of platinum nanoparticle fuel cell electrocatalyst degradation. *J. Am. Chem. Soc.* **2012**, *134*, 14823–14833.

(21) Gilbert, J. A.; Kariuki, N. N.; Wang, X.; Kropf, A. J.; Yu, K.; Groom, D. J.; Ferreira, P. J.; Morgan, D.; Myers, D. J. Pt catalyst degradation in aqueous and fuel cell environments studied via in-operando anomalous small-angle X-ray scattering. *Electrochim. Acta* **2015**, *173*, 223–234.

(22) Hemberg, O.; Otendal, M.; Hertz, H. M. Liquid-metal-jet anode electron-impact x-ray source. *Appl. Phys. Lett.* **2003**, *83*, 1483–1485.

(23) Bartzsch, S.; Oelfke, U. Line focus x-ray tubes—a new concept to produce high brilliance x-rays. *Phys. Med. Biol.* **2017**, *62*, 8600.

(24) Baruchel, J., Hodeau, J.-L., Lehmann, M. S., Regnard, J.-R., Schlenker, C., Eds. *Neutron and synchrotron radiation for condensed matter studies*; Springer, Heidelberg, 1994.

(25) Willmott, P. *An introduction to synchrotron radiation: Techniques and applications*; Wiley, 2019.

(26) Kaduk, J. A.; Billinge, S. J.; Dinnebier, R. E.; Henderson, N.; Madsen, I.; Černý, R.; Leoni, M.; Lutterotti, L.; Thakral, S.; Chateigner, D. Powder diffraction. *Nat. Rev. Methods Primers* **2021**, *1*, 77.

(27) Phillips, J. C.; Cerino, J. A.; Hodgson, K. O. A four-circle diffractometer on a focused, tuneable synchrotron radiation source: mechanical design, computer control and evaluation of system performance. *J. Appl. Crystallogr.* **1979**, *12*, 592–600.

(28) Lohmeier, M.; Vlieg, E. Angle calculations for a six-circle surface X-ray diffractometer. *J. Appl. Crystallogr.* **1993**, *26*, 706–716.

(29) Murphy, B.; Greve, M.; Runge, B.; Koops, C.; Elsen, A.; Stettner, J.; Seeck, O.; Magnussen, O. A novel X-ray

diffractometer for studies of liquid-liquid interfaces. *J. Synchrotron Radiat.* **2014**, *21*, 45–56.

(30) Schlepütz, C. M.; Mariager, S. O.; Pauli, S. A.; Feidenhans'l, R.; Willmott, P. R. Angle calculations for a (2+3)-type diffractometer: focus on area detectors. *J. Appl. Crystallogr.* **2010**, *44*, 73–83.

(31) Kieffer, J.; Karkoulis, D. PyFAI, a versatile library for azimuthal regrouping. *J. Phys. Conf. Ser.* **2013**, *425*, 202012.

(32) Drnec, J.; Zhou, T.; Pintea, S.; Onderwaater, W.; Vlieg, E.; Renaud, G.; Felici, R. Integration techniques for surface X-ray diffraction data obtained with a two-dimensional detector. *J. Appl. Crystallogr.* **2014**, *47*, 365–377.

(33) Roobol, S.; Onderwaater, W.; Drnec, J.; Felici, R.; Frenken, J. BINoculars: data reduction and analysis software for two-dimensional detectors in surface X-ray diffraction. *J. Appl. Crystallogr.* **2015**, *48*, 1324–1329.

(34) Harlow, G. S.; Pfaff, S.; Abbondanza, G.; Hegedüs, Z.; Lienert, U.; Lundgren, E. HAT: a high-energy surface X-ray diffraction analysis toolkit. *J. Appl. Crystallogr.* **2023**, *56*, 312–321.

(35) Favre-Nicolin, V.; Girard, G.; Leake, S.; Carnis, J.; Chushkin, Y.; Kieffer, J.; Paleo, P.; Richard, M.-I. *PyNX*: high-performance computing toolkit for coherent X-ray imaging based on operators. *J. Appl. Crystallogr.* **2020**, *53*, 1404–1413.

(36) GSAS-II. `https://subversion.xray.aps.anl.gov/trac/pyGSAS`, Accessed: 2023-04-11.

(37) TOPAS. `https://www.bruker.com/fr/products-and-solutions/diffractometers-and-x-ray-microscopes/x-ray-diffractometers/diffrac-suite-software/diffrac-topas.html`, Accessed: 2023-04-11.

(38) FullProf. `https://www.ill.eu/sites/fullprof/`, Accessed: 2023-04-11.

(39) PDFGUI. `https://www.diffpy.org/products/pdfgui.html`, Accessed: 2023-04-11.

(40) DISCUS. `https://tproffen.github.io/DiffuseCode/`, Accessed: 2023-04-11.

(41) SASView. `https://www.sasview.org/`, Accessed: 2023-04-11.

(42) BornAgain. `https://www.bornagainproject.org/`, Accessed: 2023-04-11.

(43) GenX. `https://aglavic.github.io/genx/`, Accessed: 2023-04-11.

(44) ANA-ROD. `https://www.esrf.fr/computing/scientific/joint_projects/ANA-ROD/index.htm`, Accessed: 2023-04-11.

(45) BINoculars. `https://github.com/id03/binoculars`, Accessed: 2023-04-11.

(46) pyNX. `https://www.esrf.fr/computing/scientific/PyNX/README.html`, Accessed: 2023-04-11.

(47) IUCr software. `https://www.iucr.org/resources/other-directories/software`, Accessed: 2023-04-11.

(48) Stoecker, W. C.; Starbuck, J. W. Effect of soller slits on X-ray intensity in a modern diffractometer. *Rev. Sci. Instrum.* **1965**, *36*, 1593–1598.

(49) Kowarik, S.; Bogula, L.; Boitano, S.; Carlà, F.; Pithan, H.; Schäfer, P.; Wilming, H.; Zykov, A.; Pithan, L. A novel 3D printed radial collimator for x-ray diffraction. *Rev. Sci. Instrum.* **2019**, *90*, 035102.

(50) Olsson, A.; Hellsing, M. S.; Rennie, A. R. New possibilities using additive manufacturing with materials that are difficult to process and with complex structures. *Phys. Scripta* **2017**, *92*, 053002.

(51) Chen, Y.; Han, D.; Wang, J.; Yang, Y.; Hu, W. Stacking of micro-aperture arrays: A new strategy to construct Söller collimator for x rays. *Rev. Sci. Instrum.* **2020**, *91*.

(52) Magnussen, O.; Krug, K.; Ayyad, A.; Stettner, J. In situ diffraction studies of electrode surface structure during gold electrodeposition. *Electrochim. Acta* **2008**, *53*, 3449–3458.

(53) Reikowski, F.; Maroun, F.; Pacheco, I.; Wiegmann, T.; Allongue, P.; Stettner, J.; Magnussen, O. M. Operando surface X-ray diffraction studies of structurally defined Co3O4 and CoOOH thin films during oxygen evolution. *ACS Catal.* **2019**, *9*, 3811–3821.

(54) Asset, T.; Gommes, C. J.; Drnec, J.; Bordet, P.; Chattot, R.; Martens, I.; Nelayah, J.; Job, N.; Maillard, F.; Dubau, L. Disentangling the degradation pathways of highly defective PtNi / C nanostructures – an operando wide and small angle X-ray scattering study. *ACS Catal.* **2019**, *9*, 160–167.

(55) Redoxme AB, Magnetic mount gas diffusion electrode X-ray diffraction electrochemical cell. 2023; `https://redox.me/collections/spectro-electrochemical-cells/products/gde-xrd-ec-1-75-ml-gas-diffusion-electrode-x-ray-diffraction-electrochemical-cell`.

(56) Petkov, V. et al. Nanoalloy catalysts inside fuel cells: An atomic-level perspective on the functionality by combined in operando x-ray spectroscopy and total scattering. *Nano Energy* **2018**, *49*, 209–220.

(57) Martens, I. et al. X-ray transparent proton-exchange membrane fuel cell design for in situ wide and small angle scattering tomography. *J. Power Sources* **2019**, *437*, 226906.

(58) Moss, A. B.; Hätinen, J.; Kúš, P.; Garg, S.; Mirolo, M.; Chorkendorff, I.; Seger, B.; Drnec, J. Versatile high energy X-ray transparent electrolysis cell for operando measurements. *J. Power Sources* **2023**, *562*, 232754.

(59) Benck, J. D.; Rettenwander, D.; Jackson, A.; Young, D.; Chiang, Y.-M. Apparatus for *operando* x-ray diffraction of fuel electrodes in high temperature solid oxide electrochemical cells. *Rev. Sci. Instrum.* **2019**, *90*, 023910.

(60) Chattot, R. et al. Electrochemical strain dynamics in noble metal nanocatalysts. *J. Am. Chem. Soc.* **2021**, *143*, 17068–17078.

(61) Henderson, R. The potential and limitations of neutrons, electrons and X-rays for atomic resolution microscopy of unstained biological molecules. *Q. Rev. Biophys.* **1995**, *28*, 171–193.

(62) Bras, W.; Myles, D. A. A.; Felici, R. When x-rays alter the course of your experiments. *J. Phys.: Condens. Matter* **2021**, *33*, 423002.

(63) Caër, S. L. Water radiolysis: Influence of oxide surfaces on H2 production under ionizing radiation. *Water* **2011**, *3*, 235–253.

(64) Hill, M.; Smith, F. Calculation of initial and primary yields in the radiolysis of water. *Radiat. Phys. Chem.* **1994**, *43*, 265–280.

(65) Uehara, S.; Nikjoo, H. Monte Carlo simulation of water radiolysis for low-energy charged particles. *J. Radiat. Res.* **2006**, *47*, 69–81.

(66) Terrissol, M.; Beaudre, A. Simulation of space and time evolution of radiolytic species induced by electrons in water. *Radiat. Prot. Dosim.* **1990**, *31*, 175–177.

(67) Swallow, A. J. In *Radiation chemistry of organic compounds: International series*

of monographs on radiation effects in materials; Charlesby, A., Ed.; Pergamon: Amsterdam, 2016; OCLC: 1100973316.

(68) Roots, R.; Okada, S. Estimation of life times and diffusion distances of radicals involved in X-ray-induced DNA strand breaks or killing of mammalian cells. *Radiat. Res.* **1975**, *64*, 306.

(69) Spotheim-Maurizot, M.; Mostafavi, M.; Douki, T.; Belloni, J. *Radiation chemistry : From basics to applications in material and life sciences*; EDP Sciences, Les Ulis, France, 2008.

(70) Fritsch, B.; Körner, A.; Couasnon, T.; Blukis, R.; Taherkhani, M.; Benning, L. G.; Jank, M. P. M.; Spieker, E.; Hutzler, A. Tailoring the acidity of liquid media with ionizing radiation – rethinking the acid-base correlation beyond pH. *J. Phys. Chem. Lett.* **2023**, *14*, 4644–4651.

(71) Thomä, S. L. J.; Zobel, M. Beam-induced redox chemistry in iron oxide nanoparticle dispersions at ESRF–EBS. *J. Synchrotron Radiat.* **2023**, *30*, 440–444.

(72) Fritsch, B. et al. Radiolysis-driven evolution of gold nanostructures – model verification by scale bridging in situ liquid-phase transmission electron microscopy and X-ray diffraction. *Adv. Sci.* **2022**, *9*, 2202803.

(73) Fourme, R.; Honkimäki, V.; Girard, E.; Medjoubi, K.; Dhaussy, A.-C.; Kahn, R. Reduction of radiation damage and other benefits of short wavelengths for macromolecular crystallography data collection. *J. Appl. Crystallogr.* **2012**, *45*, 652–661.

(74) Pfeifer, M. A.; Williams, G. J.; Vartanyants, I. A.; Harder, R.; Robinson, I. K. Three-dimensional mapping of a deformation field inside a nanocrystal. *Nature* **2006**, *442*, 63–66.

(75) Robinson, I.; Harder, R. Coherent X-ray diffraction imaging of strain at the nanoscale. *Nat. Mater.* **2009**, *8*, 291–8.

(76) Ulvestad, A.; Singer, A.; Clark, J. N.; Cho, H. M.; Kim, J. W.; Harder, R.; Maser, J.; Meng, Y. S.; Shpyrko, O. G. Topological defect dynamics in operando battery nanoparticles. *Science* **2015**, *348*, 1344–1347.

(77) Singer, A. et al. Nucleation of dislocations and their dynamics in layered oxide cathode materials during battery charging. *Nat. Energy* **2018**, *3*, 641–647.

(78) Renaud, G.; Lazzari, R.; Leroy, F. Probing surface and interface morphology with Grazing Incidence Small Angle X-Ray Scattering. *Surf. Sci. Rep.* **2009**, *64*, 255–380.

(79) Hejral, U. et al. High-energy X-ray diffraction from surfaces and nanoparticles. *Phys. Rev. B* **2017**, *96*, 195433/1.

(80) Egami, T.; Billinge, S. J. In *Pergamon Materials Series*, 2nd ed.; Takeshi Egami, S. J. B., Ed.; Elsevier Inc., 2012; Vol. 16; p 55–111.

(81) Clearfield, A.; Reibenspies, J. H.; Bhuvanesh, N. E. *Principles and applications of powder diffraction*; Wiley, 2009.

(82) Pfeiffer, F. X-ray ptychography. *Nat. Photonics* **2017**, *12*, 9–17.

(83) Park, C.; Fenter, P. A.; Sturchio, N. C.; Regalbuto, J. R. Probing outer-sphere adsorption of aqueous metal complexes at the oxide-water interface with resonant anomalous X-ray reflectivity. *Phys. Rev. Lett.* **2005**, *94*, 076104.

(84) Park, C.; Fenter, P. A. Phasing of resonant anomalous X-ray reflectivity spectra and direct Fourier synthesis of element-specific partial structures at buried interfaces. *J. Appl. Crystallogr.* **2007**, *40*, 290–301.

(85) Li, T.; Senesi, A. J.; Lee, B. Small angle X-ray scattering for nanoparticle research. *Chem. Rev.* **2016**, *116*, 11128–11180.

(86) Pauw, B. R. Everything SAXS: small-angle scattering pattern collection and correction. *J. Phys.: Condens. Matter* **2013**, *25*, 383201.

(87) Dinnebier, R. E.; Billinge, S. J. L. *Powder diffractiom: theory and practice*; Royal Society of Chemistry, 2008.

(88) Percharsky, K., Vitalij; Zavalij, P. Y. *Fundamentals of powder diffraction and structural characterization of materials*; Springer US: Boston, MA, 2009.

(89) Bunge, H. J. Influence of texture on powder diffraction. *Texture. Microstruct.* **1997**, *29*, 1–26.

(90) Rietveld, H. M. A profile refinement method for nuclear and magnetic structures. *J. Appl. Crystallogr.* **1969**, *2*, 65–71.

(91) Thompson, P.; Cox, D. E.; Hastings, J. B. Rietveld refinement of Debye–Scherrer synchrotron X-ray data from Al2O3. *J. Appl. Crystallogr.* **1987**, *20*, 79–83.

(92) Balzar, D. et al. Size-strain line-broadening analysis of the ceria round-robin sample. *J. Appl. Crystallogr.* **2004**, *37*, 911–924.

(93) Scherrer, P. Bestimmung der größe und der inneren struktur von kolloidteilchen mittels röntgenstrahlen. *Nachrichten von der Gesellschaft der Wissenschaften zu Göttingen, Mathematisch-Physikalische Klasse* **1918**, *1918*, 98–100.

(94) Takeshi, E.; Billinge, S. J. *Pergamon Materials Series*; 2012; Vol. 16; p 55–111.

(95) Festersen, S.; Runge, B.; Koops, C.; Bertram, F.; Ocko, B.; Deutsch, M.; Murphy, B. M.; Magnussen, O. M. Nucleation and growth of PbBrF crystals at the liquid mercury-electrolyte interface studied by operando X-ray scattering. *Langmuir* **2020**, *36*, 10905–10915.

(96) Magnussen, O. M.; Ocko, B. M.; Wang, J. X.; Adzic, R. R. In-situ X-ray diffraction and STM studies of bromide adsorption on Au(111) electrodes. *J. Phys. Chem.* **1996**, *100*, 5500–5508.

(97) Gustafson, J.; Shipilin, M.; Zhang, C.; Stierle, A.; Hejral, U.; Ruett, U.; Gutowski, O.; Carlsson, P. A.; Skoglundh, M.; Lundgren, E. High-energy surface X-ray diffraction for fast surface structure determination. *Science* **2014**, *343*, 758–761.

(98) Fuchs, T.; Drnec, J.; Calle-Vallejo, F.; Stubb, N.; Sandbeck, D. J. S.; Ruge, M.; Cherevko, S.; Harrington, D. A.; Magnussen, O. M. Structure dependency of the atomic-scale mechanisms of platinum electro-oxidation and dissolution. *Nat. Catal.* **2020**, *3*, 754–761.

(99) Fuchs, T.; Briega-Martos, V.; Drnec, J.; Stubb, N.; Martens, I.; Calle-Vallejo, F.; Harrington, D. A.; Cherevko, S.; Magnussen, O. M. Anodic and cathodic platinum dissolution processes involve different oxide species. *Angew. Chem. Int. Ed.* **2023**, *34*, e202304293.

(100) Fuchs, T.; Briega-Martos, V.; Fehrs, J. O.; Qiu, C. R.; Mirolo, M.; Yuan, C. T.; Cherevko, S.; Drnec, J.; Magnussen, O. M.; Harrington, D. A. Driving force of the initial step in electrochemical Pt(111) oxidation. *J. Phys. Chem. Lett.* **2023**, *14*, 3589–3593.

(101) Jacobse, L.; Vonk, V.; McCrum, I. T.; Seitz, C.; Koper, M. T.; Rost, M. J.; Stierle, A. Electrochemical oxidation of Pt(111) beyond the place-exchange model. *Electrochim. Acta* **2022**, *407*, 139881.

(102) Reikowski, F.; Wiegmann, T.; Stettner, J.; Drnec, J.; Honkimaeki, V.; Maroun, F.; Allongue, P.; Magnussen, O. M. Transmission surface diffraction for operando studies of heterogeneous interfaces. *J. Phys. Chem. Lett.* **2017**, *8*, 1067–1071.

(103) Wiegmann, T.; Drnec, J.; Reikowski, F.; Stettner, J.; Maroun, F.; Magnussen, O. M. In situ transmission X-ray micro-diffraction from thin metal films electrodeposited in microfluidic channels. *J. Electrochem. Soc.* **2020**, *167*, 112505.

(104) Zhang, Y.; Chen, S.; Cai, Y.; Lu, L.; Fan, D.; Shi, J.; Huang, J.; Luo, S.-N. Novel X-ray and optical diagnostics for studying energetic materials: A review. *Engineering* **2020**, *6*, 992–1005.

(105) Dekker, F.; Kuipers, B.; Petukhov, A.; Tuinier, R.; Philipse, A. Scattering from colloidal cubic silica shells: Part I, particle form factors and optical contrast variation. *J. Colloid Interface Sci.* **2020**, *571*, 419–428.

(106) Gommes, C. J.; Chattot, R.; Drnec, J. Stochastic models of dense or hollow nanoparticles and their scattering properties. *J. Appl. Crystallogr.* **2020**, *53*, 811–823.

(107) Ruge, M.; Drnec, J.; Rahn, B.; Reikowski, F.; Harrington, D. A.; Carla, F.; Felici, R.; Stettner, J.; Magnussen, O. M. Structural reorganization of Pt(111) electrodes by electrochemical oxidation and reduction. *J. Am. Chem. Soc.* **2017**, *139*, 4532–4539.

(108) Lu, X.; Yager, K. G.; Johnston, D.; Black, C. T.; Ocko, B. M. Grazing-incidence transmission X-ray scattering: surface scattering in the Born approximation. *J. Appl. Crystallogr.* **2013**, *46*, 165–172.

(109) Snigirev, A.; Kohn, V.; Snigireva, I.; Lengeler, B. A compound refractive lens for focusing high-energy X-rays. *Nature* **1996**, *384*, 49–51.

(110) Mimura, H. et al. Breaking the 10-nm barrier in hard-X-ray focusing. *Nat. Phys.* **2010**, *6*, 122–125.

(111) Singer, A.; Vartanyants, I. A. Coherence properties of focused X-ray beams at high-brilliance synchrotron sources. *J. Synchrotron Radiat.* **2014**, *21*, 5–15.

(112) Qazilbash, M. M. et al. Nanoscale imaging of the electronic and structural transitions in vanadium dioxide. *Phys. Rev. B* **2011**, *83*, 165108.

(113) Singer, A. et al. Nonequilibrium Phase Precursors during a Photoexcited Insulator-to-Metal Transition in V2O3. *Phys. Rev. Lett.* **2018**, *120*, 207601.

(114) Hruszkewycz, S. O.; Folkman, C. M.; Highland, M. J.; Holt, M. V.; Baek, S. H.; Streiffer, S. K.; Baldo, P.; Eom, C. B.; Fuoss, P. H. X-ray nanodiffraction of tilted domains in a poled epitaxial BiFeO3 thin film. *Appl. Phys. Lett.* **2011**, *99*, 232903.

(115) Luo, A. et al. X-ray nano-imaging of defects in thin film catalysts via cluster analysis. *Appl. Phys. Lett.* **2022**, *121*, 153904.

(116) Christiansen-Salameh, J. et al. Understanding nanoscale structural distortions in Pb(Zr(0.2)Ti(0.8))O(3) by utilizing X-ray nanodiffraction and clustering algorithm analysis. *J. Synchrotron Radiat.* **2021**, *28*, 207–213.

(117) Williams, G. J.; Pfeifer, M. A.; Vartanyants, I. A.; Robinson, I. K. Three-dimensional imaging of microstructure in Au nanocrystals. *Phys. Rev. Lett.* **2003**, *90*, 175501.

(118) Ulvestad, A. et al. Avalanching strain dynamics during the hydriding phase transformation in individual palladium nanoparticles. *Nat. Commun.* **2015**, *6*, 10092.

(119) Bjorling, A.; Marcal, L. A. B.; Solla-Gullon, J.; Wallentin, J.; Carbone, D.; Maia, F. Three-dimensional coherent Bragg imaging of rotating nanoparticles. *Phys. Rev. Lett.* **2020**, *125*, 246101.

(120) Wu, L.; Yoo, S.; Suzana, A. F.; Assefa, T. A.; Diao, J.; Harder, R. J.; Cha, W.; Robinson, I. K. Three-dimensional coherent X-ray diffraction imaging via deep convolutional neural networks. *Npj Comput. Mater.* **2021**, *7*, 175.

(121) Fienup, J. R. Phase retrieval algorithms: a comparison. *Appl. Opt.* **1982**, *21*, 2758–2769.

(122) Gorobtsov, O.; Singer, A. Shear displacement gradient in X-ray Bragg coherent diffractive imaging. *J. Synchrotron Radiat.* **2022**, *29*, 866–870.

(123) Newton, M. C.; Leake, S. J.; Harder, R.; Robinson, I. K. Three-dimensional imaging of strain in a single ZnO nanorod. *Nat. Mater.* **2010**, *9*, 120–4.

(124) Hofmann, F.; Phillips, N. W.; Das, S.; Karamched, P.; Hughes, G. M.; Douglas, J. O.; Cha, W.; Liu, W. Nanoscale imaging of the full strain tensor of specific dislocations extracted from a bulk sample. *Phys. Rev. Materials* **2020**, *4*, 013801.

(125) Whitehead, L. W.; Williams, G. J.; Quiney, H. M.; Vine, D. J.; Dilanian, R. A.; Flewett, S.; Nugent, K. A.; Peele, A. G.; Balaur, E.; McNulty, I. Diffractive imaging using partially coherent X-rays. *Phys. Rev. Lett.* **2009**, *103*, 243902.

(126) Clark, J. N.; Huang, X.; Harder, R.; Robinson, I. K. High-resolution three-dimensional partially coherent diffraction imaging. *Nat. Commun.* **2012**, *3*, 993.

(127) Shabalin, A. G.; Yefanov, O. M.; Nosik, V. L.; Bushuev, V. A.; Vartanyants, I. A. Dynamical effects in Bragg coherent x-ray diffraction imaging of finite crystals. *Phys. Rev. B* **2017**, *96*, 064111.

(128) Gorobtsov, O. Y.; Vartanyants, I. A. Phase of transmitted wave in dynamical theory and quasi-kinematical approximation. *Phys. Rev. B* **2016**, *93*, 184107.

(129) Rodenburg, J. M.; Hurst, A. C.; Cullis, A. G.; Dobson, B. R.; Pfeiffer, F.; Bunk, O.; David, C.; Jefimovs, K.; Johnson, I. Hard-X-ray lensless imaging of extended objects. *Phys. Rev. Lett.* **2007**, *98*, 34801.

(130) Dierolf, M.; Menzel, A.; Thibault, P.; Schneider, P.; Kewish, C. M.; Wepf, R.; Bunk, O.; Pfeiffer, F. Ptychographic X-ray computed tomography at the nanoscale. *Nature* **2010**, *467*, 436–439.

(131) Singer, A.; Boucheron, L.; Dietze, S. H.; Jensen, K. E.; Vine, D.; McNulty, I.; Dufresne, E. R.; Prum, R. O.; Mochrie, S. G. J.; Shpyrko, O. G. Domain morphology, boundaries, and topological defects in biophotonic gyroid nanostructures of butterfly wing scales. *Sci. Adv.* **2016**, *2*, e1600149–e1600149.

(132) Thibault, P.; Dierolf, M.; Menzel, A.; Bunk, O.; David, C.; Pfeiffer, F. High-resolution scanning X-ray diffraction microscopy. *Science* **2008**, *321*, 379–382.

(133) Schropp, A. et al. Full spatial characterization of a nanofocused x-ray free-electron laser beam by ptychographic imaging. *Sci. Rep.* **2013**, *3*, 1633.

(134) Donnelly, C.; Guizar-Sicairos, M.; Scagnoli, V.; Gliga, S.; Holler, M.; Raabe, J.; Heyderman, L. J. Three-dimensional magnetization structures revealed with X-ray vector nanotomography. *Nature* **2017**, *547*, 328–331.

(135) Holler, M.; Guizar-Sicairos, M.; Tsai, E. H.; Dinapoli, R.; Muller, E.; Bunk, O.; Raabe, J.; Aeppli, G.

High-resolution non-destructive three-dimensional imaging of integrated circuits. *Nature* **2017**, *543*, 402–406.

(136) Walker, F.; Specht, E. E. Resonant anomalous X-ray scattering: Theory and applications. 1994.

(137) Flagg, L. Q. et al. Resonant X-ray diffraction reveals the location of counterions in doped organic mixed ionic conductors. *Chem. Mater.* **2023**, *35*, 3960–3967.

(138) Qiu, C.; Eng, P. J.; Hennig, C.; Schmidt, M. Formation and aggregation of ZrO2 nanoparticles on muscovite (001). *J. Phys. Chem. C* **2018**, *122*, 3865–3874.

(139) Joly, Y. X-ray absorption near-edge structure calculations beyond the muffin-tin approximation. *Phys. Rev. B* **2001**, *63*, 125120.

(140) Soldo-Olivier, Y.; Sibert, E.; De Santis, M.; Joly, Y.; Grunder, Y. Unraveling the charge distribution at the metal-electrolyte interface coupling in situ surface resonant X-ray diffraction with Ab initio calculations. *ACS Catal.* **2022**, *12*, 2375–2380.

(141) Grunder, Y.; Lucas, C. A.; Thompson, P. B. J.; Joly, Y.; Soldo-Olivier, Y. Charge reorganization at the adsorbate covered electrode surface probed through in situ resonant X-ray diffraction combined with ab initio modeling. *J. Phys. Chem. C* **2022**, *126*, 4612–4619.

(142) Toney, M. In *Studies of electrodes by in situ x-ray scattering*; Melendres, C., Ed.; Synchrotron techniques in interfacial electrochemistry. NATO ASI Series; 1993; pp 109–125.

(143) Toney, M.; McBreen, J. In situ synchrotron x-ray techniques for determining atomic structures at electrode/electrolyte interfaces. *Interface* **1993**, *2*, 22–31.

(144) Toney, M.; Ocko, B. Atomic structure at electrode interfaces. *Synchroton Radiat.News* **1993**, *6*, 28–33.

(145) Ocko, B. M.; Magnussen, O. M.; Wang, J. X.; Adzic, R. R.; Wandlowski, T. The structure and phase behavior of electrodeposited halides on single-crystal metal surfaces. *Physica B Condens. Matter.* **1996**, *221*, 238–244.

(146) Ocko, B.; Wandlowski, T. Halide electroadsorption on single crystal surfaces. *Mat. Res. Soc. Symp. Proc* **1997**, *451*, 55–67.

(147) Nagy, Z.; You, H. Applications of surface X-ray scattering to electrochemistry problems. *Electrochim. Acta* **2002**, *47*, 3037–3055.

(148) Magnussen, O. Ordered anion adlayers on metal electrode surfaces. *Chem. Rev* **2002**, *102*, 679–725.

(149) Lucas, C. A.; Markovic, N. M. In-situ X-ray diffraction studies of the electrode/solution interface. *Adv. Electrochem. Sci. Eng.* **2006**, *9*, 1–45.

(150) Grunder, Y.; Lucas, C. A. Surface X-ray diffraction studies of single crystal electrocatalysts. *Nano Energy* **2016**, *29*, 378–393.

(151) You, H. X-ray scattering and imaging studies of electrode structure and dynamics. *Chem. Rec.* **2019**, *19*, 1220–1232.

(152) Fenter, P. A. X-ray reflectivity as a probe of mineral-fluid interfaces: a user guide. *Rev. Mineral. Geochem.* **2002**, *49*, 149–220.

(153) Fenter, P.; Sturchio, N. C. Mineral-water interfacial structures revealed by synchrotron x-ray scattering. *Prog. Surf. Sci.* **2005**, *77*, 171–258.

(154) Huang, K. G.; Gibbs, D.; Zehner, D. M.; Sandy, A. R.; Mochrie, S. G. J. Phase-behavior of the Au(111) surface - discom-

mensurations and kinks. *Phys. Rev. Lett.* **1990**, *65*, 3313–3316.

(155) Sandy, A. R.; Mochrie, S. G. J.; Zehner, D. M.; Huang, K. G.; Gibbs, D. Structure and phases of the Au(111) surface - X-ray-scattering measurements. *Phys. Rev. B* **1991**, *43*, 4667–4687.

(156) Sandy, A. R.; Mochrie, S. G. J.; Zehner, D. M.; Grubel, G.; Huang, K. G.; Gibbs, D. Reconstruction of the Pt(111) surface. *Phys. Rev. Lett.* **1992**, *68*, 2192–2195.

(157) Sandy, A. R.; Mochrie, S. G. J.; Zehner, D. M.; Grubel, G.; Huang, K. G.; Gibbs, D. Au(111) and Pt(111) surface phase-behavior. *Surf. Sci.* **1993**, *287*, 321–324.

(158) Grubel, G.; Gibbs, D.; Zehner, D. M.; Abernathy, D. L.; Sandy, A. R.; Mochrie, S. G. J. Phase-behavior of Au and Pt surfaces. *Surf. Sci.* **1993**, *287*, 842–846.

(159) Kolb, D. Reconstruction phenomena at metal-electrolyte interfaces. *Prog. Surf. Sci* **1996**, *51*, 109–173.

(160) Ocko, B. M.; Wang, J.; Davenport, A.; Isaacs, H. In situ X-ray reflectivity and diffraction studies of the Au(001) reconstruction in an electrochemical-cell. *Phys. Rev. Lett.* **1990**, *65*, 1466–1469.

(161) Wang, J.; Davenport, A. J.; Isaacs, H. S.; Ocko, B. M. Surface-charge induced ordering of the Au(111) surface. *Science* **1992**, *255*, 1416–1418.

(162) Wang, J.; Ocko, B. M.; Davenport, A. J.; Isaacs, H. S. In situ X-ray-diffraction and X-ray-reflectivity studies of the Au(111) electrolyte interface - reconstruction and anion adsorption. *Phys. Rev. B* **1992**, *46*, 10321–10338.

(163) Ocko, B. M.; Helgesen, G.; Schardt, B.; Wang, J.; Hamelin, A. Charge induced (1x3) reconstruction of the Au(110) surface - an X-ray-scattering study. *Phys. Rev. Lett.* **1992**, *69*, 3350–3353.

(164) Feng, Y. J.; Bohnen, K. P.; Chan, C. T. First-principles studies of Au(100)-hex reconstruction in an electrochemical environment. *Phys. Rev. B: Condens. Matter Mater. Phys.* **2005**, *72*, 125401/1.

(165) Jacob, T. Potential-induced lifting of the Au(100)-surface reconstruction studied with DFT. *Electrochim. Acta* **2007**, *52*, 2229–2235.

(166) Kondo, T.; Zegenhagen, J.; Takakusagi, S.; Uosaki, K. In situ real-time study on potential induced structure change at Au(111) and Au(100) single crystal electrode/sulfuric acid solution interfaces by surface x-ray scattering. *Surf. Sci.* **2015**, *631*, 96–104.

(167) Tidswell, I. M.; Markovic, N. M.; Lucas, C. A.; Ross, P. N. In-situ X-ray-scattering study of the Au(001) reconstruction in alkaline and acidic electrolytes. *Phys. Rev. B* **1993**, *47*, 16542–16553.

(168) Tidswell, I.; Markovic, N.; Ross, P. Potential dependent structure of single crystal gold interfaces in alkaline electrolyte: an in situ x-ray scattering study. *Surf. Sci* **1994**, *317*, 241–252.

(169) Grunder, Y.; Harlow, G. S.; Cocklin, E.; Fogg, J.; Beane, J. W.; Lucas, C. A. Potential-dependent surface compression of gold and its link to electrocatalytic reactivity. *Surf. Sci.* **2019**, *680*, 113–118.

(170) Gao, X.; Hamelin, A.; Weaver, M. Atomic relaxation at ordered electrochemical surfaces probed by scanning tunneling microscopy: Au(111) in aqueous solution compared with ultrahigh-vacuum environments. *J. Chem. Phys* **1991**, *95*, 6993–6996.

(171) Gao, X.; Hamelin, A.; Weaver, M. Potential-dependent reconstruction at

ordered Au(100)-aqueous interfaces as probed by atomic-resolution scanning tunneling microscopy. *Phys. Rev. Lett* **1991**, *67*, 618–621.

(172) Gao, X.; Hamelin, A.; Weaver, M. Reconstruction at ordered Au(110)-aqueous interfaces as probed by atomic resolution scanning tunneling microscopy. *Phys. Rev. B* **1991**, *44*, 10983–10986.

(173) Gao, X.; Weaver, M. Electrode potential-induced reconstruction of Au(100): Effect of chemisorption on nanoscale dynamics as probed by in-situ scanning tunneling microscopy. *J. Phys. Chem* **1993**, *97*, 8685–8689.

(174) Magnussen, O.; Hotlos, J.; Behm, R.; Batina, N.; Kolb, D. An in-situ scanning tunneling microscopy study of electrochemically induced 'hex' <-> transitions on Au(100) electrodes. *Surf. Sci* **1993**, *296*, 310–332.

(175) Magnussen, O.; Wiechers, J.; Behm, R. In situ scanning tunneling microscopy observations of the potential-dependent (1x2) reconstruction on Au(110) in acidic electrolytes. *Surf. Sci* **1993**, *289*, 139–151.

(176) Lucas, C.; Markovic, N.; Ross, P. Surface structure and relaxation at the Pt(110)/electrolyte interface. *Phys. Rev. Lett* **1996**, *77*, 4922–4925.

(177) Markovic, N. M.; Grgur, B. N.; Lucas, C. A.; Ross, P. N. Surface electrochemistry of CO on Pt(110)-(1x2) and Pt(110)-(1x1) surfaces. *Surf. Sci.* **1997**, *384*, L805–L814.

(178) Kibler, L.; Cuesta, A.; Kleinert, M.; Kolb, D. In-situ STM characterization of the surface morphology of platinum single crystal electrodes as a function of their preparation. *J. Electroanal. Chem* **2000**, *484*, 73–82.

(179) LaGraff, J.; Gewirth, A. In-situ observation of oxygen adlayer formation on Cu(110) electrode surfaces. *Surf. Sci* **1995**, *326*, L461–L466.

(180) Broekmann, P.; Wilms, M.; Spänig, A.; Hommrich, J.; Stuhlmann, C.; Wandelt, K. In-situ STM study of the sulfate induced Cu(111) reconstruction. *ECS Meeting Abstract* **1999**, *99-1*, 1111–1111.

(181) Broekmann, P.; Wilms, M.; Wandelt, K. Atomic structures of a Cu(111) surface under electrochemical conditions: an in-situ STM study. *Surf. Rev. Lett* **1999**, *6*, 907–916.

(182) Broekmann, P.; Wilms, M.; Spaenig, A.; Wandelt, K. Formation of adsorbate structures on Cu(111) during hydrogen evolution. *Proc. Electrochem. Soc.* **2002**, *2000-30*, 124–129.

(183) Wan, L.-J.; Itaya, K. In situ scanning tunneling microscopy of Cu(110): atomic structures of halide adlayers and anodic dissolution. *J. Electroanal. Chem* **1999**, *473*, 10–18.

(184) Maurice, V.; Strehblow, H.-H.; Marcus, P. In situ STM study of the initial stages of oxidation of Cu(111) in aqueous solution. *Surf. Sci* **2000**, *458*, 185–194.

(185) Matsushima, H.; Taranovskyy, A.; Haak, C.; Gründer, Y.; Magnussen, O. Reconstruction of Cu(100) electrode surfaces during hydrogen evolution. *J. Am. Chem. Soc* **2009**, *131*, 10362–10363.

(186) Lucas, C. A. et al. Temperature-induced ordering of metal/adsorbate structures at electrochemical interfaces. *J. Am. Chem. Soc.* **2009**, *131*, 7654–7661.

(187) Grunder, Y.; Markovic, N. M.; Thompson, P.; Lucas, C. A. Temperature effects on the atomic structure and kinetics in single crystal electrochemistry. *Surf. Sci.* **2015**, *631*, 123–129.

(188) Pierce, M. S.; Komanicky, V.; Barbour, A.; Hennessy, D. C.; Zhu, C.; Sandy, A.; You, H. Dynamics of the Au

(001) surface in electrolytes: in situ coherent X-ray scattering. *Phys. Rev. B: Condens. Matter Mater. Phys.* **2012**, *86*, 085410/1–085410/7.

(189) You, H.; Pierce, M.; Komanicky, V.; Barbour, A.; Zhu, C. Study of electrode surface dynamics using coherent surface X-ray scattering. *Electrochim. Acta* **2012**, *82*, 570–575.

(190) Lucas, C. A. Surface relaxation at the metal/electrolyte interface. *Electrochim. Acta* **2002**, *47*, 3065–3074.

(191) Tidswell, I.; Markovic, N.; Ross, P. Potential dependent surface relaxation of the Pt(001)/ electrolyte interface. *Phys. Rev. Lett* **1993**, *71*, 1601–1604.

(192) Lucas, C. A. Atomic structure at the electrochemical interface. *J. Phys. D: Appl. Phys.* **1999**, *32*, A198–A201.

(193) Lucas, C.; Markovic, N.; Ross, P. Adsorption of halide anions at the Pt(111)-solution interface studied by in situ surface x-ray scattering. *Phys. Rev. B* **1997**, *55*, 7964–7971.

(194) Wang, J. X.; Robinson, I. K.; Ocko, B. M.; Adzic, R. R. Adsorbate-geometry specific subsurface relaxation in the CO/Pt(111) system. *J. Phys. Chem. B* **2005**, *109*, 24–26.

(195) Saracino, M.; Broekmann, P.; Gentz, K.; Becker, M.; Keller, H.; Janetzko, F.; Bredow, T.; Wandelt, K.; Dosch, H. Surface relaxation phenomena at electrified interfaces. Revealing adsorbate, potential, and solvent effects by combined x-ray diffraction, STM and DFT studies. *Phys. Rev. B: Condens. Matter Mater. Phys.* **2009**, *79*, 115448/1–115448/11.

(196) Gründer, Y.; Kaminski, D.; Golks, F.; Krug, K.; Stettner, J.; Magnussen, O.; Franke, A.; Stremme, J.; Pehlke, E. Reversal of chloride-induced Cu(001) subsurface buckling in electrochemical environment: An in situ surface x-ray diffraction and density functional theory study. *Phys. Rev. B* **2010**, *81*, 174114.

(197) Lucas, C. A.; Markovic, N. M.; Grgur, B. N.; Ross, P. N. Structural effects during CO adsorption on Pt-bimetallic surfaces I. The Pt(100) electrode. *Surf. Sci.* **2000**, *448*, 65–76.

(198) Ball, M. J.; Lucas, C. A.; Markovic, N. M.; Stamenkovic, V.; Ross, P. N. Surface X-ray scattering studies of the growth of Pd thin films on the Pt(001) electrode surface and the effects of the adsorption of CO. *Surf. Sci.* **2003**, *540*, 295–302.

(199) Gallagher, M. E.; Lucas, C. A.; Stamenkovic, V.; Markovic, N. M.; Ross, P. N. Surface structure and relaxation at the Pt3Sn(111)/electrolyte interface. *Surf. Sci.* **2003**, *544*, L729–L734.

(200) Stamenkovic, V. R.; Arenz, M.; Lucas, C. A.; Gallagher, M. E.; Ross, P. N.; Markovic, N. M. Surface chemistry on bimetallic alloy surfaces: Adsorption of anions and oxidation of CO on Pt3Sn(111). *J. Am. Chem. Soc.* **2003**, *125*, 2736–2745.

(201) Harlow, G. S.; Aldous, I. M.; Thompson, P.; Grunder, Y.; Hardwick, L. J.; Lucas, C. A. Adsorption, surface relaxation and electrolyte structure at Pt(111) electrodes in non-aqueous and aqueous acetonitrile electrolytes. *Phys. Chem. Chem. Phys.* **2019**, *21*, 8654–8662.

(202) Nichols, R. J.; Nouar, T.; Lucas, C. A.; Haiss, W.; Hofer, W. A. Surface relaxation and surface stress of Au(111). *Surf. Sci.* **2002**, *513*, 263–271.

(203) Grunder, Y.; Lucas, C. A. Potential-induced structural deformation at electrode surfaces. *Curr. Opin. Electrochem.* **2020**, *19*, 168–174.

(204) Fleischmann, M.; Olivier, A.; Robinson, J. In situ x-ray diffraction studies of electrode solution interfaces. *Electrochim. Acta* **1986**, *31*, 899–906.

(205) Fleischmann, M.; Mao, B. In situ X-ray diffraction measurements of the surface structure of Pt in the presence of "weakly" adsorbed H. *J. Electroanal. Chem* **1988**, *247*, 311–313.

(206) Fleischmann, M.; Mao, B. In-situ X-ray diffraction investigations of the UPD of the Tl and Pb on Ag and Au electrodes. *J. Electroanal. Chem* **1988**, *247*, 297–309.

(207) Melroy, O.; Toney, M.; Borges, G.; Samant, M.; Kortright, J.; Ross, P.; Blum, L. Two-dimensional compressibility of electrochemically adsorbed lead on silver (111). *Phys. Rev. B* **1988**, *38*, 10962–10965.

(208) Samant, M.; Toney, M.; Borges, G.; Blum, L.; Melroy, O. Grazing incidence X-ray diffraction of lead monolayers at a silver (111) and gold (111) electrode/ electrolyte interface. *J. Chem. Phys* **1988**, *92*, 220–225.

(209) Melroy, O.; Toney, M.; Borges, G.; Samant, M.; Kortright, J.; Ross, P.; Blum, L. An in-situ grazing incidence X-ray scattering study of the initial stages of electrochemical growth of lead on silver (111). *J. Electroanal. Chem* **1989**, *258*, 403–414.

(210) Toney, M.; Melroy, O. In situ X-ray scattering of monolayers adsorbed at electrochemical interfaces. *Mat. Res. Soc. Symp. Proc* **1989**, *143*, 37–42.

(211) Wandlowski, T. In *Thermodynamics and electrified interfaces, Encyclopedia of Electrochemistry Vol. 1*; Bard, A., Stratmann, M., Eds.; WILEY-VCH: Weinheim, 2003; Chapter 3.3, pp 383–467.

(212) Ocko, B. M.; Watson, G. M.; Wang, J. Structure and electrocompression of electrodeposited iodine monolayers on Au(111). *J. Phys. Chem.* **1994**, *98*, 897–906.

(213) Magnussen, O. M.; Ocko, B. M.; Adzic, R. R.; Wang, J. X. X-ray-diffraction studies of ordered chloride and bromide monolayers at the Au(111)-solution interface. *Phys. Rev. B* **1995**, *51*, 5510–5513.

(214) Inukai, J.; Osawa, Y.; Itaya, K. Adlayer structures of chlorine, bromine, and iodine on Cu(111) electrode in solution: in-situ STM and ex-situ studies. *J. Phys. Chem. B* **1998**, *102*, 10034–10040.

(215) Gründer, Y.; Drünkler, A.; Golks, F.; Wijts, G.; Stettner, J.; Zegenhagen, J.; Magnussen, O. Structure and electrocompression of chloride adlayers on Cu(111). *Surf. Sci* **2011**, *605*, 1732–1737.

(216) Grunder, Y.; Stettner, J.; Magnussen, O. M. Review-in-situ surface X-ray diffraction studies of copper electrodes: atomic-scale interface structure and growth behavior. *J. Electrochem. Soc.* **2019**, *166*, D3049–D3057.

(217) Wandlowski, T.; Wang, J.; Magnussen, O.; Ocko, B. Structural and kinetic aspects of bromide adsorption on Au(100). *J. Phys. Chem* **1996**, *100*, 10277–10287.

(218) Wang, J. X.; Watson, G. M.; Ocko, B. M. Ordered binary ionic adlayers on a Au(110) electrode: Coadsorption of alkali metal cations with iodide anions. *J. Phys. Chem.* **1996**, *100*, 6672–6677.

(219) Ocko, B.; Wang, J.; Wandlowski, T. Bromide adsorption on Ag(001): a potential induced two-dimensional ising order-disorder transition. *Phys. Rev. Lett* **1997**, *79*, 1511–1514.

(220) Wandlowski, T.; Wang, J.; Ocko, B. Adsorption of bromide at the Ag(100)

electrode surface. *J. Electroanal. Chem* **2001**, *500*, 418–434.

(221) Huemann, S.; Hai, N. T. M.; Broekmann, P.; Wandelt, K.; Zajonz, H.; Dosch, H.; Renner, F. X-ray diffraction and STM study of reactive surfaces under electrochemical control: Cl and I on Cu(100). *J. Phys. Chem. B* **2006**, *110*, 24955–24963.

(222) Keller, H.; Saracino, M.; Nguyen, H. M. T.; Broekmann, P. Templating the near-surface liquid electrolyte: In situ surface x-ray diffraction study on anion/cation interactions at electrified interfaces. *Phys. Rev. B: Condens. Matter Mater. Phys.* **2010**, *82*, 245425/1–245425/7.

(223) Keller, H.; Saracino, M.; Nguyen, H. M. T.; Huynh, T. M. T.; Broekmann, P. Competitive anion/water and cation/water interactions at electrified copper/electrolyte interfaces probed by in situ X-ray diffraction. *J. Phys. Chem. C* **2012**, *116*, 11068–11076.

(224) Pham, D. T.; Keller, H.; Breuer, S.; Huemann, S.; Hai, N. T. N.; Zoerlein, C.; Wandelt, K.; Broekmann, P. Anion/cation layers at electrified interfaces: a comprehensive STM, XRD and XPS case study. *Chimia* **2009**, *63*, 115–121.

(225) Mitchell, S. J.; Brown, G.; Rikvold, P. A. Dynamics of Br electrosorption on single-crystal Ag(100): a computational study. *J. Electroanal. Chem.* **2000**, *493*, 68–74.

(226) Abou Hamad, I.; Wandlowski, T.; Brown, G.; Rikvold, P. A. Electrosorption of Br and Cl on Ag(100): experiments and computer simulations. *J. Electroanal. Chem.* **2003**, *554-555*, 211–219.

(227) Tolentino, H.; De Santis, M.; Gauthier, Y.; Langlais, V. Chlorine chemisorption on Cu(001) by surface X-ray diffraction: Geometry and substrate relaxation. *Surf. Sci.* **2007**, *601*, 2962–2966.

(228) Nakamura, M.; Nakajima, Y.; Sato, N.; Hoshi, N.; Sakata, O. Structure of the electrical double layer on Ag(100): Promotive effect of cationic species on Br adlayer formation. *Phys. Rev. B* **2011**, *84*, 165433/1–165433/5.

(229) Nakamura, M.; Kaminaga, H.; Endo, O.; Tajiri, H.; Sakata, O.; Hoshi, N. Structural dynamics of the electrical double layer during capacitive charging/discharging processes. *J. Phys. Chem. C* **2014**, *118*, 22136–22140.

(230) Nakamura, M.; Sato, N.; Hoshi, N.; Sakata, O. Outer Helmholtz plane of the electrical double layer formed at the solid electrode-liquid interface. *ChemPhysChem* **2011**, *12*, 1430–1434.

(231) Tanaka, S.; Tajiri, H.; Sakata, O.; Hoshi, N.; Nakamura, M. Interfacial structure of Pt(110) electrode during hydrogen evolution reaction in alkaline solutions. *J. Phys. Chem. Lett.* **2022**, *13*, 8403–8408.

(232) Grunder, Y.; Lucas, C. A. Probing the charge distribution at the electrochemical interface. *Phys. Chem. Chem. Phys.* **2017**, *19*, 8416–8422.

(233) Kolb, D. In *Advances in electrochemistry and electrochemical engineering*; Gerischer, H., Tobias, C., Eds.; Wiley-Interscience: New York, 1978; Vol. 11; pp 125–271.

(234) Staikov, G.; Budevski, E.; Lorenz, W. *Electrochemical phase formation and growth*; VCH: Weinheim, 1997.

(235) Adzic, R.; Wang, J.; Vitus, C.; Ocko, B. The electrodeposition of Pb monolayer on low index Pt surfaces: and x-ray scattering and scanning tunneling microscopy study. *Surf. Sci.* **1993**, *293*, L876–L883.

(236) Toney, M.; Gordon, J.; Samant, M.; Borges, G.; Melroy, O. In-situ atomic structure of underpotentially deposited

monolayers of Pb and Tl on Au(111) and Ag(111): a surface X-ray scattering study. *J. Phys. Chem* **1995**, *99*, 4733–4744.

(237) Toney, M.; Gordon, J.; Samant, M.; Borges, G.; Melroy, O.; Yee, D.; Sorensen, L. Unterpotentially deposited thallium on silver(111) by in situ surface x-ray scattering. *Phys. Rev. B* **1992**, *45*, 9362–9374.

(238) Polewska, W.; Wang, J.; Ocko, B.; Adzic, R. Scanning tunnelling microscopy of electrodeposited Thallium monolayers on Au(111) in alkaline solution and a comparison with surface x-ray scattering data. *J. Electroanal. Chem* **1994**, *376*, 41–47.

(239) Wang, J. X.; Adzic, R. R.; Ocko, B. M. X-Ray-Scattering Study of Tl-Adlayers on the Au(111) Electrode in Alkaline-Solutions - Metal Monolayer, Oh- Coadsorption, and Oxide Formation. *J. Phys. Chem.* **1994**, *98*, 7182–7190.

(240) Wang, J. X.; Adzic, R. R.; Magnussen, O. M.; Ocko, B. M. Structural evolution during electrocrystallization: Deposition of Tl on Ag(100) from monolayer to bilayer and to bulk crystallites. *Surf. Sci.* **1995**, *344*, 111–121.

(241) Wang, J.; Adzic, R.; Magnussen, O.; Ocko, B. Structure of electrodeposited Tl overlayers on Au(100) studies via surface x-ray scattering. *Surf. Sci* **1995**, *335*, 120–128.

(242) Adzic, R.; Wang, J. Bromide adsorption induced formation of thallium bromide adlayers with varying composition and structure on the Au(111) electrode surface. *J. Phys. Chem. B* **1998**, *102*, 6305–6308.

(243) Wang, J.; Robinson, I.; Adzic, R. Formation of well-ordered surface compounds by coadsorption of thallium and bromide on the Au(111) electrode surface. *Surf. Sci* **1998**, *412/413*, 374–383.

(244) Toney, M.; Gordon, J.; Samant, M.; Borges, G.; Wiesler, D. In-situ surface X-ray scattering measurements of electrochemically deposited Bi on Ag(111): Structure, compressibility, and comparison with ex situ low-energy electron diffraction measurements. *Langmuir* **1991**, *7*, 796–802.

(245) Chen, C. H.; Kepler, K. D.; Gewirth, A. A.; Ocko, B. M.; Wang, J. Electrodeposited bismuth monolayers on Au(111) electrodes - comparison of surface X-ray-scattering, scanning-tunneling-microscopy, and atomic-force microscopy lattice structures. *J. Phys. Chem.* **1993**, *97*, 7290–7294.

(246) Tamura, K.; Ocko, B. M.; Wang, J. X.; Adzic, R. R. Structure of active adlayers on bimetallic surfaces: Oxygen reduction on Au(111) with Bi adlayers. *J. Phys. Chem. B* **2002**, *106*, 3896–3901.

(247) Zheng, S.; Krug, K.; Golks, F.; Kaminski, D.; Morin, S.; Magnussen, O. Study of Bi UPD structures on Au(100) using in situ surface x-ray scattering. *J. Electroanal. Chem* **2010**, *649*, 189–197.

(248) Lucas, C.; Markovic, N.; Ross, P. Underpotential deposition of lead onto Pt(001): Interface structure and the influence of adsorbed bromide. *Langmuir* **1997**, *13*, 5517–5520.

(249) Lucas, C. A.; Markovic, N. M.; Ross, P. N. Underpotential deposition of Cu on Pt(001): Interface structure and the influence of adsorbed bromide. *Phys. Rev. B* **1998**, *57*, 13184–13191.

(250) Markovic, N.; Grgur, B.; Lucas, C.; Ross, R. Underpotential deposition of lead on Pt(111) in the presence of bromide: RRDPt(111)E and X-ray scattering studies. *J. Electroanal. Chem* **1998**, *448*, 183–188.

(251) Ball, M.; Lucas, C. A.; Markovic, N. M.; Murphy, B. M.; Steadman, P.;

Schmidt, T. J.; Stamenkovic, V.; Ross, P. N. X-ray scattering studies of irreversibly adsorbed bismuth on the Pt(111) electrode surface. *Langmuir* **2001**, *17*, 5943–5946.

(252) Schmidt, T. J.; Stamenkovic, V. R.; Lucas, C. A.; Markovic, N. M.; Ross, P. N. Surface processes and electrocatalysis on the Pt(hkl)/Bi-solution interface. *Phys. Chem. Chem. Phys.* **2001**, *3*, 3879–3890.

(253) Toney, M.; Howard, J.; Richer, J.; Borges, G.; Gordon, J.; Melroy, O. Electrochemical deposition of copper on a gold electrode in sulfuric acid: resolution of the interfacial structure. *Phys. Rev. Lett* **1995**, *75*, 4472–4475.

(254) Nakamura, M.; Endo, O.; Ohta, T.; Ito, M.; Yoda, Y. Surface X-ray diffraction study of Cu UPD on Au(1 1 1) electrode in 0.5 M H2SO4 solution: the coadsorption structure of UPD copper, hydration water molecule and bisulfate anion on Au(1 1 1). *Surf. Sci.* **2002**, *514*, 227–233.

(255) Lucas, C. A.; Markovic, N. M.; Ross, P. N. Electrochemical deposition of copper onto Pt(111) in the presence of (bi)sulfate anions. *Phys. Rev. B* **1997**, *56*, 3651–3654.

(256) Markovic, N.; Gasteiger, H.; Lucas, C.; Tidswell, I.; Ross, P. The effect of chloride on the underpotential deposition of copper on Pt(111): AES, LEED, RRDE and x-ray scattering studies. *Surf. Sci* **1995**, *335*, 91–100.

(257) Tidswell, I.; Lucas, C.; Markovic, N.; Ross, P. Surface structure determination using anomalous x-ray scattering: underpotential deposition of copper on Pt(111). *Phys. Rev. B* **1995**, *51*, 10205–10208.

(258) Lucas, C. A.; Markovic, N. M.; Tidswell, I. M.; Ross, P. N. In situ X-ray scattering study of the Pt(111)-solution interface: Ordered anion structures and their influence on copper underpotential deposition. *Physica B* **1996**, *221*, 245–250.

(259) Markovic, N.; Grgur, B.; Lucas, C.; Ross, P. UPD of Cu on Pt(100): effects of anions on adsorption isotherms and interface structures. *Electrochim. Acta* **1998**, *44*, 1009–1017.

(260) Markovic, N. M.; Grgur, B. N.; Lucas, C. A.; Ross, P. N. Underpotential deposition of lead onto Pt(100) in acid solutions: Adsorption isotherms and interface structures. *J. Chem. Soc., Faraday trans.* **1998**, *94*, 3373–3379.

(261) Wang, J.; Robinson, I.; DeVilbiss, J.; Adzic, R. Structural trends among ionic metal-halide adlayers on electrode surfaces. *J. Phys. Chem. B* **2000**, *104*, 7951–7959.

(262) Wang, J. X.; Marinkovic, N. S.; Adzic, R. R.; Ocko, B. M. Anomalous lattice expansion of the electrodeposited Ag bilayer on Pt(111). *Surf. Sci.* **1998**, *398*, L291–L296.

(263) Marinkovic, N.; Wang, J.; Marinkovic, J.; Adzic, R. Unusual adsorption properties of silver adlayers on the Pt(111) electrode surface. *J. Phys. Chem* **1999**, *103*, 139–144.

(264) Markovic, N. M.; Lucas, C. A.; Climent, V.; Stamenkovic, V.; Ross, P. N. Surface electrochemistry on an epitaxial palladium film on Pt(111): surface microstructure and hydrogen electrode kinetics. *Surf. Sci.* **2000**, *465*, 103–114.

(265) Ball, M. J.; Lucas, C. A.; Markovic, N. M.; Stamenkovic, V.; Ross, P. N. From sub-monolayer to multilayer - an in situ X-ray diffraction study of the growth of Pd films on Pt(111). *Surf. Sci.* **2002**, *518*, 201–209.

(266) Lucas, C. A.; Markovic, N. M.; Ross, P. N. The adsorption and oxidation of carbon monoxide at the Pt(111)/electrolyte interface: atomic structure and surface relaxation. *Surf. Sci.* **1999**, *425*, L381–L386.

(267) Markovic, N.; Grgur, B.; Lucas, C.; Ross, R. Electrooxidation of CO and H2/CO mixtures on Pt(111) in acid solutions. *J. Phys. Chem. B* **1999**, *103*, 487–495.

(268) Markovic, N. M.; Lucas, C. A.; Rodes, A.; Stamenkovi, V.; Ross, P. N. Surface electrochemistry of CO on Pt(111): anion effects. *Surf. Sci.* **2002**, *499*, L149–L158.

(269) Tolmachev, Y. V.; Menzel, A.; Tkachuk, A. V.; Chu, Y. S.; You, H. In situ surface X-ray scattering observation of long-range ordered $(sqrt19 \times \sqrt{19})$R23.4^{circ}-13CO structure on Pt(111) in aqueous electrolytes. *Electrochem. Solid-State Lett.* **2003**, *7*, E23.

(270) Chang, K. C.; Menzel, A.; Komanicky, V.; You, H. Electrosorbed carbon monoxide monolayers on Pt(111). *Electrochim. Acta* **2007**, *52*, 5749–5758.

(271) Villegas, I.; Weaver, M. J. Carbon-monoxide adlayer structures on platinum(111) electrodes - a synergy between in-situ scanning-tunneling-microscopy and infrared-spectroscopy. *J. Chem. Phys.* **1994**, *101*, 1648–1660.

(272) Villegas, I.; Gao, X. P.; Weaver, M. J. Local-structure and phase-transitions within ordered electrochemical, adlayers - some new insights from in-situ scanning-tunneling-microscopy. *Electrochim. Acta* **1995**, *40*, 1267–1275.

(273) Lucas, C. A.; Markovic, N. M.; Ross, P. N. Structural effects induced by CO adsorption on Pt-bimetallic surfaces. *Surf. Rev. Lett.* **1999**, *6*, 917–922.

(274) Menzel, A.; Tolmachev, Y. V.; Chang, K. C.; Komanicky, V.; Chu, Y. S.; Rehr, J. J.; You, H. Polarization-dependent resonant anomalous surface x-ray scattering of CO/Pt(111). *Europhys. Lett.* **2006**, *74*, 1032–1038.

(275) Markovic, N. M.; Lucas, C. A.; Grgur, B. N.; Ross, P. N. Surface electrochemistry of CO and H2/CO mixtures at Pt(100) interface. Electrode kinetics and interfacial structures. *J. Phys. Chem. B* **1999**, *103*, 9616–9623.

(276) Wakisaka, M.; Ohkanda, T.; Yoneyama, T.; Uchida, H.; Watanabe, M. Structures of a CO adlayer on a Pt(100) electrode in HClO4 solution studied by in situ STM. *Chem. Commun.* **2005**, 2710–2712.

(277) Wakisaka, M.; Yoneyama, T.; Ashizawa, S.; Hyuga, Y.; Ohkanda, T.; Uchida, H.; Watanabe, M. Structural variations of CO adlayers on a Pt(100) electrode in 0.1 M HClO4 solution: an in situ STM study. *Phys. Chem. Chem. Phys.* **2013**, *15*, 11038–11047.

(278) Gallagher, M. E.; Blizanac, B. B.; Lucas, C. A.; Ross, P. N.; Markovic, N. M. Structure sensitivity of CO oxidation on gold single crystal surfaces in alkaline solution: Surface X-ray scattering and rotating disk measurements. *Surf. Sci.* **2005**, *582*, 215–226.

(279) Lucas, C. A.; Markovic, N. M.; Ross, P. N. Structural effects during CO adsorption on Pt-bimetallic surfaces II. The Pt(111) electrode. *Surf. Sci.* **2000**, *448*, 77–86.

(280) Lucas, C. A.; Markovic, N. M.; Ball, M.; Stamenkovic, V.; Climent, V.; Ross, P. N. Surface structure and relaxation during the oxidation of carbon monoxide on Pt-Pd bimetallic surfaces. *Surf. Sci.* **2001**, *479*, 241–246.

(281) Kondo, T.; Masuda, T.; Aoki, N.; Uosaki, K. Potential-dependent structures and potential-induced structure changes at Pt(111) single-crystal electrode/sulfuric and perchloric acid interfaces in the potential region between hydrogen underpotential deposition and surface oxide formation by in situ surface X-ray scattering. *J. Phys. Chem. C* **2016**, null.

(282) Liu, Y.; Barbour, A.; Komanicky, V.; You, H. X-ray crystal truncation rod studies of surface oxidation and reduction on Pt(111). *J. Phys. Chem. C* **2016**, *0*, acs.jpcc.6b00492.

(283) Holby, E. F.; Greeley, J.; Morgan, D. Thermodynamics and hysteresis of oxide formation and removal on platinum (111) surfaces. *J. Phys. Chem. C* **2012**, *116*, 9942–9946.

(284) Nakamura, M.; Nakajima, Y.; Hoshi, N.; Tajiri, H.; Sakata, O. Effect of nonspecifically adsorbed ions on the surface oxidation of Pt(111). *ChemPhysChem* **2013**, *14*, 2426–2431.

(285) Lucas, C. A.; Thompson, P.; Gruender, Y.; Markovic, N. M. The structure of the electrochemical double layer: Ag(111) in alkaline electrolyte. *Electrochem. Commun.* **2011**, *13*, 1205–1208.

(286) Toney, M.; Howard, J.; Richter, J.; Borges, G.; Gordon, J.; Melroy, O.; Wiesler, D.; Yee, D.; Sorensen, L. Voltage-dependent ordering of water molecules at an electrolyte-electrolyte interface. *Nature* **1994**, *368*, 444–446.

(287) Toney, M.; Howard, J.; Richer, J.; Borges, G.; Gordon, J.; Melroy, O.; Wiesler, D.; Yee, D.; Sorensen, L. Distribution of water molecules at (Ag(111)/ electrolyte interface as studied with surface X-ray scattering. *Surf. Sci* **1995**, *335*, 326–332.

(288) Karl, J., Robert M.; Barbour, A.; Komanicky, V.; Zhu, C.; Sandy, A.; Pierce, M. S.; You, H. Charge-induced equilibrium dynamics and structure at the Ag(001)-electrolyte interface. *Phys. Chem. Chem. Phys.* **2015**, *17*, 16682–16687.

(289) Spohr, E. In *Computer simulation of electrochemical interfaces*; Alkire, R., Kolb, D., Eds.; Advances in electrochemical science and engineering; VCH: Weinheim, 1999; Vol. 6; pp 1–76.

(290) Spohr, E. Molecular simulation of the electrochemical double layer. *Electrochim. Acta* **1999**, *44*, 1697–1705.

(291) Magnussen, O.; Groß, A. Toward an atomic-scale understanding of electrochemical interface structure and dynamics. *J. Am. Chem. Soc* **2019**, *141*, 4777–4790.

(292) Gross, A.; Sakong, S. Ab initio simulations of water/metal interfaces. *Chem. Rev.* **2022**, *122*, 10746–10776.

(293) Zhou, H. et al. Understanding controls on interfacial wetting at epitaxial graphene: experiment and theory. *Phys. Rev. B: Condens. Matter Mater. Phys.* **2012**, *85*, 035406/1.

(294) Hayashi, R.; Hoshi, N.; Sakata, O.; Nakamura, M. Potential dependence of the buckling structure of the interfacial water bilayer on a graphene electrode. *J. Phys. Chem. C* **2018**, *122*, 7795–7800.

(295) Mezger, M. et al. Molecular layering of fluorinated ionic liquids at a charged sapphire (0001) surface. *Science* **2008**, *322*, 424–428.

(296) Yamamoto, R.; Morisaki, H.; Sakata, O.; Shimotani, H.; Yuan, H. T.; Iwasa, Y.; Kimura, T.; Wakabayashi, Y. External electric field dependence of the structure of the electric double layer at an ionic liquid/Au interface. *Appl. Phys. Lett.* **2012**, *101*.

(297) Voegeli, W.; Arakawa, E.; Matsushita, T.; Sakata, O.; Wakabayashi, Y. Dynamical response of the electric double layer structure of the DEME-TFSI ionic liquid to potential changes observed by time-resolved X-ray reflectivity. *Z. fur Phys. Chem.* **2016**, *230*, 577–585.

(298) Uysal, A. et al. Structural origins of potential dependent hysteresis at the electrified graphene/ionic liquid interface. *J. Phys. Chem. C* **2014**, *118*, 569–574.

(299) Uysal, A. et al. Interfacial ionic 'liquids': connecting static and dynamic structures. *J. Phys.: Condens. Matter* **2014**, *27*, 032101.

(300) Petach, T. A.; Mehta, A.; Marks, R.; Johnson, B.; Toney, M. F.; Goldhaber-Gordon, D. Voltage-controlled interfacial layering in an ionic liquid on SrTiO3. *ACS Nano* **2016**, *10*, 4565–4569.

(301) Reichert, P.; Kjaer, K. S.; van Driel, T. B.; Mars, J.; Ochsmann, J. W.; Pontoni, D.; Deutsch, M.; Nielsen, M. M.; Mezger, M. Molecular scale structure and dynamics at an ionic liquid/electrode interface. *Faraday Discuss.* **2018**, *206*, 141–157.

(302) Douglas, T.; Yoo, S.; Dutta, P. Ionic liquid solutions show anomalous crowding behavior at an electrode surface. *Langmuir* **2022**, *38*, 6322–6329.

(303) Chu, M. Q.; Miller, M.; Dutta, P. Crowding and anomalous capacitance at an electrode-ionic liquid interface observed using operando X-ray scattering. *ACS Cent. Sci.* **2016**, *2*, 175–180.

(304) Chu, M.; Miller, M.; Douglas, T.; Dutta, P. Ultraslow dynamics at a charged silicon–ionic liquid interface revealed by X-ray reflectivity. *J. Phys. Chem. C* **2017**, *121*, 3841–3845.

(305) Henrich, V. E.; Cox, P. A. *The surface science of metal oxides*; Cambridge Univ. Press, Cambridge, UK, 1994.

(306) Diebold, U.; Li, S. C.; Schmid, M. Oxide surface science. *Annu. Rev. Phys. Chem.* **2010**, *61*, 129–148.

(307) Tanwar, K. S.; Catalano, J. G.; Petitto, S. C.; Ghose, S. K.; Eng, P. J.; Trainor, T. P. Hydrated α-Fe2O3 (11^{-}02) surface structure: Role of surface preparation. *Surf. Sci.* **2007**, *601*, L59–L64.

(308) Tanwar, K. S.; Lo, C. S.; Eng, P. J.; Catalano, J. G.; Walko, D. A.; Brown Jr, G. E.; Waychunas, G. A.; Chaka, A. M.; Trainor, T. P. Surface diffraction study of the hydrated hematite (1102) surface. *Surf. Sci.* **2007**, *601*, 460–474.

(309) Grumelli, D. et al. Electrochemical stability of the reconstructed Fe3O4(001) surface. *Angew. Chem., Int. Ed.* **2020**, *59*, 21904–21908.

(310) Bliem, R. et al. Subsurface cation vacancy stabilization of the magnetite (001) surface. *Science* **2014**, *346*, 1215–1218.

(311) Arndt, B.; Bliem, R.; Gamba, O.; van der Hoeven, J. E. S.; Noei, H.; Diebold, U.; Parkinson, G. S.; Stierle, A. Atomic structure and stability of magnetite Fe3O4(001): An X-ray view. *Surf. Sci.* **2016**, *653*, 76–81.

(312) Schlegel, M. L.; Nagy, K. L.; Fenter, P.; Sturchio, N. C. Structures of quartz (100)-and (101)-water interfaces determined by x-ray reflectivity and atomic force microscopy of natural growth surfaces. *Geochim. Cosmochim. Acta* **2002**, *66*, 3037–3054.

(313) Fenter, P.; McBride, M. T.; Srajer, G.; Sturchio, N. C.; Bosbach, D. Structure of barite (001)- and (210)-water interfaces. *J. Phys. Chem. B* **2001**, *105*, 8112–8119.

(314) Zhang, Z.; Fenter, P.; Sturchio, N. C.; Bedzyk, M. J.; Machesky, M. L.; Wesolowski, D. J. Structure of rutile

TiO2 (110) in water and 1 molal Rb+ at pH 12: Inter-relationship among surface charge, interfacial hydration structure, and substrate structural displacements. *Surf. Sci.* **2007**, *601*, 1129–1143.

(315) Lee, S. S.; Fenter, P.; Nagy, K. L.; Sturchio, N. C. Monovalent ion adsorption at the muscovite (001)–solution interface: Relationships among ion coverage and speciation, interfacial water structure, and substrate relaxation. *Langmuir* **2012**, *28*, 8637–8650.

(316) Lee, S. S.; Fenter, P.; Park, C.; Sturchio, N. C.; Nagy, K. L. Hydrated cation speciation at the muscovite (001)- water interface. *Langmuir* **2010**, *26*, 16647–16651.

(317) Cheng, L.; Fenter, P.; Sturchio, N. C.; Zhong, Z.; Bedzyk, M. J. X-ray standing wave study of arsenite incorporation at the calcite surface. *Geochim. Cosmochim. Acta* **1999**, *63*, 3153–3157.

(318) Callagon, E.; Fenter, P.; Nagy, K. L.; Sturchio, N. C. Incorporation of Pb at the calcite (104)–water interface. *Environ. Sci. Technol.* **2014**, *48*, 9263–9269.

(319) Rihs, S.; Sturchio, N. C.; Orlandini, K.; Cheng, L.; Teng, H.; Fenter, P.; Bedzyk, M. J. Interaction of uranyl with calcite in the presence of EDTA. *Environ. Sci. Technol.* **2004**, *38*, 5078–5086.

(320) Bracco, J. N.; Lee, S. S.; Braha, I.; Dorfman, A.; Fenter, P.; Stack, A. G. Pb sorption at the barite (001)–water interface. *J. Phys. Chem. C* **2020**, *124*, 22035–22045.

(321) Bracco, J. N.; Lee, S. S.; Stubbs, J. E.; Eng, P. J.; Jindra, S.; Warren, D. M.; Kommu, A.; Fenter, P.; Kubicki, J. D.; Stack, A. G. Simultaneous adsorption and incorporation of Sr2+ at the barite (001)–water interface. *J. Phys. Chem. C* **2018**, *123*, 1194–1207.

(322) Catalano, J. G.; Park, C.; Fenter, P.; Zhang, Z. Simultaneous inner-and outer-sphere arsenate adsorption on corundum and hematite. *Geochim. Cosmochim. Acta* **2008**, *72*, 1986–2004.

(323) Qiu, C.; Majs, F.; Eng, P. J.; Stubbs, J. E.; Douglas, T. A.; Schmidt, M.; Trainor, T. P. In situ structural study of the surface complexation of lead (II) on the chemically mechanically polished hematite (1102) surface. *J. Colloid Interface Sci.* **2018**, *524*, 65–75.

(324) Qiu, C.; Majs, F.; Douglas, T. A.; Schmidt, M.; Trainor, T. P. In situ structural study of Sb (V) adsorption on hematite (1102) using X-ray surface scattering. *Environ. Sci. Technol.* **2018**, *52*, 11161–11168.

(325) Snir, N.; Yatom, N.; Toroker, M. C. Progress in understanding hematite electrochemistry through computational modeling. *Comput. Mater. Sci.* **2019**, *160*, 411–419.

(326) Catalano, J. G.; Zhang, Z.; Fenter, P.; Bedzyk, M. J. Inner-sphere adsorption geometry of Se (IV) at the hematite (100)–water interface. *J. Colloid Interface Sci.* **2006**, *297*, 665–671.

(327) Catalano, J. G.; Zhang, Z.; Park, C.; Fenter, P.; Bedzyk, M. J. Bridging arsenate surface complexes on the hematite (012) surface. *Geochim. Cosmochim. Acta* **2007**, *71*, 1883–1897.

(328) Qiu, C.; Chen, W.; Schmidt, M.; Majs, F.; Douglas, T. A.; Trainor, T. P. Selective adsorption of Pb (II) on an annealed hematite (1102) surface: Evidence from crystal truncation rod X-ray diffraction and density functional theory. *Environ. Sci. Technol.* **2020**, *54*, 6651–6660.

(329) Diebold, U. The surface science of titanium dioxide. *Surf. Sci. Rep.* **2003**, *48*, 53–229.

(330) Zhang, Z. et al. Ion adsorption at the rutile-water interface: Linking molecular and macroscopic properties. *Langmuir* **2004**, *20*, 4954–4969.

(331) Předota, M.; Zhang, Z.; Fenter, P.; Wesolowski, D.; Cummings, P. Electric double layer at the rutile (110) surface. 2. Adsorption of ions from molecular dynamics and X-ray experiments. *J. Phys. Chem. B* **2004**, *108*, 12061–12072.

(332) Zhang, Z. et al. Structure of hydrated Zn2+ at the rutile TiO2 (110)-aqueous solution interface: Comparison of X-ray standing wave, X-ray absorption spectroscopy, and density functional theory results. *Geochim. Cosmochim. Acta* **2006**, *70*, 4039–4056.

(333) Kohli, V.; Zhang, Z.; Park, C.; Fenter, P. Rb+ and Sr2+ adsorption at the TiO2 (110)- electrolyte interface observed with resonant anomalous X-ray reflectivity. *Langmuir* **2010**, *26*, 950–958.

(334) Park, C.; Fenter, P. A.; Nagy, K. L.; Sturchio, N. C. Hydration and distribution of ions at the mica-water interface. *Phys. Rev. Lett.* **2006**, *97*, 016101.

(335) Park, C.; Fenter, P. A.; Sturchio, N. C.; Nagy, K. L. Thermodynamics, interfacial structure, and pH hysteresis of Rb+ and Sr2+ adsorption at the muscovite (001)-solution interface. *Langmuir* **2008**, *24*, 13993–14004.

(336) Schlegel, M. L.; Nagy, K. L.; Fenter, P.; Cheng, L.; Sturchio, N. C.; Jacobsen, S. D. Cation sorption on the muscovite (0 0 1) surface in chloride solutions using high-resolution X-ray reflectivity. *Geochim. Cosmochim. Acta* **2006**, *70*, 3549–3565.

(337) Lee, S. S.; Schmidt, M.; Laanait, N.; Sturchio, N. C.; Fenter, P. Investigation of structure, adsorption free energy, and overcharging behavior of trivalent yttrium adsorbed at the muscovite (001)–water interface. *J. Phys. Chem. C* **2013**, *117*, 23738–23749.

(338) Lee, S. S.; Nagy, K. L.; Fenter, P. Distribution of barium and fulvic acid at the mica–solution interface using in-situ X-ray reflectivity. *Geochim. Cosmochim. Acta* **2007**, *71*, 5763–5781.

(339) Lee, S. S.; Nagy, K. L.; Park, C.; Fenter, P. Enhanced uptake and modified distribution of mercury (II) by fulvic acid on the muscovite (001) surface. *Environ. Sci. Technol.* **2009**, *43*, 5295–5300.

(340) Lee, S. S.; Park, C.; Fenter, P.; Sturchio, N. C.; Nagy, K. L. Competitive adsorption of strontium and fulvic acid at the muscovite–solution interface observed with resonant anomalous X-ray reflectivity. *Geochim. Cosmochim. Acta* **2010**, *74*, 1762–1776.

(341) Qiu, C.; Eng, P. J.; Hennig, C.; Schmidt, M. Competitive adsorption of ZrO2 nanoparticle and alkali cations (Li+–Cs+) on muscovite (001). *Langmuir* **2018**, *34*, 12270–12278.

(342) Schmidt, M.; Wilson, R. E.; Lee, S. S.; Soderholm, L.; Fenter, P. Adsorption of plutonium oxide nanoparticles. *Langmuir* **2012**, *28*, 2620–2627.

(343) Schmidt, M.; Lee, S.; Wilson, R.; Soderholm, L.; Fenter, P. Sorption of tetravalent thorium on muscovite. *Geochim. Cosmochim. Acta* **2012**, *88*, 66–76.

(344) Schmidt, M.; Lee, S. S.; Wilson, R. E.; Knope, K. E.; Bellucci, F.; Eng, P. J.; Stubbs, J. E.; Soderholm, L.; Fenter, P. Surface-mediated formation of Pu (IV) nanoparticles at the muscovite-electrolyte interface. *Environ. Sci. Technol.* **2013**, *47*, 14178–14184.

(345) Trotochaud, L.; Young, S. L.; Ranney, J. K.; Boettcher, S. W. Nickel-iron

oxyhydroxide oxygen-evolution electrocatalysts: The role of intentional and incidental iron incorporation. *J. Am. Chem. Soc.* **2014**, *136*, 6744–6753.

(346) Cheng, L.; Fenter, P.; Nagy, K. L.; Schlegel, M. L.; Sturchio, N. C. Molecular-scale density oscillations in water adjacent to a mica surface. *Phys. Rev. Lett.* **2001**, *87*, 156103/1.

(347) Bracco, J. N.; Lee, S. S.; Stubbs, J. E.; Eng, P. J.; Heberling, F.; Fenter, P.; Stack, A. G. Hydration structure of the barite (001)–water interface: Comparison of x-ray reflectivity with molecular dynamics simulations. *J. Phys. Chem. C* **2017**, *121*, 12236–12248.

(348) Arsic, J.; Kaminski, D.; Poodt, P.; Vlieg, E. Liquid ordering at the brushite-{010}–water interface. *Phys. Rev. B* **2004**, *69*, 245406.

(349) Geissbühler, P.; Fenter, P.; DiMasi, E.; Srajer, G.; Sorensen, L.; Sturchio, N. Three-dimensional structure of the calcite–water interface by surface X-ray scattering. *Surf. Sci.* **2004**, *573*, 191–203.

(350) Fenter, P.; Sturchio, N. C. Calcite (104)-water interface structure, revisited. *Geochim. Cosmochim. Acta* **2012**, *97*, 58–69.

(351) Catalano, J. G.; Fenter, P.; Park, C. Water ordering and surface relaxations at the hematite (110)–water interface. *Geochim. Cosmochim. Acta* **2009**, *73*, 2242–2251.

(352) Catalano, J. G.; Fenter, P.; Park, C. Interfacial water structure on the (012) surface of hematite: ordering and reactivity in comparison with corundum. *Geochim. Cosmochim. Acta* **2007**, *71*, 5313–5324.

(353) Rao, R. R. et al. Towards identifying the active sites on RuO_2(110) in catalyzing oxygen evolution. *Energy Environ. Sci.* **2017**, *10*, 2626–2637.

(354) Rao, R. R. et al. Surface orientation dependent water dissociation on rutile ruthenium dioxide. *J. Phys. Chem. C* **2018**, *122*, 17802–17811.

(355) Rao, R. R. et al. Operando identification of site-dependent water oxidation activity on ruthenium dioxide single-crystal surfaces. *Nat. Catal.* **2020**, *3*, 516–525.

(356) Rao, R. R. et al. pH- and cation-dependent water oxidation on rutile RuO2(110). *J. Phys. Chem. C* **2021**, *125*, 8195–8207.

(357) Fahrenkrug, E.; Maldonado, S. Electrochemical liquid-liquid-solid (ec-LLS) crystal growth: A low-temperature strategy for covalent semiconductor crystal growth. *Acc. Chem. Res.* **2015**, *48*, 1881–1890.

(358) He, J.; Liang, S.; Li, F.; Yang, Q.; Huang, M.; He, Y.; Fan, X.; Wu, M. Recent development in liquid metal materials. *ChemistryOpen* **2021**, *10*, 360–372.

(359) Zuraiqi, K. et al. Liquid metals in catalysis for energy applications. *Joule* **2020**, *4*, 2290–2321.

(360) Elsen, A.; Murphy, B.; Ocko, B.; Taman, L.; Deutsch, M.; Kuzmenko, I.; Magnussen, O. Surface layering at the mercury - electrolyte interface. *Phys. Rev. Lett* **2010**, *104*, 105501–1–105501–4.

(361) Runge, B.; Festersen, S.; Koops, C. T.; Elsen, A.; Deutsch, M.; Ocko, B. M.; Seeck, O. H.; Murphy, B. M.; Magnussen, O. M. Temperature- and potential-dependent structure of the mercury-electrolyte interface. *Phys. Rev. B* **2016**, *93*, 165408–1 – 165408–9.

(362) Regan, M.; Kawamoto, E.; Lee, S.; Pershan, P.; Maskil, N.; Deutsch, M.; Magnussen, O.; Ocko, B.; Berman, L. Surface layering in liquid gallium: an X-ray reflectivity study. *Phys. Rev. Lett* **1995**, *75*, 2498–2501.

(363) DiMasi, E.; Tostmann, H.; Shpyrko, O. G.; Deutsch, M.; Pershan, P. S.; Ocko, B. M. Surface-induced order in liquid metals and binary alloys. *J. Condens. Matter Phys.* **2000**, *12*, A209–A214.

(364) Duval, J. F. L.; Bera, S.; Michot, L. J.; Daillant, J.; Belloni, L.; Konovalov, O.; Pontoni, D. X-Ray reflectivity at polarized liquid-Hg-aqueous-electrolyte interface: Challenging macroscopic approaches for ion-specificity issues. *Phys. Rev. Lett.* **2012**, *108*.

(365) Elsen, A.; Festersen, S.; Runge, B.; Koops, C.; Ocko, B.; Deutsch, M.; Seeck, O.; Murphy, B.; Magnussen, O. In situ x-ray studies of adlayer-induced crystal nucleation at the liquid-liquid interface. *Proc. Natl. Acad. Sci* **2013**, *110*, 6663–6668.

(366) Murphy, B. M.; Festersen, S.; Magnussen, O. M. The atomic scale structure of liquid metal-electrolyte interfaces. *Nanoscale* **2016**, *8*, 13859–13866.

(367) Hazelnis, J. P.; Sartori, A.; Cheek, Q. B.; Giri, R. P.; MacInnes, M. M.; Murphy, B. M.; Magnussen, O. M.; Maldonado, S. Detection of Ge-containing adlayers at the liquid Hg/water interface by in situ X-ray reflectivity in aqueous borate electrolytes containing dissolved GeO2. *J. Phys. Chem. C* **2022**, *126*, 8177–8189.

(368) Sartori, A.; Giri, R. P.; Fujii, H.; Hovelmann, S. C.; Warias, J. E.; Jordt, P.; Shen, C.; Murphy, B. M.; Magnussen, O. M. Role of chemisorbing species in growth at liquid metal-electrolyte interfaces revealed by in situ X-ray scattering. *Nat. Commun.* **2022**, *13*.

(369) Luo, G.; Malkova, S.; Yoon, J.; Schultz, D.; Lin, B.; Meron, M.; Benjamin, I.; Vanysek, P.; Schlossman, M. Ion distributions near a liquid-liquid interface. *Science* **2006**, *311*, 216–218.

(370) Luo, G.; Malkova, S.; Yoon, J.; Schultz, D. G.; Lin, B.; Meron, M.; Benjamin, I.; Vanysek, P.; Schlossman, M. L. Ion distributions at the nitrobenzene-water interface electrified by a common ion. *J. Electroanal. Chem.* **2006**, *593*, 142–158.

(371) Laanait, N.; Yoon, J.-S.; Hou, B.-Y.; Vanysek, P.; Meron, M.; Lin, B.-H.; Luo, G.-M.; Benjamin, I.; Schlossman, M. L. Communications: Monovalent ion condensation at the electrified liquid/liquid interface. *J. Chem. Phys.* **2010**, *132*, 171101/1.

(372) Laanait, N.; Mihaylov, M.; Hou, B.; Yu, H.; Vanysek, P.; Meron, M.; Lin, B.; Benjamin, I.; Schlossman, M. L. Tuning ion correlations at an electrified soft interface. *Proc. Natl. Acad. Sci. U. S. A., Early Ed.* **2012**, 1–6.

(373) Hou, B.; Laanait, N.; Yu, H.; Bu, W.; Yoon, J.; Lin, B.; Meron, M.; Luo, G.; Vanysek, P.; Schlossman, M. L. Ion distributions at the water/1,2-dichloroethane interface: Potential of mean force approach to analyzing X-ray reflectivity and interfacial tension measurements. *J. Phys. Chem. B* **2013**, *117*, 5365–5378.

(374) Nishi, N.; Uruga, T.; Tanida, H. Potential dependent structure of an ionic liquid at ionic liquid/water interface probed by X-ray reflectivity measurements. *J. Electroanal. Chem.* **2015**, *759*, 129–136.

(375) Katakura, S.; Amano, K.-i.; Sakka, T.; Bu, W.; Lin, B.; Schlossman, M. L.; Nishi, N. Evolution and reversible polarity of multilayering at the ionic liquid/water interface. *J. Phys. Chem. B* **2020**, *124*, 6412–6419.

(376) Yu, H.; Yzeiri, I.; Hou, B.; Chen, C.-H.; Bu, W.; Vanysek, P.; Chen, Y.-S.; Lin, B.; Kral, P.; Schlossman, M. L. Electric field effect on phospholipid monolayers at an aqueous-organic liquid-liquid

interface. *J. Phys. Chem. B* **2015**, *119*, 9319–9334.

(377) Sabatier, P. *La catalyse en chimie organique*; C. Béranger, 1920; Vol. 3.

(378) Zhao, Z.-j.; Liu, S.; Zha, S.; Cheng, D.; Studt, F.; Henkelman, G.; Gong, J. Theory-guided design of catalytic materials using scaling relationships and reactivity descriptors. *Nat. Rev. Mater.* **2019**, *4*, 792–804.

(379) Hammes-Schiffer, S. Catalysts by design: The power of theory. *Acc. Chem. Res.* **2017**, *50*, 561–566.

(380) Zhai, L.; Lo, T. W. B.; Xu, Z.-L.; Potter, J.; Mo, J.; Guo, X.; Tang, C. C.; Tsang, S. C. E.; Lau, S. P. In situ phase transformation on nickel-based selenides for enhanced hydrogen evolution reaction in alkaline medium. *ACS Energy Lett.* **2020**, *5*, 2483–2491.

(381) Hung, S. F.; Zhu, Y. P.; Tzeng, G. Q.; Chen, H. C.; Hsu, C. S.; Liao, Y. F.; Ishii, H.; Hiraoka, N.; Chen, H. M. In situ spatially coherent identification of phosphide-based catalysts: Crystallographic latching for highly efficient overall water electrolysis. *ACS Energy Lett.* **2019**, *4*, 2813–2820.

(382) Chabanier, C.; Irissou, E.; Guay, D.; Pelletier, J. F.; Sutton, M.; Lurio, L. B. Hydrogen absorption in thermally prepared RuO[sub 2] electrode. *Electrochem. Solid-State Lett.* **2002**, *5*, E40.

(383) Chabanier, C.; Guay, D. Activation and hydrogen absorption in thermally prepared RuO2 and IrO2. *J. Electroanal. Chem.* **2004**, *570*, 13–27.

(384) Weber, T.; Abb, M. J. S.; Khalid, O.; Pfrommer, J.; Carla, F.; Znaiguia, R.; Vonk, V.; Stierle, A.; Over, H. In situ studies of the electrochemical reduction of a supported ultrathin single-crystalline RuO_2(110) layer in an Acidic environment. *J. Phys. Chem. C* **2019**, *123*, 3979–3987.

(385) Weber, T.; Abb, M. J. S.; Evertsson, J.; Sandroni, M.; Drnec, J.; Vonk, V.; Stierle, A.; Lundgren, E.; Over, H. In situ studies of the cathodic stability of single-crystalline IrO_2(110) ultrathin films supported on RuO_2(110)/Ru(0001) in an acidic environment. *Phys. Chem. Chem. Phys.* **2020**, *22*, 22956–22962.

(386) Weber, T.; Vonk, V.; Abb, M. J. S.; Evertsson, J.; Sandroni, M.; Drnec, J.; Stierle, A.; Lundgren, E.; Over, H. Extraordinary stability of IrO_2(110) ultrathin films supported on TiO_2(110) under cathodic polarization. *Phys. Chem. Lett.* **2020**, *11*, 9057–9062.

(387) Over, H. Fundamental studies of planar single-crystalline oxide model electrodes (RuO_2, IrO_2) for acidic water splitting. *ACS Catal.* **2021**, *11*, 8848–8871.

(388) Chu, Y. S.; Lister, T. E.; Cullen, W. G.; You, H.; Nagy, Z. Commensurate water monolayer at the RuO2(110)/water interface. *Phys. Rev. Lett.* **2001**, *86*, 3364–3367.

(389) Chen, A.; Ostrom, C. Palladium-based nanomaterials: Synthesis and electrochemical applications. *Chem. Rev.* **2015**, *115*, 11999–12044.

(390) Adams, B. D.; Chen, A. The role of palladium in a hydrogen economy. *Mater. Today* **2011**, *14*, 282–289.

(391) Lewis, F. A. The hydrides of palladium and palladium alloys. *Platin. Met. Rev.* **1960**, *4*, 132–137.

(392) Lewis, F. A. The palladium-hydrogen system: Structures near phase transition and critical points. *Int. J. Hydrogen Energ.* **1995**, *20*, 587–592.

(393) Scholtus, N. A.; Hall, W. K. Hysteresis in the Palladium—Hydrogen System. *J. Chem. Phys.* **1963**, *39*, 868–870.

(394) Schwarz, R. B.; Khachaturyan, A. G. Thermodynamics of open two-phase systems with coherent interfaces: Application to metal-hydrogen systems. *Acta Mater.* **2006**, *54*, 313–323.

(395) Eastman, J. A.; Thompson, L. J.; Kestel, B. J. Narrowing of the palladium-hydrogen miscibility gap in nanocrystalline palladium. *Phys. Rev. B* **1993**, *48*, 84–92.

(396) Bugaev, A. L. et al. Core-shell structure of palladium hydride nanoparticles revealed by combined X-ray absorption spectroscopy and X-ray diffraction. *J. Phys. Chem. C* **2017**, *121*, 18202–18213.

(397) Johnson, N. J.; Lam, B.; MacLeod, B. P.; Sherbo, R. S.; Moreno-Gonzalez, M.; Fork, D. K.; Berlinguette, C. P. Facets and vertices regulate hydrogen uptake and release in palladium nanocrystals. *Nat. Mater.* **2019**, *18*, 454–458.

(398) Yamauchi, M.; Kobayashi, H.; Kitagawa, H. Hydrogen storage mediated by Pd and Pt nanoparticles. *ChemPhysChem* **2009**, *10*, 2566–2576.

(399) Fukai, Y.; Akuma, N. Formation of superabundant vacancies in Pd hydride under high hydrogen pressures. *Phys. Rev. Lett.* **1994**, *73*, 1640–1643.

(400) Benck, J. D.; Jackson, A.; Young, D.; Rettenwander, D.; Chiang, Y. M. Producing high concentrations of hydrogen in palladium via electrochemical insertion from aqueous and solid electrolytes. *Chem. Mater.* **2019**, *31*, 4234–4245.

(401) Berlinguette, C. P.; Chiang, Y. M.; Munday, J. N.; Schenkel, T.; Fork, D. K.; Koningstein, R.; Trevithick, M. D. Revisiting the cold case of cold fusion. *Nature* **2019**, *570*, 45–51.

(402) Felici, R.; Bertalot, L.; DeNinno, A.; LaBarbera, A.; Violante, V. In situ measurement of the deuterium (hydrogen) charging of a palladium electrode during electrolysis by energy dispersive x-ray diffraction. *Rev. Sci. Instrum.* **1995**, *66*, 3344–3348.

(403) Knies, D. L.; Violante, V.; Grabowski, K. S.; Hu, J. Z.; Dominguez, D. D.; He, J. H.; Qadri, S. B.; Hubler, G. K. In-situ synchrotron energy-dispersive x-ray diffraction study of thin Pd foils with Pd:D and Pd:H concentrations up to 1:1. *J. Appl. Phys.* **2012**, *112*, 083510.

(404) Schirber, J. E.; Morosin, B. Lattice constants of of β-PdH_x and PdD_x with x near 1.0. *Phys. Rev. B* **1975**, *12*, 117–118.

(405) Tripodi, P.; Di Gioacchino, D.; Vinko, J. D. AC electrical resistance measurements of PdHx samples versus composition x. *J. Alloy. Compd.* **2009**, *486*, 55–59.

(406) Zhang, W. S.; Zhang, Z. F.; Zhang, Z. L. Some problems on the resistance method in the in situ measurement of hydrogen content in palladium electrode. *J. Electroanal. Chem.* **2002**, *528*, 1–17.

(407) Jisrawi, N. M.; Wiesmann, H.; Ruckman, M. W.; Thurston, T. R.; Reisfeld, G.; Ocko, B. M.; Strongin, M. In situ x-ray investigation of hydrogen charging in thin film bimetallic electrodes. *J. Mater. Res.* **1997**, *12*, 2091–2098.

(408) Lebouin, C.; Soldo-Olivier, Y.; Sibert, E.; De Santis, M.; Maillard, F.; Faure, R. Evidence of the substrate effect in hydrogen electroinsertion into palladium atomic layers by means of in situ surface X-ray diffraction. *Langmuir* **2009**, *25*, 4251–4255.

(409) Soldo-Olivier, Y.; Sibert, E.; Previdello, B.; Lafouresse, M. C.; Maillard, F.; De Santis, M. H electro-insertion into Pd/Pt(1 1 1) nanofilms: an original method for isotherm measurement

coupled to in situ surface X-ray diffraction structural study. *Electrochim. Acta* **2013**, *112*, 905–912.

(410) Langhammer, C.; Zhdanov, V. P.; Zorić, I.; Kasemo, B. Size-dependent kinetics of hydriding and dehydriding of Pd nanoparticles. *Phys. Rev. Lett.* **2010**, *104*, 2–5.

(411) Syrenova, S. et al. Hydride formation thermodynamics and hysteresis in individual Pd nanocrystals with different size and shape. *Nat. Mater.* **2015**, *14*, 1236–1244.

(412) Lee, J. H.; Kattel, S.; Jiang, Z.; Xie, Z.; Yao, S.; Tackett, B. M.; Xu, W.; Marinkovic, N. S.; Chen, J. G. Tuning the activity and selectivity of electroreduction of CO2 to synthesis gas using bimetallic catalysts. *Nat. Commun.* **2019**, *10*, 1–8.

(413) Drnec, J.; Harrington, D.; Magnussen, O. Electrooxidation of Pt(111) in acid solution. *Curr. Opin. Electrochem.* **2017**, *4*, 69–75.

(414) You, H.; Zurawski, D. J.; Nagy, Z.; Yonco, R. M. *In-situ* x-ray reflectivity study of incipient oxidation of Pt(111) surface in electrolyte solutions. *J. Chem. Phys.* **1994**, *100*, 4699–4702.

(415) Chu, Y. S.; You, H.; Tanzer, J. A.; Lister, T. E.; Nagy, Z. Surface resonance X-ray scattering observation of core-electron binding-energy shifts of Pt(111)-surface atoms during electrochemical oxidation. *Phys. Rev. Lett.* **1999**, *83*, 552–555.

(416) You, H.; Chu, Y. S.; Lister, T. E.; Nagy, Z.; Ankudiniv, A. L.; Rehr, J. J. Resonance X-ray scattering from Pt(111) surfaces under water. *Physica B Condens. Matter.* **2000**, *283*, 212–216.

(417) Drnec, J.; Ruge, M.; Reikowski, F.; Rahn, B.; Carla, F.; Felici, R.; Stettner, J.; Magnussen, O. M.; Harrington, D. A. Initial stages of Pt(111) electrooxidation: dynamic and structural studies by surface X-ray diffraction. *Electrochim. Acta* **2017**, *224*, 220–227.

(418) Drnec, J.; Ruge, M.; Reikowski, F.; Rahn, B.; Carla, F.; Felici, R.; Stettner, J.; Magnussen, O. M.; Harrington, D. A. Pt oxide and oxygen reduction at Pt(111) studied by surface X-ray diffraction. *Electrochem. Commun.* **2017**, *84*, 50–52.

(419) Ruge, M.; Drnec, J.; Rahn, B.; Reikowski, F.; Harrington, D.; Carlà, F.; Felici, R.; Stettner, J.; Magnussen, O. Electrochemical oxidation of smooth and nanoscale rough Pt(111): An in situ surface X-ray scattering study. *J. Electrochem. Soc* **2017**, *164*, H608–H614.

(420) Fowler, B.; Lucas, C. A.; Omer, A.; Wang, G.; Stamenković, V. R.; Marković, N. M. Segregation and stability at Pt3Ni(111) surfaces and Pt75Ni25 nanoparticles. *Electrochim. Acta* **2008**, *53*, 6076–6080.

(421) Kumeda, T.; Otsuka, N.; Tajiri, H.; Sakata, O.; Hoshi, N.; Nakamura, M. Interfacial structure of PtNi surface alloy on Pt(111) electrode for oxygen reduction reaction. *ACS Omega* **2017**, *2*, 1858–1863.

(422) Kobayashi, S.; Aoki, M.; Wakisaka, M.; Kawamoto, T.; Shirasaka, R.; Suda, K.; Tryk, D. A.; Inukai, J.; Kondo, T.; Uchida, H. Atomically flat Pt skin and striking enrichment of Co in underlying alloy at $Pt_3Co(111)$ single crystal with unprecedented activity for the oxygen reduction reaction. *ACS Omega* **2018**, *3*, 154–158.

(423) Yang, R.; Strasser, P.; Toney, M. F. Dealloying of $Cu_3Pt(111)$ studied by surface X-ray scattering. *J. Phys. Chem. C* **2011**, *115*, 9074–9080.

(424) Drnec, J.; Bizzotto, D.; Carlà, F.; Fiala, R.; Sode, A.; Balmes, O.; Detlefs, B.;

Dufrane, T.; Felici, R. An in-situ X-ray diffraction study on the electrochemical formation of PtZn alloys on Pt(1 1 1) single crystal electrode. *Appl. Surf. Sci.* **2015**, *354*, 443–449.

(425) Escudero-Escribano, M.; Pedersen, A. F.; Ulrikkeholm, E. T.; Jensen, K. D.; Hansen, M. H.; Rossmeisl, J.; Stephens, I. E. L.; Chorkendorff, I. Active-phase formation and stability of Gd/Pt(111) electrocatalysts for oxygen reduction: An in situ grazing incidence X-Ray diffraction study. *Chem. - Eur. J.* **2018**, *24*, 12280–12290.

(426) Abbou, S.; Chattot, R.; Martin, V.; Claudel, F.; Solà-Hernandez, L.; Beauger, C.; Dubau, L.; Maillard, F. Manipulating the Corrosion Resistance of SnO2Aerogels through Doping for Efficient and Durable Oxygen Evolution Reaction Electrocatalysis in Acidic Media. *ACS Catal.* **2020**, *10*, 7283–7294.

(427) Daiane Ferreira da Silva, C.; Claudel, F.; et al. Oxygen evolution reaction activity and stability benchmarks for supported and unsupported IrO. *ACS Catal.* **2021**, *11*, 4107–4116.

(428) Ehelebe, K.; Seeberger, D.; Paul, M. T. Y.; Thiele, S.; Mayrhofer, K. J. J.; Cherevko, S. Evaluating electrocatalysts at relevant currents in a half-cell: The impact of Pt loading on oxygen reduction reaction. *J. Electrochem. Soc.* **2019**, *166*, F1259–F1268.

(429) Geiger, S. et al. The stability number as a metric for electrocatalyst stability benchmarking. *Nat. Catal.* **2018**, *1*, 508–515.

(430) Kasian, O.; Geiger, S.; Mayrhofer, K. J.; Cherevko, S. Electrochemical on-line ICP-MS in electrocatalysis research. *Chem. Rec.* **2019**, *19*, 2130–2142.

(431) Lopes, P. P. et al. Eliminating dissolution of platinum-based electrocatalysts at the atomic scale. *Nat. Mater.* **2020**, *19*, 1207–1214.

(432) Sandbeck, D. J.; Sandbeck, D. J.; Inaba, M.; Quinson, J.; Bucher, J.; Zana, A.; Arenz, M.; Arenz, M.; Cherevko, S. Particle size effect on platinum dissolution: Practical considerations for fuel cells. *ACS Appl. Mater. Interfaces* **2020**, *12*, 25718–25727.

(433) Stariha, S.; Macauley, N.; Sneed, B. T.; Langlois, D.; More, K. L.; Mukundan, R.; Borup, R. L. Recent advances in catalyst accelerated stress tests for polymer electrolyte membrane fuel cells. *J. Electrochem. Soc.* **2018**, *165*, F492–F501.

(434) Topalov, A. A.; Cherevko, S.; Zeradjanin, A. R.; Meier, J. C.; Katsounaros, I.; Mayrhofer, K. J. Towards a comprehensive understanding of platinum dissolution in acidic media. *Chem. Sci.* **2014**, *5*, 631–638.

(435) Uchimura, M.; Sugawara, S.; Suzuki, Y.; Zhang, J.; Kocha, S. S. Electrocatalyst durability under simulated automotive drive cycles. *ECS Trans.* **2008**, *16*, 225–234.

(436) Borup, R.; Meyers, J.; et al. Scientific aspects of polymer electrolyte fuel cell durability and degradation. *Chem. Rev.* **2007**, *107*, 3904–3951.

(437) De Bruijn, F. A.; Dam, V. A.; Janssen, G. J. Review: Durability and degradation issues of PEM fuel cell components. *Fuel Cells* **2008**, *8*, 3–22.

(438) Dubau, L. et al. A review of PEM fuel cell durability: Materials degradation, local heterogeneities of aging and possible mitigation strategies. *Wiley Interdiscip. Rev.: Energy Environ.* **2014**, *3*, 540–560.

(439) Weiß, A.; Siebel, A.; Bernt, M.; Shen, T.-H.; Tileli, V.; Gasteiger, H. A. Impact of intermittent operation on lifetime and performance of a PEM water electrolyzer. *J. Electrochem. Soc.* **2019**, *166*, F487–F497.

(440) Meier, J. C.; Galeano, C.; Katsounaros, I.; Witte, J.; Bongard, H. J.; Topalov, A. A.; Baldizzone, C.; Mezzavilla, S.; Schüth, F.; Mayrhofer, K. J. Design criteria for stable Pt/C fuel cell catalysts. *Beilstein J. Nanotechnol.* **2014**, *5*, 44–67.

(441) Goerigk, G.; Haubold, H.-G.; Lyon, O.; Simon, J.-P. Anomalous small-angle X-ray scattering in materials science. *J. Appl. Crystallogr.* **2003**, *36*, 425–429.

(442) Haubold, H.-G.; Wang, X.; Jungbluth, H.; Goerigk, G.; Schilling, W. In situ anomalous small-angle X-ray scattering and X-ray absorption near-edge structure investigation of catalyst structures and reactions. *J. Mol. Struct.* **1996**, *383*, 283–289.

(443) Haubold, H. G.; Wang, X. H.; Goerigk, G.; Schilling, W. In situ anomalous small-angle X-ray scattering investigation of carbon-supported electrocatalysts. *J. Appl. Crystallogr.* **1997**, *30*, 653–658.

(444) Smith, M. C.; Gilbert, J. A.; Mawdsley, J. R.; Seifert, S.; Myers, D. J. In situ small-angle X-ray scattering observation of Pt catalyst particle growth during potential cycling. *J. Am. Chem. Soc.* **2008**, *130*, 8112–8113.

(445) Povia, M.; Herranz, J.; Binninger, T.; Nachtegaal, M.; Diaz, A.; Kohlbrecher, J.; Abbott, D. F.; Kim, B. J.; Schmidt, T. J. Combining SAXS and XAS to study the operando degradation of carbon-supported Pt-nanoparticle fuel cell catalysts. *ACS Catal.* **2018**, *8*, 7000–7015.

(446) Yu, C.; Holby, E. F.; Yang, R.; Toney, M. F.; Morgan, D.; Strasser, P. Growth trajectories and coarsening mechanisms of metal nanoparticle electrocatalysts. *ChemCatChem* **2012**, *4*, 766–770.

(447) Tuaev, X.; Rudi, S.; Petkov, V.; Hoell, A.; Strasser, P. In situ study of atomic structure transformations of Pt-Ni nanoparticle catalysts during electrochemical potential cycling. *ACS Nano* **2013**, *7*, 5666–5674.

(448) Schröder, J.; Pittkowski, R. K.; Du, J.; Kirkensgaard, J. J. K.; Arenz, M. Investigating the particle growth in bimodal Pt/C catalysts by in-situ small-angle X-ray scattering: Challenges in the evaluation of stress test protocol-dependent degradation mechanisms. *J. Electrochem. Soc.* **2022**, *169*, 104504.

(449) Schröder, J.; Pittkowski, R. K.; Martens, I.; Chattot, R.; Drnec, J.; Quinson, J.; Kirkensgaard, J. J.; Arenz, M. Tracking the catalyst layer depth-dependent electrochemical degradation of a bimodal Pt/C fuel cell catalyst: A combined operando small- and wide-angle X-ray scattering study. *ACS Catal.* **2022**, *12*, 2077–2085.

(450) Sasaki, K.; Marinkovic, N.; Isaacs, H. S.; Adzic, R. R. Synchrotron-based in situ characterization of carbon-supported platinum and platinum monolayer electrocatalysts. *ACS Catal.* **2016**, *6*, 69–76.

(451) Martens, I.; Chattot, R.; Drnec, J. Decoupling catalyst aggregation, ripening, and coalescence processes inside operating fuel cells. *J. Power Sources* **2022**, *521*, 230851.

(452) Sekizawa, O. et al. Key structural transformations and kinetics of Pt nanoparticles in PEFC Pt/C electrocatalysts by a simultaneous operando time-resolved QXAFS–XRD technique. *Top. Catal.* **2018**, *61*, 889–901.

(453) Uruga, T.; Tada, M.; Sekizawa, O.; Takagi, Y.; Yokoyama, T.; Iwasawa, Y. SPring-8 BL36XU: Synchrotron radiation X-ray-based multi-analytical beamline for polymer electrolyte fuel cells

under operating conditions. *Chem. Rec.* **2019**, *19*, 1444–1456.

(454) Martens, I.; Chattot, R.; Rasola, M.; Blanco, M. V.; Honkimäki, V.; Bizzotto, D.; Wilkinson, D. P.; Drnec, J. Probing the dynamics of platinum surface oxides in fuel cell catalyst layers Using in situ X-ray diffraction. *ACS Appl. Energy Mater.* **2019**, *2*, 7772–7780.

(455) Hornberger, E. et al. In situ stability studies of platinum nanoparticles supported on ruthenium-titanium mixed oxide (RTO) for fuel cell cathodes. *ACS Catal.* **2018**, *8*, 9675–9683.

(456) Schmies, H. et al. Unravelling degradation pathways of oxide-supported Pt fuel cell nanocatalysts under in situ operating conditions. *Adv. Energy Mater.* **2018**, *8*, 1–13.

(457) Schmies, H. et al. Anisotropy of Pt nanoparticles on carbon- And oxide-support and their structural response to electrochemical oxidation probed by-And situ techniques. *Phys. Chem. Chem. Phys.* **2020**, *22*, 22260–22270.

(458) Hornberger, E. et al. Impact of carbon N-doping and pyridinic-N content on the fuel cell performance and durability of carbon-supported Pt nanoparticle catalysts. *ACS Appl. Mater. Interfaces* **2022**, *14*, 18420–18430.

(459) Schmies, H. et al. Impact of carbon support functionalization on the electrochemical stability of Pt fuel cell catalysts. *Chem. Mater.* **2018**, *30*, 7287–7295.

(460) Martens, I.; Vamvakeros, A.; et al. Imaging heterogeneous electrocatalyst stability and decoupling degradation mechanisms in operating hydrogen fuel cells. *ACS Energy Lett.* **2021**, *6*, 2742–2749.

(461) Chattot, R.; Mirolo, M.; Martens, I.; Kumar, K.; Martin, V.; Gasmi, A.; Dubau, L.; Maillard, F.; Castanheira, L.; Drnec, J. Beware of cyclic voltammetry! Measurement artefact in accelerated stress test of fuel cell cathode revealed by operando X-ray diffraction. *J. Power Sources* **2023**, *555*, 232345.

(462) Redmond, E. L.; Setzler, B. P.; Juhas, P.; Billinge, S. J.; Fuller, T. F. In-situ monitoring of particle growth at PEMFC cathode under accelerated cycling conditions. *Electrochem. Solid-State Lett.* **2012**, *15*, 72–74.

(463) Mistry, H.; Varela, A. S.; Kühl, S.; Strasser, P.; Cuenya, B. R. Nanostructured electrocatalysts with tunable activity and selectivity. *Nat. Rev. Mater.* **2016**, *1*.

(464) Beermann, V.; Holtz, M. E.; Padgett, E.; De Araujo, J. F.; Muller, D. A.; Strasser, P. Real-time imaging of activation and degradation of carbon supported octahedral Pt-Ni alloy fuel cell catalysts at the nanoscale using: In situ electrochemical liquid cell STEM. *Energy Environ. Sci.* **2019**, *12*, 2476–2485.

(465) Beker, A. F.; Sun, H.; Lemang, M.; Van Omme, J. T.; Spruit, R. G.; Bremmer, M.; Basak, S.; Pérez Garza, H. H. In situ electrochemistry inside a TEM with controlled mass transport. *Nanoscale* **2020**, *12*, 22192–22201.

(466) Jinschek, J. R. Advances in the environmental transmission electron microscope (ETEM) for nanoscale in situ studies of gas-solid interactions. *Chem. Commun.* **2014**, *50*, 2696–2706.

(467) Lončar, A.; Escalera-López, D.; Cherevko, S.; Hodnik, N. Interrelationships between Oxygen Evolution and Iridium Dissolution Mechanisms. *Angew. Chem. Int. Ed.* **2022**, *61*, e202114437.

(468) Wagner, J. B.; Cavalca, F.; Damsgaard, C. D.; Duchstein, L. D.;

Hansen, T. W. Exploring the environmental transmission electron microscope. *Micron* **2012**, *43*, 1169–1175.

(469) Zhu, G. Z.; Prabhudev, S.; Yang, J.; Gabardo, C. M.; Botton, G. A.; Soleymani, L. In situ liquid cell TEM study of morphological evolution and degradation of Pt-Fe nanocatalysts during potential cycling. *J. Phys. Chem. C* **2014**, *118*, 22111–22119.

(470) Mavrikakis, M.; Hammer, B.; Nørskov, J. K. Effect of strain on the reactivity of metal surfaces. *Phys. Rev. Lett.* **1998**, *81*, 2819–2822.

(471) Strasser, P. et al. Lattice-strain control of the activity in dealloyed core-shell fuel cell catalysts. *Nat. Chem.* **2010**, *2*, 454–460.

(472) Chattot, R. et al. Break-in bad: On the conditioning of fuel cell nanoalloy catalysts. *ACS Catal.* **2022**, 15675–15685.

(473) Petkov, V.; Maswadeh, Y.; Vargas, J. A.; Shan, S.; Kareem, H.; Wu, Z.-P.; Luo, J.; Zhong, C.-J.; Shastri, S.; Kenesei, P. Deviations from Vegard's law and evolution of the electrocatalytic activity and stability of Pt-based nanoalloys inside fuel cells by in operando X-ray spectroscopy and total scattering. *Nanoscale* **2019**, *11*, 5512–5525.

(474) Hornberger, E. et al. On the electrocatalytical oxygen reduction reaction activity and stability of quaternary RhMo-doped PtNi/C octahedral nanocrystals. *Chem. Sci.* **2022**, *13*, 9295–9304.

(475) Kong, Z. et al. Origin of high activity and durability of twisty nanowire alloy catalysts under oxygen reduction and fuel cell operating conditions. *J. Am. Chem. Soc.* **2020**, *142*, 1287–1299.

(476) Wu, Z. P. et al. Alloying–realloying enabled high durability for Pt–Pd-3d-transition metal nanoparticle fuel cell catalysts. *Nat. Commun.* **2021**, *12*, 1–14.

(477) Atlan, C. et al. Imaging the strain evolution of a platinum nanoparticle under electrochemical control. *Nat. Mater.* **2023**,

(478) Reier, T.; Oezaslan, M.; Strasser, P. Electrocatalytic oxygen evolution reaction (OER) on Ru, Ir, and Pt catalysts: A comparative study of nanoparticles and bulk materials. *ACS Catal.* **2012**, *2*, 1765–1772.

(479) Danilovic, N. et al. Activity-stability trends for the oxygen evolution reaction on monometallic oxides in acidic environments. *Phys. Chem. Lett.* **2014**, *5*, 2474–2478.

(480) Cherevko, S. et al. Oxygen and hydrogen evolution reactions on Ru, RuO_2 , Ir, and IrO_2 thin film electrodes in acidic and alkaline electrolytes: A comparative study on activity and stability. *Catal. Today* **2016**, *262*, 170–180.

(481) Weber, T. et al. Potential-induced pitting corrosion of an IrO_2(110)-RuO_2(110)/Ru(0001) model electrode under oxygen evolution reaction conditions. *ACS Catal.* **2019**, *9*, 6530–6539.

(482) Weber, T. et al. Operando stability studies of ultrathin single-crystalline IrO_2(110) films under acidic oxygen evolution reaction conditions. *ACS Catal.* **2021**, *11*, 12651–12660.

(483) Weber, T.; Vonk, V.; Abb, M. J. S.; Evertsson, J.; Stierle, A.; Lundgren, E.; Over, H. In situ synchrotron-based studies of IrO_2(110)-TiO_2(110) under harsh acidic water splitting conditions: Anodic stability and radiation damages. *J. Phys. Chem. C* **2022**, *126*, 20243–20250.

(484) Povia, M. et al. Operando X-ray characterization of high surface area iridium oxides to decouple their activity losses for the oxygen evolution reaction. *Energy Environ. Sci.* **2019**, *12*, 3038–3052.

(485) McCrory, C. C. L.; Jung, S.; Ferrer, I. M.; Chatman, S. M.; Peters, J. C.; Jaramillo, T. F. Benchmarking hydrogen evolving reaction and oxygen evolving reaction electrocatalysts for solar water splitting devices. *J. Am. Chem. Soc.* **2015**, *137*, 4347–4357.

(486) Burke, M. S.; Enman, L. J.; Batchellor, A. S.; Zou, S.; Boettcher, S. W. Oxygen evolution reaction electrocatalysis on transition metal oxides and (oxy)hydroxides: Activity trends and design principles. *Chem. Mater.* **2015**, *27*, 7549–7558.

(487) Han, L.; Dong, S.; Wang, E. Transition-metal (Co, Ni, and Fe)-based electrocatalysts for the water oxidation reaction. *Adv. Mater. (Weinheim, Ger.)* **2016**, *28*, 9266–9291.

(488) Zhao, Q.; Yan, Z.; Chen, C.; Chen, J. Spinels: Controlled preparation, oxygen reduction/evolution reaction application, and beyond. *Chem. Rev.* **2017**, *117*, 10121–10211.

(489) Song, F.; Bai, L.; Moysiadou, A.; Lee, S.; Hu, C.; Liardet, L.; Hu, X. Transition metal oxides as electrocatalysts for the oxygen evolution reaction in alkaline solutions: An application-inspired renaissance. *J. Am. Chem. Soc.* **2018**, *140*, 7748–7759.

(490) Pourbaix, M. *Atlas of electrochemical equilibria in aqueous solutions*; Pergammon Press, london, 1966.

(491) Bergmann, A.; Martinez-Moreno, E.; Teschner, D.; Chernev, P.; Gliech, M.; Ferreira de Araujo, J.; Reier, T.; Dau, H.; Strasser, P. Reversible amorphization and the catalytically active state of crystalline Co3O4 during oxygen evolution. *Nat. Commun.* **2015**, *6*, 8625.

(492) Gao, L.; Cui, X.; Sewell, C. D.; Li, J.; Lin, Z. Recent advances in activating surface reconstruction for the high-efficiency oxygen evolution reaction. *Chem. Soc. Rev.* **2021**, *50*, 8428–8469.

(493) Tung, C.-W.; Hsu, Y.-Y.; Shen, Y.-P.; Zheng, Y.; Chan, T.-S.; Sheu, H.-S.; Cheng, Y.-C.; Chen, H. M. Reversible adapting layer produces robust single-crystal electrocatalyst for oxygen evolution. *Nat. Commun.* **2015**, *6*, 8106.

(494) Wang, H. Y.; Hung, S. F.; Hsu, Y. Y.; Zhang, L. L.; Miao, J. W.; Chan, T. S.; Xiong, Q. H.; Liu, B. In situ spectroscopic identification of mu-OO bridging on spinel Co3O4 water oxidation electrocatalyst. *J. Phys. Chem. Lett.* **2016**, *7*, 4847–4853.

(495) Wiegmann, T. et al. Operando identification of the reversible skin layer on Co3O4 as a three-dimensional reaction zone for oxygen evolution. *ACS Catal.* **2022**, *12*, 3256–3268.

(496) Hsu, C.-S.; Suen, N.-T.; Hsu, Y.-Y.; Lin, H.-Y.; Tung, C.-W.; Liao, Y.-F.; Chan, T.-S.; Sheu, H.-S.; Chen, S.-Y.; Chen, H. M. Valence- and element-dependent water oxidation behaviors: in situ X-ray diffraction, absorption and electrochemical impedance spectroscopies. *Phys. Chem. Chem. Phys.* **2017**, *19*, 8681–8693.

(497) May, K. J.; Carlton, C. E.; Stoerzinger, K. a.; Risch, M.; Suntivich, J.; Lee, Y.-L.; Grimaud, A.; Shao-Horn, Y. Influence of oxygen evolution during water oxidation on the surface of perovskite oxide catalysts. *Phys. Chem. Lett.* **2012**, *3*, 3264–3270.

(498) Risch, M.; Grimaud, A.; May, K. J.; Stoerzinger, K. A.; Chen, T. J.; Mansour, A. N.; Shao-Horn, Y. Structural changes of cobalt-based perovskites upon water oxidation investigated by EXAFS. *J. Phys. Chem. C* **2013**, *117*, 8628–8635.

(499) Fabbri, E. et al. Dynamic surface self-reconstruction is the key of highly active

perovskite nano-electrocatalysts for water splitting. *Nat. Mater.* **2017**, *16*, 925–931.

(500) Baeumer, C. et al. Tuning electrochemically driven surface transformation in atomically flat $LaNiO_3$ thin films for enhanced water electrolysis. *Nat. Mater.* **2021**, *20*, 674.

(501) Samira, S.; Hong, J.; Camayang, J. C. A.; Sun, K.; Hoffman, A. S.; Bare, S. R.; Nikolla, E. Dynamic surface reconstruction unifies the electrocatalytic oxygen evolution performance of nonstoichiometric mixed metal Oxides. *JACS Au* **2021**, *1*, 2224–2241.

(502) Wan, G. et al. Amorphization mechanism of $SrIrO_3$ electrocatalyst: How oxygen redox initiates ionic diffusion and structural reorganization. *Sci. Adv.* **2021**, *7*, eabc7323.

(503) Hori, Y. Electrochemical CO2 reduction on metal electrodes. *Mod. Aspects Electrochem.* **2008**, *42*, 89–189.

(504) Nitopi, S. et al. Progress and perspectives of electrochemical CO2 reduction on copper in aqueous electrolyte. *Chem. Rev.* **2019**, *119*, 7610–7672.

(505) Birdja, Y. Y.; Perez-Gallent, E.; Figueiredo, M. C.; Gottle, A. J.; Calle-Vallejo, F.; Koper, M. T. M. Advances and challenges in understanding the electrocatalytic conversion of carbon dioxide to fuels. *Nat. Energy* **2019**, *4*, 732–745.

(506) Scott, S. B. et al. Absence of oxidized phases in Cu under CO reduction conditions. *ACS Energy Lett.* **2019**, *4*, 803–804.

(507) Lee, S. H. et al. Oxidation state and surface reconstruction of Cu under CO2 reduction conditions from in situ X-ray characterization. *J. Am. Chem. Soc.* **2021**, *143*, 588–592.

(508) Lei, Q. et al. Structural evolution and strain generation of derived-Cu catalysts during CO2 electroreduction. *Nat. Commun.* **2022**, *13*, 4857.

(509) Timoshenko, J. et al. Steering the structure and selectivity of CO2 electroreduction catalysts by potential pulses. *Nat. Catal.* **2022**, *5*, 259–267.

(510) Amirbeigiarab, R.; Tian, J.; Herzog, A.; Qiu, C. R.; Bergmann, A.; Cuenya, B. R.; Magnussen, O. M. Atomic-scale surface restructuring of copper electrodes under CO2 electroreduction conditions. *Nat. Catal.* **2023**, *https://doi.org/10.1038/s41929-023-01009-z*.

(511) Chang, C.-J.; Lin, S.-C.; Chen, H.-C.; Wang, J.; Zheng, K. J.; Zhu, Y.; Chen, H. M. Dynamic reoxidation/reduction-driven atomic interdiffusion for highly selective CO2 reduction toward methane. *J. Am. Chem. Soc.* **2020**, *142*, 12119–12132.

(512) Dutta, A.; Montiel, I. Z.; Erni, R.; Kiran, K.; Rahaman, M.; Drnec, J.; Broekmann, P. Activation of bimetallic AgCu foam electrocatalysts for ethanol formation from CO2 by selective Cu oxidation/reduction. *Nano Energy* **2020**, *68*, 104331.

(513) Medina-Ramos, J. et al. Structural dynamics and evolution of bismuth electrodes during electrochemical reduction of CO2 in imidazolium-based ionic liquid solutions. *ACS Catal.* **2017**, *7*, 7285–7295.

(514) Medina-Ramos, J. et al. Cathodic corrosion at the bismuth-ionic liquid electrolyte interface under conditions for CO2 reduction. *Chem. Mater.* **2018**, *30*, 2362–2373.

(515) Gao, L.-F. et al. Domino effect: Gold electrocatalyzing lithium reduction to accelerate nitrogen fixation. *Angew. Chem. Int. Ed.* **2021**, *60*, 5257–5261.

(516) Blair, S. J. et al. Lithium-mediated electrochemical nitrogen reduction: Tracking electrode–electrolyte enterfaces via time-resolved neutron reflectometry. *ACS Energy Lett.* **2022**, *7*, 1939–1946.

(517) Patil, S. B. et al. Enhanced N_2 affinity of $1\,T-MoS_2$ with a unique pseudo-six-membered ring consisting of N-Li-S-Mo-S-Mo for high ambient ammonia electrosynthesis performance. *J. Mater. Chem.A* **2021**, *9*, 1230–1239.

(518) Liu, S.; Wang, M.; Qian, T.; Ji, H.; Liu, J.; Yan, C. Facilitating nitrogen accessibility to boron-rich covalent organic frameworks via electrochemical excitation for efficient nitrogen fixation. *Nat. Commun.* **2019**, *10*, 3898.

(519) Principi, E.; Di Cicco, A.; Witkowska, A.; Marassi, R. Performance of a fuel cell optimized for *in situ* X-ray absorption experiments. *J. Synchrotron Radiat.* **2007**, *14*, 276–281.

(520) Petrova, O.; Kulp, C.; van den Berg, M. W. E.; Klementiev, K. V.; Otto, B.; Otto, H.; Lopez, M.; Bron, M.; Grünert, W. A spectroscopic proton-exchange membrane fuel cell test setup allowing fluorescence x-ray absorption spectroscopy measurements during state-of-the-art cell tests. *Rev. Sci. Instrum.* **2011**, *82*, 044101.

(521) Vamvakeros, A. et al. DLSR: a solution to the parallax artefact in X-ray diffraction computed tomography data. *J. Appl. Crystallogr.* **2020**, *53*, 1531–1541.

(522) Petkov, V.; Prasai, B.; Shan, S.; Ren, Y.; Wu, J.; Cronk, H.; Luo, J.; Zhong, C.-J. Structural dynamics and activity of nanocatalysts inside fuel cells by in operando atomic pair distribution studies. *Nanoscale* **2016**, *8*, 10749–10767.

(523) Hardy, J. S.; Coyle, C. A.; Bonnett, J. F.; Templeton, J. W.; Canfield, N. L.; Edwards, D. J.; Mahserejian, S. M.; Ge, L.; Ingram, B. J.; Stevenson, J. W. Evaluation of cation migration in lanthanum strontium cobalt ferrite solid oxide fuel cell cathodes via *in-operando* X-ray diffraction. *J. Mater. Chem.A* **2018**, *6*, 1787–1801.

(524) Yang, X.; Hardy, J. S.; Coyle, C. A.; Bonnett, J. F.; Mahserejian, S. M.; Stevenson, J. W. In-operando XRD study of the effects of water vapor on phase formation in LSM/YSZ SOFC cathodes. *J. Electrochem. Soc.* **2022**, *169*, 024512.

(525) Khan, M. Z.; Song, R.-H.; Mehran, M. T.; Lee, S.-B.; Lim, T.-H. Controlling cation migration and inter-diffusion across cathode/interlayer/electrolyte interfaces of solid oxide fuel cells: A review. *Ceram. Int.* **2021**, *47*, 5839–5869.

(526) Liu, D.-J.; Almer, J.; Cruse, T. Characterization of Cr poisoning in a solid oxide fuel cell cathode using a high energy X-ray microbeam. *J. Electrochem. Soc.* **2010**, *157*, B744.

(527) Korjus, O.; Aruväli, J.; Kivi, I.; Kodu, M.; Lust, E.; Nurk, G. Simultaneous operando characterization of crystallographic and electrochemical properties of $Ni-Ce_Gd_{0.1}O_{2-s}$ solid oxide fuel cell anode. *J. Electrochem. Soc.* **2018**, *165*, F1043–F1050.

(528) Li, T. et al. Design of next-generation ceramic fuel cells and real-time characterization with synchrotron X-ray diffraction computed tomography. *Nat. Commun.* **2019**, *10*, 1497.

(529) Moss, A. B.; Garg, S.; Mirolo, M.; Rodriguez, C. A. G.; Ilvonen, R.; Chorkendorff, I.; Drnec, J.; Seger, B. In operando investigations of oscillatory water and carbonate effects in MEA-based CO2 electrolysis devices. *Joule* **2023**, *7*, 350–365.

(530) Garg, S.; Xu, Q.; Moss, A. B.; Mirolo, M.; Deng, W.; Chorkendorff, I.; Drnec, J.; Seger, B. How alkali cations affect salt precipitation and CO_2 electrolysis performance in membrane electrode assembly electrolyzers. *Energy Environ. Sci.* **2023**, *16*, 1631–1643.

(531) Rosenfeld, G.; Poelsema, B.; Comsa, G. In *Growth and properties of ultrathin epitaxial layers*; King, D., Woodruff, D., Eds.; The chemical physics of solid surface; Elsevier Science B.V.: Amsterdam, 1999; Vol. 8; Chapter 3, pp 66–101.

(532) Evans, J. W.; Thiel, P. A.; Bartelt, M. C. Morphological evolution during epitaxial thin film growth: Formation of 2D islands and 3D mounds. *Surf. Sci. Rep.* **2006**, *61*, 1–128.

(533) Krug, K.; Stettner, J.; Magnussen, O. In-situ surface x-ray diffraction studies of homoepitaxial electrochemical growth on Au(100). *Phys. Rev. Lett* **2006**, *96*, 246101/1–246101/4.

(534) Ruge, M.; Golks, F.; Zegenhagen, J.; Magnussen, O.; Stettner, J. In operando GISAXS studies of mound coarsening in electrochemical homoepitaxy. *Phys. Rev. Lett* **2014**, *112*, 055503/1–055503/5.

(535) Giesen, M.; Beltramo, G.; Dieluweit, S.; Müller, J.; Ibach, H.; Schmickler, W. The thermodynamics of electrochemical annealing. *Surf. Sci* **2005**, *595*, 127–137.

(536) Giesen, M. Step and island dynamics at solid vacuum and solid/liquid interfaces. *Prog. Surf. Sci* **2001**, *68*, 1–153.

(537) Labayen, M.; Ramirez, C.; Schattke, W.; Magnussen, O. Quasi-collective motion of nanoscale metal strings in metal surfaces. *Nat. Mater.* **2003**, *2*, 783–787.

(538) Kaminski, D.; Radenovic, N.; Deij, M. A.; van Enckevort, W. J. P.; Vlieg, E. Liquid ordering at the KDP 100-solution interface. *Cryst. Growth Des.* **2006**, *6*, 588–591.

(539) Ayyad, A.; Stettner, J.; Magnussen, O. Electrocompression of the Au(111) surface layer during Au electrodeposition. *Phys. Rev. Lett* **2005**, *94*, 066106.

(540) Golks, F.; Stettner, J.; Gründer, Y.; Krug, K.; Zegenhagen, J.; Magnussen, O. Anomalous potential dependence in homoepitaxial Cu(001) electrodeposition: an in situ surface x-ray diffraction study. *Phys. Rev. Lett* **2012**, *108*, 256101/1–256101/5.

(541) Golks, F.; Gründer, Y.; Stettner, J.; Krug, K.; Zegenhagen, J.; Magnussen, O. In situ surface x-ray diffraction studies of homoepitaxial growth on Cu(001) from aqueous acidic electrolyte. *Surf. Sci* **2014**, *631*, 112–122.

(542) Golks, F.; Gründer, Y.; Drünkler, A.; Roy, J.; Stettner, J.; Zegenhagen, J.; Magnussen, O. In-situ surface X-ray diffraction studies of the influence of the PEG-Cl-complex on homoepitaxial electrodeposition on Cu(001). *J. Electrochem. Soc* **2014**, *160*, D3165–D3170.

(543) Krug, K.; Kaminski, D.; Golks, F.; Stettner, J.; Magnussen, O. Real-time surface X-ray scattering study of Au(111) electrochemical dissolution. *J. Phys. Chem. C* **2010**, *114*, 18634–18644.

(544) Golks, F.; Krug, K.; Gründer, Y.; Zegenhagen, J.; Stettner, J.; Magnussen, O. High-speed in situ surface x-ray diffraction studies of the electrochemical dissolution of Au(001). *J. Am. Chem. Soc* **2011**, *133*, 3772–3775.

(545) Renner, F. U.; Stierle, A.; Dosch, H.; Kolb, D. M.; Lee, T. L.; Zegenhagen, J. Initial corrosion observed on the atomic scale. *Nature* **2006**, *439*, 707–710.

(546) Renner, F. U.; Stierle, A.; Dosch, H.; Kolb, D. M.; Zegenhagen, J. The influence of chloride on the initial anodic dissolution of Cu3Au(111). *Electrochem. Commun.* **2007**, *9*, 1639–1642.

(547) Renner, F. U.; Grunder, Y.; Lyman, P. F.; Zegenhagen, J. In-situ X-ray diffraction study of the initial dealloying of $Cu_3Au(001)$ and $Cu_0 \cdot 83\,Pd_0 \cdot 17\,(001)$. *Thin Solid Films* **2007**, *515*, 5574–5580.

(548) Renner, F. U.; Stierle, A.; Dosch, H.; Kolb, D. M.; Lee, T. L.; Zegenhagen, J. In situ x-ray diffraction study of the initial dealloying and passivation of Cu3Au(111) during anodic dissolution. *Phys. Rev. B* **2008**, *77*, 235433.

(549) Renner, F. U.; Ankah, G. N.; Pareek, A. In-situ surface-sensitive X-ray diffraction study on the influence of iodide over the selective electrochemical etching of Cu3Au (111). *Surf. Sci.* **2012**, *606*, L37–L40.

(550) Ankah, G. N.; Pareek, A.; Cherevko, S.; Topalov, A. A.; Rohwerder, M.; Renner, F. U. The influence of halides on the initial selective dissolution of Cu3Au (111). *Electrochim. Acta* **2012**, *85*, 384–392.

(551) Ankah, G. N.; Meimandi, S.; Renner, F. U. Dealloying of Cu_3Pd single crystal surfaces. *J. Electrochem. Soc.* **2013**, *160*, C390–C395.

(552) Ankah, G. N.; Pareek, A.; Cherevko, S.; Zegenhagen, J.; Renner, F. U. Hierarchical nanoporous films obtained by surface cracking on Cu-Au and ethanethiol on Au(001). *Electrochim. Acta* **2014**, *140*, 352–358.

(553) Pareek, A.; Ankah, G. N.; Cherevko, S.; Ebbinghaus, P.; Mayrhofer, K. J. J.; Erbe, A.; Renner, F. U. Effect of thiol self-assembled monolayers and plasma polymer films on dealloying of Cu-Au alloys. *RSC Adv.* **2013**, *3*, 6586–6595.

(554) Erlebacher, J. An atomistic description of dealloying - Porosity evolution, the critical potential, and rate-limiting behavior. *J. Electrochem. Soc.* **2004**, *151*, C614–C626.

(555) Van Petegem, S.; Brandstetter, S.; Maass, R.; Hodge, A. M.; El-Dasher, B. S.; Biener, J.; Schmitt, B.; Borca, C.; Van Swygenhoven, H. On the microstructure of nanoporous gold: An x-ray diffraction study. *Nano Lett.* **2009**, *9*, 1158–1163.

(556) Dotzler, C. J.; Ingham, B.; Illy, B. N.; Wallwork, K.; Ryan, M. P.; Toney, M. F. In-situ observation of strain development and porosity evolution in nanoporous gold foils. *Adv. Funct. Mater.* **2011**, *21*, 3938–3946.

(557) Lin, B.; Kong, L.; Hodgson, P. D.; Mudie, S.; Hawley, A.; Dumee, L. F. Controlled porosity and pore size of nano-porous gold by thermally assisted chemical dealloying - a SAXS study. *RSC Adv.* **2017**, *7*, 10821–10830.

(558) Goessler, M.; Hengge, E.; Bogar, M.; Albu, M.; Knez, D.; Amenitsch, H.; Wuerschum, R. In situ study of nanoporosity evolution during dealloying AgAu and CoPd by grazing-incidence small-angle X-ray scattering. *J. Phys. Chem. C* **2022**, *126*, 4037–4047.

(559) Chen-Wiegart, Y.-c. K.; Harder, R.; Dunand, D. C.; McNulty, I. Evolution of dealloying induced strain in nanoporous gold crystals. *Nanoscale* **2017**, *9*, 5686–5693.

(560) Schofield, E. J.; Ingham, B.; Turnbull, A.; Toney, M. F.; Ryan, M. P. Strain development in nanoporous metallic foils formed by dealloying. *Appl. Phys. Lett.* **2008**, *92*, 043118/1.

(561) Teng, H. H.; Fenter, P.; Cheng, L.; Sturchio, N. C. Resolving orthoclase dissolution processes with atomic force microscopy and X-ray reflectivity. *Geochim. Cosmochim. Acta* **2001**, *65*, 3459–3474.

(562) Fenter, P.; Lee, S. S. Hydration layer structure at solid-water interfaces. *MRS Bull.* **2014**, *39*, 1056–1061.

(563) Fenter, P.; Park, C.; Cheng, L.; Zhang, Z.; Krekeler, M.; Sturchio, N. Orthoclase dissolution kinetics probed by in situ X-ray reflectivity: Effects of temperature, pH, and crystal orientation. *Geochim. Cosmochim. Acta* **2003**, *67*, 197–211.

(564) Fenter, P.; Lee, S.; Park, C.; Catalano, J.; Zhang, Z.; Sturchio, N. Probing interfacial reactions with X-ray reflectivity and X-ray reflection interface microscopy: Influence of NaCl on the dissolution of orthoclase at pOH 2 and 85° C. *Geochim. Cosmochim. Acta* **2010**, *74*, 3396–3411.

(565) Budevski, E.; Staikov, G.; Lorenz, W. *Electrochemical phase formation and growth*; Advances in Electrochemical Science and Engineering; VCH, Weinheim, 1996.

(566) Soldo-Olivier, Y.; De Santis, M.; Liang, W.; Sibert, E. Growth mechanisms of Pd nanofilms electrodeposited onto Au(111): an in situ grazing incidence X-ray diffraction study. *Phys. Chem. Chem. Phys.* **2016**, *18*, 2830–2839.

(567) Ocko, B. M.; Robinson, I. K.; Weinert, M.; Randler, R. J.; Kolb, D. M. Thickness induced buckling of bcc copper films. *Phys. Rev. Lett.* **1999**, *83*, 780–783.

(568) Randler, R. J.; Kolb, D. M.; Ocko, B. M.; Robinson, I. K. Electrochemical copper deposition on Au(100): a combined in situ STM and in situ surface X-ray diffraction study. *Surf. Sci.* **2000**, *447*, 187–200.

(569) Pfeifer, M. A.; Robach, O.; Ocko, B. M.; Robinson, I. K. Thickness-related instability of Cu thin films on Ag(100). *Physica B Condens. Matter.* **2005**, *357*, 152–158.

(570) Schindler, W.; Koop, T.; Kazimirov, A.; Scherb, G.; Zegenhagen, J.; Schultz, T.; Feidenhans'l, R.; Kirschner, J. Noncoherent growth patches in pseudomorphic films: Unusual strain relief in electrodeposited Co on Cu(001). *Surf. Sci. Lett.* **2000**, *465*, L783–L788.

(571) Schindler, W. Electrodeposited magnetic monolayers: In-situ studies of magnetism and structure. *Top. Appl. Phys.* **2003**, *85*, 243–258.

(572) Lucas, C. A.; Maroun, F.; Sisson, N.; Thompson, P.; Grunder, Y.; Cortes, R.; Allongue, P. Film and interface atomic structures of electrodeposited Co/Au(111) layers: An in situ X-ray scattering study as a function of the surface chemistry and the electrochemical potential. *J. Phys. Chem. C* **2016**, *120*, 3360–3370.

(573) Maroun, F.; Reikowski, F.; Di, N.; Wiegmann, T.; Stettner, J.; Magnussen, O. M.; Allongue, P. Potential dependence of the structure and magnetism of electrodeposited Pd/Co/Au(111) layers. *J. Electroanal. Chem.* **2018**, *819*, 322–330.

(574) Zegenhagen, J.; Renner, F. U.; Reitzle, A.; Lee, T. L.; Warren, S.; Stierle, A.; Dosch, H.; Scherb, G.; Fimland, B. O.; Kolb, D. M. In situ X-ray analysis of solid/electrolyte interfaces: electrodeposition of Cu and Co on Si(111): H and GaAs(001) and corrosion of Cu3Au(111). *Surf. Sci.* **2004**, *573*, 67–79.

(575) Reitzle, A.; Renner, F. U.; Lee, T. L.; Zegenhagen, J.; Kolb, D. M. Electrochemical growth of copper on well-defined n-Si(111): H surfaces. *Surf. Sci.* **2005**, *576*, 19–28.

(576) Ziegler, J. C.; Scherb, G.; Bunk, O.; Kazimirov, A.; Cao, L. X.; Kolb, D. M.; Johnson, R. L.; Zegenhagen, J. Pb deposition on n-Si(111):H electrodes: an in situ X-ray study. *Surf. Sci.* **2000**, *452*, 150–160.

(577) Warren, S.; Reitzle, A.; Kazimirov, A.; Ziegler, J. C.; Bunk, O.; Cao, L. X.; Renner, F. U.; Kolb, D. M.; Bedzyk, M. J.; Zegenhagen, J. A structure study of the electroless deposition of Au on Si(111): H. *Surf. Sci.* **2002**, *496*, 287–298.

(578) Zegenhagen, J.; Lee, T. L.; Gruender, Y.; Renner, F. U.; Fimland, B. O. The adsorption and growth of copper on as-terminated GaAs(001): Physical vapour versus electrochemical deposition. *Z. fur Phys. Chem.* **2007**, *221*, 1273–1286.

(579) Grunder, Y.; Renner, F. U.; Lee, T. L.; Dheeraj, D. L.; Fimland, B. O.; Zegenhagen, J. The electrodeposition of copper onto UHV-prepared GaAs(001) surfaces. *Surf. Sci.* **2009**, *603*, L105–L108.

(580) Munford, M.; Maroun, F.; Cortès, R.; Allongue, P.; Pasa, A. Electrochemical growth of gold on well-defined vicinal H-Si(111) surfaces studied by AFM and XRD. *Surf. Sci.* **2003**, *537*, 95–112.

(581) Borissov, D.; Pareek, A.; Renner, F. U.; Rohwerder, M. Electrodeposition of Zn and Au-Zn alloys at low temperature in an ionic liquid. *Phys. Chem. Chem. Phys.* **2010**, *12*, 2059–2062.

(582) Tsuyuki, Y.; Fujimura, T.; Kunimoto, M.; Fukunaka, Y.; Pianetta, P.; Homma, T. Analysis of cathodic reaction process of SiCl4 during Si electrodeposition in ionic liquids. *J. Electrochem. Soc.* **2017**, *164*, D994–D998.

(583) Renner, F. U.; Kageyama, H.; Siroma, Z.; Shikano, M.; Schoder, S.; Grunder, Y.; Sakata, O. Gold model anodes for Li-ion batteries: Single crystalline systems studied by in situ X-ray diffraction. *Electrochim. Acta* **2008**, *53*, 6064–6069.

(584) Esbenshade, J. L.; Barile, C. J.; Fister, T. T.; Bassett, K. L.; Fenter, P.; Nuzzo, R. G.; Gewirth, A. A. Improving electrodeposition of Mg through an open circuit potential hold. *J. Phys. Chem. C* **2015**, *119*, 23366–23372.

(585) Ingham, B. et al. Particle size effect of hydrogen-induced lattice expansion of palladium nanoclusters. *Phys. Rev. B* **2008**, *78*, 245408.

(586) Ustarroz, J.; Hammons, J. A.; Van Ingelgem, Y.; Tzedaki, M.; Hubin, A.; Terryn, H. Multipulse electrodeposition of Ag nanoparticles on HOPG monitored by in-situ by Small-Angle X-ray Scattering. *Electrochem. Commun.* **2011**, *13*, 1320–1323.

(587) Ustarroz, J.; Altantzis, T.; Hammons, J. A.; Hubin, A.; Bals, S.; Terryn, H. The role of nanocluster aggregation, coalescence, and recrystallization in the electrochemical deposition of platinum nanostructures. *Chem. Mater.* **2014**, *26*, 2396–2406.

(588) Richardson, S. J.; Burton, M. R.; Luo, X.; Staniec, P. A.; Nandhakumar, I. S.; Terrill, N. J.; Elliott, J. M.; Squires, A. M. Watching mesoporous metal films grow during templated electrodeposition with in situ SAXS. *Nanoscale* **2017**, *9*, 10227–10232.

(589) Hammons, J. A.; Ilavsky, J. Surface Pb nanoparticle aggregation, coalescence and differential capacitance in a deep eutectic solvent using a simultaneous sample-rotated small angle X-ray scattering and electrochemical methods approach. *Electrochim. Acta* **2017**, *228*, 462–473.

(590) Hammons, J. A.; Besford, Q. A.; Ilavsky, J.; Christofferson, A. J. Manipulating meso-scale solvent structure from Pd nanoparticle deposits in deep eutectic solvents. *J. Chem. Phys.* **2021**, *155*, 074505.

(591) Keist, J. S.; Hammons, J. A.; Wright, P. K.; Evans, J. W.; Orme, C. A. Coupling in situ atomic force microscopy (AFM) and ultra-small-angle X-ray scattering (USAXS) to study the evolution

of zinc morphology during electrodeposition within an imidazolium based ionic liquid electrolyte. *Electrochim. Acta* **2020**, *342*, 136073.

(592) Liang, Y.-C. et al. Formation process of mesostructured PtRu nanoparticles electrodeposited on a microemulsion lyotropic liquid crystalline template as revealed by in situ XRD, SAXS, and XANES. *J. Phys. Chem. C* **2012**, *116*, 26649–26655.

(593) Dupont, M. F.; Dose, W. M.; Donne, S. W. In-situ investigation of the electrodeposition of manganese dioxide using small angle X-ray scattering. *J. Electrochem. Soc.* **2015**, *162*, A1809.

(594) Dupont, M. F.; Gibson, A. J.; Elbourne, A.; Forghani, M.; Cross, A. D.; Donne, S. W. In situ investigation of the electrodeposition mechanism of manganese dioxide from a citrate electrolyte: the effect of intermediate stabilization on material morphology. *J. Electrochem. Soc.* **2020**, *167*, 040520.

(595) Moehl, G. E.; Bartlett, P. N.; Hector, A. L. Using GISAXS to detect correlations between the locations of gold particles electrodeposited from an aqueous solution. *Langmuir* **2020**, *36*, 4432–4438.

(596) Pattadar, D.; Cheek, Q.; Sartori, A.; Zhao, Y.; Giri, R. P.; Murphy, B.; Magnussen, O.; Maldonado, S. Evidence for facilitated surface transport during Ge crystal growth by indium in liquid Hg-In alloys at room temperature. *Cryst. Growth Des.* **2021**, *21*, 1645–1656.

(597) Sanyal, M. K.; Agrawal, V. V.; Bera, M. K.; Kalyanikutty, K. P.; Daillant, J.; Blot, C.; Kubowicz, S.; Konovalov, O.; Rao, C. N. R. Formation and ordering of gold nanoparticles at the toluene-water interface. *J. Phys. Chem. C* **2008**, *112*, 1739–1743.

(598) Sanyal, M. K. The use of grazing incidence X-ray scattering techniques to probe chemical reactions at the liquid-liquid interface: the formation and ordering of gold nanoparticles. *J. Mater. Chem.* **2009**, *19*, 4300–4306.

(599) Bera, M. K.; Sanyal, M. K.; Yang, L.; Biswas, K.; Gibaud, A.; Rao, C. N. R. Small-angle x-ray scattering study of the aggregation of gold nanoparticles during formation at the toluene-water interface. *Phys. Rev. B* **2010**, *81*, 115415.

(600) Maiti, S.; Sanyal, M. K.; Varghese, N.; Satpati, B.; Dasgupta, D.; Daillant, J.; Carriere, D.; Konovolov, O.; Rao, C. N. R. Formation of single-crystalline CuS at the organic-aqueous interface. *J. Phys.: Condens. Matter* **2013**, *25*, 395401.

(601) Maiti, S.; Sanyal, M. K.; Jana, M. K.; Runge, B.; Murphy, B. M.; Biswas, K.; Rao, C. N. R. Evidence of contact epitaxy in the self-assembly of HgSe nanocrystals formed at a liquid-liquid interface. *J. Phys.: Condens. Matter* **2017**, *29*, 095101.

(602) Toney, M.; Davenport, A.; Oblongsky, L.; Ryan, M.; Vitus, C. Atomic structure of the passive oxide film formed on iron. *Phys. Rev. Lett* **1997**, *79*, 4282–4285.

(603) Davenport, A. J.; Oblonsky, L. J.; Ryan, M. P.; Toney, M. F. The structure of the passive film that forms on iron in aqueous environments. *J. Electrochem. Soc.* **2000**, *147*, 2162–2173.

(604) Magnussen, O. M.; Scherer, J.; Ocko, B. M.; Behm, R. J. In situ X-ray scattering study of the passive film on Ni(111) in sulfuric acid solution. *J. Phys. Chem. B* **2000**, *104*, 1222–1226.

(605) Scherer, J.; Ocko, B. M.; Magnussen, O. M. Structure, dissolution, and passivation of Ni(111) electrodes in sulfuric acid solution: an in situ STM, X-ray

scattering, and electrochemical study. *Electrochim. Acta* **2003**, *48*, 1169–1191.

(606) Medway, S. L.; Lucas, C. A.; Kowal, A.; Nichols, R. J.; Johnson, D. In situ studies of the oxidation of nickel electrodes in alkaline solution. *J. Electroanal. Chem.* **2006**, *587*, 172–181.

(607) Reikowski, F.; Maroun, F.; Allongue, P.; Ruge, M.; Stettner, J.; Magnussen, O. In situ surface X-ray diffraction study of ultrathin epitaxial Co films on Au(111) in alkaline solution. *Electrochim. Acta* **2016**, *197*, 273–281.

(608) Chu, Y. S.; Robinson, I. K.; Gewirth, A. A. Comparison of aqueous and native oxide formation on Cu(111). *J. Chem. Phys.* **1999**, *110*, 5952–5959.

(609) Maurice, V.; Marcus, P. Progress in corrosion science at atomic and nanometric scales. *Prog. Mater. Sci.* **2018**, *95*, 132–171.

(610) Melendres, C. A.; You, H.; Maroni, V. A.; Nagy, Z.; Yun, W. Specular x-ray reflection for the "in situ" study of electrode surfaces. *J. Electroanal. Chem. Interfacial Electrochem.* **1991**, *297*, 549.

(611) You, H.; Nagy, Z.; Melendres, C. A.; Zurawski, D. J.; Chiarello, R. P.; Yonco, R. M.; Kim, H. K.; Maroni, V. A. X-ray reflectivity studies of the metal/solution interphase. *Proc. Electrochem. Soc.* **1992**, *92-1*, 73–88.

(612) Melendres, C. A.; Feng, Y. P.; Lee, D. D.; Sinha, S. K. X-ray diffuse scattering for the in situ study of electrochemically induced pitting on metal surfaces. *J. Electrochem. Soc.* **1995**, *142*, L19.

(613) Angerer, P.; Mann, R.; Gavrilovic, A.; Nauer, G. E. In situ X-ray diffraction study of the electrochemical reaction on lead electrodes in sulphate electrolytes. *Mater. Chem. Phys.* **2009**, *114*, 983–989.

(614) Kim, D. H.; Lee, H. H.; Kim, S. S.; Kang, H. C.; Noh, D. Y.; Kim, H.; Sinha, S. K. Chemical depth profile of passive oxide on stainless steel. *Appl. Phys. Lett.* **2004**, *85*, 6427–6429.

(615) Ingham, B.; Ko, M.; Kear, G.; Kappen, P.; Laycock, N.; Kimpton, J. A.; Williams, D. E. In situ synchrotron X-ray diffraction study of surface scale formation during CO2 corrosion of carbon steel at temperatures up to 90 degrees C. *Corros. Sci.* **2010**, *52*, 3052–3061.

(616) Ingham, B.; Ko, M.; Laycock, N.; Burnell, J.; Kappen, P.; Kimpton, J. A.; Williams, D. E. In situ synchrotron X-ray diffraction study of scale formation during CO2 corrosion of carbon steel in sodium and magnesium chloride solutions. *Corros. Sci.* **2012**, *56*, 96–104.

(617) Ko, M.; Laycock, N. J.; Ingham, B.; Williams, D. E. In situ synchrotron X-ray diffraction studies of CO2 corrosion of carbon steel with scale inhibitors ATMPA and PEI at 80 degrees C. *Corrosion* **2012**, *68*, 1085–1093.

(618) Ko, M.; Ingham, B.; Laycock, N.; Williams, D. E. In situ synchrotron X-ray diffraction study of the effect of chromium additions to the steel and solution on CO2 corrosion of pipeline steels. *Corros. Sci.* **2014**, *80*, 237–246.

(619) Ingham, B.; Ko, M.; Laycock, N.; Kirby, N. M.; Williams, D. E. First stages of siderite crystallisation during CO2 corrosion of steel evaluated using in situ synchrotron small- and wide-angle X-ray scattering. *Faraday Discuss.* **2015**, *180*, 171–190.

(620) Ko, M.; Ingham, B.; Laycock, N.; Williams, D. E. In situ synchrotron X-ray diffraction study of the effect of microstructure and boundary layer conditions on CO2 corrosion of pipeline steels. *Corros. Sci.* **2015**, *90*, 192–201.

(621) Sk, M. H.; Abdullah, A. M.; Ko, M.; Ingham, B.; Laycock, N.; Arul, R.; Williams, D. E. Local supersaturation and the growth of protective scales during CO2 corrosion of steel: Effect of pH and solution flow. *Corros. Sci.* **2017**, *126*, 26–36.

(622) Ingham, B.; Holmes-Hewett, W.; Ko, M.; Kirby, N. M.; Sk, M. H.; Abdullah, A. M.; Laycock, N. J.; Williams, D. E. Surface layer formation in the earliest stages of corrosion of steel in CO2-Saturated Brine at 80 °C: studied by in situ synchrotron X-ray methods. *J. Electrochem. Soc.* **2018**, *165*, C842.

(623) Ingham, B.; Ko, M.; Shaw, P.; Sk, M. H.; Abdullah, A. M.; Laycock, N.; Williams, D. E. Effects of oxygen on scale formation in CO2 corrosion of steel in hot brine: In situ synchrotron X-ray diffraction study of anodic products. *J. Electrochem. Soc.* **2018**, *165*, C756–C761.

(624) Bertram, F.; Zhang, F.; Evertsson, J.; Carla, F.; Pan, J.; Messing, M. E.; Mikkelsen, A.; Nilsson, J. O.; Lundgren, E. In situ anodization of aluminum surfaces studied by x-ray reflectivity and electrochemical impedance spectroscopy. *J. Appl. Phys.* **2014**, *116*, 034902/1.

(625) Lee, W.; Park, S.-J. Porous anodic aluminum oxide: Anodization and templated synthesis of functional nanostructures. *Chem. Rev.* **2014**, *114*, 7487–7556.

(626) Napolskii, K. S.; Roslyakov, I. V.; Eliseev, A. A.; Byelov, D. V.; Petukhov, A. V.; Grigoryeva, N. A.; Bouwman, W. G.; Lukashin, A. V.; Chumakov, A. P.; Grigoriev, S. V. The kinetics and mechanism of long-range pore ordering in anodic films on aluminum. *J. Phys. Chem. C* **2011**, *115*, 23726–23731.

(627) Roslyakov, I. V.; Chumakov, A. P.; Eliseev, A. A.; Leontiev, A. P.; Konovalov, O. V.; Napolskii, K. S. Evolution of pore ordering during anodizing of aluminum single crystals: In situ small-angle X-ray scattering study. *J. Phys. Chem. C* **2021**, *125*, 9287–9295.

(628) Gorisse, T.; Dupre, L.; Zelsmann, M.; Vlad, A.; Coati, A.; Garreau, Y.; Buttard, D. In situ investigation of the early-stage growth of nanoporous alumina. *J. Nanomater.* **2018**, *2018*, 6428271.

(629) Vinogradov, N. A.; Harlow, G. S.; Carla, F.; Evertsson, J.; Rullik, L.; Linpe, W.; Felici, R.; Lundgren, E. Observation of pore growth and self-organization in anodic alumina by time-resolved X-ray scattering. *ACS Appl. Nano Mater.* **2018**, *1*, 1265–1271.

(630) Evertsson, J.; Vinogradov, N. A.; Harlow, G. S.; Carla, F.; McKibbin, S. R.; Rullik, L.; Linpe, W.; Felici, R.; Lundgren, E. Self-organization of porous anodic alumina films studied in situ by grazing-incidence transmission small-angle X-ray scattering. *RSC Adv.* **2018**, *8*, 18980–18991.

(631) Harlow, G. S.; Drnec, J.; Wiegmann, T.; Lipe, W.; Evertsson, J.; Persson, A. R.; Wallenberg, R.; Lundgren, E.; Vinogradov, N. A. Observing growth under confinement: Sn nanopillars in porous alumina templates. *Nanoscale Adv.* **2019**, *1*, 4764–4771.

(632) Linpe, W.; Harlow, G. S.; Evertsson, J.; Hejral, U.; Abbondanza, G.; Lenrick, F.; Seifert, S.; Felici, R.; Vinogradov, N. A.; Lundgren, E. The state of electrodeposited Sn nanopillars within porous anodic alumina from in situ X-ray observations. *ACS Appl. Nano Mater.* **2019**, *2*, 3031–3038.

(633) Richter, K.; Bornmann, P. X-ray heating chamber investigations of reforming

$Pt-Al_2O_3$ catalysts. *Cryst. Res. Technol.* **1981**, *16*, 367–375.

(634) Ushakov, V.; Moroz, E. X-ray diffraction studies of reforming platinum-alumina catalysts in a high-temperature chamber. *React. Kinet. Catal. L.* **1985**, *27*, 351–355.

(635) Srinivasan, R.; De Angelis, R.; Davis, B. Alloy formation in Pt-Sn-Alumina Catalysts: In situ X-ray Diffraction Study. *J. Catal.* **1987**, *106*, 449–457.

(636) Xiong, Y. et al. Revealing the atomic ordering of binary intermetallics using in situ heating techniques at multilength scales. *Proc. Natl. Acad. Sci. U. S. A.* **2019**, *116*, 1974–1983.

(637) Zeng, W. J.; Wang, C.; Yan, Q. Q.; Yin, P.; Tong, L.; Liang, H. W. Phase diagrams guide synthesis of highly ordered intermetallic electrocatalysts: separating alloying and ordering stages. *Nat. Commun.* **2022**, *13*, 1–8.

(638) Schnepp, Z.; Danks, A. E.; Hollamby, M. J.; Pauw, B. R.; Murray, C. A.; Tang, C. C. In situ synchrotron X-ray diffraction study of the sol-gel synthesis of Fe3N and Fe3C. *Chem. Mater.* **2015**, *27*, 5094–5099.

(639) Chambers, M. S.; Hunter, R. D.; Hollamby, M. J.; Pauw, B. R.; Smith, A. J.; Snow, T.; Danks, A. E.; Schnepp, Z. In situ and ex situ X-ray diffraction and small-angle X-ray scattering investigations of the sol–gel synthesis of Fe_3N and Fe_3C. *Inorg. Chem.* **2022**, *61*, 6742–6749.

(640) Chattot, R.; Asset, T.; Drnec, J.; Bordet, P.; Nelayah, J.; Dubau, L.; Maillard, F. Atomic-scale snapshots of the formation and growth of hollow PtNi/C nanocatalysts. *Nano Lett.* **2017**, *17*, 2447–2453.

(641) Brant, W. R.; Li, D.; Gu, Q.; Schmid, S. Comparative analysis of ex-situ and operando X-ray diffraction experiments for lithium insertion materials. *J. Power Sources* **2016**, *302*, 126–134.

(642) Diaz-Lopez, M.; Cutts, G. L.; Allan, P. K.; Keeble, D. S.; Ross, A.; Pralong, V.; Spiekermann, G.; Chater, P. A. Fast *operando* X-ray pair distribution function using the DRIX electrochemical cell. *J. Synchrotron Radiat.* **2020**, *27*, 1190–1199.

(643) Villevieille, C.; Sasaki, T.; Novák, P. Novel electrochemical cell designed for operando techniques and impedance studies. *RSC Adv.* **2014**, *4*, 6782–6789.

(644) Suzuki, K. et al. High-energy X-ray compton scattering imaging of 18650-type lithium-ion battery cell. *Condens. Matter* **2019**, *4*, 66.

(645) Reimers, J. N.; Dahn, J. R. Electrochemical and in situ X-ray diffraction studies of lithium intercalation in Li_xCoO_2. *J. Electrochem. Soc.* **1992**, *139*, 2091–2097.

(646) Amatucci, G. G.; Tarascon, J. M.; Klein, L. C. CoO2, The end member of the Lix CoO2 solid solution. *J. Electrochem. Soc.* **1996**, *143*, 1114.

(647) Sottmann, J.; Pralong, V.; Barrier, N.; Martin, C. An electrochemical cell for *operando* bench-top X-ray diffraction. *J. Appl. Crystallogr.* **2019**, *52*, 485–490.

(648) Borkiewicz, O. J.; Shyam, B.; Wiaderek, K. M.; Kurtz, C.; Chupas, P. J.; Chapman, K. W. The AMPIX electrochemical cell: a versatile apparatus for *in situ* X-ray scattering and spectroscopic measurements. *J. Appl. Crystallogr.* **2012**, *45*, 1261–1269.

(649) Tripathi, A. M.; Su, W.-N.; Hwang, B. J. In situ analytical techniques for battery interface analysis. *Chem. Soc. Rev.* **2018**, *47*, 736–851.

(650) Jung, R.; Linsenmann, F.; Thomas, R.; Wandt, J.; Solchenbach, S.; Maglia, F.; Stinner, C.; Tromp, M.; Gasteiger, H. A.

Nickel, manganese, and cobalt dissolution from Ni-rich NMC and their effects on NMC622-graphite cells. *J. Electrochem. Soc.* **2019**, *166*, A378.

(651) Huang, J. J. et al. Disorder dynamics in battery nanoparticles during phase transitions revealed by operando single-particle diffraction. *Adv. Energy Mater.* **2022**, *12*, 2103521.

(652) Singer, A.; Ulvestad, A.; Cho, H.-M.; Kim, J. W.; Maser, J.; Harder, R.; Meng, Y. S.; Shpyrko, O. G. Nonequilibrium structural dynamics of nanoparticles in LiNi1/2Mn3/2O4 cathode under operando conditions. *Nano Lett.* **2014**, *14*, 5295–5300.

(653) Liang, G.; Hao, J.; D'Angelo, A. M.; Peterson, V. K.; Guo, Z.; Pang, W. K. A robust coin-cell design for in situ synchrotron-based X-ray powder diffraction analysis of battery materials. *Batter. Supercaps* **2021**, *4*, 380–384.

(654) Ghanty, C. et al. Li^+-ion extraction/insertion of Ni-rich $Li_{1+x}(Ni_yCo_zMn_z)_wO_2$ ($0.005<x<0.03$; y:z=8:1, $w\approx1$) electrodes: In situ XRD and raman spectroscopy study. *ChemElectroChem* **2015**, *2*, 1479–1486.

(655) Lu, X. et al. 3D microstructure design of lithium-ion battery electrodes assisted by X-ray nano-computed tomography and modelling. *Nat. Commun.* **2020**, *11*, 2079.

(656) Ziesche, R. F. et al. 4D imaging of lithium-batteries using correlative neutron and X-ray tomography with a virtual unrolling technique. *Nat. Commun.* **2020**, *11*, 777.

(657) Chianelli, R. R.; Scanlon, J. C.; Rao, B. M. L. Dynamic X-ray diffraction. *J. Electrochem. Soc.* **1978**, *125*, 1563–1566.

(658) Dahn, J. Structure and electrochemistry of Li1±yNiO2 and a new Li2NiO2 phase with the Ni (OH)2 structure. *Solid State Ion.* **1990**, *44*, 87–97.

(659) Borkiewicz, O. J.; Wiaderek, K. M.; Chupas, P. J.; Chapman, K. W. Best practices for operando battery experiments: Influences of X-ray experiment design on observed electrochemical reactivity. *Phys. Chem. Lett.* **2015**, *6*, 2081–2085.

(660) Thurston, T. R.; Jisrawi, N. M.; Mukerjee, S.; Yang, X. Q.; McBreen, J.; Daroux, M. L.; Xing, X. K. Synchrotron x-ray diffraction studies of the structural properties of electrode materials in operating battery cells. *Appl. Phys. Lett.* **1996**, *69*, 194–196.

(661) Martens, I.; Vostrov, N.; Mirolo, M.; Colalongo, M.; Kúš, P.; Richard, M.-I.; Wang, L.; Zhu, X.; Schülli, T. U.; Drnec, J. Revisiting phase transformation mechanisms in $LiNi_{0.5}Mn_{1.5}O_4$ high voltage cathodes with operando microdiffraction. *ACS Mater. Lett.* **2022**, *4*, 2528–2536.

(662) Whitehead, A. H.; Edström, K.; Rao, N.; Owen, J. R. In situ X-ray diffraction studies of a graphite-based Li-ion battery negative electrode. *J. Power Sources* **1996**, *63*, 41–45.

(663) Hatchard, T. D.; Dahn, J. R. In Situ XRD and electrochemical study of the reaction of lithium with amorphous silicon. *J. Electrochem. Soc.* **2004**, *151*, A838.

(664) Misra, S.; Liu, N.; Nelson, J.; Hong, S. S.; Cui, Y.; Toney, M. F. In situ X-ray diffraction studies of (de)lithiation mechanism in silicon nanowire anodes. *ACS Nano* **2012**, *6*, 5465–5473.

(665) Nelson, J.; Misra, S.; Yang, Y.; Jackson, A.; Liu, Y. J.; Wang, H. L.; Dai, H. J.; Andrews, J. C.; Cui, Y.; Toney, M. F. In operando X-ray diffraction and transmission X-ray microscopy of lithium sulfur batteries. *J. Am. Chem. Soc.* **2012**, *134*, 6337–6343.

(666) Lin, F. et al. Synchrotron X-ray analytical techniques for studying materials electrochemistry in rechargeable batteries. *Chem. Rev.* **2017**, *117*, 13123–13186.

(667) Matras, D. et al. Emerging chemical heterogeneities in a commercial 18650 NCA Li-ion battery during early cycling revealed by synchrotron X-ray diffraction tomography. *J. Power Sources* **2022**, *539*, 231589.

(668) Shearing, P. et al. Mapping internal temperatures during high-rate battery applications. *Nature* **2023**, *617*, 507–512.

(669) Harlow, J. E. et al. A wide range of testing results on an excellent lithium-ion cell chemistry to be used as benchmarks for new battery technologies. *J. Electrochem. Soc.* **2019**, *166*, A3031–A3044.

(670) Daubinger, P.; Schelter, M.; Petersohn, R.; Nagler, F.; Hartmann, S.; Herrmann, M.; Giffin, G. A. Impact of bracing on large format prismatic lithium-ion battery cells during aging. *Adv. Energy Mater.* **2021**, *12*, 2102448.

(671) Berhaut, C. L.; Dominguez, D. Z.; Kumar, P.; Jouneau, P.-H.; Porcher, W.; Aradilla, D.; Tardif, S.; Pouget, S.; Lyonnard, S. Multiscale multiphase lithiation and delithiation mechanisms in a composite electrode unraveled by simultaneous *operando* small-angle and wide-angle X-ray scattering. *ACS Nano* **2019**, *13*, 11538–11551.

(672) Berhaut, C. L. et al. Prelithiation of silicon/graphite composite anodes: Benefits and mechanisms for long-lasting Li-Ion batteries. *Energy Stor. Mater.* **2020**, *29*, 190–197.

(673) Möhl, G. E.; Metwalli, E.; Müller-Buschbaum, P. In operando small-angle X-ray scattering investigation of nanostructured polymer electrolyte for lithium-ion batteries. *ACS Energy Lett.* **2018**, *3*, 1525–1530.

(674) Wiaderek, K. M.; Borkiewicz, O. J.; Castillo-Martínez, E.; Robert, R.; Pereira, N.; Amatucci, G. G.; Grey, C. P.; Chupas, P. J.; Chapman, K. W. Comprehensive insights into the structural and chemical changes in mixed-anion FeOF electrodes by using operando PDF and NMR Spectroscopy. *J. Am. Chem. Soc.* **2013**, *135*, 4070–4078.

(675) Hua, X.; Robert, R.; Du, L.-S.; Wiaderek, K. M.; Leskes, M.; Chapman, K. W.; Chupas, P. J.; Grey, C. P. Comprehensive study of the CuF_2 conversion reaction mechanism in a lithium ion battery. *J. Phys. Chem. C* **2014**, *118*, 15169–15184.

(676) Key, B.; Morcrette, M.; Tarascon, J.-M.; Grey, C. P. Pair distribution function analysis and solid state NMR studies of silicon electrodes for lithium ion batteries: Understanding the (de)lithiation mechanisms. *J. Am. Chem. Soc.* **2010**, *133*, 503–512.

(677) Sottmann, J.; Di Michiel, M.; Fjellvåg, H.; Malavasi, L.; Margadonna, S.; Vajeeston, P.; Vaughan, G. B. M.; Wragg, D. S. Chemical structures of specific sodium ion battery components determined by operando pair distribution function and X-ray diffraction computed tomography. *Angew. Chem. Int. Ed.* **2017**, *56*, 11385–11389.

(678) Vitoux, L.; Reichardt, M.; Sallard, S.; Novák, P.; Sheptyakov, D.; Villevieille, C. A cylindrical cell for operando neutron diffraction of Li-ion battery electrode materials. *Front. Energy Res.* **2018**, *6*, Article 76.

(679) Taminato, S. et al. Real-time observations of lithium battery reactions—operando neutron diffraction analysis during practical operation. *Sci. Rep.* **2016**, *6*, 28843.

(680) Zhang, X.; van Hulzen, M.; Singh, D. P.; Brownrigg, A.; Wright, J. P.; van

Dijk, N. H.; Wagemaker, M. Direct view on the phase evolution in individual LiFePO4 nanoparticles during Li-ion battery cycling. *Nat. Commun.* **2015**, *6*, 8333.

(681) van Hulzen, M.; Ooms, F. G. B.; Wright, J. P.; Wagemaker, M. Revealing operando transformation dynamics in individual Li-ion electrode crystallites using X-Ray microbeam diffraction. *Front. Energy Res.* **2018**, *6*, Article 56.

(682) Ulvestad, A. P.; Singer, A.; Cho, H.-M.; Clark, J. N.; Harder, R.; Maser, J.; Meng, Y. S.; Shpyrko, O. G. Single particle nanomechanics in operando batteries via lensless strain mapping. *Nano Lett.* **2014**, *14*, 5123–5127.

(683) Assefa, T. A.; Suzana, A. F.; Wu, L.; Koch, R. J.; Li, L.; Cha, W.; Harder, R. J.; Bozin, E. S.; Wang, F.; Robinson, I. K. Imaging the phase transformation in single particles of the lithium titanate anode for lithium-ion batteries. *ACS Appl. Energy Mater.* **2021**, *4*, 111–118.

(684) Liu, T. et al. Origin of structural degradation in Li-rich layered oxide cathode. *Nature* **2022**, *606*, 305–312.

(685) Chao, S.-C.; Yen, Y.-C.; Song, Y.-F.; Chen, Y.-M.; Wu, H.-C.; Wu, N.-L. A study on the interior microstructures of working Sn particle electrode of Li-ion batteries by in situ X-ray transmission microscopy. *Electrochem. Commun.* **2010**, *12*, 234–237.

(686) Cahn, J. W.; Hilliard, J. E. Free energy of a nonuniform system. I. Interfacial free energy. *J. Chem. Phys.* **1958**, *28*, 258.

(687) Van der Ven, A.; Ceder, G. Lithium diffusion in layered Li_xCoO_2. *Electrochem. Solid-State Lett.* **1999**, *3*, 301.

(688) Gorobtsov, O. et al. Interaction and transformation of metastable defects in intercalation materials. *arXiv* **2021**, *2106*, 12145.

(689) Choi, S. et al. In situ strain svolution on Pt nanoparticles during hydrogen peroxide decomposition. *Nano Lett.* **2020**, *20*, 8541–8548.

(690) Kawaguchi, T.; Komanicky, V.; Latyshev, V.; Cha, W.; Maxey, E. R.; Harder, R.; Ichitsubo, T.; You, H. Electrochemically induced strain evolution in Pt–Ni alloy nanoparticles observed by Bragg coherent diffraction imaging. *Nano Lett.* **2021**, *21*, 5945–5951.

(691) Dupraz, M. et al. Imaging the facet surface strain state of supported multifaceted Pt nanoparticles during reaction. *Nat. Commun.* **2022**, *13*, 3003.

(692) Sheyfer, D.; Mariano, R. G.; Kawaguchi, T.; Cha, W.; Harder, R. J.; Kanan, M. W.; Hruszkewycz, S. O.; You, H.; Highland, M. J. Operando nanoscale imaging of electrochemically induced strain in a locally polarized Pt grain. *Nano Lett.* **2022**, *23*, 1–7.

(693) Hirayama, M.; Sakamoto, K.; Hiraide, T.; Mori, D.; Yamada, A.; Kanno, R.; Sonoyama, N.; Tamura, K.; Mizuki, J. Characterization of electrode/electrolyte interface using in situ X-ray reflectometry and LiNi0.8Co0.2O2 epitaxial film electrode synthesized by pulsed laser deposition method. *Electrochim. Acta* **2007**, *53*, 871–881.

(694) Hirayama, M. et al. Characterization of electrode/electrolyte interface for lithium batteries using in situ synchrotron X-ray reflectometry—A new experimental technique for LiCoO2 model electrode. *J. Power Sources* **2007**, *168*, 493–500.

(695) Hirayama, M.; Sonoyama, N.; Ito, M.; Minoura, M.; Mori, D.; Yamada, A.; Tamura, K.; Mizuki, J.; Kanno, R. Characterization of electrode/electrolyte interface with X-ray reflectometry and

epitaxial-film $LiMn_2O_4$ electrode. *J. Electrochem. Soc.* **2007**, *154*, A1065.

(696) Hirayama, M.; Ido, H.; Kim, K.; Cho, W.; Tamura, K.; Mizuki, J.; Kanno, R. Dynamic structural changes at LiMn2O4/electrolyte interface during lithium battery reaction. *J. Am. Chem. Soc.* **2010**, *132*, 15268–76.

(697) Yu, X.; Chen, X.; Buchholz, D. B.; Li, Q.; Wu, J.; Fenter, P. A.; Bedzyk, M. J.; Dravid, V. P.; Barnett, S. A. Pulsed laser deposition and characterization of heteroepitaxial LiMn2O4/La0.5Sr0.5CoO3 bilayer thin films as model lithium ion battery cathodes. *ACS Appl. Nano Mater.* **2018**, *1*, 642–653.

(698) Chattopadhyay, S.; Lipson, A. L.; Karmel, H. J.; Emery, J. D.; Fister, T. T.; Fenter, P. A.; Hersam, M. C.; Bedzyk, M. J. In situ X-ray study of the solid electrolyte interphase (SEI) formation on graphene as a model Li-ion battery anode. *Chem. Mater.* **2012**, *24*, 3038–3043.

(699) Fister, T. T.; Long, B. R.; Gewirth, A. A.; Shi, B.; Assoufid, L.; Lee, S. S.; Fenter, P. Real-time observations of interfacial lithiation in a metal silicide thin film. *J. Phys. Chem. C* **2012**, *116*, 22341–22345.

(700) Fister, T. T.; Esbenshade, J.; Chen, X.; Long, B. R.; Shi, B.; Schlepuetz, C. M.; Gewirth, A. A.; Bedzyk, M. J.; Fenter, P. Lithium intercalation behavior in multilayer silicon electrodes. *Adv. Energy Mater.* **2014**, *4*, 1301494/1.

(701) Evmenenko, G.; Fister, T. T.; Buchholz, D. B.; Li, Q.; Chen, K.-S.; Wu, J.; Dravid, V. P.; Hersam, M. C.; Fenter, P.; Bedzyk, M. J. Morphological evolution of multilayer Ni/NiO thin film electrodes during lithiation. *ACS Appl. Mater. Interfaces* **2016**, *8*, 19979–19986.

(702) Fister, T. T. et al. Dimensionally controlled lithiation of chromium oxide. *Chem. Mater.* **2016**, *28*, 47–54.

(703) Chen, X.; Fister, T. T.; Esbenshade, J.; Shi, B.; Hu, X.; Wu, J.; Gewirth, A. A.; Bedzyk, M. J.; Fenter, P. Reversible Li-ion conversion reaction for a TixGe alloy in a Ti/Ge multilayer. *ACS Appl. Mater. Interfaces* **2017**, *9*, 8169–8176.

(704) Evmenenko, G.; Warburton, R. E.; Yildirim, H.; Greeley, J. P.; Chan, M. K. Y.; Buchholz, D. B.; Fenter, P.; Bedzyk, M. J.; Fister, T. T. Understanding the role of overpotentials in lithium ion conversion reactions: Visualizing the interface. *ACS Nano* **2019**, *13*, 7825–7832.

(705) Kim, J. J. et al. Structural changes during the conversion reaction of tungsten oxide electrodes with tailored, mesoscale porosity. *ACS Nano* **2022**, *16*, 5384–5392.

(706) Cao, C. T.; Steinrck, H. G.; Shyam, B.; Toney, M. F. The atomic scale electrochemical lithiation and delithiation process of silicon. *Adv. Mater. Interfaces* **2017**, *4*, 1700771.

(707) Cao, C. T.; Steinruck, H. G.; Shyam, B.; Stone, K. H.; Toney, M. F. In situ study of silicon electrode lithiation with X-ray reflectivity. *Nano Lett.* **2016**, *16*, 7394–7401.

(708) Cao, C. T.; Abate, I. I.; Sivonxay, E.; Shyam, B.; Jia, C. J.; Moritz, B.; Devereaux, T. P.; Persson, K. A.; Steinruck, H. G.; Toney, M. F. Solid electrolyte interphase on native oxide-terminated silicon anodes for Li-ion batteries. *Joule* **2019**, *3*, 762–781.

(709) Cao, C. T. et al. Toward unraveling the origin of lithium fluoride in the solid electrolyte interphase. *Chem. Mater.* **2021**, *33*, 7315–7336.

(710) Steinruck, H. G.; Cao, C. T.; Veith, G. M.; Toney, M. F. Toward quantifying capacity losses due to solid electrolyte interphase evolution in silicon thin film batteries. *J. Chem. Phys.* **2020**, *152*, 084702.

(711) Cao, C.; Shyam, B.; Wang, J.; Toney, M. F.; Steinruck, H. G. Shedding X-ray light on the interfacial electrochemistry of silicon anodes for Li-ion batteries. *Acc. Chem. Res.* **2019**, *52*, 2673–2683.

(712) Linpe, W.; Harlow, G. S.; Larsson, A.; Abbondanza, G.; Ramisch, L.; Pfaff, S.; Zetterberg, J.; Evertsson, J.; Lundgren, E. An electrochemical cell for 2-dimensional surface optical reflectance during anodization and cyclic voltammetry. *Rev. Sci. Instrum.* **2020**, *91*, 044101.

(713) Linpe, W. et al. Revisiting optical reflectance from Au(111) electrode surfaces with combined high-energy surface X-ray diffraction. *J. Electrochem. Soc.* **2021**, *168*, 96511.

(714) Sokolowski-Tinten, K.; von der Linde, D. Ultrafast phase transitions and lattice dynamics probed using laser-produced x-ray pulses. *J. Condens. Matter Phys.* **2004**, *16*, R1517–R1536.

(715) Ihee, H.; Wulff, M.; Kim, J.; Adachi, S. Ultrafast X-ray scattering: structural dynamics from diatomic to protein molecules. *Int. Rev. Phys. Chem.* **2010**, *29*, 453–520.

(716) Hau-Riege, S. P. et al. Ultrafast transitions from solid to liquid and plasma states of graphite induced by X-ray free-electron laser pulses. *Phys. Rev. Lett.* **2012**, *108*, 217402.

(717) Singer, A. et al. Photoinduced enhancement of the charge density wave amplitude. *Phys. Rev. Lett.* **2016**, *117*, 056401–1 – 056401–6.

(718) Wingert, J. et al. Direct time-domain determination of electron-phonon coupling strengths in chromium. *Phys. Rev. B* **2020**, *102*, 041101.

TOC Graphic